

Analysis and Removal of Product Gas Contaminants Present in Gasification Processes

THÈSE N° 7673 (2017)

PRÉSENTÉE LE 28 AVRIL 2017

À LA FACULTÉ DE L'ENVIRONNEMENT NATUREL, ARCHITECTURAL ET CONSTRUIT
GROUPE LUDWIG
PROGRAMME DOCTORAL EN ENERGIE

ÉCOLE POLYTECHNIQUE FÉDÉRALE DE LAUSANNE

POUR L'OBTENTION DU GRADE DE DOCTEUR ÈS SCIENCES

PAR

Sven Philip EDINGER

acceptée sur proposition du jury:

Prof. F. Maréchal, président du jury
Prof. C. Ludwig, Dr A. Testino, directeurs de thèse
Prof. M. Seemann, rapporteur
Dr T. Schildhauer, rapporteur
Dr J. Van Herle, rapporteur



ÉCOLE POLYTECHNIQUE
FÉDÉRALE DE LAUSANNE

Suisse
2017

Du bist die Aufgabe.
Kein Schüler weit und breit.
— Franz K.

Summary

Energy demand and economic development are intrinsically linked. Earlier economic development came at the price of serious environmental pollution, posing a risk to life on earth. Thus, a transition from fossil to renewable energy is needed. Among the renewable energy technologies, gasification of biomass promises high process efficiency and flexibility concerning the feedstock and products.

In such a process, gas contaminants have to be removed to protect downstream equipment and the environment. Finding an optimal configuration of process steps in gas cleanup chains, offering reliability, availability and high efficiency at low operating and capital costs is still a challenge and one of the major hurdles for commercial deployment of biomass gasification processes.

This thesis aimed to investigate the gas cleanup chain as part of gasification processes. Two aspects, the analysis of gas contaminants and their elimination, were examined. At first, three analytical methods, aimed at the detection of sulphur containing hydrocarbons, tars and trace elements, were developed. In the next step, these analytical tools were employed to investigate the performance of gas cleanup units, intended for the removal of the sulphur containing hydrocarbon thiophene, tars and the trace element Se.

The removal of thiophene by activated carbons (AC) was explored experimentally and theoretically. Experiments were performed in a packed bed column between 100-200 °C. The adsorption process was described by a 1D approach, including mass transfer phenomena and axial dispersion. Experimental validation showed good agreement between measured and predicted breakthrough times and capacities. A global sensitivity analysis (GSA) was performed to rank the importance of model input factors and gain further process insight. The work showed that ACs are a promising option for thiophene removal and provided a generic approach for the application of GSA to adsorption models. In this context, the analysis demonstrated that the selection of common model assumptions deserves as much attention as the model parameters.

Further work chapter aimed at understanding the effect of H_2O , H_2 and H_2S on the decomposition of thiophene over CaO . Experiments were performed in a fixed bed reactor at 810 °C. The factors were varied as part of a full factorial design at two levels. Results were fitted to a linear model with interactions. Analysis showed that H_2O and H_2S had a major effect on thiophene conversion, while that of H_2 was less pronounced. Interactions between varied factors were found to be negligible.

A UV-Vis method was developed to obtain online information on tar compound concentrations in real process gases in the low ppmv region. Spectra were analysed for their tar composition by two chemometric approaches. Applied to two case studies, the developed method proved to be a rapid, sensitive tool, applicable to qualitative process monitoring with the added benefit of quantification in gases with a limited number of tar compounds.

An ICP-MS was employed as a tool for the online detection of trace elements. The low detection limits (< 2 ppbv for H_2Se , PH_3 ; < 0.1 ppbv for AsH_3 ; < 0.01 ppbv for Hg) and the high temporal resolution render this method a quick and robust tool for the performance evaluation of sorbent materials. A case study investigated the capture of H_2Se by a $\text{Zn}/\text{Al}_2\text{O}_3$ sorbent between 150 - 350°C . While the support could retain H_2Se at dry reaction conditions, a Zn phase was needed for its capture in steam laden gas.

Keywords: Gasification; Producer gas; Renewable energy; Biomass; Coal; Contaminant; Sulphur; Thiophene; Tar; Trace element; Selenium; Online; UV-Vis; Classical least squares; Partial least squares; ICP-MS; Gas cleanup; Activated carbon; Catalyst; Limestone; Zinc; Sorption; Global sensitivity analysis; Adsorption model; Breakthrough curve; Fixed bed

Zusammenfassung

Energieverbrauch und wirtschaftliche Entwicklung sind eng miteinander verknüpft. Die bisherige wirtschaftliche Entwicklung basierte vorwiegend auf fossile Energien, deren Nutzung nachteilige Auswirkungen auf unsere Umwelt heute hat. Um diese Auswirkungen zukünftig zu minimieren, ist ein Umstieg auf erneuerbare Ressourcen nötig. Die Vergasung von Biomasse ist eine Technologie, welche einen hohen Wirkungsgrad bei gleichzeitig vielfältigen Einsatzmöglichkeiten bietet.

Die Verunreinigungen, die in diesem Vergasungsprozess im Produktgas auftreten, erfordern eine Gasreinigung um nachgeschaltete Anlagen und die Umwelt zu schonen. Eine optimale Kombination von Prozesseinheiten zu einer Reinigungsstufe, die zuverlässig und energieeffizient ist, aber gleichzeitig niedrige Investitions- und Betriebskosten aufweist, bleibt allerdings weiterhin eine Hürde für die Verbreitung von Biomassevergasungsprozessen.

Ziel dieser Arbeit war die Untersuchung der Gasreinigungskette in Vergasungsprozessen. Als Teil davon wurde einerseits die Analyse von Gasverunreinigungen und andererseits deren Abtrennung betrachtet. Dafür wurden drei analytische Methoden zur Detektion von schwefelhaltigen Kohlenwasserstoffen, Teeren und Spurenelementen entwickelt. Basierend auf diesen Methoden wurde die Reinigung von Thiophen als einem Repräsentanten von schwefelhaltigen Kohlenwasserstoffen sowie die Reinigung von Teeren und dem Spurenelement Selen analysiert.

Die Adsorption von Thiophen auf Aktivkohle wurde experimentell und mit Hilfe eines Modells untersucht. Experimente wurden in einem Festbettreaktor bei Temperaturen von 100-200 °C durchgeführt. Darauffolgend wurde die Thiophenabscheidung durch ein eindimensionales Modell unter Berücksichtigung von Stofftransport- und Dispersionseffekten beschrieben. Eine Validierung des Modells zeigte eine gute Übereinstimmung mit den experimentellen Ergebnissen. Ausgehend von diesem Modell wurde eine globale Sensitivitätsanalyse durchgeführt, um den Einfluss diverser Eingangsparameter auf die Durchbruchskurve zu evaluieren und ein besseres Modellverständnis zu erlangen.

Nachfolgend wurde der Einfluss von H_2O , H_2 und H_2S auf den Abbau von Thiophen über CaO bei 810 °C in einem Festbettreaktor ermittelt. Die Einflussparameter wurden entsprechend eines vollfaktoriellen Versuchsplans variiert und der resultierende Thiophenumsatz durch ein lineares Modell mit Interaktionen beschrieben. Eine Analyse des Modells zeigt, dass H_2O und H_2S einen bedeutenden und H_2 einen kleineren negativen Einfluss auf den Thiophenabbau haben. Eine Interaktion der Eingangsparameter konnte dabei nicht nachgewiesen werden.

Die online Detektion von Teerkomponenten im niedrigen Konzentrationsbereich in Prozessgasen wurde durch eine neu entwickelte UV-Vis Methode ermöglicht. Die bei der Messung erfassten Spektren wurden auf den Gehalt einzelner Teerspezies hin mit Hilfe von zwei che-

mometrischen Methoden überprüft. Die anschließende Überprüfung der Fähigkeiten der entwickelten Methode in zwei Fallstudien zeigte, dass sie ein wertvolles Hilfsmittel zur Prozessüberwachung ist und im Fall von Gasen mit einer geringen Anzahl von Teerkomponenten auch deren Quantifizierung ermöglicht.

Basierend auf einem Massenspektrometer mit induktiv gekoppeltem Plasma (ICP-MS) wurde anschließend eine Methode zur Detektion von Spurenelementen in Prozessgasen entwickelt und angewendet. Niedrige Nachweisgrenzen (< 2 ppbv für H_2Se , PH_3 ; < 0.1 ppbv für AsH_3 ; < 0.01 ppbv für Hg) und eine hohe zeitliche Auflösung ermöglichen eine effiziente Überprüfung der Materialien hinsichtlich ihrer Sorptionseigenschaften. In einem Fallbeispiel wurde dabei die Sorption von H_2Se auf $\text{Zn}/\text{Al}_2\text{O}_3$ zwischen $150\text{--}350^\circ\text{C}$ analysiert. Während das Trägermaterial H_2Se in trockenen Bedingungen zurückhalten konnte, war eine Zinkphase nötig, um dies auch in wasserdampfbeladenem Gas zu ermöglichen.

Stichwörter: Vergasung; Produktgas; Erneuerbare Energie; Biomasse; Kohle; Verunreinigung; Schwefel; Thiophen; Teer, Spurenelement; Selen; Online; UV-Vis; Classical least squares; Partial least squares; ICP-MS; Gasreinigung; Aktivkohle; Katalysator; Kalkstein; Zink; Sorption; Globale Sensitivitätsanalyse; Adsorptionsmodell; Durchbruchskurve; Festbett

Résumé

La demande d'énergie et le développement économique sont intrinsèquement liés. En effet, l'impact du développement économique sur l'environnement est si grave qu'il représente aujourd'hui un risque pour la vie sur terre. Ceci a donc nécessité la transition de l'énergie fossile à l'énergie renouvelable. Figurant parmi la liste des technologies d'énergie renouvelable, la gazéification de la biomasse est une technologie qui promet une grande efficacité et flexibilité, et ceci par la possibilité d'utiliser divers types de matière première ainsi que d'obtenir une large gamme de produits.

Cependant, les contaminants gazeux produits moyennant ce procédé doivent être éliminés pour protéger les équipements de l'installation ainsi que l'environnement. Trouver une configuration optimale des chaînes de nettoyage de gaz, qui soit à la fois fiable, efficace mais aussi disponible à des coûts de fonctionnement et d'investissement relativement faibles, est l'un des principaux obstacles à la réalisation commerciale de cette technologie.

Cette thèse présente ainsi à étudier la chaîne de nettoyage des gaz dans les processus de gazéification, et en particulier deux aspects : l'analyse des contaminants gazeux et leur élimination. En un premier temps, trois méthodes analytiques visant à détecter le soufre dans les hydrocarbures, les goudrons et les éléments traces ont été développées. Par la suite, ces outils analytiques ont été utilisés pour étudier la performance des unités de nettoyage de gaz, destinées à l'élimination du soufre sous forme de thiophène dans les hydrocarbures, des goudrons et de l'éléments-trace Se.

L'élimination du thiophène par les charbons activés (AC) a été explorée expérimentalement et théoriquement. Les expériences ont été effectuées à une température comprise entre 100-200 °C dans une colonne garnie de AC. L'adsorption a été décrite par l'approche 1D, incluant les phénomènes de transfert de masse et de dispersion axiale. La validation expérimentale a démontré un bon accord entre les valeurs mesurées et les valeurs prédites du temps de perçage et des capacités. Une analyse de sensibilité globale (GSA) a été performée pour classer l'importance des facteurs d'entrée du modèle et obtenir ainsi de plus amples informations sur le processus. Ce travail a démontré que les AC représentent une option prometteuse pour l'élimination du thiophène et a fourni également une approche pour l'application de la GSA aux modèles d'adsorption. Dans ce contexte, l'analyse a démontré que la sélection des hypothèses communes du modèle mérite autant d'attention que les paramètres du modèle.

Un chapitre de travail supplémentaire visant à comprendre l'effet des molécules H_2O , H_2 et H_2S sur la décomposition du thiophène en présence de l'oxyde de calcium CaO est présenté dans cette thèse. Les expériences ont été effectuées dans un réacteur à lit fixe à 810 °C. Les facteurs ont été modifiés dans le cadre d'un plan factoriel complet à deux niveaux. Les résultats ont été adaptés à un modèle linéaire avec interactions. L'analyse a démontré que H_2O et H_2S ont un effet majeur sur la conversion du thiophène, tandis que l'effet du H_2 était moins prononcé. Les interactions entre les facteurs ont été jugées négligeables.

Une méthode UV-Vis a été développée pour obtenir des informations en temps réel sur les concentrations de composés goudronnés (à des faibles concentrations en ppmv) qui sont détectés dans le gaz. Les spectres obtenus ont été analysés par deux approches chimiométriques. Appliqués aux deux études de cas, les outils développés au cours de ce travail étaient rapides et sensibles et sont donc applicables à la surveillance qualitative des processus avec comme avantage, la possibilité de quantifier un nombre limité de composés goudronnés présents dans le gaz.

La méthode ICP-MS est utilisée pour la détection en ligne d'éléments traces. La basse limite de détection (< 2 ppbv pour le H_2Se et le PH_3 ; < 0.1 ppbv pour le AsH_3 ; < 0.01 ppbv pour le Hg) et la haute résolution temporelle font de cette technique un outil rapide et robuste pour l'évaluation de la performance d'un matériau adsorbant. Une étude des cas a été effectuée pour la capture du H_2Se par un adsorbent à base de $\text{Zn}/\text{Al}_2\text{O}_3$ entre 150 - 350 °C. Tandis que le support retenait le H_2Se sous conditions sèches, une phase de Zn était nécessaire pour l'adsorption à partir d'un gaz chargé de vapeur d'eau.

Mots-clés : Gazéification ; Gaz de synthèse ; Énergie renouvelable ; Biomasse ; Charbon ; Impureté ; Soufre ; Thiophène ; Goudron ; Trace ; Sélénium ; En ligne ; UV-Vis ; Classical least squares ; Partial least squares ; ICP-MS ; Épuration des émissions gazeuses ; Charbon actif ; Catalyseur ; Calcaire ; Zinc ; Sorption ; Analyse de sensibilité globale ; Courbe de perçage ; Colonne d'absorption

Contents

| | |
|--|--------------|
| Summary (English / Deutsch / Français) | v |
| Contents | xi |
| Nomenclature | xiii |
| Acronyms | xviii |
| 1 Introduction | 1 |
| 1.1 Motivation | 3 |
| 1.1.1 A global perspective | 3 |
| 1.1.2 Emission mitigation | 4 |
| 1.1.3 Biomass gasification | 4 |
| 1.2 Objectives. | 10 |
| 1.3 Thesis outline. | 10 |
| 1.4 Author's contributions | 11 |
| References | 12 |
| 2 Experimental setups | 21 |
| 2.1 Gasmix setup | 23 |
| 2.2 Trace element setup. | 25 |
| References | 28 |
| 3 Adsorption of thiophene by activated carbon | 29 |
| 3.1 Introduction | 33 |
| 3.2 Theoretical section | 35 |
| 3.2.1 Model description | 35 |
| 3.2.2 Sensitivity analysis. | 40 |
| 3.2.3 Key figures | 44 |
| 3.2.4 Implementation | 44 |
| 3.3 Experimental section | 46 |
| 3.3.1 Material | 46 |
| 3.3.2 Experimental procedure | 46 |
| 3.3.3 Analytical method | 46 |
| 3.4 Results and discussion | 48 |
| 3.4.1 Adsorption isotherm modeling | 48 |
| 3.4.2 Breakthrough curve results. | 48 |
| 3.4.3 Sensitivity analysis. | 52 |
| References | 56 |

| | |
|--|------------|
| 4 High temperature conversion of thiophene over CaO | 63 |
| 4.1 Introduction | 67 |
| 4.2 Experimental section | 68 |
| 4.2.1 Material | 68 |
| 4.2.2 Experimental procedure | 68 |
| 4.2.3 Design of experiments | 68 |
| 4.3 Results and discussion | 72 |
| 4.3.1 Material characterization | 72 |
| 4.3.2 Testing criteria | 72 |
| 4.3.3 Effects of factors on thiophene conversion. | 75 |
| References | 77 |
| 5 Online tar measurement by UV-Vis spectroscopy | 81 |
| 5.1 Introduction | 85 |
| 5.2 Experimental section | 88 |
| 5.2.1 Chemicals | 88 |
| 5.2.2 Sampling system. | 88 |
| 5.2.3 UV-Vis apparatus | 91 |
| 5.2.4 Case studies | 92 |
| 5.2.5 Tar quantification | 93 |
| 5.3 Results and discussion | 97 |
| 5.3.1 Model gas | 97 |
| 5.3.2 Real producer gas | 100 |
| References | 103 |
| 6 Detection and retention of selenium | 107 |
| 6.1 Introduction | 111 |
| 6.1.1 Gas matrix | 112 |
| 6.1.2 Matrix effects | 113 |
| 6.2 Experimental section | 115 |
| 6.2.1 Analytical method | 115 |
| 6.2.2 Sorbent material | 116 |
| 6.2.3 Experimental procedures | 116 |
| 6.3 Results and discussion | 119 |
| 6.3.1 Analytical performance | 119 |
| 6.3.2 H ₂ Se capture by Zn/Al ₂ O ₃ | 123 |
| References | 131 |
| 7 Concluding remarks | 137 |
| 7.1 Conclusions. | 139 |
| 7.2 Outlook | 141 |
| References | 144 |
| A Co-Authorships | 147 |
| Publication 1. | 149 |
| Publication 2. | 153 |
| References | 156 |

| | |
|--|------------|
| B Adsorption of thiophene by activated carbon | 157 |
| B.1 Model flow chart | 158 |
| B.2 Experimental results | 159 |
| B.3 Convergence plots | 160 |
| B.4 Numerical results of sensitivity analysis. | 161 |
| B.5 EE plots without Henry isotherm | 161 |
| B.6 Parallel coordinate plots | 162 |
| B.7 Effect of temperature on breakthrough behaviour | 164 |
| B.8 EE on model variables | 165 |
| References | 169 |
| C High temperature conversion of thiophene over CaO | 171 |
| C.1 SEM pictures | 171 |
| D Online tar measurement by UV-Vis spectroscopy | 173 |
| D.1 Experimental equipment | 173 |
| D.2 Partial least squares calibration | 175 |
| D.3 Results of model gas case study | 178 |
| D.4 Online gas phase tar measurement by UV-Vis spectroscopy. | 180 |
| D.4.1 Experimental | 180 |
| D.4.2 Results | 180 |
| E Detection and retention of selenium | 183 |
| E.1 Estimation of expected Se emission limitation | 183 |
| E.2 Literature overview of matrix effects | 183 |
| E.3 Spectral analysis of signals measured with setup 2 | 186 |
| E.4 Calculation of physical properties of flow through sorbent bed | 188 |
| E.5 Equilibrium constants | 188 |
| E.6 Sorbent characterization | 189 |
| E.7 Influence of operating conditions on sorbent capacity | 191 |
| E.8 Online detection of trace contaminants. | 193 |
| E.8.1 Experimental | 193 |
| E.8.2 Results | 193 |
| References | 196 |
| List of publications | 199 |
| Acknowledgements | 201 |
| Curriculum Vitæ | 203 |

Nomenclature

Roman Letters

| | |
|------------------|--|
| A_{SSA} | specific surface area ($\text{m}^2 \text{kg}^{-1}$) |
| a | effect |
| a_v | specific surface area (m^{-1}) |
| b, b_{Tref} | Langmuir equilibrium constant, its pre-exponential factor ($\text{m}^3 \text{mol}^{-1}$) |
| Bo | Bodenstein number ($L_{Bed} u_s / D_{ax}$) |
| Ca | Carberry number (-) |
| c | thiophene gas phase concentration (mol m^{-3}) |
| $c_{p,c}$ | heat capacity of AC ($\text{kJ kg}^{-1} \text{K}^{-1}$) |
| $c_{p,g}$ | heat capacity of gas ($\text{J mol}^{-1} \text{K}^{-1}$) |
| d_{cyl} | cylinder diameter (m) |
| d_p | particle diameter (m) |
| d_{SSA} | volume surface mean diameter (m) |
| d_t | reactor diameter (m) |
| D_{ax} | axial dispersion coefficient ($\text{m}^2 \text{s}^{-1}$) |
| D_K | Knudsen diffusivity ($\text{m}^2 \text{s}^{-1}$) |
| D_m | molecular diffusivity of $\text{C}_4\text{H}_4\text{S}$ in Ar ($\text{m}^2 \text{s}^{-1}$) |
| $D_{m,eff}$ | effective molecular diffusivity ($\text{m}^2 \text{s}^{-1}$) |
| D_p | particle diffusivity ($\text{m}^2 \text{s}^{-1}$) |
| EE | elementary effect |
| f | fitting parameter |
| F | molar flow (mol s^{-1}) |
| h_{cyl} | cylinder height (m) |
| I | intensity |
| k | mass transfer coefficient (s^{-1}) |
| k_{EE} | number of input factors (-) |
| k_f | film mass transfer coefficient (m s^{-1}) |
| K_H, K_{HTref} | Henry constant, its pre-exponential factor ($\text{m}^3 \text{kg}^{-1}$) |
| k_r | reaction rate constant |
| K_T, K_{TTref} | Tóth isotherm parameter, its pre-exponential factor ($\text{m}^3 \text{kg}^{-1}$) |
| l | reaction order (-) |
| L | bed length (m) |
| m_{Bed} | bed mass (kg) |
| m_{cyl} | mass of cylinder content (kg) |
| \bar{M} | molecular weight (g mol^{-1}) |
| $n_{Se,cap}$ | molar amount Se captured (mol) |
| n_T, n_{TTref} | Tóth isotherm heterogeneity parameter, its pre-exponential factor (-) |
| n_{ZnO} | molar amount of ZnO (mol) |
| p | total pressure (Pa) |
| Pe | particle Péclet number ($d_p u_i / D_{ax}$) |

| | |
|----------------------|---|
| Pe_m | bed Péclet number (Lu_i/D_{ax}) |
| Pe_∞ | parameter in axial dispersion correlation (-) |
| q | average solid phase concentration of C_4H_4S (mol kg^{-1}) |
| q^* | particle surface equilibrium concentration (mol kg^{-1}) |
| q_{90} | sorption capacity until t_{90} (mol kg^{-1}) |
| q_{mL} | saturation value of Langmuir isotherm (mol kg^{-1}) |
| q_{mT}, q_{mTTref} | saturation value of Tóth isotherm, its pre-exponential factor (mol kg^{-1}) |
| q_{Se} | Se sorption capacity (g kg^{-1}) |
| Q | dimensionless solid phase concentration (-) |
| Q^* | dimensionless particle surface equilibrium concentration (-) |
| Q_1, Q_3 | lower quartile (Q_1) and upper quartile (Q_3) (-) |
| R^2_{adj} | adjusted coefficient of determination (-) |
| r_e | pore radius (m) |
| r_{EE} | number of EE (-) |
| $r_{C_4H_4S}$ | thiophene reaction rate ($\text{mol s}^{-1} \text{kg}^{-1}$) |
| Re_p | Reynolds number ($u_s d_p / \nu_{Ar}$) |
| R_g | gas constant ($\text{J mol}^{-1} \text{K}^{-1}$) |
| s_{50} | slope of breakthrough curve at t_{50} (min^{-1}) |
| $s_{90,10}$ | slope of breakthrough curve $s_{90,10} = 0.8 / (t_{90} - t_{10})$ (min^{-1}) |
| s_{cal} | slope of calibration curve |
| Sc | Schmidt number (ν_{Ar} / D_m) |
| Sh | Sherwood number ($k_f d_p / D_m$) |
| STD_{EE} | standard deviation of EE |
| T | reactor temperature (K) |
| T_{ref} | reference temperature (273 K) |
| t | time (s) |
| t_i | breakthrough time with $i = 100 \times c / c_0$ (min) |
| u_{iv} | interstitial velocity (m s^{-1}) |
| u_s | superficial velocity (m s^{-1}) |
| \dot{V} | flow rate (Nml min^{-1}) |
| V_m | molar volume ($\text{m}^3 \text{mol}^{-1}$) |
| $\dot{V}_{tot,n}$ | total gas flow rate at standard conditions (Nml min^{-1}) |
| V_{cyl} | cylinder diameter (m^3) |
| w_{H_2O} | mass fraction of water (-) |
| x | coded factor |
| X^a | core matrix of EE method |
| X^{ab} | ray matrix of EE method |
| $X_{C_4H_4S}$ | thiophene conversion (-) |
| X_{ZnO} | ZnO conversion (-) |
| y | thiophene gas phase molar fraction (ppmv) |
| Y | model output |
| y_{H_2O} | steam content (vol%) |
| z | distance from bed inlet (m) |

Greek Letters

| | |
|----------------------|---|
| α | parameter defining the temperature dependency of n_T (-) |
| γ_1, γ_2 | parameters in axial dispersion correlation |
| ΔH | heat of adsorption (J mol^{-1}) |
| ΔH° | enthalpy of reaction (J mol^{-1}) |
| Δp | pressure drop (Pa) |
| ΔT | temperature difference (K) |
| ϵ | voidage (-) |
| ζ | dimensionless concentration (-) |
| ξ | dimensionless axial distance (-) |
| ν_{Ar} | kinematic viscosity of Ar ($\text{m}^2 \text{s}^{-1}$) |
| ν_{mix} | kinematic viscosity of gas mixture ($\text{m}^2 \text{s}^{-1}$) |
| ρ | density (kg m^{-3}) |
| ρ_s | skeletal density (kg m^{-3}) |
| τ | dimensionless time (tu_s/L_{Bed}) |
| τ_{tor} | tortuosity factor (-) |
| σ | standard deviation |
| Φ | fractional yield (-) |
| χ | parameter defining the temperature dependency of q_{mT} (-) |
| Ω | Wheeler-Weisz modulus (-) |

Subscripts

| | |
|-----------|-----------------------|
| 0 | inlet condition |
| b | bulk |
| bt | breakthrough |
| blk | blank |
| H | Henry isotherm |
| i | sequence number |
| j | sequence number |
| liq | liquid |
| L | Langmuir isotherm |
| p | particle |
| ref | reference |
| s | surface |
| T | Tóth isotherm |
| T_{ref} | reference temperature |
| v | on volume basis |
| χ | concentration limit |

Superscripts

| | |
|-------|---------------------|
| 0 | inlet condition |
| obs | observed |
| s | standard conditions |

Acronyms

| | |
|-----------|---|
| AC | activated carbon |
| BET | Brunauer-Emmett-Teller |
| BJH | Barrett-Joyner-Halenda |
| CCS | carbon capture and storage |
| CLS | classical least squares |
| cps | counts per second |
| CST | cold solvent trapping |
| DME | dimethyl ether |
| EE | elementary effect |
| EI | electron impact |
| EPA | environmental protection agency |
| ETV | electro-thermal vaporisation |
| FID | flame ionization detector |
| FT | Fischer Tropsch |
| GC/IT-MS | gas chromatography/ion trap mass spectrometry |
| GC-FID | gas chromatography - flame ionization detection |
| GC-MS | gas chromatography - mass spectrometry |
| GDP | gross domestic product |
| GHG | greenhouse gas |
| GSA | global sensitivity analysis |
| HDS | hydrodesulphurization |
| HGC | hot gas cleanup |
| IC | internal combustion |
| ICP-MS | inductively coupled plasma mass spectrometer |
| ICP-OES | inductively coupled plasma atomic emission spectroscopy |
| IGCC | integrated gasification combined cycle |
| IMR | ion molecule reaction |
| KIT | Karlsruhe institute of technology |
| LA-ICP-MS | laser ablation inductively coupled mass spectrometer |
| LDF | linear driving force |
| LH | latin hypercube |
| LIF | laser-induced fluorescence |
| LOD | limit of detection |
| MB | molecular-beam |
| MCR-ALS | multivariate curve resolution-alternating least squares |
| MDEA | methyldiethanolamine |
| MFC | mass flow controller |
| MOL | method of lines |
| MS | mass spectrometer |
| MTBE | methyl tert-butyl ether |

| | |
|---------|--|
| NTUA | national technical university of Athens |
| OAT | one-factor-at-a-time |
| OECD | organisation for economic co-operation and development |
| ORS | octopole reaction system |
| PDE | partial differential equation |
| PEEK | polyetheretherketon |
| PID | photo ionization detection |
| PLS | partial least squares |
| ppbv | parts per billion by volume |
| ppmv | parts per million by volume |
| PSI | Paul Scherrer institute |
| PTFE | polytetrafluorethylen |
| RDD | rotary disk diluter |
| REMPI | resonance-enhanced multiphoton ionization |
| REP | relative error of prediction |
| RF | radio frequency |
| RME | rapeseed methyl ester |
| RMSE | root mean squared error |
| RMSE-CV | root mean squared error of cross-validation |
| RMSE-P | root mean squared error of prediction |
| RSD | relative standard deviation |
| SA | sensitivity analysis |
| SEM | scanning electron microscope |
| SNG | synthetic natural gas |
| SOFC | solid oxide fuel cell |
| SPA | solid phase adsorption |
| SPI | single photon ionization |
| SSA | specific surface area |
| STD | standard deviation |
| SV | switch valve |
| TDA | tar dew point analyser |
| THT | tetrahydrothiophene |
| TRA | time resolved analysis |
| VIF | variance inflation factor |
| XRD | X-ray diffraction |

1

Introduction

1.1. Motivation

1.1.1. A global perspective

FOR centuries, energy has been a driving force for our civilization. Its easy availability helped to progress industry, transport and other sectors. A measure of this intrinsic link between economic growth and energy consumption is the energy intensity, defined as energy consumption per unit of GDP¹. This measure takes a seemingly unbreakable pattern over time in form of a skewed bell curve. As an economy evolves its energy intensity first rises, peaks and then slowly declines again, thereby tracking the different steps of economic development.

If this function is applied to current developing countries and the hunger for energy is satisfied by fossil fuels, the projected CO₂ emissions will be immense. This trend has therefore the potential to far outweigh efforts already undertaken by some OECD countries to lower their energy intensity for a variety of reasons including energy security, local air quality and global warming. If so, the goal to limit global warming to 2 °C will be a very distant one². The aim is therefore to balance the perceived right of developing countries to gain prosperity on the one hand and the justifiable cause of wealthier countries to preserve and protect the environment, something that should be in interest of mankind.

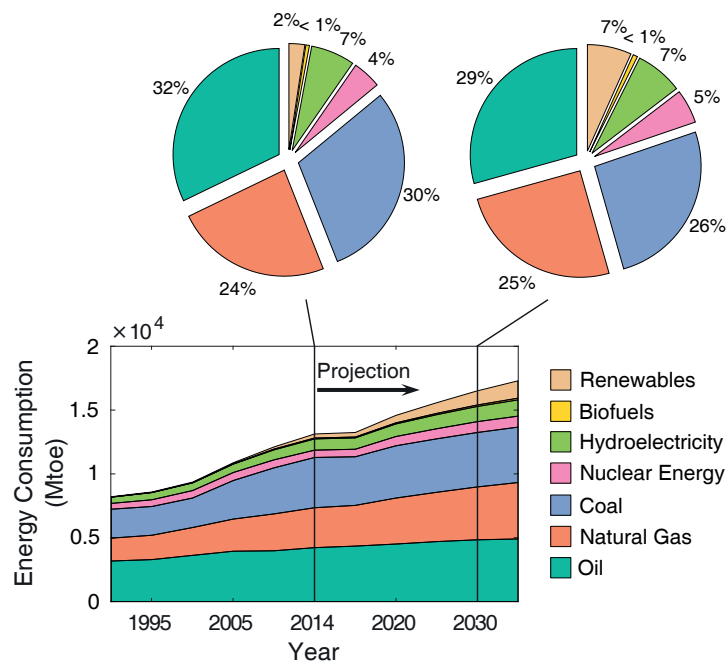


Figure 1.1 – Worldwide primary energy consumption by fuel (plot created with data from³)

The outlined dilemma can be further illustrated by a projection of the worldwide energy mix until the year 2035, given in Fig. 1.1³. Though the validity of such forecasts may be challenged, two important implications can nevertheless be derived: The overall primary energy consumption in future is likely to increase rather than stagnate or even recede. And at the same time, fossil fuels will remain an important part of the global energy mix as emerging countries strive for affordable, reliable energy.

1

1.1.2. Emission mitigation

An approach to solve this problem is to take different measures at different time scales. In the short-term, one will have to deal with the negative impacts of fossil fuel utilization on the environment. Measures will not only have to include the reduction in CO₂ emissions (e.g. by CCS) but also the emission control of trace elements such as Hg, Se or As⁴. In the mid- to long-term future, however, one has to try to break the above described pattern as well as shift the energy supply from fossil fuels to renewable alternatives which include solar, wind, biomass and hydro-power.

Several features of biomass make it stand out from the other candidates. Because it already is an important energy source, a basic supply infrastructure exists. Especially in African and Asian countries it is used for heating and cooking and accounts, as a consequence, for more than one third of the total energy consumption. Compared to fossil fuels, biomass is more uniformly distributed over the world which can be advantageous when energy security and logistics are considered. Moreover, it is easily storable (e.g. wood), thereby making its availability less dependent on weather, the time of day or season.

While combustion is the prevailing method for biomass use today⁵, other processes promise distinct advantages. As such, the gasification of biomass offers higher process efficiencies and overall system flexibility⁶. The process allows, on one hand, to utilize different types of biomass as feedstock. On the other, it can provide a range of useful products in form of electricity, heat and chemicals⁷. The latter include synthetic natural gas (SNG), H₂, Fischer-Tropsch (FT) liquids, methanol and its derivatives (methyl *tert*-butyl ether (MTBE) and dimethyl ether (DME))⁸.

1.1.3. Biomass gasification

The basic concept of a classic gasification process chain is given in Fig. 1.2. Initial conversion of the feedstock takes place in a reactor called gasifier. Several reactor configurations with individual sets of disadvantages and advantages exist. An extensive overview has been compiled by Sikarwar et al.⁹.

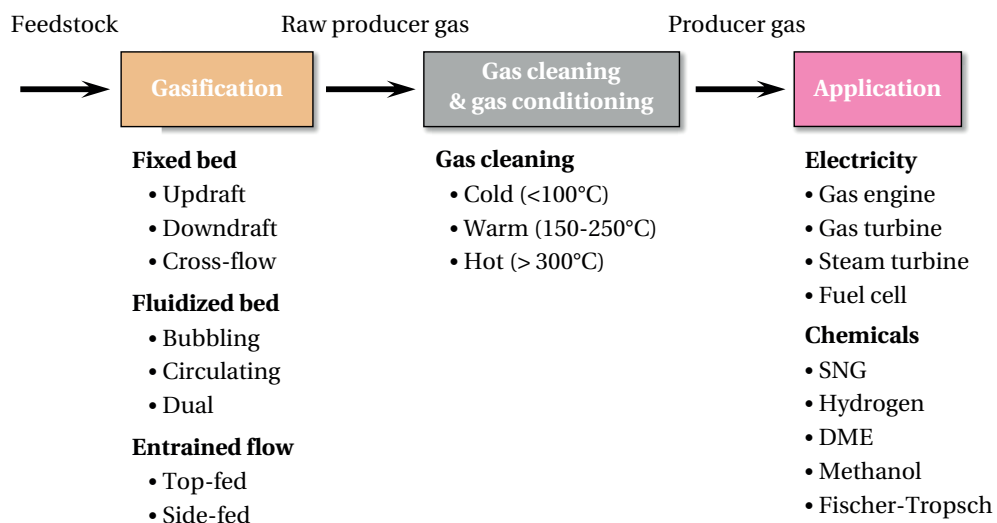


Figure 1.2 – Generic representation of classic gasification processes

Though the geometry may alter, the reaction principle of gasification itself remains. It consists of a series of steps which take place between 600 to 1000 °C and include drying of the feedstock, pyrolysis to give pyrolysis gas, tars and solid char residue and then further reaction of the pyrolysis products^{10,11}. The gasifying medium driving these reactions consists of air, O₂, steam, CO₂ or a mixture thereof. The composition of the resulting so called raw producer gas depends on the feedstock, type of gasifier, operating conditions and the presence of a catalyst or sorbent¹². It mainly contains CH₄, CO, CO₂, H₂, H₂O and N₂ if air is used as gasifying medium.

Contaminants

Besides the mentioned main constituents, the gas also includes minor but significant quantities of undesired by-products in form of particulates, tars, sulphur and nitrogen compounds, alkali metals, halides and other trace elements which are present in the feedstock¹³. Their concentration and speciation depend, similarly to the main gasification products, on the feedstock and gasification parameters. The following paragraphs provide a brief overview of their characteristics, gas concentrations and effects on downstream equipment and the environment.

Particulate matter is emitted in particle sizes ranging from the sub-micron level to several µm. The particles are typically made up from inorganic and residual carbon compounds including coke. If not sufficiently removed, particulates can cause blockage, corrosion and erosion of pipelines and equipment^{14,15}.

Tars can be defined as hydrocarbons with a molecular weight greater than benzene¹⁶. They are formed during gasification in a series of complex reactions¹⁷. Typical concentrations in the raw gas range from 0.01 to 150 g Nm⁻³¹⁸. When cooled down, tars can condense while increased temperatures can result in the formation of more complex compounds with higher boiling points. This can cause clogging and fouling of pipes, heat exchangers, particulate filters or other potential downstream units, such as fuel cells or catalysts¹⁹.

Sulphur concentrations in biomass such as wood are usually significantly lower compared to coal. The sulphur contained in the biomass feedstock is converted to H₂S, COS, thiophenic compounds and mercaptanes²⁰. The resulting total sulphur content in the raw producer gas ranges from 20 to 200 ppmv with typical concentrations of around 100 ppmv for woody and herbaceous biomass^{21,22}. While H₂S makes up most of the gas phase sulphur species, organic sulphur compounds, including thiophene (C₄H₄S), benzothiophene (C₈H₆S) and dibenzothiophene (C₁₂H₈S), can make up a significant fraction. They can add-up to 30 to 45 ppmv in grass gasification²⁰ and 2 to 10 ppmv in wood gasification processes, respectively^{20,23–25}. If not retained, these sulphur compounds can cause corrosion of downstream piping²⁶ and poisoning of catalysts²⁷ used for methanation²⁸, FT synthesis^{29,30} and fuel cells^{31,32}.

Nitrogen contaminants are mostly present in form of NH₃ and to a lesser extent (≈ factor 10) in form of HCN and heterocyclic compounds such as pyridine (C₅H₅N). The gas concentration of nitrogen compounds ranges from several hundred to a few thousand ppmv³³. Though these nitrogen species might harm downstream equipment such as FT catalysts and SOFCs, regulatory emission limitations are the major cause for their control³⁴.

1

Alkali metals melt and evaporate at gasification conditions, leaving the gasifier as aerosols and vapours in form of chlorides, hydroxides and sulfates^{35–37}. The most abundant alkali metals are K and Na. Their total gas phase concentrations range from the sub-ppmv level to a few ppmv^{38,39}. If cooled down they start to condensate on surfaces, causing fouling and corrosion in gas turbines and heat-exchangers⁴⁰. In addition there is some evidence of detrimental effects on the performance of catalysts¹⁹.

Halide gases primarily contain chlorides in form of HCl while other hydrogen halides such as HF and HBr are present in lower concentrations. Their concentrations range from a few ppmv up to 200 ppmv^{41,42}. At such concentrations halides can not only cause substantial corrosion to system components including catalysts⁴³ but also increase the volatility of other contaminants, including metals^{44,45}.

Trace elements are volatilized to different extent during gasification. Thermodynamic studies show that elements which are most volatile and predominantly remain in the gas phase are Hg, Br, Cl, F, B, Se, I and As^{46–49}. Of these elements As, B, Hg and Se were categorized by the Environmental Protection Agency (EPA) as elements of major concern due to their high toxicity to biological systems^{50,51}. And of these elements of major concern in turn, As and Se can also negatively affect downstream equipment⁸. Both As and Se are known poisons for SOFC catalysts^{31,52,53} and As is known as a poison for catalysts employed in methanol production⁵⁴ and other synthesis reactions⁵⁵.

Gas cleaning concepts

Because of their detrimental effect on downstream equipment and the environment, gas contaminants have to be removed from the raw producer gas. The level of cleaning required in this gas cleaning step depends on the type of application and/or environmental legislation (see Table 1.1).

Table 1.1 – Maximum permissible contaminant concentrations in producer gas for various applications^{8,17,32,56–58}. Ranges in permissible contaminant concentrations result from different data sources.

| Contaminants | Unit | Applications | | | | |
|--------------|------------------------|--------------|-----------|----------|------------|------------|
| | | Gas turbine | IC engine | SOFC | SNG | FT |
| Particulates | (mg Nm ⁻³) | < 0.1-120 | < 30-50 | < 10 | | < 0.02-0.2 |
| Tars | (mg Nm ⁻³) | < 1-5 | < 100 | < 0.1 | | < 0.1-1 |
| Sulphur | (ppmv) | < 1-20 | | < 0.06-1 | < 0.02-0.1 | < 0.01 |
| Nitrogen | (ppmv) | < 50 | | | | < 0.02 |
| Alkali | (ppmv) | < 0.02-0.1 | < 0.1 | < 0.1 | | < 0.01 |
| Halides | (ppmv) | < 1 | | < 10 | | < 0.01 |

In order to comply with these limits, numerous gas cleaning concepts have been proposed with comprehensive overviews being given by Woolcock and Brown⁵⁷, Asadullah⁵⁸ and Abdoulmoumine et al.¹³. The concepts can essentially be classified according to their operating temperature into cold, warm and hot gas cleanup processes. Cold refers in this context to temperatures which allow steam to condense, warm to temperatures above the boiling point of water and hot to a temperature greater than 300 °C.

The following paragraphs look more closely at two proposed cold and hot gas cleanup process configurations presented in Fig. 1.3a.

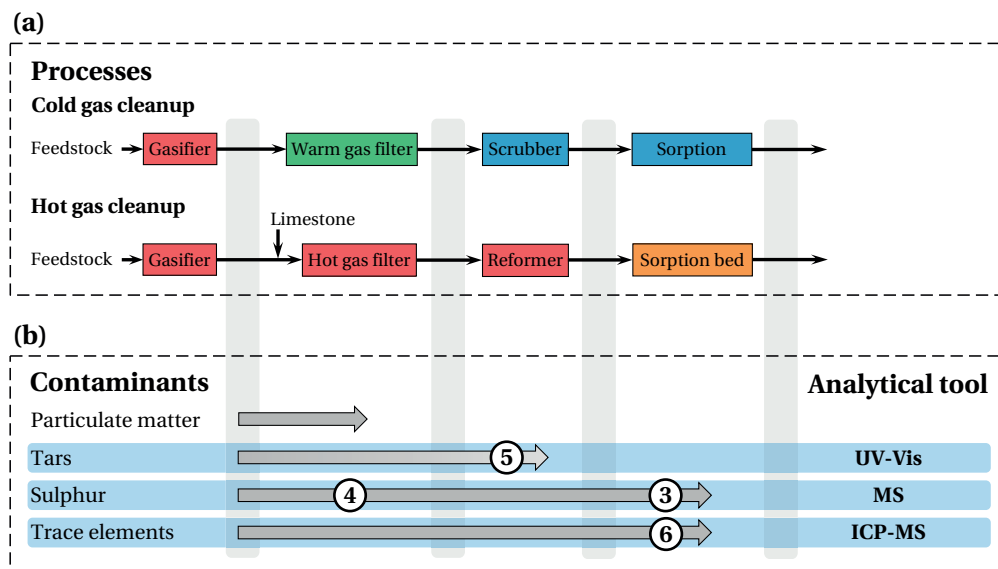


Figure 1.3 – (a) Schematic representation of two gas cleaning concepts in gasification processes; (b) schematic representation of the fate of gas contaminants in gas cleanup processes and analytical tools developed in this work for their online detection. In this coordinate system, the inscribed circles define the topics covered by the respective chapters of this thesis (ICP-MS: inductively coupled plasma mass spectrometer; MS: mass spectrometer). Colour-coded temperature of unit operations: 20-50 °C 150-250 °C 300-450 °C 700-850 °C

Cold gas cleanup is performed in a series of steps starting with the removal of particulates to avoid deterioration of further cleanup equipment. The proposed process employs bag filters to barricade the flow of particles while allowing the remaining gas constituents to pass. Typical materials for bag filters are woven synthetic fibers which tolerate temperatures up to 250 °C^{14,59}.

Tars are removed by means of gas scrubbing at temperatures below the boiling point of water. At such temperatures, both the majority of gas contained water and tar condense. Typical scrubbing liquids include water and oil based solvents, where the latter exhibit superior absorption efficiencies^{60,61}.

Sulphur capture is performed by gas scrubbing with regenerable physical or chemical solvents⁶². Two processes, based on physical solvents, are the Selexol (polyethylene glycol, 0 to 40 °C) and the Rectisol (methanol, -30 to -60 °C) process. They allow sulphur removal to < 10 ppmv (Selexol) and < 0.1 ppmv in case of the Rectisol process⁸. An alternative are amine based washers that operate at 30 to 60 °C and have lower investment costs compared to the described physical solvent processes. Sulphur capture in these amine processes is based on the formation of a weak chemical bond between H₂S and an amine component such as the recently favoured methyldiethanolamine (MDEA)⁶³. Using this solvent, H₂S exit gas concentrations between 10 to 20 ppmv can be achieved⁶⁴. Organic sulphur species are not efficiently captured, therefore requiring prior hydrogenation or dedicated capture (e.g. by activated carbon beds). All three processes have in common that guard beds are needed to further

1

reduce the sulphur content to parts per billion (ppbv) levels, depending on downstream applications⁶⁵. These beds typically employ ZnO as a solid sorbent that, however, again is incapable of removing organic sulphur species such as thiophene (C_4H_4S)^{23,24,66}. Trace element species, able to pass the low temperature gas cleaning steps, may be captured by activated carbon beds^{67,68}.

Hot gas cleanup consists of a series of four steps. The initial step involves the addition of limestone ($CaCO_3$), either directly into the gasifier (*in-situ*) or to the gas flow downstream before the gas filter, to serve as a bifunctional material. As such, it acts as a catalyst for the decomposition of tars and sulphur containing hydrocarbons on the one hand and as a sorbent for the capture of sulphur^{69–75}, trace elements (As, Se)^{76–80} and HCl⁸¹ on the other. Being a natural material with relatively low cost, the limestone is applied as a once-through material, captured after use by the gas filter and subsequently disposed of together with the particulate matter. Reactions of limestone with the raw producer gas can take place in the gasifier, during the flight of the particles to the gas filter and in the filter cake. The catalytic properties for tar decomposition of limestone have been investigated in several studies with various tar model compounds (heptane, benzene, toluene, naphthalene) and in different gasification atmospheres⁸². Operating above the calcination temperature (typically $> 750^\circ C$) proved to be essential as only the calcite CaO exhibits sufficient catalytic performance⁸³. Similarly, sorption should take place above the calcination temperature because CaO shows superior sulphidation characteristics compared to $CaCO_3$ with its limited conversion and slow reaction rates^{70,71,84}. The minimum mole fraction of H_2S at equilibrium is found close to the calcination temperature and typically lies above 50 ppmv, depending on pressure, CO_2 concentration and steam content^{85–87}. Lower H_2S concentrations have been reported in experimental studies but were ascribed to the presence of further metal species in the natural material⁸⁸. Limestone can therefore act as a bulk H_2S sorbent, especially useful in processes with feedstocks that contain large amounts of sulphur, including black liquor and several grasses^{22,89}.

The spent sorbent and particulates entrained in the gas flow are then separated by a filter. Employed filters are constructed from ceramic or metallic materials, allowing them to exceed operating temperatures of $400^\circ C$ ^{15,90}. They usually form porous, hollow tubes, called filter candles, which allow the gas to pass while particles are deposited on the outside surface, forming a filter cake which is periodically re-cleaned by pressure pulses⁹¹.

The particulate-free gas still contains various sulphur species and, depending on the operating parameters, residual amounts of tars. These operating parameters include the amount of limestone fed and its residence time in the process. Both have to be optimized with regard to the costs for limestone, filtration intensity and the presence and size of a downstream catalytic reformer unit for the decomposition of remaining tars and sulphur containing hydrocarbons. Several catalytic materials, including naturally occurring and synthetic catalysts, have been investigated for this purpose in the past^{19,82,92–94}. They are typically employed in fixed bed reactors, monoliths and as of late in catalytic filters^{95,96}. If necessary, the process chain may also include a separate hydrodesulphurization (HDS) catalyst bed, dedicated for the conversion of sulphur containing hydrocarbons. Able to pass several sorbent materials (e.g. ZnO²⁴), intended for sulphur capture, these sulphur compounds can cause harm to downstream equipment²³. In the petroleum industry, conversion of such species is traditionally achieved by HDS catalysts. These typically comprise of Mo or W sulphide, promoted by Ni or Co (CoMoS, NiMoS, CoWS, NiWS)⁹⁷. Even though operating conditions in oil refining are vastly different (liquid phase, 300 to $400^\circ C$, H_2 partial pressure of 10 to 200 bar), their applicability to biomass

conversion processes has been shown recently^{25,98,99}.

H₂S, escaping the bulk desulphurization step or produced by the conversion of sulphur containing hydrocarbons is retained in a sorption bed. Sorption of H₂S at high temperatures is typically performed by single/mixed (supported) metal oxides¹⁰⁰. The basis for much of the research in this field was laid by Westmoreland and Harrison¹⁰¹ who performed a thermodynamic screening of the high temperature desulphurization potential of 28 solids with most of them being metal oxides. Of the remaining eleven, feasible candidates (based upon the metals Fe, Zn, Mo, Mn, V, Ca, Si, Ba, Co, Cu, and W) the oxide ZnO exhibits one of the most favourable H₂S sulphidation thermodynamics, making it a widely used H₂S sorbent in the oil and gas industry¹⁰². Operation above 600 °C, however, causes substantial sorbent loss by ZnO reduction and subsequent evaporation of elemental Zn¹⁰³. Research therefore focused on stabilizing Zn in mixed metal oxides and found two promising candidates in zinc ferrite¹⁰⁴ and zinc titanate¹⁰⁵. Further research included Cu, Mn, Fe and Ce based sorbents. While each metal oxide features their specific disadvantages and advantages, much of the current research uses mixed metal oxides and promoters to combine their individual properties¹⁰⁶. The research on high temperature trace element removal from producer gas focuses primarily on Hg and to a lesser extent on Se and As⁸. High removal rates of Hg, Se and As have been shown for Pd/Al₂O₃ in the temperature range from 200 to 370 °C^{107–109}. Selenium may be captured by zinc titanate, similarly to H₂S⁷⁹. Further work by Riess and Muller¹¹⁰ indicated that copper containing sorbents have good As sorption characteristics, even at temperatures reaching up to 800 °C.

In comparison, cold gas cleanup processes often use commercially available, rather mature technologies. Whilst economically sensible in large scale fossil fuel applications⁶⁵, high capital cost and laborious regeneration of waste solvent streams can make them unattractive at the small scale, often found in biomass gasification processes. The process economics are further impaired by the cool-down of the raw producer gas below the steam dew point and the intended application operating temperature, as the required reheating and addition of steam cause a reduction in the overall process efficiency. Warm and hot cleanup processes, on the other hand, avoid the cool-down, condensation, heat-up and steam addition, thereby promising an increase in process efficiencies of 3 to 5 %-points^{111,112}. Omitting the auxiliary equipment needed in cold gas cleanup for heat integration, the regeneration of scrubbing solvents and cooling allow at the same time for lower capital and operating costs. However, these processes are, today, mostly at development stage, plagued by issues caused by the extreme conditions the system components are employed in.

Finding an optimal configuration of process steps in the gas cleanup chain that offers reliability, availability and high process efficiency at low operating and capital costs is therefore still a challenge and seen as one of the major hurdles for commercial deployment of biomass gasification processes^{113,114}.

1

1.2. Objectives

This thesis investigated the gas cleanup chain as part of gasification processes. Two aspects, the analysis of gas contaminants and subsequently their retention, were examined as visualized in Fig. 1.3b.

At first, the development of three analytical methods for the online detection of gas contaminants was addressed. These included sulphur containing hydrocarbons, tars and trace elements. While the measurement of thiophene as a representative of sulphur containing hydrocarbons was based on a basic method implemented with a process mass spectrometer (MS), tar compounds and trace elements were investigated by advanced, novel methods. Particularly, UV-Vis spectroscopy, coupled with a liquid quench sampling system, was used for tar characterisation. Trace elements, including Se (in form of H_2Se), Hg and As (in form of AsH_3) were detected at ppbv levels by means of the direct introduction of the gas to an inductively coupled plasma mass spectrometer (ICP-MS).

These established analytical tools were then employed to investigate the performance of gas cleanup units, intended for the removal of sulphur containing hydrocarbons, tars and the trace element Se. Herein, the removal of thiophene was explored by means of two units. These included the warm cleanup by an activated carbon bed and the hot gas cleanup over CaO particles. Similarly, the retention of tars was investigated on the basis of two units which included a cold pilot-scale gas scrubber and a hot laboratory-scale catalytic reformer. Finally, the removal of H_2Se was investigated by means of an ZnO bed at warm temperatures.

1.3. Thesis outline

This thesis is divided into seven chapters and five appendices. Herein, **Chapter 1** embeds the work into a broader social, technical and scientific context.

Chapter 2: Experimental setups

This chapter provides a general explanation of the two experimental setups used throughout the thesis. Detailed descriptions, including the analytical methods and experimental procedures can be found in the respective chapters.

Chapter 3: Adsorption of thiophene by activated carbon

This chapter investigates the removal of the sulphur containing hydrocarbon representative thiophene ($\text{C}_4\text{H}_4\text{S}$) by a commercial activated carbon at temperatures up to 200 °C. The process was rigorously modelled and evaluated by means of a global sensitivity analysis.

Chapter 4: High temperature conversion of thiophene over CaO

This chapter is concerned with the catalytic conversion of the sulphur containing hydrocarbon representative thiophene ($\text{C}_4\text{H}_4\text{S}$) over calcined limestone (CaO). The effects of different gas constituents on the overall catalytic performance were investigated by means of a design of experiments approach.

Chapter 5: Online tar measurement by UV-Vis spectroscopy

This chapter is dedicated to the online measurement of tar compounds by UV-Vis spectroscopy. Different regression techniques were applied to evaluate spectra, obtained from a lab-scale tar reformer and a pilot-scale gas scrubber.

Chapter 6: Detection and retention of selenium

This chapter develops an online analytical method for the measurement of trace elements. The method was successfully implemented and applied to a case study that investigated the sorption performance of a supported Zn sorbent towards H_2Se .

The last chapter (**Chapter 7**) provides a summary and conclusions of this thesis and presents an outlook and recommendations for future research.

1.4. Author's contributions

Chapters 3 to 6 form the basis for four publications. Of these, Chapters 5 and 6 have been published, Chapter 3 has been submitted and Chapter 4 is in preparation. The author's contributions to these chapters are:

Chapter 3: Adsorption of thiophene by activated carbon

The author defined the research plan. Experimental work was performed at Paul Scherrer Institute (PSI) in collaboration with the National Technical University of Athens (NTUA). As part of this collaboration, the author supervised an external PhD student for several experiments and conducted the remaining himself. Further, the author performed the calculations/modelling, interpreted the results and wrote the manuscript.

Chapter 4: High temperature conversion of thiophene over CaO

The author defined the research plan. Experimental work was performed at Paul Scherrer Institute (PSI) in collaboration with the Karlsruhe Institute of Technology (KIT). As part of this collaboration, the author supervised an external diploma student for few experiments and conducted the remaining himself. Further, the author performed the calculations/modelling, interpreted the results and wrote the manuscript.

Chapter 5: Online tar measurement by UV-Vis spectroscopy

The author defined much of the research plan and carried out most of the experiments. The case study experiments were carried out by J. Regler and J. Schneebeil. The author performed the calculations/modelling, interpreted the results and wrote the manuscript.

Chapter 6: Detection and retention of selenium

The author defined the research plan, carried out the experiments, performed the calculations/modelling, interpreted the results and wrote the manuscript.

References

- [1] Christof Rühl, Paul Appleby, Julian Fennema, Alexander Naumov, and Mark Schaffer. Economic development and the demand for energy: A historical perspective on the next 20 years. *Energy Policy*, 50:109–116, 2012.
- [2] Rajendra K Pachauri, MR Allen, VR Barros, J Broome, W Cramer, R Christ, JA Church, L Clarke, Q Dahe, and P Dasgupta. Climate change 2014: Synthesis report. contribution of working groups i, ii and iii to the fifth assessment report of the intergovernmental panel on climate change. 2014.
- [3] British petroleum, BP energy outlook 2035. Report, 2015.
- [4] Hermine Nalbandian. Trace element emissions from coal. Report, 2012.
- [5] Sjaak Van Loo and Jaap Koppejan. *The handbook of biomass combustion and co-firing*. Earthscan, London ; Sterling, VA, 2008.
- [6] Steffen Heidenreich and Pier Ugo Foscolo. New concepts in biomass gasification. *Progress in Energy and Combustion Science*, 46:72–95, 2015.
- [7] George W. Huber, Sara Iborra, and Avelino Corma. Synthesis of transportation fuels from biomass: Chemistry, catalysts, and engineering. *Chemical Reviews*, 106(9):4044–4098, 2006.
- [8] Christopher Higman and Samuel Tam. Advances in coal gasification, hydrogenation, and gas treating for the production of chemicals and fuels. *Chemical Reviews*, 114(3): 1673–1708, 2014.
- [9] Vineet Singh Sikarwar, Ming Zhao, Peter Clough, Joseph Yao, Xia Zhong, Mohammad Zaki Memon, Nilay Shah, Edward J. Anthony, and Paul S. Fennell. An overview of advances in biomass gasification. *Energy & Environmental Science*, 9(10):2939–2977, 2016.
- [10] A. V. Bridgwater. Renewable fuels and chemicals by thermal processing of biomass. *Chemical Engineering Journal*, 91(2–3):87–102, 2003.
- [11] A. Gómez-Barea and B. Leckner. Modeling of biomass gasification in fluidized bed. *Progress in Energy and Combustion Science*, 36(4):444–509, 2010.
- [12] Prakash Parthasarathy and K. Sheeba Narayanan. Hydrogen production from steam gasification of biomass: Influence of process parameters on hydrogen yield – a review. *Renewable Energy*, 66:570–579, 2014.
- [13] Nourredine Abdoulmoumine, Sushil Adhikari, Avanti Kulkarni, and Shyamsundar Chatteranathan. A review on biomass gasification syngas cleanup. *Applied Energy*, 155:294–307, 2015.
- [14] J. P. K. Seville. *Gas cleaning in demanding applications*. Blackie Academic & Professional, London, 1997.
- [15] S. D. Sharma, M. Dolan, D. Park, L. Morpeth, A. Ilyushechkin, K. McLennan, D. J. Harris, and K. V. Thambimuthu. A critical review of syngas cleaning technologies — fundamental limitations and practical problems. *Powder Technology*, 180(1–2):115–121, 2008.

- [16] K. Maniatis and Aacm Beenackers. Tar protocols. iea bioenergy gasification task. *Biomass & Bioenergy*, 18(1):1–4, 2000.
- [17] Thomas A Milne, Nicolas Abatzoglou, and Robert J Evans. *Biomass gasifier" tars": their nature, formation, and conversion*. Golden (Colorado): National Renewable Energy Laboratory. 1998.
- [18] Zia Ud Din and Z. A. Zainal. Biomass integrated gasification–sofc systems: Technology overview. *Renewable and Sustainable Energy Reviews*, 53:1356–1376, 2016.
- [19] P. V. Aravind and Wiebren de Jong. Evaluation of high temperature gas cleaning options for biomass gasification product gas for solid oxide fuel cells. *Progress in Energy and Combustion Science*, 38(6):737–764, 2012.
- [20] M. D. K. Rechulski, T. J. Schildhauer, S. M. A. Biollaz, and C. Ludwig. Sulfur containing organic compounds in the raw producer gas of wood and grass gasification. *Fuel*, 128: 330–339, 2014.
- [21] E. Magnus Johansson, Magnus Berg, Johan Kjellström, and Sven G. Järås. Catalytic combustion of gasified biomass: poisoning by sulphur in the feed. *Applied Catalysis B: Environmental*, 20(4):319–332, 1999.
- [22] Melita Jazbec, Karina Sendt, and Brian S. Haynes. Kinetic and thermodynamic analysis of the fate of sulphur compounds in gasification products. *Fuel*, 83(16):2133–2138, 2004.
- [23] Rudolf P. W. J. Struis, Tilman J. Schildhauer, Izabela Czekaj, Markus Janousch, Serge M. A. Biollaz, and Christian Ludwig. Sulphur poisoning of ni catalysts in the sng production from biomass: A tpo/xps/xas study. *Applied Catalysis A: General*, 362(1–2):121–128, 2009.
- [24] Hong Cui, Scott Q. Turn, Vheissu Keffer, Donald Evans, Thai Tran, and Michael Foley. Contaminant estimates and removal in product gas from biomass steam gasification. *Energy & Fuels*, 24:1222–1233, 2010.
- [25] Luc P. L. M. Rabou and Lex Bos. High efficiency production of substitute natural gas from biomass. *Applied Catalysis B: Environmental*, 111–112:456–460, 2012.
- [26] S. Mrowec. The problem of sulfur in high-temperature corrosion. *Oxidation of Metals*, 44(1–2):177–209, 1995.
- [27] Calvin H. Bartholomew. Mechanisms of catalyst deactivation. *Applied Catalysis A: General*, 212(1–2):17–60, 2001.
- [28] W. D. Fitzharris, J. R. Katzer, and W. H. Manogue. Sulfur deactivation of nickel methanation catalysts. *Journal of Catalysis*, 76(2):369–384, 1982.
- [29] C. G. Visconti, L. Lietti, P. Forzatti, and R. Zennaro. Fischer-tropsch synthesis on sulphur poisoned co/al₂o₃ catalyst. *Applied Catalysis a-General*, 330:49–56, 2007.
- [30] Kiyomi Okabe, Kazuhisa Murata, Masakazu Nakanishi, Tomoko Ogi, Mohammad Nurunnabi, and Yangyong Liu. Fischer–tropsch synthesis over ru catalysts by using syngas derived from woody biomass. *Catalysis Letters*, 128(1):171–176, 2009.

- [31] Fatma Nihan Cayan, Mingjia Zhi, Suryanarayana Raju Pakalapati, Ismail Celik, Nian-qiang Wu, and Randall Gemmen. Effects of coal syngas impurities on anodes of solid oxide fuel cells. *Journal of Power Sources*, 185(2):595–602, 2008.
- [32] Hossein Madi. *Investigations into the Effects of Biofuel Contaminants on Solid Oxide Fuel Cells*. Thesis, 2016.
- [33] Jukka Leppälahti and Tiina Koljonen. Nitrogen evolution from coal, peat and wood during gasification: Literature review. *Fuel Processing Technology*, 43(1):1–45, 1995.
- [34] Venkat Ramana Rao Pendyala, Muthu Kumaran Gnanamani, Gary Jacobs, Wenping Ma, Wilson D. Shafer, and Burtron H. Davis. Fischer–tropsch synthesis: effect of ammonia impurities in syngas feed over a cobalt/alumina catalyst. *Applied Catalysis A: General*, 468:38–43, 2013.
- [35] Torsten Kowalski, Christian Ludwig, and Alexander Wokaun. Qualitative evaluation of alkali release during the pyrolysis of biomass. *Energy & Fuels*, 21(5):3017–3022, 2007.
- [36] Marco Wellinger, Serge Biollaz, Jörg Wochele, and Christian Ludwig. Sampling and online analysis of alkalis in thermal process gases with a novel surface ionization detector. *Energy & Fuels*, 25(9):4163–4171, 2011.
- [37] P. Monkhouse. On-line spectroscopic and spectrometric methods for the determination of metal species in industrial processes. *Progress in Energy and Combustion Science*, 37(2):125–171, 2011.
- [38] David C. Dayton, Richard J. French, and Thomas A. Milne. Direct observation of alkali vapor release during biomass combustion and gasification. 1. application of molecular beam/mass spectrometry to switchgrass combustion. *Energy & Fuels*, 9(5):855–865, 1995.
- [39] Scott Q. Turn, Charles M. Kinoshita, Darren M. Ishimura, Ty T. Hiraki, Jiachun Zhou, and Stephen M. Masutani. An experimental investigation of alkali removal from biomass producer gas using a fixed bed of solid sorbent. *Industrial & Engineering Chemistry Research*, 40(8):1960–1967, 2001.
- [40] S. Q. Turn, C. M. Kinoshita, D. M. Ishimura, and J. C. Zhou. The fate of inorganic constituents of biomass in fluidized bed gasification. *Fuel*, 77(3):135–146, 1998.
- [41] Pekka A. Simell, Nina A. K. Hakala, Heikki E. Haario, and A. Outi I. Krause. Catalytic decomposition of gasification gas tar with benzene as the model compound. *Industrial & Engineering Chemistry Research*, 36(1):42–51, 1997.
- [42] Scott Q. Turn. Chemical equilibrium prediction of potassium, sodium, and chlorine concentrations in the product gas from biomass gasification. *Industrial & Engineering Chemistry Research*, 46(26):8928–8937, 2007.
- [43] J. P. Trembly, R. S. Gemmen, and D. J. Bayless. The effect of coal syngas containing hcl on the performance of solid oxide fuel cells: Investigations into the effect of operational temperature and hcl concentration. *Journal of Power Sources*, 169(2):347–354, 2007.

- [44] Marc Bläsing, Mostafa Zini, and Michael Müller. Influence of feedstock on the release of potassium, sodium, chlorine, sulfur, and phosphorus species during gasification of wood and biomass shells. *Energy & Fuels*, 27(3):1439–1445, 2013.
- [45] Dirk Porbatzki, Michael Stemmler, and Michael Müller. Release of inorganic trace elements during gasification of wood, straw, and miscanthus. *Biomass and Bioenergy*, 35, Supplement 1:79–86, 2011.
- [46] M. Diaz-Somoano and M. R. Martinez-Tarazona. Trace element evaporation during coal gasification based on a thermodynamic equilibrium calculation approach. *Fuel*, 82(2): 137–145, 2003.
- [47] Dirk Porbatzki, Michael Stemmler, and Michael Mueller. Release of inorganic trace elements during gasification of wood, straw, and miscanthus. *Biomass & Bioenergy*, 35: 79–86, 2011.
- [48] K. Froment, F. Defoort, C. Bertrand, J. M. Seiler, J. Berjonneau, and J. Poirier. Thermodynamic equilibrium calculations of the volatilization and condensation of inorganics during wood gasification. *Fuel*, 107:269–281, 2013.
- [49] K. Froment, J. M. Seiler, F. Defoort, and S. Ravel. Inorganic species behaviour in thermochemical processes for energy biomass valorisation. *Oil & Gas Science and Technology- Revue D Ifp Energies Nouvelles*, 68(4):725–739, 2013.
- [50] United States environmental protection agency, national emission standards for hazardous air pollutants from coal- and oil-fired electric utility steam generating units and standards of performance for fossil-fuel-fired electric utility, industrial-commercial-institutional, and small industrial-commercial-institutional steam generating units; final rule. 77(32):9304–9513, 2012.
- [51] D. J. Swaine. Why trace elements are important. *Fuel Processing Technology*, 65:21–33, 2000.
- [52] J. P. Trembly, R. S. Gemmen, and D. J. Bayless. The effect of coal syngas containing ash₃ on the performance of sofc: Investigations into the effect of operational temperature, current density and ash₃ concentration. *Journal of Power Sources*, 171(2):818–825, 2007.
- [53] JianEr Bao, Gopala N. Krishnan, Palitha Jayaweera, Kai-Hung Lau, and Angel Sanjurjo. Effect of various coal contaminants on the performance of solid oxide fuel cells: Part ii. ppm and sub-ppm level testing. *Journal of Power Sources*, 193(2):617–624, 2009.
- [54] R. Quinn, T. Mebrahtu, T. A. Dahl, F. A. Lucrezi, and B. A. Toseland. The role of arsine in the deactivation of methanol synthesis catalysts. *Applied Catalysis a-General*, 264(1): 103–109, 2004.
- [55] B. Nielsen and J. Villadsen. Poisoning of nickel catalysts by arsenic. *Applied Catalysis*, 11 (1):123–138, 1984.
- [56] Michael Stemmler. *Chemische Heissgasreinigung bei Biomassevergasungsprozessen*. Thesis, 2010.
- [57] Patrick J. Woolcock and Robert C. Brown. A review of cleaning technologies for biomass-derived syngas. *Biomass & Bioenergy*, 52:54–84, 2013.

- [58] Mohammad Asadullah. Biomass gasification gas cleaning for downstream applications: A comparative critical review. *Renewable and Sustainable Energy Reviews*, 40:118–132, 2014.
- [59] Friedrich Löffler. *Staubabscheidung mit Schlauchfiltern und Taschenfiltern*. Vieweg, Braunschweig, 2nd edition, 1991.
- [60] Robin Zwart. *Gas Cleaning: Downstream Biomass Gasification: Status Report 2009*. ECN, 2009.
- [61] Thana Phuphuakrat, Tomoaki Namioka, and Kunio Yoshikawa. Absorptive removal of biomass tar using water and oily materials. *Bioresource Technology*, 102(2):543–549, 2011.
- [62] Christopher Higman and Maarten van der Burgt. *Gasification*. Elsevier, Amsterdam, 2nd edition, 2008.
- [63] E. I. Koytsoumpa, K. Atsonios, K. D. Panopoulos, S. Karellas, E. Kakaras, and J. Karl. Modelling and assessment of acid gas removal processes in coal-derived sng production. *Applied Thermal Engineering*, 74:128–135, 2015.
- [64] P. Mondal, G. S. Dang, and M. O. Garg. Syngas production through gasification and cleanup for downstream applications — recent developments. *Fuel Processing Technology*, 92(8):1395–1410, 2011.
- [65] David A. Bell, Brian F. Towler, and Maohong Fan. *Coal gasification and its applications*. Elsevier William Andrew, Amsterdam, 2011.
- [66] Tomas Jirsak, Joseph Dvorak, and José A. Rodriguez. Chemistry of thiophene on zno, s/zno, and cs/zno surfaces: effects of cesium on desulfurization processes. *The Journal of Physical Chemistry B*, 103(26):5550–5559, 1999.
- [67] R. A. Jadhav, R. Agnihotri, H. Gupta, and L. S. Fan. Mechanism of selenium sorption by activated carbon. *Canadian Journal of Chemical Engineering*, 78(1):168–174, 2000.
- [68] Evan J. Granite, Henry W. Pennline, and Constance Senior. *Mercury Control: for Coal-Derived Gas Streams*. Wiley-VCH, 2014.
- [69] Lawrence A. Ruth, Arthur M. Squires, and Robert A. Graff. Desulfurization of fuels with half-calcined dolomite. first kinetic data. *Environmental Science & Technology*, 6(12):1009–1014, 1972.
- [70] Laurent A. Fenouil and Scott Lynn. Study of calcium-based sorbents for high-temperature h₂S removal. 1. kinetics of h₂S sorption by uncalcined limestone. *Industrial & Engineering Chemistry Research*, 34(7):2324–2333, 1995.
- [71] Laurent A. Fenouil and Scott Lynn. Study of calcium-based sorbents for high-temperature h₂S removal. 2. kinetics of h₂S sorption by calcined limestone. *Industrial & Engineering Chemistry Research*, 34(7):2334–2342, 1995.
- [72] Laurent A. Fenouil and Scott Lynn. Study of calcium-based sorbents for high-temperature h₂S removal. 3. comparison of calcium-based sorbents for coal gas desulfurization. *Industrial & Engineering Chemistry Research*, 34(7):2343–2348, 1995.

- [73] M. Hartman, K. Svoboda, O. Trnka, and J. Cermak. Reaction between hydrogen sulfide and limestone calcines. *Industrial & Engineering Chemistry Research*, 41(10):2392–2398, 2002.
- [74] L. F. de Diego, A. Abad, F. Garcia-Labiano, J. Adanez, and P. Gayan. Simultaneous calcination and sulfidation of calcium-based sorbents. *Industrial & Engineering Chemistry Research*, 43(13):3261–3269, 2004.
- [75] Y. Q. Hu, M. Watanabe, C. Aida, and M. Horio. Capture of H_2S by limestone under calcination conditions in a high-pressure fluidized-bed reactor. *Chemical Engineering Science*, 61(6):1854–1863, 2006.
- [76] A. GhoshDastidar, S. Mahuli, R. Agnihotri, and L. S. Fan. Selenium capture using sorbent powders: Mechanism of sorption by hydrated lime. *Environmental Science & Technology*, 30(2):447–452, 1996.
- [77] S. Mahuli, R. Agnihotri, S. Chauk, A. GhoshDastidar, and L. S. Fan. Mechanism of arsenic sorption by hydrated lime. *Environmental Science & Technology*, 31(11):3226–3231, 1997.
- [78] R. Agnihotri, S. Chauk, S. Mahuli, and L. S. Fan. Selenium removal using ca-based sorbents: Reaction kinetics. *Environmental Science & Technology*, 32(12):1841–1846, 1998.
- [79] M. Diaz-Somoano and M. R. Martinez-Tarazona. Retention of arsenic and selenium compounds using limestone in a coal gasification flue gas. *Environmental Science & Technology*, 38(3):899–903, 2004.
- [80] M. Diaz-Somoano, M. A. Lopez-Anton, F. E. Huggins, and M. R. Martinez-Tarazona. The stability of arsenic and selenium compounds that were retained in limestone in a coal gasification atmosphere. *Journal of Hazardous Materials*, 173(1-3):450–454, 2010.
- [81] José Corella, José M. Toledo, and Gregorio Molina. Performance of cao and mgo for the hot gas clean up in gasification of a chlorine-containing (rdf) feedstock. *Bioresource Technology*, 99(16):7539–7544, 2008.
- [82] W. Torres, S. S. Pansare, and J. G. Goodwin. Hot gas removal of tars, ammonia, and hydrogen sulfide from biomass gasification gas. *Catalysis Reviews-Science and Engineering*, 49(4):407–456, 2007.
- [83] Pekka A. Simell, Jukka K. Leppaelahti, and Esa A. Kurkela. Tar-decomposing activity of carbonate rocks under high CO_2 partial pressure. *Fuel*, 74(6):938–945, 1995.
- [84] K. P. Yrjas, C. A. P. Zevenhoven, and M. M. Hupa. Hydrogen sulfide capture by limestone and dolomite at elevated pressure .1. sorbent performance. *Industrial & Engineering Chemistry Research*, 35(1):176–183, 1996.
- [85] L. A. Fenouil and S. Lynn. Design of entrained-flow and moving-, packed-, and fluidized-bed sorption systems: Grain-model kinetics for hot coal-gas desulfurization with limestone. *Industrial & Engineering Chemistry Research*, 35(4):1024–1043, 1996.

- [86] X. M. Meng, W. De Jong, and A. H. M. Verkooijen. Thermodynamic analysis and kinetics model of h₂S sorption using different sorbents. *Environmental Progress & Sustainable Energy*, 28(3):360–371, 2009.
- [87] Vincent Girard, Arnaud Baudot, David Chiche, Delphine Bazer-Bachi, Christine Bounie, and Christophe Geantet. Rational selection of single oxide sorbents for syngas desulfurization regenerable at reduced temperature: Thermochemical calculations and experimental study. *Fuel*, 128:220–230, 2014.
- [88] Michael Stemmler, Angela Tamburro, and Michael Müller. Laboratory investigations on chemical hot gas cleaning of inorganic trace elements for the “unique” process. *Fuel*, 108:31–36, 2013.
- [89] Henrik Wiinikka, Ann-Christine Johansson, Jonas Wennebro, Per Carlsson, and Olov G. W. Öhrman. Evaluation of black liquor gasification intended for synthetic fuel or power production. *Fuel Processing Technology*, 139:216–225, 2015.
- [90] Wolfgang Peukert. High temperature filtration in the process industry. *Filtration & Separation*, 35(5):461–464, 1998.
- [91] Steffen Heidenreich. Hot gas filtration – a review. *Fuel*, 104:83–94, 2013.
- [92] Z. Abu El-Rub, E. A. Bramer, and G. Brem. Review of catalysts for tar elimination in biomass gasification processes. *Industrial & Engineering Chemistry Research*, 43(22): 6911–6919, 2004.
- [93] Yafei Shen and Kunio Yoshikawa. Recent progresses in catalytic tar elimination during biomass gasification or pyrolysis—a review. *Renewable and Sustainable Energy Reviews*, 21:371–392, 2013.
- [94] Guoqing Guan, Malinee Kaewpanha, Xiaogang Hao, and Abuliti Abudula. Catalytic steam reforming of biomass tar: Prospects and challenges. *Renewable and Sustainable Energy Reviews*, 58:450–461, 2016.
- [95] U. Rhyner, P. Edinger, T. J. Schildhauer, and S. M. A. Biollaz. Applied kinetics for modeling of reactive hot gas filters. *Applied Energy*, 113:766–780, 2014.
- [96] U. Rhyner, P. Edinger, T. J. Schildhauer, and S. M. A. Biollaz. Experimental study on high temperature catalytic conversion of tars and organic sulfur compounds. *International Journal of Hydrogen Energy*, 39(10):4926–4937, 2014.
- [97] Henrik Topsøe, Bjerne S. Clausen, and Franklin E. Massoth. *Hydrotreating Catalysis*, page 269. Springer, Berlin, Heidelberg, 1996.
- [98] C. F. J. König, P. Schuh, T. J. Schildhauer, and M. Nachttegaal. High-temperature sulfur removal from biomass-derived synthesis gas over bifunctional molybdenum catalysts. *Chemcatchem*, 5(12):3700–3711, 2013.
- [99] Marcelo Daniel Kaufman Rechulski. *Catalysts for High Temperature Gas Cleaning in the Production of Synthetic Natural Gas from Biomass*. Thesis, 2012.

- [100] X. M. Meng, W. de Jong, R. Pal, and A. H. M. Verkooijen. In bed and downstream hot gas desulphurization during solid fuel gasification: A review. *Fuel Processing Technology*, 91(8):964–981, 2010.
- [101] Phillip R. Westmoreland and Douglas P. Harrison. Evaluation of candidate solids for high-temperature desulfurization of low-btu gases. *Environmental Science & Technology*, 10(7):659–661, 1976.
- [102] Amir Moezzi, Andrew M. McDonagh, and Michael B. Cortie. Zinc oxide particles: Synthesis, properties and applications. *Chemical Engineering Journal*, 185:1–22, 2012.
- [103] Eiji Sasaoka, Shigeru Hirano, Shigeaki Kasaoka, and Yusaku Sakata. Stability of zinc oxide high-temperature desulfurization sorbents for reduction. *Energy & Fuels*, 8(3):763–769, 1994.
- [104] R. Gupta, S. K. Gangwal, and S. C. Jain. Development of zinc ferrite sorbents for desulfurization of hot coal gas in a fluid-bed reactor. *Energy & Fuels*, 6(1):21–27, 1992.
- [105] Susan Lew, Kandaswami Jothimurugesan, and Maria Flytzani-Stephanopoulos. High-temperature hydrogen sulfide removal from fuel gases by regenerable zinc oxide-titanium dioxide sorbents. *Industrial & Engineering Chemistry Research*, 28(5):535–541, 1989.
- [106] S. Cheah, D. L. Carpenter, and K. A. Magrini-Bair. Review of mid- to high-temperature sulfur sorbents for desulfurization of biomass- and coal-derived syngas. *Energy & Fuels*, 23:5291–5307, 2009.
- [107] J. P. Baltrus, E. J. Granite, H. W. Pennline, D. Stanko, H. Hamilton, L. Rowsell, S. Poulston, A. Smith, and W. Chu. Surface characterization of palladium-alumina sorbents for high-temperature capture of mercury and arsenic from fuel gas. *Fuel*, 89(6):1323–1325, 2010.
- [108] S. Poulston, E. J. Granite, H. W. Pennline, H. Hamilton, and A. W. J. Smith. Palladium based sorbents for high temperature arsine removal from fuel gas. *Fuel*, 90(10):3118–3121, 2011.
- [109] E. C. Rupp, E. J. Granite, and D. C. Stanko. Laboratory scale studies of pd/gamma-al2o3 sorbents for the removal of trace contaminants from coal-derived fuel gas at elevated temperatures. *Fuel*, 108:131–136, 2013.
- [110] M. Riess and M. Muller. High temperature sorption of arsenic in gasification atmosphere. *Energy & Fuels*, 25(4):1438–1443, 2011.
- [111] A. O. Omosun, A. Bauert, N. P. Brandon, C. S. Adjiman, and D. Hart. Modelling system efficiencies and costs of two biomass-fuelled sofc systems. *Journal of Power Sources*, 131(1-2):96–106, 2004.
- [112] Martin Gassner and Francois Marechal. Thermo-economic optimisation of the polygeneration of synthetic natural gas (sng), power and heat from lignocellulosic biomass by gasification and methanation. *Energy & Environmental Science*, 5(2):5768–5789, 2012.

- [113] J. A. Ruiz, M. C. Juarez, M. P. Morales, P. Munoz, and M. A. Mendivil. Biomass gasification for electricity generation: Review of current technology barriers. *Renewable & Sustainable Energy Reviews*, 18:174–183, 2013.
- [114] Stefan Heyne, Truls Liliedahl, and Magnus Marklund. Biomass gasification - a synthesis of technical barriers and current research issues for the deployment at large scale. Report, 2013.

2

Experimental setups

This chapter describes the two experimental setups used in the present work. Detailed explanations, including the analytical methods and experimental procedures can be found in the respective chapters.

- **Gasmix setup:** This setup allows to feed gas contaminants (H_2S , $\text{C}_4\text{H}_4\text{S}$) in a complex gas matrix to a small-sized reactor. The reactor outlet or bypass gas composition can be analysed by a process mass spectrometer. The setup has been used in Chapters 3 and 4.
- **Trace element setup:** This setup allows to continuously feed trace elements (Se, Hg, As, P) in a multi-component gas matrix to a sorbent bed. The resulting response at the bed exit is analysed by an appropriate analytical method (e.g. ICP-MS). The setup has been used in two configurations in Chapter 6.

2

2.1. Gasmix setup

The apparatus can be divided into four sections, consisting of a gas mixing, gas distribution, reactor and gas analysis section. A schema and photograph of the experimental setup are presented in Figs. 2.1 and 2.2.

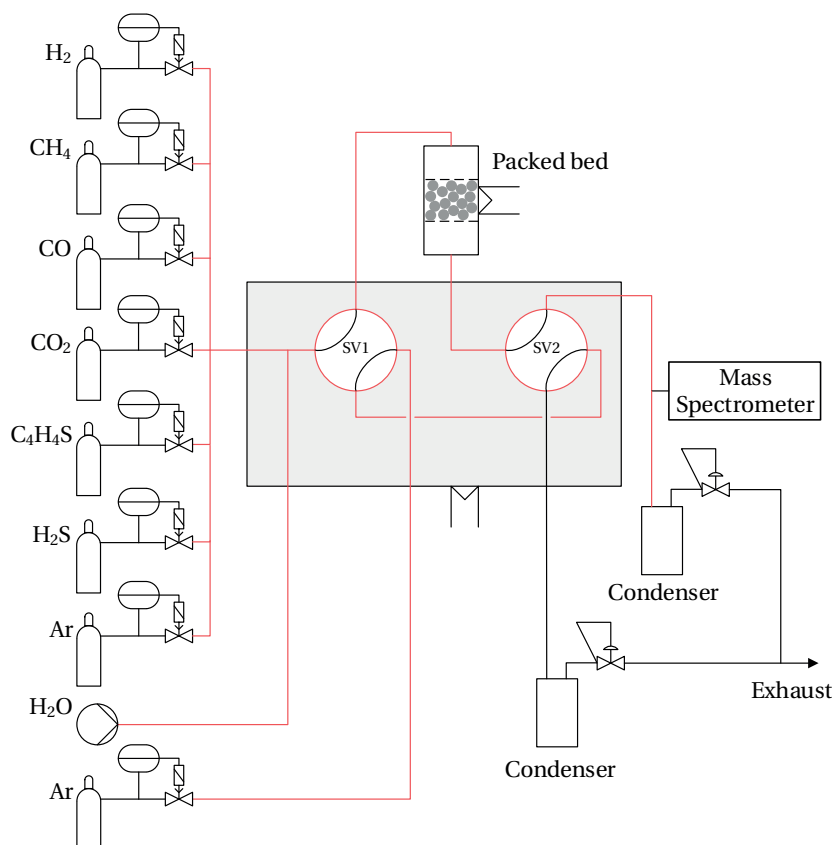


Figure 2.1 – Schematic representation of the Gasmix setup

The gas mixing section uses a set of mass flow controllers (MFC, Bronkhorst, EL-FLOW) to deliver defined amounts of gases. H_2 , CH_4 , CO , CO_2 and Ar were taken from gas cylinders and house-supply in pure form (quality > 4.5). H_2S (0.5 vol% in Ar) and $\text{C}_4\text{H}_4\text{S}$ (0.5 vol% in He) on the other hand from premixed gas cylinders. Steam was supplied by pumping (syringe pump, PHD 2000, Harvard Apparatus) deionized water through a fused silica capillary into a heated cross-piece where its vapour was mixed with the bulk gas stream. All metal tubing in contact with sulphur species (indicated red in Fig. 2.1) was SiO_2 coated (SilcoNert 2000, SilcoTek) and heated above 70 °C to minimise adsorption effects.

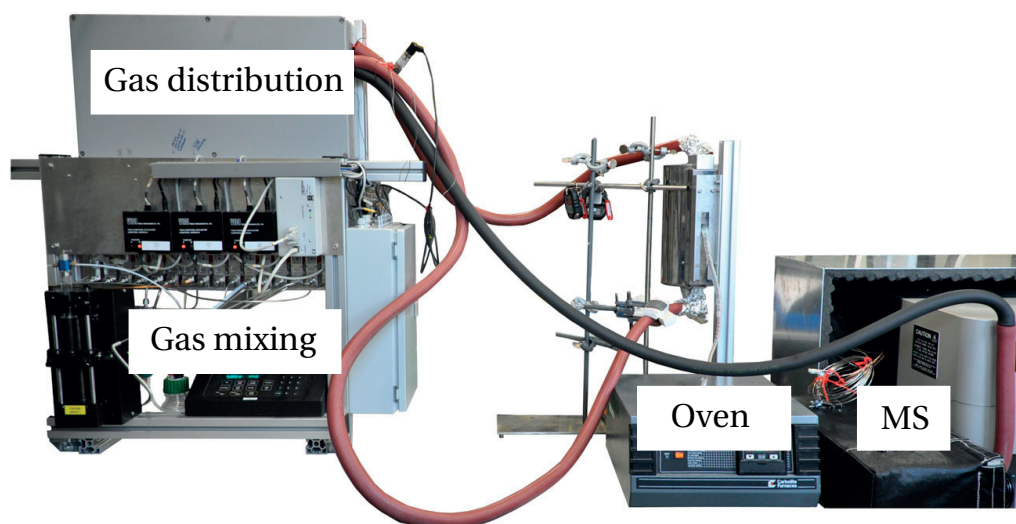


Figure 2.2 – Photograph of the Gasmix setup

The temperature of the gas distribution section (indicated by grey shaded area in Fig. 2.1) was kept above 100 °C for the same reason. This section consists of two four-port switch valves (SV, VICI) which were used to send the gas mixture either to the column or bypass line while the respective other line was flushed by Ar. The system pressure was maintained at 0.5 barg by means of two backpressure regulators (EL-Press, Bronkhorst). The packed bed column was placed in a vertical cylindrical oven (Carbolite Furnaces, MTF 12/25A) operated in down-flow mode. The temperature of the sample was determined from a previously recorded temperature profile, assuming isothermal conditions.

Online gas analysis was performed by extracting a fraction ($\approx 1 \text{ Nml min}^{-1}$) of the gas exiting the outlet of valve SV2 (see Fig. 2.1) through a fused silica capillary (inner diameter 180 μm) to a process mass spectrometer (MAX 300-LG, Extrel, inlet temperature at 120 °C).

2.2. Trace element setup

Two setups were used to perform calibration and sorption experiments. Schematic representations are given in Figs. 2.3a and 2.3b, respectively.

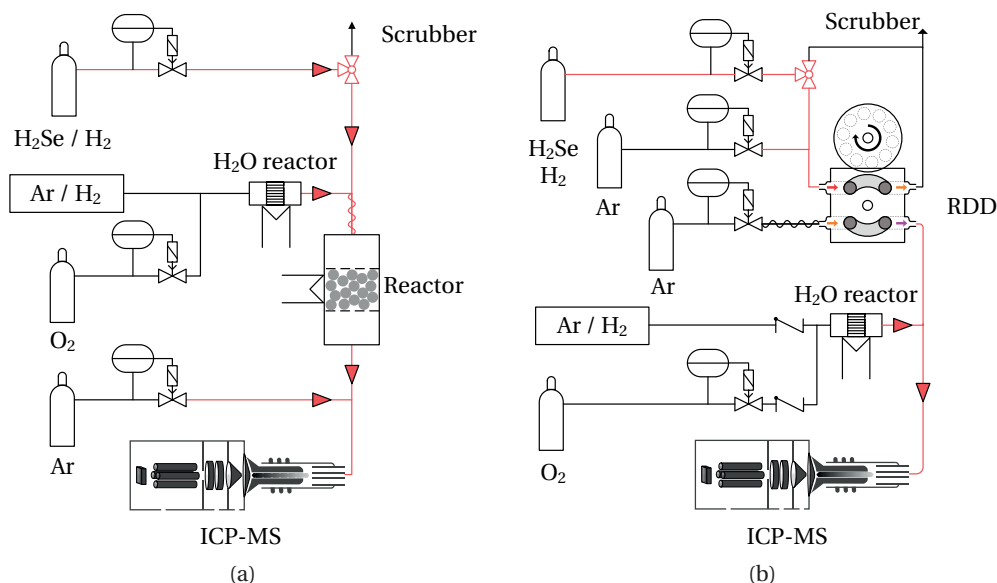


Figure 2.3 – Schematic representations of the Trace element setup. (a) Experimental setup (setup 1) used for experiments concerning the analytical performance and sorption experiments; (b) experimental setup (setup 2) used for verification of the calculated detection limit. (ICP-MS: Inductively coupled plasma mass spectrometer; RDD: rotary disk diluter)

The first experimental setup (Fig. 2.3a) was used for all sorption experiments. This experimental setup can be divided into four sections consisting of gas mixing, the reactor, gas analysis and gas scrubbing.

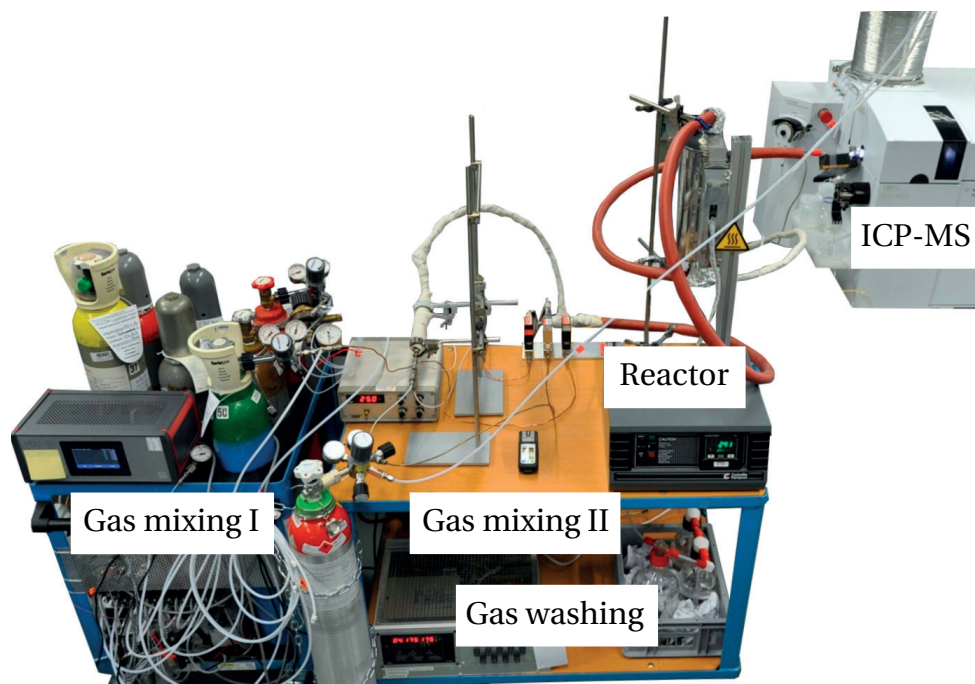
The gas mixing section uses two sets of MFCs (EL-Flow, Bronkhorst, Netherland; red-y, Vögtlin, Switzerland) to deliver defined amounts of gases. Ar (quality 6.0), H₂ (4.6) and O₂ (4.8) were taken in pure form from gas cylinders. H₂Se on the other hand was obtained from a gas mixture (106.1 ± 5 ppmv H₂Se, balance H₂, Linde Specialty Gases, Germany). Tubing in contact with H₂Se (indicated in orange colour in Fig. 2.3) was quartz coated (SilcoNert 2000, SilcoTek, USA) and heated to 160 °C (HT 60, Horst, Germany) in order to minimize adsorption effects. In contrast to the SiO₂ coated tubing, different tubing materials (PTFE and PEEK) showed significant washout times and loss of analyte at low H₂Se concentrations. The H₂Se gas flow was directed either to the gas mixture of Ar, H₂ and H₂O flowing towards the quartz reactor, or to the gas scrubbing section, consisting of two impinger bottles filled with 0.7 M HNO₃ for H₂Se removal before venting the cleaned gas to the lab fume hood. This allowed for conditioning of the reactor and defined start/stop times of experiments.

Pulsation-free supply of steam was achieved by a controlled reaction of H₂ and O₂ over a catalyst at 250 °C¹. For this purpose, a stream of Ar and H₂ were brought into contact with O₂ (H₂/O₂ > 6) in a tubular reactor (inner diameter 10 mm), consisting of two 20 mm long platinum-covered (Pt-loading: 90 g ft⁻³, OM-group, USA) ceramic cordierite monoliths (400 cpsi, NGK, Japan) held in place by quartz wool plugs.

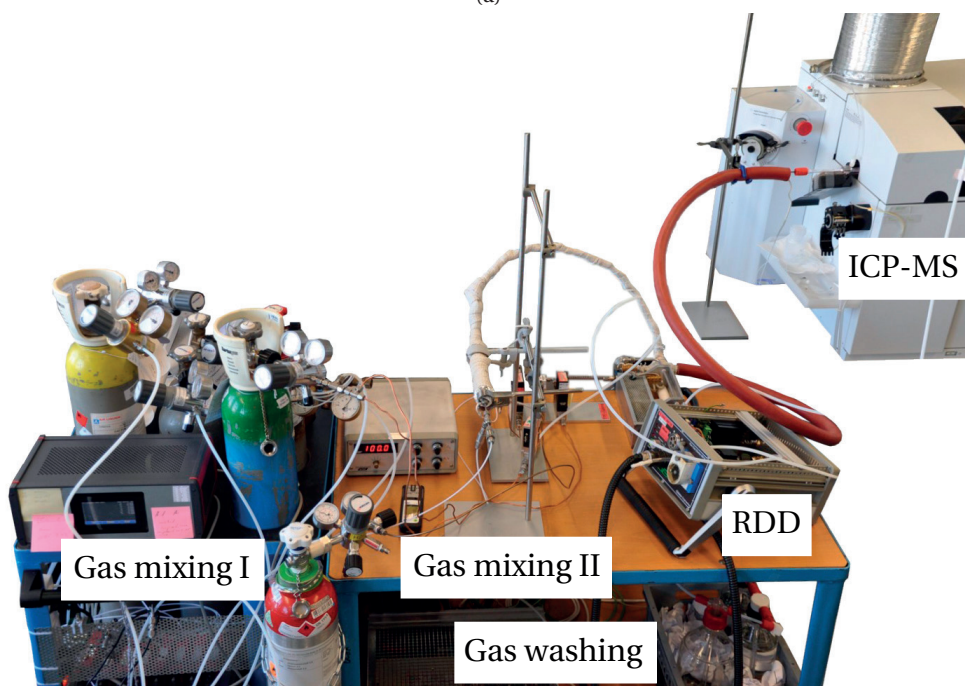
2

The total gas flow, entering the reactor, was kept at 100 Nml min^{-1} and subsequently diluted with an Ar stream before introducing it into the ICP-MS to give a total carrier gas flowrate of $1100 \text{ Nml min}^{-1}$. The analyte concentration, on a molar basis, can therefore be given in terms of a concentration measured at the ICP-MS inlet (denoted by the term ICP) and a reactor concentration (denoted by the term rx).

The second experimental setup (Fig. 2.3b) was used for the verification of detection limits. It is based on the same modular components utilized in setup 1, but in a different arrangement. In order to deliver H_2Se gas concentrations three orders of magnitude below what is achievable by setup 1, a rotary disk diluter (RDD, MD19-2E, Matter Aerosol, Switzerland) was employed. The RDD consists of a heatable steel block equipped with two channels and a disk with several cavities, allowing for a wide dilution range (up to 1:1500)². A gas stream of 1 Nl min^{-1} , containing H_2Se , Ar and H_2 is fed to the RDD inlet. Depending on the rotating speed and the number of cavities of the disk, different amounts of the concentrated gas are transported to the heated dilution gas stream (1 Nl min^{-1}). The diluted gas is further diluted by a gas (with a flow of 100 Nml min^{-1}), consisting of H_2 , H_2O and Ar in order to achieve comparable gas compositions to experiments performed with setup 1.



(a)



(b)

Figure 2.4 – Photographs of the Trace element setup. (a) Experimental setup (setup 1) used for experiments concerning the analytical performance and sorption experiments; (b) experimental setup (setup 2) used for verification of the calculated detection limit.

References

- [1] D. Peitz, A. Bernhard, M. Elsener, and O. Kroeher. Laboratory test reactor for the investigation of liquid reducing agents in the selective catalytic reduction of nox. *Review of Scientific Instruments*, 82(8):1–8, 2011.
- [2] C. Hueglin, L. Scherrer, and H. Bertscher. An accurate, continuously adjustable dilution system (1:10 to 1:104) for submicron aerosols. *Journal of Aerosol Science*, 28(6):1049–1055, 1997.

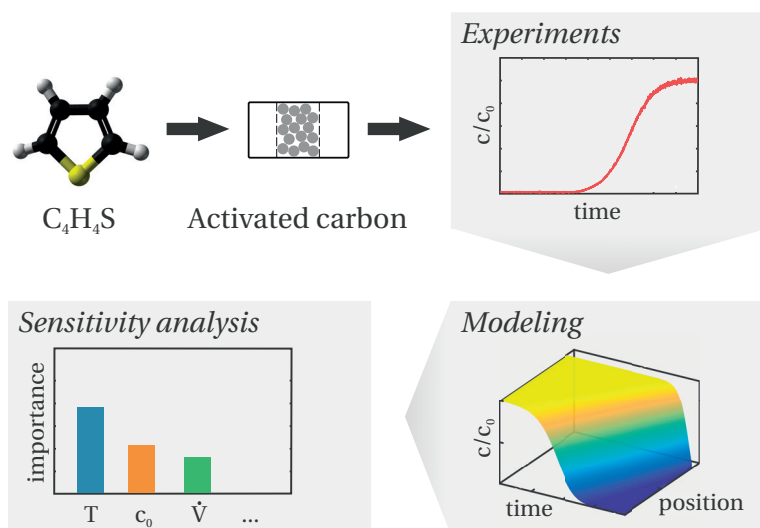
3

Adsorption of thiophene by activated carbon: A global sensitivity analysis

This chapter is adapted from **P. Edinger** et al., *Adsorption of thiophene by activated carbon: A global sensitivity analysis*, Under review.

Abstract

The removal of sulphur compounds in biomass gasification processes is crucial to protect downstream equipment. While conventional sorbent materials can retain H_2S , many fail to capture heterocyclic sulphur compounds such as thiophene (C_4H_4S). This work explored activated carbons (AC) for the removal of thiophene from the gas phase both experimentally and by employing different models. Experiments were performed in a laboratory packed bed column between 100–200°C at various gas flow-rates and inlet concentrations. The transient adsorption process was described by a 1D approach, including mass transfer phenomena and axial dispersion. Experimental validation showed good agreement between measured and predicted breakthrough times and capacities. A global sensitivity analysis (GSA) was performed to obtain a ranking of importance of model input factors and gain further process insight. The GSA included 12 model parameters and a selection of axial dispersion correlations and isotherm models. Based on the chosen range of input factors, the GSA indicated that the type of isotherm model, axial dispersion correlation, and temperature have a major effect on the predicted breakthrough time. The calculated slope of the curve is strongly affected by the isotherm model and axial dispersion correlation. Overall, this work showed that ACs are a promising option for thiophene removal and provided a generic approach for the application of GSA to adsorption models. In the given context the analysis demonstrated that the selection of common model assumptions deserves as much attention as the model parameters.



3.1. Introduction

THE USE of biomass as a feedstock in energy conversion processes provides a viable mean to reduce future greenhouse gas (GHG) emissions¹. One promising technology is the thermochemical conversion through gasification into a syngas that can be used for electricity, heat, fuel and chemicals production^{2,3}. The raw syngas exiting the gasifier contains, depending on gasification parameters, different amounts of H₂, CO, CO₂, CH₄, H₂O and a variety of gas contaminants.

These contaminants include particulates, tars, sulphur and nitrogen compounds, HCl and alkali metals⁴. The feedstock contained sulphur is converted to various species (H₂S, COS, thiophenic compounds, mercaptanes⁵) with a total concentration of several hundreds parts per million (ppmv). These sulphur compounds can cause corrosion of downstream piping⁶ and poisoning of catalysts⁷ used for methanation⁸, Fischer Tropsch (FT) synthesis^{9,10} and fuel cells^{11,12}. As a consequence, all sulphur species should be adequately removed from the gas.

State of the art sulphur capture is performed in cold gas cleaning processes ($T < 100^{\circ}\text{C}$) by gas scrubbing with regenerable physical or chemical solvents¹³. Two processes, based on physical solvents, are the Selexol (polyethylene glycol, 0 to 40 °C) and the Rectisol (methanol, -30 to -60 °C) process¹⁴. Their high associated capital costs can make them unattractive, especially at the small scale, predominantly encountered in biomass gasification processes. An alternative are amine based washers that operate at 30 to 60 °C and have comparably lower investment but higher operating costs. All three processes have in common that guard beds are needed to further reduce the sulphur content to parts per billion (ppbv) levels¹⁵. These beds typically employ ZnO as a solid sorbent that, however, is incapable of removing thiophene (C₄H₄S)^{16–18}. Researchers therefore proposed the use of hydrodesulphurization (HDS) catalysts, embedded in hot gas cleaning processes (HGC, 300 to 850 °C), to convert thiophene to H₂S^{19,20}. Aside from the fact that most HGC processes still face technical obstacles²¹, low temperature alternatives should be investigated for economical comparison.

Activated carbons (AC) are widely used for emission control at low concentrations because of their high cost effectiveness, capture efficiency and regenerability²². While adsorption of thiophene on AC has been studied for deep desulphurisation of transportation fuels in the liquid phase^{23–25}, literature concerning gas phase adsorption is more scarce. As such, the retention of the saturated thiophene analogue tetrahydrothiophene (THT) by commercial ACs has been investigated experimentally^{26–29}. Its presence in pipeline gases, where it serves as an odorant, can cause catalyst poisoning in downstream equipment (e.g. fuel cells³⁰). Though reported sorption capacities are promising, experiments were performed at ambient conditions while the envisaged application of AC in gasification processes demands elevated ones.

Mathematical models of the transient adsorption process can serve as a tool to assess the performance of AC as sorption material in a process chain and optimize the corresponding operating parameters. In subsequent up-scaling considerations they can further help to lower costs by reducing the number of required experiments. Such models typically involve a set of coupled partial differential equations (PDE) derived from the conservation of mass and energy, accompanied by auxiliary equations describing adsorption equilibrium, transport and empirical correlations³¹. A common approach to simplify this stiff problem is to model the rate of mass transfer in the sorbent particles using a linear driving force (LDF) assumption³².

The obtained models are typically evaluated by means of a sensitivity analysis (SA) that aims to link the variation in model output to a variation of the input factors. These SA are,

however, often not extensive in the regard that only selected parameters are varied locally, often one-factor-at-a-time (OAT), in ranges that not necessarily have a representative background^{33–38}. Performing SA on such basis may result in misleading results when the model is non-linear and/or interaction between input factors occur. Global sensitivity analysis (GSA) methods, in comparison, explore the entire input space, thus allowing more robust predictions³⁹. Several GSA methods have been developed in the past^{39,40}. Of these, a variance based approach has been used by Fassò et al.⁴¹ to investigate the bio-sorption of heavy metals in packed bed columns. Apart from taking place in the liquid phase, the study focused only on few model parameters. Another GSA tool is the elementary effects (EE) method^{42,43}, a popular ranking/screening method with low computational cost. It overcomes the disadvantages of the OAT approach by applying it at different points in the input factor hyperspace.

The aim of this work is therefore twofold. At first, the applicability of an AC as a sorbent for thiophene retention is investigated experimentally. In the second step, a mathematical model is developed and validated. Based on this model, the work then aims to explore the effect of input factors on the predicted thiophene breakthrough behaviour by means of a GSA. Herein, the input factors not only include model parameters but also model assumptions concerning the chosen isotherm and axial dispersion correlation.

3.2. Theoretical section

3.2.1. Model description

In the following, a model (see Fig. B.1 for model flow chart) is presented which was developed in order to describe the dynamics of adsorption of thiophene onto AC in a packed bed column. The model is based on the following assumptions:

- (i) adsorption of one component which is present in trace amounts
- (ii) equilibrium between solid- and fluid-phase concentrations can be explained by an isotherm with exponential temperature dependence
- (iii) mass transfer rate is described by the LDF model
- (iv) flow pattern described by axially dispersed plug flow
- (v) isothermal conditions
- (vi) radial effects are negligible
- (vii) removal of adsorbate doesn't affect superficial velocity
- (viii) negligible pressure drop across bed
- (ix) ideal gas behaviour

3

Gas phase material balance

The gas phase material balance can be derived from a differential element of the packed bed given in Fig. 3.1. In this schematic representation, z is the axial coordinate, c the thiophene gas concentration, u_s the superficial velocity and j_{ax} the axial dispersion flux.

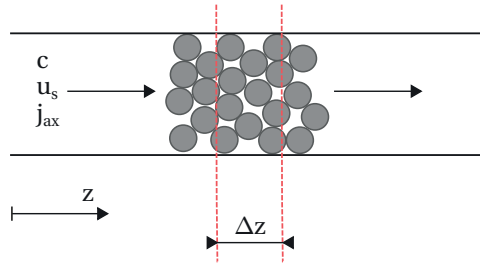


Figure 3.1 – Element of packed bed

The resulting balance includes terms for accumulation, convection, axial dispersion and adsorption.

$$\underbrace{\frac{\partial}{\partial t} (\Delta z A \epsilon_b c)}_{\text{accumulation}} = \underbrace{(A u_s c)|_z - (A u_s c)|_{z+\Delta z}}_{\text{convection}} + \underbrace{(A \epsilon_b j_{ax})|_z - (A \epsilon_b j_{ax})|_{z+\Delta z}}_{\text{axial dispersion}} - \underbrace{\rho_b \Delta z A \frac{\partial q}{\partial t}}_{\text{adsorption}} \quad (3.1)$$

In this equation, t is the time, A the cross-sectional area of the column, ρ_b the bulk density, ϵ_b the bulk porosity and q the average concentration inside the particle. After rearranging and taking the limit $\Delta z \rightarrow 0$ one obtains

$$\epsilon_b \frac{\partial c}{\partial t} + \frac{\partial}{\partial z} (u_s c) + \epsilon_b \frac{\partial j_{ax}}{\partial z} + \rho_b \frac{\partial q}{\partial t} = 0 \quad (3.2)$$

The axial dispersion flux can be described by Fick's first law

$$j_{ax} = -D_{ax} \frac{\partial c}{\partial z} \quad (3.3)$$

where D_{ax} is the axial dispersion coefficient. Including this definition and after applying assumption (vii), Eq. (3.2) becomes

$$\epsilon_b \frac{\partial c}{\partial t} + u_s \frac{\partial c}{\partial z} - \epsilon_b D_{ax} \frac{\partial^2 c}{\partial z^2} + \rho_b \frac{\partial q}{\partial t} = 0 \quad (3.4)$$

After further rearrangement one obtains

$$\frac{\partial c}{\partial t} + u_{iv} \frac{\partial c}{\partial z} - D_{ax} \frac{\partial^2 c}{\partial z^2} + \frac{\rho_b}{\epsilon_b} \frac{\partial q}{\partial t} = 0 \quad (3.5)$$

where u_{iv} is the interstitial velocity.

The thiophene gas phase concentration c can be related to its molar fraction y by

$$c = \frac{yp}{R_g T} \quad (3.6)$$

where p refers to the total pressure, R_g the universal gas constant and T the column temperature.

Axial dispersion coefficients

Axial dispersion of fluid flow in packed beds is the result of molecular diffusion, turbulent mixing by flow splitting and recombination around particles and flow non-uniformities as a consequence of irregular packing⁴⁴. Its effect on the breakthrough behaviour is often negligible in industrial applications while this is not necessarily the case in lab-scale experiments^{34,45}. Ideally, the combined effects of mixing are determined experimentally using tracer techniques in the actual column⁴⁶. If deemed infeasible, one may revert to correlations that describe both molecular diffusion and turbulent mixing (neglecting flow non-uniformities) by relating the particle Péclet number Pe to the product of the Reynolds number Re_p and Schmidt number Sc

$$Re_p = \frac{u_s d_p}{\nu_{Ar}} \quad Sc = \frac{\nu_{Ar}}{D_m} \quad (3.7)$$

where d_p is the particle diameter and ν_{Ar} the kinematic viscosity of Ar based on the DIPPR 801 Database⁴⁷. The molecular diffusivity D_m of thiophene in Ar is calculated according to Fuller et al.⁴⁸.

The axial dispersion correlations typically take the form of

$$\frac{1}{Pe} = \frac{D_{ax}}{d_p u_{iv}} = \frac{\gamma_1 \epsilon_b}{Re_p Sc} + \left(Pe_\infty \left(1 + \frac{\gamma_1 \gamma_2 \epsilon_b}{Re_p Sc} \right) \right)^{-1} \quad (3.8)$$

where parameters γ_1 , γ_2 and Pe_∞ are correlation specific and summarized for six frequently used correlations in Table 3.1.

Another approach to describe D_{ax} is taken by Koch and Brady⁵³

$$\frac{1}{Pe} = \frac{\epsilon_b}{Re_p Sc} + \frac{3}{4} \epsilon_b + \frac{\pi^2 \epsilon_b (1 - \epsilon_b)}{6} \ln(Re_p Sc) \quad (3.9)$$

Figure 3.2 illustrates the variation of the Pe number as a function of the product $Re_p Sc$ for the seven presented axial dispersion correlations. The curves show a considerable amount of scatter, especially as $Re_p Sc$ increases, that, can in part be related to the particle size^{50,54}, porosity and adsorption effects^{31,55}.

Table 3.1 – Correlations to describe axial dispersion

| No. | Author | Ref. | γ_1 | Pe_∞ | γ_2 |
|-----|-----------------|------|----------------------|-------------|-------------------------|
| 1 | Edwards (1986) | 49 | 0.73 | 2 | 13 |
| 2 | Hsu (1981) (i) | 50 | 0.76 | 0.3 | 1.8 |
| 3 | Hsu (1981) (ii) | 50 | 0.9 | 0.28 | 0.7 |
| 4 | Wen (1975) | 51 | 0.3 | 2 | $12.67 \epsilon_b^{-1}$ |
| 5 | Wakao (1978) | 52 | $20 \epsilon_b^{-1}$ | 2 | 0 |
| 6 | Ruthven (1984) | 31 | 0.7 | 2 | 0 |

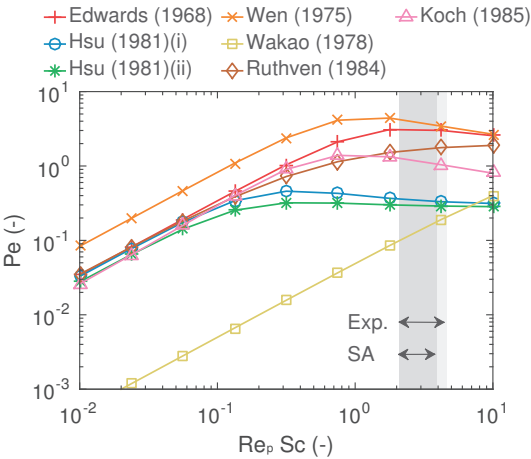


Figure 3.2 – Variation of Pe number with the product $Re_p Sc$ for different axial dispersion correlations. The gray bands indicate the range of $Re_p Sc$ in this work (Exp.: Experiments; SA: Sensitivity analysis).

Mass transfer rate

Thiophene uptake by the particles is described by means of a LDF approach⁵⁶

$$\frac{\partial q}{\partial t} = k(q^* - q) \quad (3.10)$$

It relates the mass transfer rate between gas- and solid-phase to the linear difference between a particle surface equilibrium concentration q^* , obtained from an isotherm, and the average solid phase concentration q . The mass transfer coefficient k in this equation can be described by the lumped sum of both extra- and intra-particle mass transfer resistances⁵⁷

$$\frac{1}{k} = \underbrace{\frac{d_p q_0 \rho_p}{6k_f c_0}}_{\text{film resistance}} + \underbrace{\frac{d_p^2 q_0 \rho_p}{60\epsilon_p c_0 D_p}}_{\text{macro-pore resistance}} \quad (3.11)$$

In this equation, c_0 is the inlet concentration, $q_0 = q^*(c_0)$ at bed temperature T , ρ_p the particle density, ϵ_p the particle porosity and D_p the particle diffusivity. For the range $1.4 \leq Re_p \leq 2.5$ found in this work, the film mass transfer coefficient k_f can be calculated by a Sherwood (Sh) correlation⁵⁸

$$Sh = \frac{k_f d_p}{D_m} = 1.15 \left(\frac{Re_p}{\epsilon_b} \right)^{1/2} Sc^{1/3} \quad (3.12)$$

The particle diffusivity D_p is obtained from

$$\frac{1}{D_p} = \frac{1}{D_K} + \frac{1}{D_{m,eff}} \quad (3.13)$$

where D_K refers to the Knudsen diffusivity and $D_{m,eff}$ to the effective molecular diffusivity. D_K is calculated using

$$D_K = 97r_e \left(\frac{T}{\widetilde{M}_{Thio}} \right)^{1/2} \quad (3.14)$$

where r_e is the mean pore radius and \widetilde{M}_{Thio} the molecular weight of thiophene. $D_{m,eff}$ is taken from

$$D_{m,eff} = \frac{\epsilon_p D_m}{\tau_{tor}} \quad (3.15)$$

where τ_{tor} is the tortuosity factor.

Equilibrium models

A range of isotherm equations have been proposed to relate the quantity of molecules adsorbed onto the sorbent to their gas concentration⁵⁹. In the current work, three models incorporating one to three parameters were selected to fit the measured equilibrium data. Each of them was chosen as a representative of their parameter class.

The one-parametric Henry isotherm

$$q^* = K_H c \quad (3.16)$$

was selected as a basic model, usually employed at very low contaminant concentrations. Though this condition is often not satisfied⁶⁰, the model has been used frequently in the past to provide simplified, analytical solutions of breakthrough curve models^{61,62}. It is included in this work to investigate the effect that such a simplifying assumption on the prediction capabilities of a model has.

The two-parametric Langmuir model

$$q^* = \frac{q_{mL}bc}{1+bc} \quad (3.17)$$

assumes that adsorption occurs on a homogeneous surface in one layer without interaction between sorbed molecules. It is one of the most frequently employed models in literature, often providing good agreement with experimental data although the underlying assumptions are not necessarily fulfilled.

The Tóth isotherm

$$q^* = \frac{q_{mT}K_Tc}{(1+(K_Tc)^{n_T})^{1/n_T}} \quad (3.18)$$

was chosen as a representative of three-parameter models⁶³. It is an empirical model, developed for heterogeneous materials such as activated carbon.

In the introduced isotherm equations K_H is the Henry constant, q_{mL} the saturation value of the Langmuir isotherm, b the Langmuir equilibrium constant and q_{mT} , K_T , n_T are Tóth isotherm parameters. The temperature dependence of the three isotherms was described by means of an exponential approach⁶⁴

$$K_H = K_{HTref} \exp\left(\frac{\Delta H_H}{RT_{ref}} \left(1 - \frac{T_{ref}}{T}\right)\right) \quad (3.19)$$

$$b = b_{Tref} \exp\left(\frac{\Delta H_L}{RT_{ref}} \left(1 - \frac{T_{ref}}{T}\right)\right) \quad (3.20)$$

$$K_T = K_{TTref} \exp\left(\frac{\Delta H_T}{RT_{ref}} \left(1 - \frac{T_{ref}}{T}\right)\right) \quad (3.21)$$

In these equations, K_{HTref} , b_{Tref} and K_{TTref} are pre-exponential factors, ΔH the heats of adsorption and T_{ref} a reference temperature (273 K). Both parameters q_{mT} and n_T in the Tóth isotherm are dependent upon temperature as described by Do⁶⁵.

$$q_{mT} = q_{mTTref} \exp\left(\chi \left(1 - \frac{T_{ref}}{T}\right)\right) \quad n_T = n_{TTref} + \alpha \left(1 - \frac{T_{ref}}{T}\right) \quad (3.22)$$

Initial and boundary conditions

The initial conditions for a bed of length L are

$$c = 0 \quad 0 \leq z \leq L \quad t < 0 \quad (3.23)$$

$$q = 0 \quad 0 \leq z \leq L \quad t < 0 \quad (3.24)$$

The boundary conditions according to Danckwerts⁶⁶ are

$$-D_{ax}\epsilon_b \frac{\partial c}{\partial z} = u_s(c_0 - c) \quad z = 0 \quad t \geq 0 \quad (3.25)$$

$$\frac{\partial c}{\partial z} = 0 \quad z = L \quad t \geq 0 \quad (3.26)$$

Non-dimensionalisation

Upon defining the dimensionless variables

$$\tau = \frac{u_{iv}t}{L}; \quad \xi = \frac{z}{L}; \quad \zeta = \frac{c}{c_0}; \quad Q = \frac{q}{q_0}; \quad Q^* = \frac{q^*}{q_0} \quad (3.27)$$

One can calculate the following partial derivatives

$$\frac{\partial c}{\partial t} = \frac{u_i c_{in}}{L} \frac{\partial \zeta}{\partial \tau}; \quad \frac{\partial c}{\partial z} = \frac{c_{in}}{L} \frac{\partial \zeta}{\partial \xi}; \quad \frac{\partial^2 c}{\partial z^2} = \frac{c_{in}}{L^2} \frac{\partial^2 \zeta}{\partial \xi^2}; \quad \frac{\partial q}{\partial t} = \frac{u_i q_0}{L} \frac{\partial Q}{\partial \tau} \quad (3.28)$$

Implementing these definitions into Eq. (3.5) one obtains

$$\frac{\partial \zeta}{\partial \tau} + \frac{\partial \zeta}{\partial \xi} - \underbrace{\frac{D_{ax}}{u_{iv}L}}_{Pe_m^{-1}} \frac{\partial^2 \zeta}{\partial \xi^2} + \frac{\rho_b q_0}{\epsilon_b c_0} \frac{\partial Q}{\partial \tau} = 0 \quad (3.29)$$

The Henry isotherm in Eq. (3.16) combined with Eq. (3.10) becomes

$$\frac{\partial Q}{\partial \tau} = \frac{kL}{u_{iv}} \left[\left(\frac{K_H c_0}{q_0} \right) \zeta - Q \right] \quad (3.30)$$

Similarly the Langmuir isotherm in Eq. (3.17) can be rewritten as

$$\frac{\partial Q}{\partial \tau} = \frac{kL}{u_{iv}} \left[\left(\frac{q_{mL} b c_0}{q_0} \right) \frac{\zeta}{1 + b c_0 \zeta} - Q \right] \quad (3.31)$$

And the Tóth isotherm in Eq. (3.18) becomes

$$\frac{\partial Q}{\partial \tau} = \frac{kL}{u_{iv}} \left[\left(\frac{q_{mT} K_T c_0}{q_0} \right) \frac{\zeta}{(1 + (K_T c_0 \zeta)^{n_T})^{1/n_T}} - Q \right] \quad (3.32)$$

The initial conditions transform to

$$\zeta = 0 \quad 0 \leq \xi \leq 1 \quad \tau < 0 \quad (3.33)$$

$$Q = 0 \quad 0 \leq \xi \leq 1 \quad \tau < 0 \quad (3.34)$$

And the boundary conditions become

$$\frac{\partial \zeta}{\partial \xi} = Pe_m (\zeta - 1) \quad \xi = 0 \quad \tau \geq 0 \quad (3.35)$$

$$\frac{\partial \zeta}{\partial \xi} = 0 \quad \xi = 1 \quad \tau \geq 0 \quad (3.36)$$

3.2.2. Sensitivity analysis

Sampling points for the EE method were generated by a Latin hypercube (LH) approach⁶⁷ that has proven to be more efficient than the initially suggested trajectory method^{68,69}. The $r_{EE}(k_{EE} + 1)$ points are located in $(k_{EE} + 1)$ matrices, where r_{EE} is the number of calculated elementary effects and k_{EE} is the number of input factors. Matrix X^a represents the 'core' matrix of this design

$$X^a = \begin{pmatrix} x_{1,1}^a & \cdots & x_{1,j}^a & \cdots & x_{1,k_{EE}}^a \\ \cdots & \cdots & x_{i,j}^a & \cdots & \cdots \\ x_{r_{EE},1}^a & \cdots & x_{r_{EE},j}^a & \cdots & x_{r_{EE},k_{EE}}^a \end{pmatrix} \quad (3.37)$$

whereas the k_{EE} matrices X_j^{ab} , that alter from X^a only by one column consisting of coordinates $x_{i,j}^b$, can be interpreted as its rays.

$$X_j^{ab} = \begin{pmatrix} x_{1,1}^a & \cdots & x_{1,(j-1)}^a & x_{1,j}^b & x_{1,(j+1)}^a & \cdots & x_{1,k_{EE}}^a \\ \cdots & \cdots & x_{i,(j-1)}^a & x_{i,j}^b & x_{i,(j+1)}^a & \cdots & \cdots \\ x_{r_{EE},1}^a & \cdots & x_{r_{EE},(j-1)}^a & x_{r_{EE},j}^b & x_{r_{EE},(j+1)}^a & \cdots & x_{r_{EE},k_{EE}}^a \end{pmatrix} \quad (3.38)$$

The elementary effects $EE_{i,j}$ of the individual rays are calculated according to Eq. (3.39) as the ratio of finite differences of the model outputs Y and the perturbed input factors.

$$EE_{i,j} = \frac{[Y(X_j^{ab}) - Y(X^a)]_i}{[X_j^{ab} - X^a]_i} \Delta x_j \quad (3.39)$$

Herein, Δx_j is the range of the individual input factors. The mean elementary effect EE_j and the corresponding standard deviation $STD EE_j$ of each factor j are calculated using

$$EE_j = \frac{\sum_{i=1}^{r_{EE}} EE_{i,j}}{r_{EE}} \quad STD EE_j = \frac{\sum_{i=1}^{r_{EE}} (EE_{i,j} - EE_j)^2}{r_{EE}} \quad (3.40)$$

Input factor ranges

The input factor space of this SA (see Table 3.2) encompasses 12 model parameters and two non-numerical inputs (no. 13, 14) that describe model assumptions concerning the chosen isotherm model and axial dispersion correlation. Three types of probability distributions were assigned to these inputs according to available data and knowledge. Normal distributions were assigned to parameters with *a priori* knowledge of mean and standard deviation. Without such information available, uniform distributions were assigned to the parameters. Discrete uniform distributions were assigned to non-numerical input factors.

VtotN (volume flow rate) Two MFCs control the flow with associated uncertainty of thiophene in He ($\dot{V}_1 \pm \sigma_{V1}$) and Ar ($\dot{V}_2 \pm \sigma_{V2}$) to the column. Upon mixing, the uncertainty σ_{V3} of the resulting flow \dot{V}_3 can be calculated according to

$$\sigma_{V3} = \sqrt{\sigma_{V1}^2 + \sigma_{V2}^2} \quad (3.41)$$

where

$$\sigma_{V1} = 0.06 \text{ Nml min}^{-1}$$

$$\sigma_{V2} = 0.93 \text{ Nml min}^{-1}$$

yInPpmv (feed mole fraction) The uncertainty of the thiophene mole fraction σ_{y3} in \dot{V}_3 before the column can be calculated by

$$\frac{\sigma_{y3}}{y_3} = \sqrt{\left(\frac{\sigma_{y1}}{y_1}\right)^2 + \left(\frac{\sigma_{V1}}{\dot{V}_1}\right)^2 + \left(\frac{\sigma_{V3}}{\dot{V}_3}\right)^2} \quad (3.42)$$

where σ_{y1} is the uncertainty of the thiophene mole fraction y_1 in the gas cylinder

$$y_1 \pm \sigma_{y1} = (5.0 \pm 0.1) \times 10^{-4}$$

$$\dot{V}_1 = 1.27 \text{ Nml min}^{-1}$$

$$\dot{V}_3 = 42.5 \text{ Nml min}^{-1}$$

Table 3.2 – List of input factors for sensitivity analysis

| No. | Input factor | Notation | Unit | Mean value | Distribution | STD/bounds | Comment |
|-----|------------------------|---------------------|-----------------|-----------------------|------------------|----------------------------|--|
| 1 | volume flow rate | $V_{tot}N$ | $Nml\ min^{-1}$ | 42.5 | normal | 0.9 | Calculated from uncertainty of individual MFCs |
| 2 | feed mole fraction | $y_{in}P_{mix}$ | ppmv | 15 | normal | 0.9 | Calculated from uncertainty of individual MFCs and thiophene concentration in gas cylinder |
| 3 | column temperature | T_0 | K | - | uniform | [396, 400] | Based on axial temperature measurements and an approximation concerning the temperature rise for adsorption in an adiabatic column |
| 4 | column pressure | p_0 | Pa | - | uniform | [1.48, 1.52] $\times 10^5$ | Based on estimated pressure drop in the packed bed ⁷⁰ and the variation of ambient pressure during experiments |
| 5 | column diameter | d_i | m | 2.0×10^{-3} | normal | 0.1×10^{-3} | Measured by caliper |
| 6 | particle diameter | d_p | m | 1.38×10^{-4} | normal | 0.05×10^{-4} | Measured by imaging particle analysis (Image) |
| 7 | pore radius | r_e | m | 13×10^{-10} | normal | 1×10^{-10} | Measured (see Section 3.3.1) |
| 8 | bulk voidage | ϵ_{psBulk} | - | - | uniform | [0.390, 0.400] | Based on literature ⁷¹ |
| 9 | bulk density | ρ_{oBulk} | $kg\ m^{-3}$ | 497 | normal | 12 | Calculated from measurement uncertainties (see 3.2.2) |
| 10 | skeletal density | ρ_{oS} | $kg\ m^{-3}$ | 2450 | normal | 51 | Measured (see Section 3.3.1) |
| 11 | tortuosity | tortuosity | - | - | uniform | [2, 6] | Based on literature ³¹ |
| 12 | bed mass | mBed | kg | 2.00×10^{-5} | normal | 0.01×10^{-5} | Based on measurement accuracy of scale and transfer process of sorbent to column. |
| 13 | isotherm model | Isotherm | - | - | uniform discrete | [1, 3] | - |
| 14 | axial dispersion model | DaxModel | - | - | uniform discrete | [1, 8] | - |

T0 (column temperature) Two sources of error concerning the bed temperature were identified:

1. Figure 3.3 depicts the axial temperature profile of the oven at 150 °C. The temperature drops with increasing distance from the axial center (0 mm). Considering a bed length of ca. 1 cm and positioning errors during column installation, results in an approximated column temperature error of 2 to 3 °C.

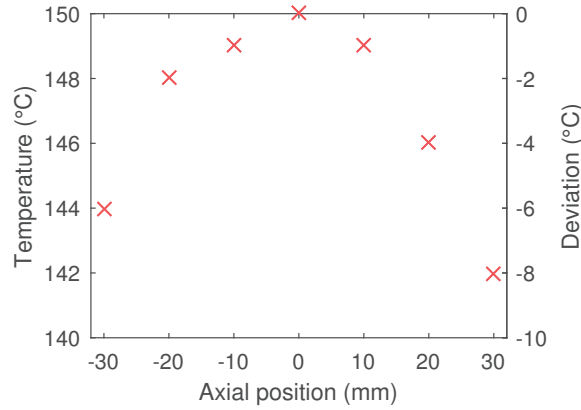


Figure 3.3 – Temperature error of oven. Zero axial position refers to the center of the oven.

2. An additional error may be caused by a temperature rise due to the exothermic nature of adsorption which is not accounted for in the developed model in Section 3.2.1. The temperature increase may be approximated by the limiting case of an adiabatic column⁷². With values for ΔH_L and q^* as determined in Section 3.4.1 and a heat capacity $c_{p,c}$ of the AC taken from literature⁷³ one can calculate the temperature rise ΔT according to

$$\Delta T \approx \frac{\Delta H_L q^*}{c_{p,c}} = \frac{0.1 \text{ mol kg}^{-1} 49 \text{ kJ mol}^{-1}}{1.3 \text{ kJ kg}^{-1} \text{ K}^{-1}} = 3.8 \text{ K} \quad (3.43)$$

rhoBulk (bulk density) The bulk density was estimated by weighing an amount m_{cyl} of AC into a cylinder with diameter d_{cyl} with a bed height of h_{cyl} as depicted in Fig. 3.4.

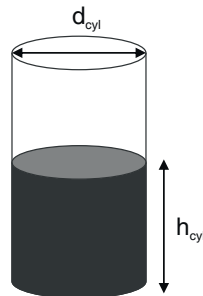


Figure 3.4 – Schematic representation of cylinder used to determine the bulk density of the activated carbon

$$\rho_b = \frac{m_{cyl}}{V_{cyl}} = \frac{4m_{cyl}}{\pi d_{cyl}^2 h_{cyl}} \quad (3.44)$$

Based on Eq. (3.44) the uncertainty σ_{ρ_b} can be estimated by

$$\frac{\sigma_{\rho_b}}{\rho_b} = \sqrt{\left(\frac{\sigma_{m_{cyl}}}{m_{cyl}}\right)^2 + \left(\frac{\sigma_{h_{cyl}}}{h_{cyl}}\right)^2 + \left(\frac{\sigma_{d_{cyl}}}{d_{cyl}}\right)^2} \quad (3.45)$$

where

$$m_{cyl} \pm \sigma_{m_{cyl}} = (5.71 \pm 0.03) \times 10^{-3} \text{ kg}$$

$$h_{cyl} \pm \sigma_{h_{cyl}} = (6.5 \pm 0.1) \times 10^{-2} \text{ m}$$

$$d_{cyl} \pm \sigma_{d_{cyl}} = (1.50 \pm 0.01) \times 10^{-2} \text{ m}$$

3.2.3. Key figures

Solving the system of PDEs yields a breakthrough curve in form of a matrix rather than a scalar that could easily be implemented into a SA. Different key figures that describe the shape and position of the curve were therefore defined and compared in correlation plots. Based on this analysis, two key figures were chosen for further investigation.

Quantiles of the breakthrough curve in form of breakthrough times (here t_1 , t_{10} , t_{50} , t_{90} , t_{99}) are convenient measures to describe the curve's position/shape. The width of the breakthrough curve can be characterized by $t_{90} - t_{10}$. The slope of the curve was evaluated by means of two key figures s_{50} and $s_{90,10}$. Here s_{50} is the derivative of the breakthrough curve at t_{50} while $s_{90,10}$ is calculated according to

$$s_{90,10} = \frac{0.9 - 0.1}{t_{90} - t_{10}} \quad (3.46)$$

The breakthrough capacity q_{90} until time t_{90} is a more inclusive key figure.

The defined key figures were calculated for all model evaluations of the SA and the results are visualized in form of a correlation matrix in Fig. 3.5.

Based on this plot, the variation between the resulting breakthrough curves was decomposed into two key figures with little correlation: A measure of the slope and one of the shift of the breakthrough curve. The slope $s_{90,10}$ was chosen as a more robust measure of slope compared to s_{50} that is evaluated at just one point. The value t_{50} was chosen as a measure of the shift of the breakthrough curve.

3.2.4. Implementation

The non-dimensionalised system of PDEs was solved numerically by the method of lines (MOL) using Mathematica 10.4 (Wolfram Research). The Mathematica kernel was called by MATLAB 2015a (The MathWorks) which was used for data handling and SA with an adapted version of the SAFE 1.1 toolbox⁷⁴. The SA was performed with 2000 samples resulting in a total of 3×10^4 model evaluations (see Appendix B.3 for convergence analysis).

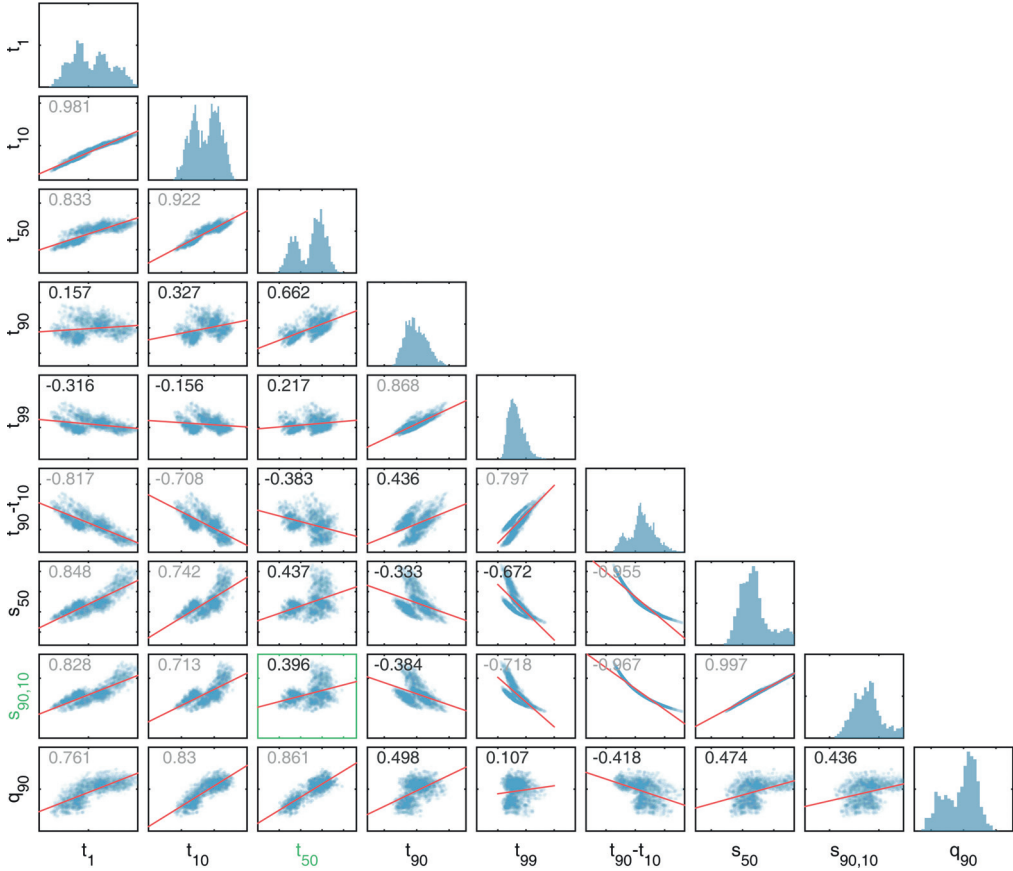


Figure 3.5 – Correlation matrix for various key figures. Selected key figures are marked green.

3.3. Experimental section

3.3.1. Material

A commercial activated carbon (ACM40-4WA, CECA) was used in this study. The material was crushed, sieved and the sieve fraction 125 to 160 μm used for experiments. The specific surface area (SSA, BET method) and pore size distribution (BJH method) of the sorbent were measured by N_2 physisorption using a Tristar II (Micromeritics) after degassing at 150 $^{\circ}\text{C}$ for 3 h. The skeletal density of the material was determined by an AccuPyc II 1340 pycnometer (Micromeritics). An overview of the sorbent properties is given in Table 3.3.

3

Table 3.3 – Sorbent properties

| Adsorbent | CECA ACM40-4WA |
|------------------------------------|----------------------|
| d_p (m) | 138×10^{-6} |
| r_e (m) | 13×10^{-10} |
| ρ_b (kgm^{-3}) | 497 |
| ρ_s (kgm^{-3}) | 2450 |
| SSA ($\text{m}^2 \text{g}^{-1}$) | 991 |

3.3.2. Experimental procedure

For experiments, ca. 20 mg (corrected for moisture content) of fresh sorbent were transferred to a glass column (2 mm i.d., 6 mm o.d.) and held in place by quartz wool. The column was connected to the experimental setup and a gas leak test was performed. The column was subsequently heated to 150 $^{\circ}\text{C}$ for 30 min in Ar atmosphere for moisture removal. Next, the operating conditions were adjusted according to Table 3.4. After 30 min, experiments were started by switching valves SV1 and SV2. The resulting change in gas composition at the column inlet (98 % signal in <1 min) was considered to be a step change.

Table 3.4 – List of experimental conditions

| Run | T ($^{\circ}\text{C}$) | $\dot{V}_{tot,n}$ (Nml min^{-1}) | y_0 (ppmv) |
|-----|----------------------------|---|--------------|
| 1 | 150 | 30.0 | 15.0 |
| 2 | 100 | 30.0 | 15.0 |
| 3 | 150 | 55.0 | 15.0 |
| 4 | 150 | 42.5 | 15.0 |
| 5 | 150 | 30.0 | 8.5 |
| 6 | 150 | 30.0 | 30.0 |
| 7 | 100 | 30.0 | 8.5 |
| 8 | 100 | 30.0 | 30.0 |
| 9 | 200 | 30.0 | 15.0 |
| 10 | 200 | 30.0 | 30.0 |

3.3.3. Analytical method

A mass spectrometer (MS, Extrel MAX 300-LG, inlet temperature at 120 $^{\circ}\text{C}$) was used to characterize the gas composition. Calibration of thiophene was performed by measuring the inlet

gas mixture, fed over the bypass to the MS. After switching to the reactor path, the gas molar fraction y of thiophene was calculated according to Eq. (3.47) where He served as an internal standard.

$$y = \frac{\left(\frac{I_{84, C_4H_4S}}{I_{4, He}} \right) y_{ref}}{\left(\frac{I_{84, C_4H_4S}}{I_{4, He}} \right)_{ref}} \quad (3.47)$$

In this equation, I refers to the measured intensities (averaged over 15 min) at the corresponding m/z . The limit of detection (LOD) and quantification (LOQ) of thiophene for the applied method were calculated to be 0.14 ppmv and 0.47 ppmv, respectively.

3.4. Results and discussion

3.4.1. Adsorption isotherm modeling

The three isotherm models introduced in Section 3.2.1 were fitted to the experimental data set using a non-linear least squares approach (Levenberg-Marquardt algorithm). A summary of estimated adsorption isotherm parameters is given in Table 3.5.

Table 3.5 – Isotherm fitting results

| Isotherm | R^2_{adj} | Parameter | Unit | Estimate |
|----------|-------------|--------------|------------------------------|---------------------|
| Henry | 0.9150 | K_{HTref} | $\text{m}^3 \text{kg}^{-1}$ | 6.35×10^3 |
| | | ΔH_H | J mol^{-1} | -3.48×10^4 |
| Langmuir | 0.9946 | q_{mL} | mol kg^{-1} | 0.24 |
| | | b_{Tref} | $\text{m}^3 \text{mol}^{-1}$ | 3.08×10^5 |
| | | ΔH_L | J mol^{-1} | -4.94×10^4 |
| Tóth | 0.9939 | K_{TTref} | $\text{m}^3 \text{mol}^{-1}$ | 2.43×10^2 |
| | | ΔH_T | J mol^{-1} | -3.14×10^4 |
| | | q_{mTTref} | mol kg^{-1} | 3.48×10^3 |
| | | χ | - | -2 |
| | | n_{TTref} | - | 0.11 |
| | | α | - | -0.1 |

Figure 3.6a presents the experimentally determined sorption capacities and corresponding model fits at three temperatures 100, 150 and 200 °C. The associated residuals are plotted in Fig. 3.6b.

As temperatures rise, adsorption capacities generally decrease. At the same time, the multi-parameter isotherms become less favourable, thereby successively approaching the linear Henry isotherm. The latter model fits data at all investigated temperatures with average relative errors in the range of 16 to 30 % and an adjusted coefficient of determination R^2_{adj} of 0.9150. Both the Langmuir and Tóth model have superior R^2_{adj} of 0.9945 and 0.9939, respectively. Especially at low temperatures they fit experimental data better with relative errors of 0.2 to 2.3 % at 100 °C which gradually increase to 17 to 23 % as temperatures rise.

3.4.2. Breakthrough curve results

This section compares experimental with modelling results and discusses the effects of gas flow rate, temperature and thiophene inlet concentration on the breakthrough behaviour.

In order to predict the output response of the model to a step input, the input factors listed in Table 3.2 have to be fixed appropriately. They can be classified into three groups:

1. The experimental settings encompass V_{totN} , y_{InPpmv} and T_0 whose values were taken from Table 3.4 as well as the system pressure p_0 and inner column diameter d_i .
2. The sorbent properties. These can be further subdivided into:
 - (a) Measured properties, including d_p , r_e , ρ_{Bulk} , ρ_S and m_{Bed} .

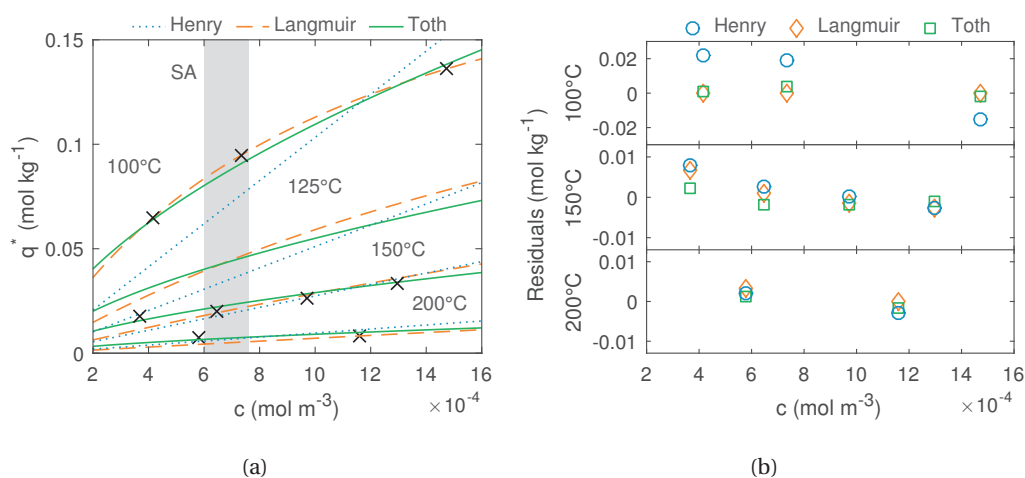


Figure 3.6 – Adsorption isotherm fitting results. (a) Adsorption isotherms. Crosses represent experimental data and lines fits by the Henry, Langmuir and Tóth isotherm models. The gray band indicates the parameter range of the inlet concentration c_0 used in the SA with an average temperature of 125 °C; (b) residuals plot for three equilibrium models at three temperatures.

- (b) Properties estimated from available literature data^{31,71}. These include the bulk voidage (0.4) and the tortuosity (2).

3. Model assumptions which include:

- The choice of isotherm model. Here, the Langmuir isotherm was chosen based on its superior R^2_{adj} .
- The choice of axial dispersion correlation. Here, axial dispersion coefficients were estimated from the correlation given by Edwards and Richardson⁴⁹ as it fitted the breakthrough curves best compared to other correlations discussed in Section 3.2.1.

Parity plots for breakthrough time t_{90} and the corresponding sorption capacity q_{90} in Fig. 3.7, respectively give a summary of the predictive abilities of the developed model. Both the predicted t_{90} and q_{90} lie well within the $\pm 15\%$ error lines, with the exception of run 9 whose t_{90} and q_{90} are under-predicted by 24 to 27 %.

Among the varying conditions studied, the highest thiophene capacity of 138 mmol kg^{-1} was observed at a temperature of 100 °C, 30 Nml min⁻¹ total gas flow rate and 30 ppmv C₄H₄S in the feed stream. On the other hand, the lowest capacity of 7 mmol kg^{-1} was measured at 200 °C, 30 Nml min⁻¹ total gas flow rate and 30 ppmv C₄H₄S in the feed stream.

Effect of gas flow rate

The effect of gas flow rate on breakthrough behaviour was investigated in the range 30 to 55 Nml min⁻¹ at 150 °C with a thiophene inlet concentration of 15 ppmv. Experimental and modeling results in Fig. 3.8b agree well for flow rates up to 42.5 Nml min⁻¹. In case of a flow rate of 55 Nml min⁻¹, the experimentally determined curve is steeper with a later onset of the breakthrough curve.

The flow rate affects the breakthrough capacity only to a small extent with a variation <3 % within the flow range studied. Breakthrough times t_{90} , on the other hand, decreased

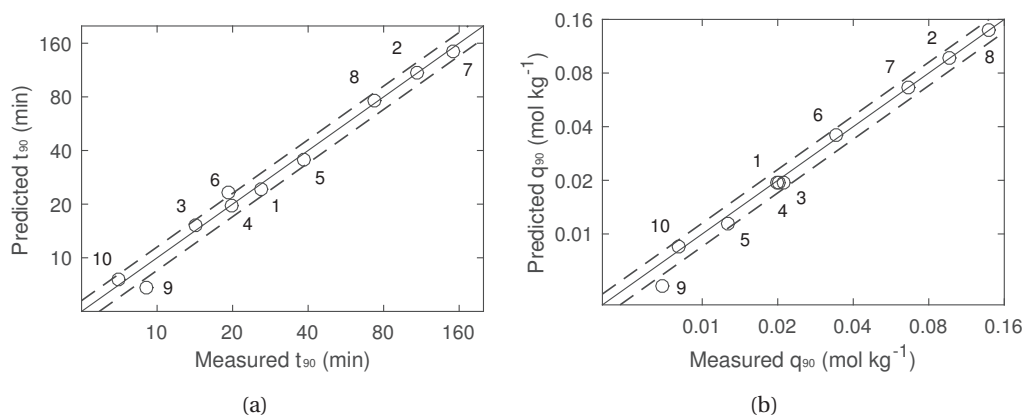


Figure 3.7 – Parity plots with $\pm 15\%$ error lines. Numbers attached to the markers indicate the experimental run as listed in Table 3.4. (a) Predicted *versus* measured breakthrough time t_{90} ; (b) predicted *versus* measured breakthrough time q_{90} .

significantly from 26 to 14 min when increasing the flow rate from 30 to 55 Nml min⁻¹ because more thiophene molecules entered the column per unit time, causing the concentration front to move faster through the bed.

At the same time a steepening of the breakthrough curve is observed. An enhanced film transfer coefficient, that increases with the square root of the gas velocity, can be excluded as a reason for the observed phenomenon. Its contribution to the mass transfer resistance $1/k$ in Eq. (3.11) is minor ($\approx 6\%$) compared to the macro-pore resistance and will therefore have little effect on the overall value of k . The observed curve steepening is rather a consequence of the increased number of thiophene molecules entering each slab of bed per time, while the corresponding adsorption rate doesn't increase proportionally. To further investigate the effect of flow rate, the eluent concentration is plotted in Fig. 3.9 *versus* a normalized time $\tau = tu_s/L_{bed}$ that can also be interpreted as the number of bed volumes.

The adjusted breakthrough curves now exhibit a flattening as the flow rate increases that can be related to an internal mass transfer limitation. As the flow rate rises, the residence time in each slab of bed decreases while the time required for a thiophene molecule to diffuse into a particle remains constant. The adsorption rate decreases and as a consequence the breakthrough curves flatten.

Effect of temperature

Temperature greatly affects the adsorption of thiophene onto activated carbon having both an effect on the breakthrough capacity q_{90} and the breakthrough curve shape. These phenomena are visualized in Fig. 3.8a where modelling and experimental results agree well. At 100 °C, an inlet concentration of 15 ppmv C₄H₄S and a flow rate of 30 Nml min⁻¹, the sample had a capacity of 97 mmol kg⁻¹. An increase in temperature to 150 °C results in a 80 % drop in capacity. The trend continues at 200 °C, where the sorbent loses another 65 % of its sorption capacity. This observed decrease is a consequence of the exothermic nature of the adsorption process.

The shape of the breakthrough curve is affected by several factors. Their steepening with increasing temperature can, in part (see also Fig. B.5), be related to the associated increase in flow rate under operating conditions (a temperature rise from 100 to 200 °C causes a 27 %

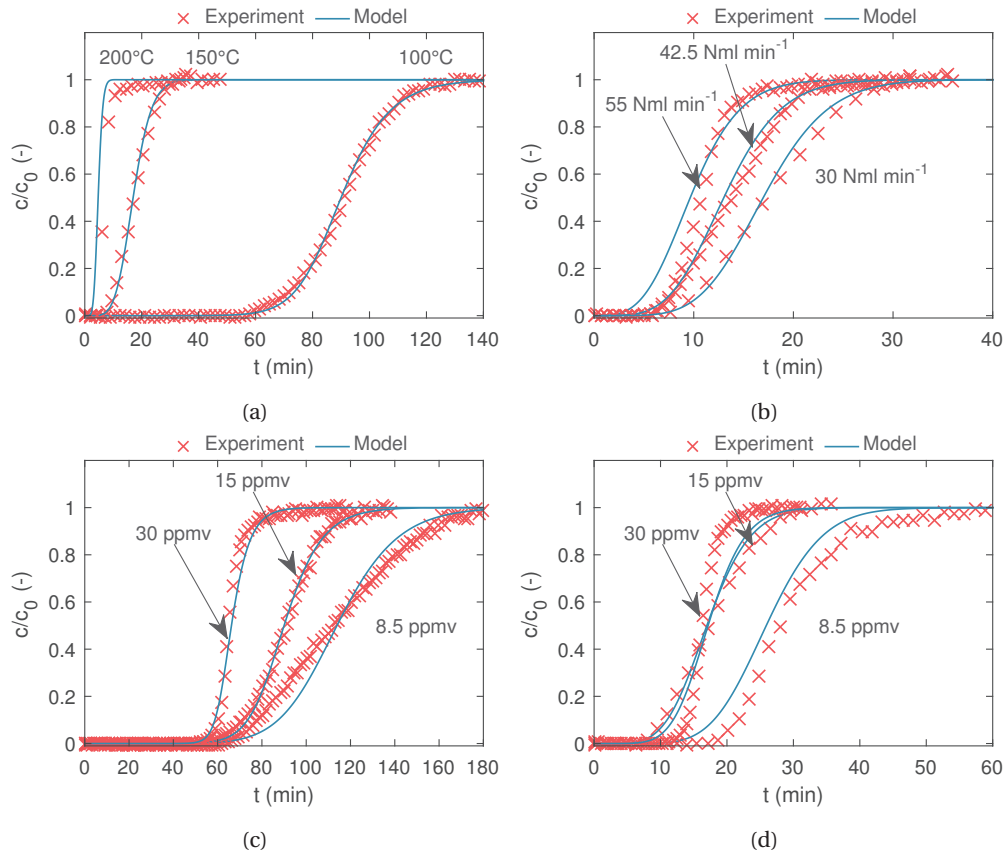


Figure 3.8 – Experimental and predicted breakthrough curves for the adsorption of thiophene on AC. (a) Breakthrough curves at 100, 150 and 200 °C (C_4H_4S inlet concentration: 15 ppmv, total flow rate: 30 Nml min⁻¹); (b) breakthrough curves for flow rates of 30, 42.5 and 55 Nml min⁻¹ (C_4H_4S inlet concentration: 15 ppmv, temperature: 150 °C); (c) breakthrough curves for thiophene inlet concentrations of 8.5, 15 and 30 ppmv (temperature 100 °C, total flow rate: 30 Nml min⁻¹); (d) breakthrough curves for thiophene inlet concentrations of 8.5, 15 and 30 ppmv (temperature 150 °C, total flow rate: 30 Nml min⁻¹).

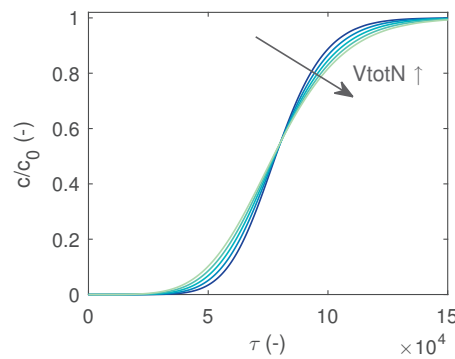


Figure 3.9 – Calculated breakthrough curves for five gas inlet flows ranging from 30 to 55 Nml min⁻¹ (C_4H_4S inlet concentration: 15 ppmv, total flow rate: 30 Nml min⁻¹) versus normalized time $\tau = tu_s/L_{bed}$

flow rate increase). Besides, the shape of the concentration front is affected by the counter-acting forces of the favourable Langmuir isotherm, having a sharpening effect on one hand and the dispersive effects of mass transfer resistance and axial dispersion on the other. The dependence of axial dispersion on temperature is small compared to other factors (see also Fig. B.6k). As temperatures rise, the isotherm becomes less favourable. This effect is, however, outweighed by the increase in pore diffusion, thereby reducing the mass transfer resistance, causing an overall steepening of the breakthrough curve.

3

Effect of thiophene inlet concentration

The effect of varying thiophene concentration in the range of 8.5 to 30 ppmv was evaluated at 100 and 150 °C for a total flow rate of 30 Nml min⁻¹. Both the experimental and modeling results are depicted in Figs. 3.8c and 3.8d. The model predicts the experimental curves well at 100 °C though a steeper breakthrough curve is predicted at 8.5 ppmv. At 150 °C model and experimental results match though the slope at 30 ppmv is underestimated by the model.

An increase in temperature from 100 to 150 °C significantly decreases breakthrough capacities and times at all considered thiophene concentrations as already discussed in Section 3.4.2. Raising the inlet concentration generally increased the sorption capacity as a result of the isotherm shape. At the same time t_{90} decrease by 50 to 52 % as more thiophene molecules enter the bed per unit time. The slope of the breakthrough curves increases at both investigated temperatures as the thiophene inlet concentration is raised because the mass transfer rate increases caused by the higher driving force.

3.4.3. Sensitivity analysis

The previous section investigated the effect of three operating parameters and the validity of the proposed model. This model is now employed to perform a more comprehensive SA to elucidate the effect of a multitude of input factors and their ranking of importance.

The ranking of effects of input factors on the model outputs $Y_{t_{50}}$ and $Y_{s_{90,10}}$ is visualized by plotting the absolute means of EE ($|EE|$) versus their standard deviation (Fig. 3.10, see Table B.2 for numerical results). In these plots, $|EE|$, as a relative measure of sensitivity, assesses the overall importance of a factor. The standard deviation (STD EE) determines whether a factor has a non-linear effect on the model output and/or interacts with other input factors.

Three input factors dominate the effect on breakthrough time t_{50} in Fig. 3.10a: The type of isotherm and axial dispersion correlation as well as the column temperature. While the former show a high standard deviation, indicating non-linearity and/or interaction effects, the latter does not. The slope $s_{90,10}$ in Fig. 3.10b is strongly affected by both the type of isotherm model and axial dispersion correlation.

The effect of these two input factors is investigated more closely by means of a scatter plot of $s_{90,10}$ versus t_{50} , given in Fig. 3.11.

Three distinct point clouds corresponding to the color-coded isotherm models can be identified. The kernel density plots show two groups with regard to t_{50} . Distributions for Langmuir and Tóth isotherms with a mean t_{50} of 29 min overlap. The distribution corresponding to the Henry isotherm is shifted towards shorter breakthrough times (average 23 min) as a result of underestimated breakthrough capacities presented in Fig. 3.6a. The calculated strong effect of the isotherm model on t_{50} in Fig. 3.10a is therefore attributed to the disparity in the ability to describe experimental capacities between the Henry isotherm on one hand and the Langmuir, Tóth isotherms on the other. Neglecting the Henry isotherm, the effect of isotherm model on t_{50} is therefore significantly smaller when more accurate isotherm models are employed (see Fig. B.3a).

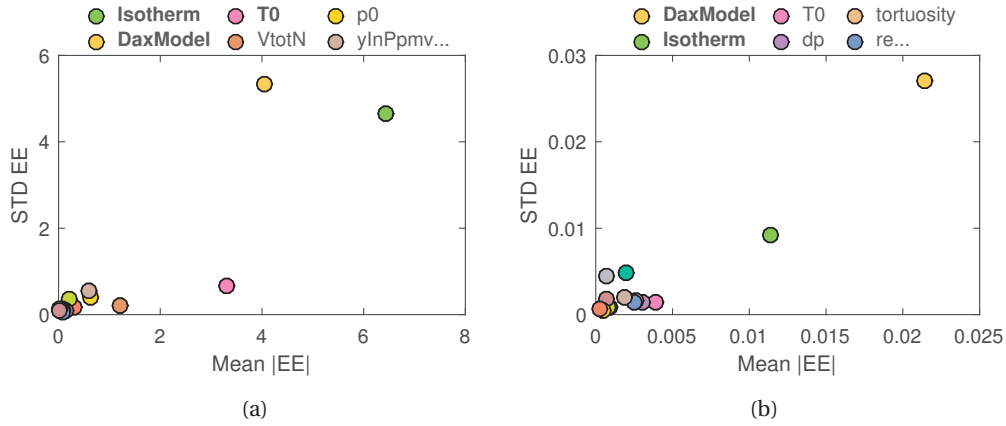


Figure 3.10 – Plots of the standard deviation of EE *versus* mean |EE|. The six most important parameters in the legend are listed in decreasing order of importance. (a) Key figure t_{50} ; (b) key figure $s_{90,10}$.

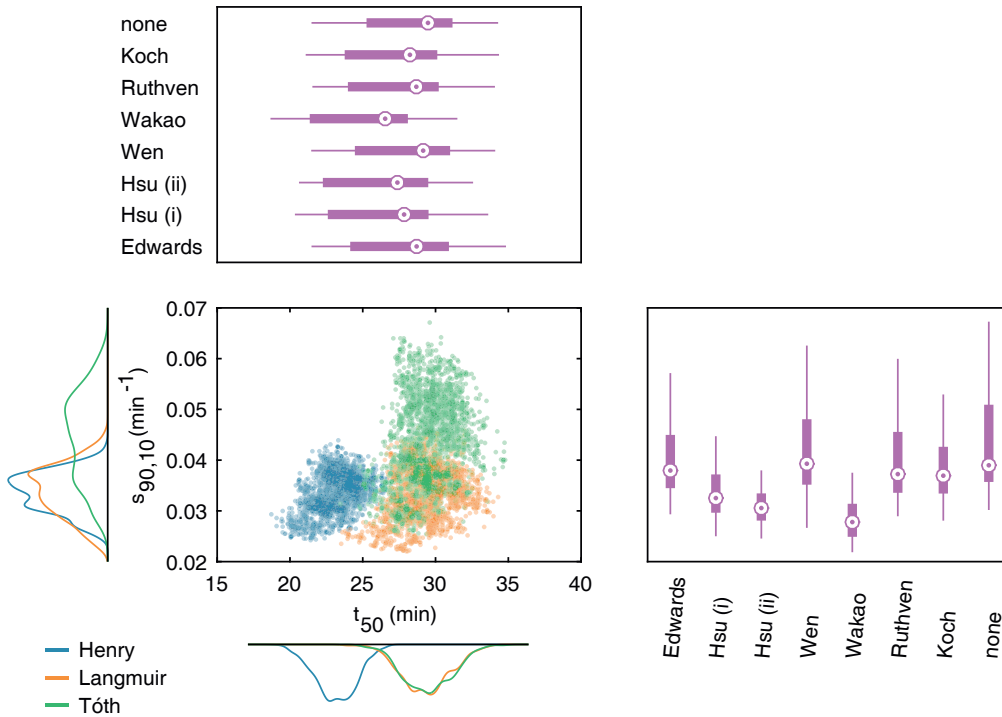


Figure 3.11 – Scatter plot, kernel density plots and box plots to visualize the relationship between key figures t_{50} , $s_{90,10}$ and type of isotherm model (color coded) and axial dispersion correlation. The boxes bound the interquartile range ($IQR = Q_3 - Q_1$) divided by the median, and whiskers extend to a maximum of $1.5 \times IQR$.

The slope $s_{90,10}$ of breakthrough curves is similar for Henry and Langmuir isotherms while the distribution for the Tóth isotherm is wider. All three distributions have a bimodal character that can be related to the axial dispersion correlation. The box plot indicates that the axial dispersion correlations can be divided into two groups with regard to their effect on isotherm slope. The first group with flatter curves is represented by the Hsu(i), Hsu(ii) and Wakao correlations (see also parallel coordinate plots in Fig. B.4). Their lower slopes correspond to lower Pe numbers in Fig. 3.2, indicating a higher degree of axial dispersion. The second group with steeper slopes is represented by the remaining correlations. Results for the model neglecting axial dispersion fit into the latter group, albeit a slightly higher slope is observed. The effect of axial dispersion correlations on t_{50} is less pronounced. Medians group around a breakthrough time of 28.6 min with the notable exception of the Wakao correlation that shows earlier breakthrough times.

Plotting the mean EE instead of $|EE|$ can help to further investigate the underlying mechanisms of the model by inspecting the signs of the individual effects. This definition of EE involves the risk that effects cancel out if the model response is non-monotonous, thus underestimating the importance of a factor⁴³. Bearing in mind that the ranking of importance might be compromised, the mean EE are plotted in Fig. 3.12 and the effects of important input factors are discussed.

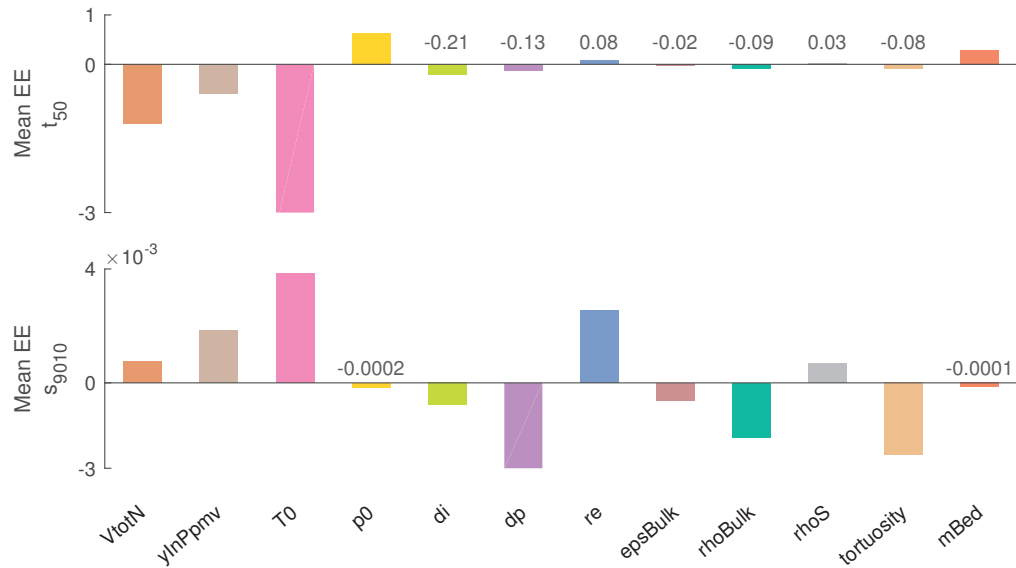


Figure 3.12 – Plots of the mean EE for key figures t_{50} and $s_{90,10}$. Non-numerical input factors are excluded from the plot. Numerical values are given for input factors with small effect.

The breakthrough time t_{50} is negatively affected by three input factors (VtotN, yInPpmv, T0) that have already been discussed in Section 3.4.2. Further important factors are p0 and mBed, both of which affect the breakthrough time positively. An increase in system pressure increases the sorption capacity q^* due to an increase in thiophene concentration while the bed mass has an immediate effect on t_{50} as more sorbent material is present.

The slope $s_{90,10}$ is positively affected by the three factors (VtotN, yInPpmv, T0) discussed in Section 3.4.2. Further factors having a significant effect are dp, re, rhoBulk and the tortuosity.

An increase in particle diameter has a dispersive effect as both the axial dispersion coefficient and the mass transfer resistance k^{-1} are increased. The latter increases as a result of the increased diffusion path lengths molecules have to travel inside the particles. An increase in pore radius positively affects the slope $s_{90,10}$ as molecules in the Knudsen regime collide less frequently with pore walls, thereby increasing the particle diffusivity and mass transfer coefficient k . The bulk density and tortuosity both decrease the slope as they cause an increase in mass transfer resistance k^{-1} .

References

- [1] A. V. Bridgwater. Renewable fuels and chemicals by thermal processing of biomass. *Chemical Engineering Journal*, 91(2–3):87–102, 2003.
- [2] Steffen Heidenreich and Pier Ugo Foscolo. New concepts in biomass gasification. *Progress in Energy and Combustion Science*, 46:72–95, 2015.
- [3] Vineet Singh Sikarwar, Ming Zhao, Peter Clough, Joseph Yao, Xia Zhong, Mohammad Zaki Memon, Nilay Shah, Edward J. Anthony, and Paul S. Fennell. An overview of advances in biomass gasification. *Energy & Environmental Science*, 9(10):2939–2977, 2016.
- [4] Nourredine Abdoulmoumine, Sushil Adhikari, Avanti Kulkarni, and Shyamsundar Chattanathan. A review on biomass gasification syngas cleanup. *Applied Energy*, 155:294–307, 2015.
- [5] M. D. K. Rechulski, T. J. Schildhauer, S. M. A. Biollaz, and C. Ludwig. Sulfur containing organic compounds in the raw producer gas of wood and grass gasification. *Fuel*, 128:330–339, 2014.
- [6] S. Mrowec. The problem of sulfur in high-temperature corrosion. *Oxidation of Metals*, 44(1-2):177–209, 1995.
- [7] Calvin H. Bartholomew. Mechanisms of catalyst deactivation. *Applied Catalysis A: General*, 212(1–2):17–60, 2001.
- [8] W. D. Fitzharris, J. R. Katzer, and W. H. Manogue. Sulfur deactivation of nickel methanation catalysts. *Journal of Catalysis*, 76(2):369–384, 1982.
- [9] C. G. Visconti, L. Lietti, P. Forzatti, and R. Zennaro. Fischer-tropsch synthesis on sulphur poisoned co/al₂o₃ catalyst. *Applied Catalysis a-General*, 330:49–56, 2007.
- [10] Kiyomi Okabe, Kazuhisa Murata, Masakazu Nakanishi, Tomoko Ogi, Mohammad Nurunnabi, and Yangyong Liu. Fischer–tropsch synthesis over ru catalysts by using syngas derived from woody biomass. *Catalysis Letters*, 128(1):171–176, 2009.
- [11] Fatma Nihan Cayan, Mingjia Zhi, Suryanarayana Raju Pakalapati, Ismail Celik, Nianqiang Wu, and Randall Gemmen. Effects of coal syngas impurities on anodes of solid oxide fuel cells. *Journal of Power Sources*, 185(2):595–602, 2008.
- [12] Hossein Madi. *Investigations into the Effects of Biofuel Contaminants on Solid Oxide Fuel Cells*. Thesis, 2016.
- [13] S. Cheah, D. L. Carpenter, and K. A. Magrini-Bair. Review of mid- to high-temperature sulfur sorbents for desulfurization of biomass- and coal-derived syngas. *Energy & Fuels*, 23:5291–5307, 2009.
- [14] E. I. Koytsoumpa, K. Atsonios, K. D. Panopoulos, S. Karellas, E. Kakaras, and J. Karl. Modelling and assessment of acid gas removal processes in coal-derived sng production. *Applied Thermal Engineering*, 74:128–135, 2015.
- [15] David A. Bell, Brian F. Towler, and Maohong Fan. *Coal gasification and its applications*. Elsevier William Andrew, Amsterdam, 2011.

- [16] Tomas Jirsak, Joseph Dvorak, and José A. Rodriguez. Chemistry of thiophene on zno, s/zno, and cs/zno surfaces: effects of cesium on desulfurization processes. *The Journal of Physical Chemistry B*, 103(26):5550–5559, 1999.
- [17] Rudolf P. W. J. Struis, Tilman J. Schildhauer, Izabela Czekaj, Markus Janousch, Serge M. A. Biollaz, and Christian Ludwig. Sulphur poisoning of ni catalysts in the sng production from biomass: A tpo/xps/xas study. *Applied Catalysis A: General*, 362(1–2):121–128, 2009.
- [18] Hong Cui, Scott Q. Turn, Vheissu Keffer, Donald Evans, Thai Tran, and Michael Foley. Contaminant estimates and removal in product gas from biomass steam gasification. *Energy & Fuels*, 24:1222–1233, 2010.
- [19] Luc P. L. M. Rabou and Lex Bos. High efficiency production of substitute natural gas from biomass. *Applied Catalysis B: Environmental*, 111–112:456–460, 2012.
- [20] Christian Felix Julian Konig. *High temperature desulfurization of biomass-derived synthesis gas probed by X-ray absorption spectroscopy*. Thesis, 2013.
- [21] Patrick J. Woolcock and Robert C. Brown. A review of cleaning technologies for biomass-derived syngas. *Biomass & Bioenergy*, 52:54–84, 2013.
- [22] Roop Chand Bansal and Meenakshi Goyal. *Activated carbon adsorption*. Taylor & Francis, Boca Raton, 2005.
- [23] Yosuke Sano, Ki-Hyouk Choi, Yozo Korai, and Isao Mochida. Adsorptive removal of sulfur and nitrogen species from a straight run gas oil over activated carbons for its deep hydrodesulfurization. *Applied Catalysis B: Environmental*, 49(4):219–225, 2004.
- [24] Wei Dai, Yaping Zhou, Shengqiang Wang, Wei Su, Yan Sun, and Li Zhou. Desulfurization of transportation fuels targeting at removal of thiophene/benzothiophene. *Fuel Processing Technology*, 89(8):749–755, 2008.
- [25] C. Delitala, E. Cadoni, D. Delpiano, D. Meloni, S. Melis, and I. Ferino. Liquid-phase thiophene adsorption on MCM-22 zeolite and activated carbon. *Microporous and Mesoporous Materials*, 110(2–3):197–215, 2008.
- [26] P. J. de Wild, R. G. Nyqvist, F. A. de Bruijn, and E. R. Stobbe. Removal of sulphur-containing odorants from fuel gases for fuel cell-based combined heat and power applications. *Journal of Power Sources*, 159(2):995–1004, 2006.
- [27] Isabel A. A. C. Esteves, Marta S. S. Lopes, Pedro M. C. Nunes, and José P. B. Mota. Adsorption of natural gas and biogas components on activated carbon. *Separation and Purification Technology*, 62(2):281–296, 2008.
- [28] B. Boulinguez and P. Le Cloirec. Adsorption/desorption of from natural gas onto granular and fiber-cloth activated carbon for fuel cell applications. *Energy & Fuels*, 23(1):912–919, 2009.
- [29] Hong Cui, Scott Q. Turn, and Mark A. Reese. Removal of sulfur compounds from utility pipelined synthetic natural gas using modified activated carbons. *Catalysis Today*, 139(4):274–279, 2009.

- [30] Chunshan Song. Fuel processing for low-temperature and high-temperature fuel cells: Challenges, and opportunities for sustainable development in the 21st century. *Catalysis Today*, 77(1–2):17–49, 2002.
- [31] Douglas M. Ruthven. *Principles of adsorption and adsorption processes*. Wiley, New York, 1984.
- [32] Mohammad Saleh Shafeeyan, Wan Mohd Ashri Wan Daud, and Ahmad Shamiri. A review of mathematical modeling of fixed-bed columns for carbon dioxide adsorption. *Chemical Engineering Research and Design*, 92(5):961–988, 2014.
- [33] Federico Ferretti, Andrea Saltelli, and Stefano Tarantola. Trends in sensitivity analysis practice in the last decade. *Science of The Total Environment*, 568:666–670, 2016.
- [34] P. G. Aguilera and F. J. Gutiérrez Ortiz. Prediction of fixed-bed breakthrough curves for h₂S adsorption from biogas: Importance of axial dispersion for design. *Chemical Engineering Journal*, 289:93–98, 2016.
- [35] Kaushal Naresh Gupta, Nandagiri Jagannatha Rao, and Govind Kumar Agarwal. Gaseous phase adsorption of volatile organic compounds on granular activated carbon. *Chemical Engineering Communications*, 202(3):384–401, 2015.
- [36] Mohammad Saleh Shafeeyan, Wan Mohd Ashri Wan Daud, Ahmad Shamiri, and Nasrin Aghamohammadi. Modeling of carbon dioxide adsorption onto ammonia-modified activated carbon: Kinetic analysis and breakthrough behavior. *Energy & Fuels*, 29(10): 6565–6577, 2015.
- [37] Dereje Tamiru Tefera, Masoud Jahandar Lashaki, Mohammadreza Fayaz, Zaher Hashisho, John H. Philips, James E. Anderson, and Mark Nichols. Two-dimensional modeling of volatile organic compounds adsorption onto beaded activated carbon. *Environmental Science & Technology*, 47(20):11700–11710, 2013.
- [38] T. Grant Glover and M. Douglas LeVan. Sensitivity analysis of adsorption bed behavior: Examination of pulse inputs and layered-bed optimization. *Chemical Engineering Science*, 63(8):2086–2098, 2008.
- [39] Andrea Saltelli, Marco Ratto, Stefano Tarantola, and Francesca Campolongo. Update 1 of: Sensitivity analysis for chemical models. *Chemical Reviews*, 112(5):1–21, 2012.
- [40] Francesca Pianosi, Keith Beven, Jim Freer, Jim W. Hall, Jonathan Rougier, David B. Stephenson, and Thorsten Wagener. Sensitivity analysis of environmental models: A systematic review with practical workflow. *Environmental Modelling & Software*, 79: 214–232, 2016.
- [41] A. Fassò, A. Esposito, E. Porcu, A. P. Reverberi, and F. Vegliò. Statistical sensitivity analysis of packed column reactors for contaminated wastewater. *Environmetrics*, 14(8):743–759, 2003.
- [42] Max D. Morris. Factorial sampling plans for preliminary computational experiments. *Technometrics*, 33(2):161–174, 1991.

- [43] Francesca Campolongo, Jessica Cariboni, and Andrea Saltelli. An effective screening design for sensitivity analysis of large models. *Environmental Modelling & Software*, 22(10):1509–1518, 2007.
- [44] E. Wicke. Bedeutung der molekularen diffusion für chromatographische verfahren. *Berichte der Bunsengesellschaft für physikalische Chemie*, 77(3):160–171, 1973.
- [45] James C. Knox, Armin D. Ebner, M. Douglas LeVan, Robert F. Coker, and James A. Ritter. Limitations of breakthrough curve analysis in fixed-bed adsorption. *Industrial & Engineering Chemistry Research*, 55(16):4734–4748, 2016.
- [46] James J Carberry. *Chemical and catalytic reaction engineering*. Courier Dover Publications, 2001.
- [47] Design Institute for Physical Properties. Dippr project 801. 2016.
- [48] Edward N. Fuller, Keith Ensley, and J. Calvin Giddings. Diffusion of halogenated hydrocarbons in helium. the effect of structure on collision cross sections. *The Journal of Physical Chemistry*, 73(11):3679–3685, 1969.
- [49] M. F. Edwards and J. F. Richardson. Gas dispersion in packed beds. *Chemical Engineering Science*, 23(2):109–123, 1968.
- [50] L. K. P. Hsu and H. W. Haynes. Effective diffusivity by the gas chromatography technique: Analysis and application to measurements of diffusion of various hydrocarbons in zeolite nay. *AIChE Journal*, 27(1):81–91, 1981.
- [51] C. Y. Wen and L. T. Fan. *Models for flow systems and chemical reactors*, volume 20. Marcel Dekker, New York, 1975.
- [52] N. Wakao and T. Funazkri. Effect of fluid dispersion coefficients on particle-to-fluid mass transfer coefficients in packed beds. *Chemical Engineering Science*, 33(10):1375–1384, 1978.
- [53] Donald L. Koch and John F. Brady. Dispersion in fixed beds. *Journal of Fluid Mechanics*, 154:399–427, 1985.
- [54] G. Langer, A. Roethe, K. P. Roethe, and D. Gelbin. Heat and mass transfer in packed beds—iii. axial mass dispersion. *International Journal of Heat and Mass Transfer*, 21(6):751–759, 1978.
- [55] J. M. P. Q. Delgado. A critical review of dispersion in packed beds. *Heat and Mass Transfer*, 42(4):279–310, 2005.
- [56] E. Glueckauf and J. I. Coates. 241. theory of chromatography. part iv. the influence of incomplete equilibrium on the front boundary of chromatograms and on the effectiveness of separation. *Journal of the Chemical Society*, (0):1315–1321, 1947.
- [57] Shamsuzzaman Farooq and Douglas M. Ruthven. Heat effects in adsorption column dynamics. 2. experimental validation of the one-dimensional model. *Industrial & Engineering Chemistry Research*, 29(6):1084–1090, 1990.

- [58] James J. Carberry. A boundary-layer model of fluid-particle mass transfer in fixed beds. *AIChE Journal*, 6(3):460–463, 1960.
- [59] K. Y. Foo and B. H. Hameed. Insights into the modeling of adsorption isotherm systems. *Chemical Engineering Journal*, 156(1):2–10, 2010.
- [60] Bryan J. Schindler, Leonard C. Buettner, and M. Douglas LeVan. Transition to henry's law in ultra-low concentration adsorption equilibrium for n-pentane on BPL activated carbon. *Carbon*, 46(10):1285–1293, 2008.
- [61] Chi Tien. *Adsorption calculations and modeling*. Butterworth-Heinemann series in chemical engineering. Butterworth-Heinemann, Boston, 1994.
- [62] F. J. Gutiérrez Ortiz, P. G. Aguilera, and P. Ollero. Modeling and simulation of the adsorption of biogas hydrogen sulfide on treated sewage-sludge. *Chemical Engineering Journal*, 253: 305–315, 2014.
- [63] J Toth. State equations of the solid-gas interface layers. *Acta Chimica Academiae Scientiarum Hungaricae*, 69(3):311–317, 1971.
- [64] George E. P. Box. Fitting empirical data. *Annals of the New York Academy of Sciences*, 86 (3):792–816, 1960.
- [65] Duong D Do. *Adsorption Analysis: Equilibrium and Kinetics*. Imperial College Press, London, 1998.
- [66] P. V. Danckwerts. Continuous flow systems. *Chemical Engineering Science*, 2(1):1–13, 1953.
- [67] M. D. McKay, R. J. Beckman, and W. J. Conover. A comparison of three methods for selecting values of input variables in the analysis of output from a computer code. *Technometrics*, 21(2):239–245, 1979.
- [68] A. van Griensven, T. Meixner, S. Grunwald, T. Bishop, M. Diluzio, and R. Srinivasan. A global sensitivity analysis tool for the parameters of multi-variable catchment models. *Journal of Hydrology*, 324(1–4):10–23, 2006.
- [69] Francesca Campolongo, Andrea Saltelli, and Jessica Cariboni. From screening to quantitative sensitivity analysis. a unified approach. *Computer Physics Communications*, 182(4): 978–988, 2011.
- [70] S. Ergun. Fluid flow through packed columns. *Chemical Engineering Progress*, 48(2): 89–94, 1952.
- [71] D. P. Haughey and G. S. G. Beveridge. Structural properties of packed beds — a review. *The Canadian Journal of Chemical Engineering*, 47(2):130–140, 1969.
- [72] F. Rezaei and P. Webley. Structured adsorbents in gas separation processes. *Separation and Purification Technology*, 70(3):243–256, 2010.
- [73] Sylvain Giraudet, Pascaline Pré, and Pierre Le Cloirec. Modeling the heat and mass transfers in temperature-swing adsorption of volatile organic compounds onto activated carbons. *Environmental Science & Technology*, 43(4):1173–1179, 2009.

- [74] Francesca Pianosi, Fanny Sarrazin, and Thorsten Wagener. A matlab toolbox for global sensitivity analysis. *Environmental Modelling & Software*, 70:80–85, 2015.

4

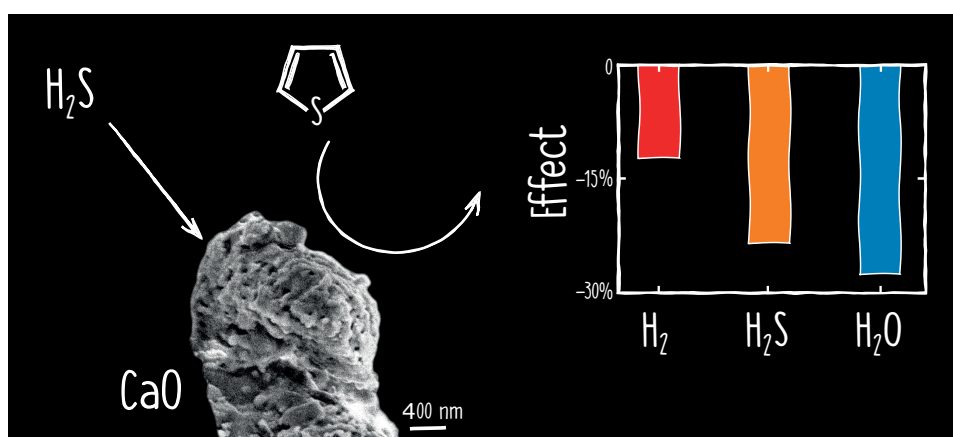
High temperature conversion of thiophene over CaO

This chapter is adapted from **P. Edinger** et al., *High temperature conversion of thiophene over CaO*, In preparation.

Abstract

Sulphur contained in the gas of biomass gasification processes can cause damage to downstream equipment. While H_2S can be removed by current warm gas cleanup processes employing metal oxides such as ZnO , this is not the case for heterocyclic sulphur compounds. An option for decomposing these compounds to H_2S is the use of catalytically active materials, such as CaO . This work is aimed to understand the factors that influence the decomposition of the heterocyclic sulphur model compound thiophene at a fixed temperature of $810\text{ }^{\circ}\text{C}$. These factors, H_2O , H_2 and H_2S were varied as part of a full factorial design at two levels. The results were fitted to a linear model. Analysis showed that H_2O and H_2S had a major effect on thiophene conversion, while that of H_2 was less pronounced. Interactions between factors were found to be negligible.

4



4.1. Introduction

GREENHOUSE gas (GHG) emissions from anthropogenic sources are a major driver of climate change. In order to prevent the adverse effects of climate change on mankind, fossil energy has to be replaced by renewable alternatives. Among them, the gasification of biomass is a promising option¹. The gas exiting such gasifiers is, depending on feedstock, gasifier type and operating parameters, mainly composed of CH₄, CO, CO₂, H₂ and H₂O. Besides, several undesired by-products in form of particulates, tars, sulphur and nitrogen compounds, HCl and alkali metals are present².

The entrained sulphur species have typically total gas phase concentrations ranging from 20 to 200 ppmv^{3,4}, although higher concentrations have been reported for black liquor and grass feedstocks^{5,6}. While H₂S makes up most of the gas phase sulphur species, sulphur containing hydrocarbons such as thiophene (C₄H₄S) can represent a significant fraction⁴. If not adequately removed, these species can cause corrosion of downstream piping⁷ and poisoning of catalysts used for methanation⁸, Fischer Tropsch (FT) synthesis⁹ and fuel cells¹⁰.

State-of-the-art removal of sulphur compounds is achieved by low temperature processes (e.g. RME scrubber at 20 to 50 °C) which allow the majority of water and organic impurities to condense¹¹. The need for repeated cool down and subsequent heat up for downstream processes (methanation 300 to 400 °C, FT 150 to 300 °C) as well as the need for steam addition for steam reforming and/or prevention of coke deposition result in an efficiency penalty^{12,13}.

Warm and cold gas cleanup processes avoid the repeated cool down and heat up, promising better process efficiencies as well as lower capital and operating costs. Sulphur capture in these processes is typically achieved by metal oxides such as ZnO which, however, are incapable of retaining sulphur containing hydrocarbons^{14–16}. Recent research therefore focused on dedicated hydrodesulphurization (HDS) catalysts for their conversion to H₂S^{17–19}.

This current work proposes limestone, employed either directly in the gasifier (*in-situ*) or downstream, to serve as a bi-functional material. As such, it may act as a sorbent for bulk sulphur removal^{20–24}, trace elements^{25–29} and HCl^{30–32} on one hand and as a catalyst for the decomposition of tars and sulphur containing hydrocarbons on the other. Being a natural resource with relatively low cost, the limestone is applied as a disposable material. While the desulphurization by limestone has been investigated intensively, literature concerning the conversion of sulphur containing hydrocarbons is more scarce. Johannes and Hamrin³³ investigated the HDS of thiophene over CaCO₃, finding some catalytic activity, although significantly less compared to commercial CoMo catalysts. The conversion of hydrocarbons over CaO based materials has been studied in more detail using various tar model compounds (heptane, benzene, toluene, naphthalene)^{34,35}. These studies indicated dry and steam reforming as predominant decomposition reactions and postulated the Ca²⁺-O²⁻ ion pair as the active site. Steam, H₂ and CO were found to have an inhibitive effect while the presence of H₂S on the catalyst performance was not studied^{36,37}.

Knowledge about the decomposition kinetics of sulphur containing hydrocarbons can be incorporated into techno-economic models. Their evaluation can indicate whether the use of disposable materials as sorbent and catalyst at high temperature are superior to current technology.

The aim of this work is therefore to evaluate CaO as a catalyst for the decomposition of thiophene in gasification atmosphere at first. In the next step the effect of H₂, H₂O and H₂S on the catalyst performance are studied by means of a design of experiments approach.

4.2. Experimental section

4.2.1. Material

Limestone (Mikrosöhl Reasorb TAV, VKD) from the quarry Söhlde (Germany) was used in this study. The material was crushed, sieved and the 125 to 160 μm size fraction separated for experiments. The elemental composition of the material was analysed by an ICP-MS (7700x, Agilent, USA) after microwave aided 2-step digestion with an aqueous solution of HCl, HNO_3 and HF. The specific surface area (SSA, 7-point BET method) of the samples was measured by nitrogen physisorption using an Autosorb-1 (Quantachrome Instruments, USA). The samples were degassed for at least 2 h at 200 $^\circ\text{C}$ (criterion: $\dot{p} < 0.01 \text{ mmHg min}^{-1}$) and subsequently measured at 77.4 K. The morphology of the uncalcined and calcined limestone was investigated by scanning electron microscopy (SEM, Ultra 55, Zeiss, Germany).

4

4.2.2. Experimental procedure

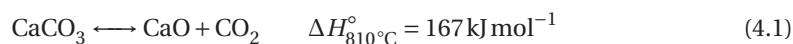
For each experiment 55.0 mg of CaCO_3 were weighed into the quartz reactor (2 mm i.d., 6 mm o.d.) and held in place by quartz wool plugs. Because alkali and alkaline earth metals, present in the carbonate rocks, can react with quartz to form silicates and thereby erode the reactor walls, reactors were replaced after each run. The reactor was then connected to the experimental setup and flushed with Ar (65 Nml min^{-1}). Calcination of the sample was performed *in-situ* by heating the reactor up to 870 $^\circ\text{C}$ ($30 \text{ }^\circ\text{C min}^{-1}$) at a pressure of 0.5 barg. The temperature was held constant for 30 min while the CO_2 signal (m/z 44) at the reactor outlet was monitored. Afterwards, the reactor was cooled down to 810 $^\circ\text{C}$, the operating conditions adjusted according to Table 4.2 and the gas sent to the reactor. The signal was then allowed to stabilize. After the experiment, the reactor was cooled down in Ar atmosphere and the sample transferred to a glass vial. Later kinetic analysis was based on the calcined sample weight. In order to exclude thermal decomposition as cause of observed thiophene conversion, a blank experiment with an SiC bed was carried out. Detected thiophene conversion in this case was smaller than 2 %. Though quantification of the main gas constituents was not performed, recorded ion currents suggest that no significant change in their composition occurred when fed over the CaO bed.

4.2.3. Design of experiments

Factors

The reaction temperature is expected to have a significant effect on thiophene conversion but is limited to a small range due to certain constraints. These encompass the operating temperature of the gasifier on one hand and considerations concerning the catalyst activity and sorption capability of limestone on the other.

Thermal decomposition of limestone occurs according to



and is dependent on temperature and CO_2 partial pressure as plotted in Fig. 4.1b.

Experimental studies have shown that CaO exhibits a significantly better catalytic activity and superior sulphidation rates and conversion compared to CaCO_3 ^{21,38,39}. The lower operating temperature limit is therefore given by the calcination temperature. The upper limit is given both by the operating temperature of the gasifier (600 to 1000 $^\circ\text{C}$) and considerations

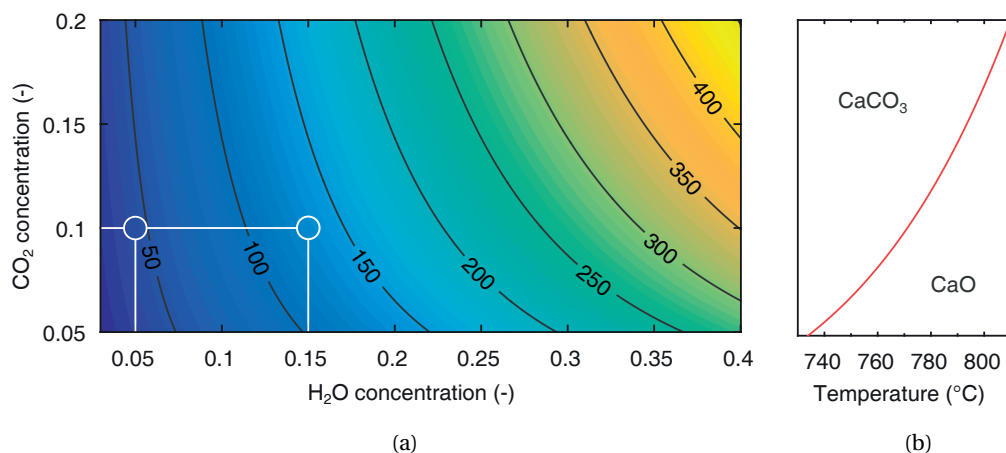


Figure 4.1 – Calculations were performed with the HSC Chemistry 7 software package at a total pressure of 1.5 bar. (a) Minimum mole fraction of H₂S at equilibrium in ppmv plotted as a function of CO₂ and H₂O concentration. The temperature at each point is given by the calcination temperature. White circles indicate operating conditions employed in this study as listed in Table 4.2; (b) CO₂ gas concentration as a function of calcination temperature.

concerning the minimum mole fraction of H₂S at equilibrium. The underlying reactions are



While Eq. (4.2) is exothermic, Eq. (4.3) is endothermic. The minimum H₂S mole fraction at equilibrium is therefore found at the calcination temperature and dependant on the partial pressure of H₂O and CO₂. The relation is illustrated in Fig. 4.1a for a total pressure of 1.5 bar. Depending on the H₂O and CO₂ concentration, different minimum H₂S fractions at equilibrium can be achieved when the temperature is adjusted accordingly. Based on a representative CO₂ concentration of 10 vol%, a temperature of 810 °C was chosen in this study to ensure a CaO phase.

Table 4.1 – Possible reactions of thiophene. Reaction enthalpies were calculated in the HSC Chemistry 7 software package.

| Reaction | Equation | $\Delta H_{810^\circ\text{C}}^\circ$ (kJ mol ⁻¹) |
|-----------------------|--|--|
| Hydrodesulphurization | $\text{C}_4\text{H}_4\text{S} + 4\text{H}_2 \longrightarrow \text{H}_2\text{S} + \text{C}_4\text{H}_{10}$ | -287 |
| Hydrocracking | $\text{C}_4\text{H}_4\text{S} + 7\text{H}_2 \longrightarrow \text{H}_2\text{S} + 4\text{CH}_4$ | -489 |
| Steam reforming | $\text{C}_4\text{H}_4\text{S} + 4\text{H}_2\text{O} \longrightarrow \text{H}_2\text{S} + 4\text{CO} + 5\text{H}_2$ | 412 |
| | $\text{C}_4\text{H}_4\text{S} + 8\text{H}_2\text{O} \longrightarrow \text{H}_2\text{S} + 4\text{CO}_2 + 9\text{H}_2$ | 276 |
| Dry reforming | $\text{C}_4\text{H}_4\text{S} + 4\text{CO}_2 \longrightarrow \text{H}_2\text{S} + 8\text{CO} + \text{H}_2$ | 549 |
| | $\text{C}_4\text{H}_4\text{S} + 5\text{CO}_2 \longrightarrow \text{H}_2\text{S} + 9\text{CO} + \text{H}_2\text{O}$ | 583 |
| Thermal cracking | $\text{C}_4\text{H}_4\text{S} \longrightarrow \text{products}^1$ | - |
| Carbon deposition | $\text{C}_4\text{H}_4\text{S} \longrightarrow 4\text{C} + 2\text{H}_2 + \text{S}$ | 176 |

¹ Products including various hydrocarbons and sulphur compounds

The impact of further gas components on the conversion of thiophene over CaO has to be considered on different levels. Firstly, they can act as reactants. Several reactions of thiophene where a change in reactant concentration may affect the reaction rate can be thought of (see Table 4.1).

Secondly, present gas species might adsorb competitively on the active site for thiophene decomposition, thereby slowing the reaction rate. Such effects have been reported for the decomposition of toluene over CaO based materials where H_2 and H_2O inhibited the reaction^{36,37}. Thirdly, the constituents might react with the catalyst itself. Depending on the H_2S inlet concentration (see Fig. 4.1a) CaO will react with H_2S to form CaS, with presumably different catalytic activity.

Based on this consideration, three factors were chosen for an experimental design, including H_2 , H_2S and H_2O (each at two levels). The factors were varied in ranges summarized in Table 4.2.

4

Table 4.2 – Experimental factors

| Factor | Unit | Variables | Min | Max |
|--------|------|-----------|-----|-----|
| H_2 | vol% | x_1 | 5 | 30 |
| H_2S | ppmv | x_2 | 0 | 200 |
| H_2O | vol% | x_3 | 5 | 15 |

The gas concentrations of the remaining gas constituents are held constant, their values being listed in Table 4.3.

Table 4.3 – Concentrations of fixed gas components in Ar

| CO (vol%) | CO ₂ (vol%) | C ₄ H ₄ S (ppmv) | He (vol%) |
|--------------|---------------------------|---|--------------|
| 10 | 10 | 100 | 20 |

Response

Assuming a constant gas flow rate across the packed bed reactor, the thiophene conversion can be calculated according to

$$X_{C_4H_4S} = \frac{y_0 - y}{y_0} \quad (4.4)$$

where y_0 is the reactor inlet concentration. Based on the calculated LOD of thiophene, discussed in Section 3.3.3, the maximum detectable conversion is 99.53 %.

Model

The objective of this work was to find the main factors influencing the conversion of thiophene over CaO. The underlying rate law can, in a first approximation, be described by an empirical power law

$$r_{C_4H_4S} = k_r \prod_{i=1}^3 c_i^{l_i} \quad (4.5)$$

where $c_i^{l_i}$ represent the concentrations of the three factors and the order of reaction and k_r a temperature dependent reaction rate constant. The rate of reaction $r_{C_4H_4S}$ is proportional to the conversion of thiophene $X_{C_4H_4S}$ over the CaO bed of mass m_{bed}

$$X_{C_4H_4S} = \frac{-1}{F_{C_4H_4S,0}} \int_0^{m_{bed}} r_{C_4H_4S} dm_{bed}^* \propto r_{C_4H_4S} \quad (4.6)$$

Herein, $F_{C_4H_4S,0}$ is the molar inlet flow of thiophene. Taking the logarithm of Eq. (4.5) results in the linearised form, represented by

$$\ln(r_{C_4H_4S}) = \ln(k_r) + \sum_{i=1}^3 \ln(c_i) l_i \quad (4.7)$$

The observations can therefore be described by a linearised model with interactions, where the latter describe observations not accounted for by the power law model. This linear model with interactions has the form of

$$X_{C_4H_4S} = a_0 + \sum_{i=1}^3 a_i x_i + \sum_{i \neq j}^3 a_{ij} x_i x_j \quad (4.8)$$

where a_0 is the constant effect, a_i are the main half effects, a_{ij} the first order half effects and x the coded factors.

Two designs were considered to determine the model coefficients:

- Factorial design at two levels with $2^3 = 8$ experiments.
- Fractional factorial design at two levels with $2^{3-1}_{III} = 4$ experiments and resolution III.

In this work, a full factorial design was chosen. Even though it uses twice as many runs compared to the fractional factorial design, the absolute number of runs is still low. Another reasoning is the fact that the fractional factorial design with resolution III confounds main effects with first order interaction effects which could be of importance. The matrix of experiments of the full factorial design is shown in Table 4.4. Herein, columns 2 to 4 represent the coded factors, with -1 describing the lower and +1 the upper level.

Table 4.4 – Matrix of experiments

| No. | x_1 | x_2 | x_3 | H ₂ (vol%) | H ₂ S (ppmv) | H ₂ O (vol%) |
|-----|-------|-------|-------|--------------------------|----------------------------|----------------------------|
| 1 | -1 | -1 | -1 | 5 | 0 | 5 |
| 2 | 1 | -1 | -1 | 30 | 0 | 5 |
| 3 | -1 | 1 | -1 | 5 | 200 | 5 |
| 4 | 1 | 1 | -1 | 30 | 200 | 5 |
| 5 | -1 | -1 | 1 | 5 | 0 | 15 |
| 6 | 1 | -1 | 1 | 30 | 0 | 15 |
| 7 | -1 | 1 | 1 | 5 | 200 | 15 |
| 8 | 1 | 1 | 1 | 30 | 200 | 15 |

The model matrix is calculated as given in Table 4.5.

Table 4.5 – Model matrix

| No. | x_1 | x_2 | x_3 | $x_1 x_2$ | $x_1 x_3$ | $x_2 x_3$ | $x_1 x_2 x_3$ |
|-----|-------|-------|-------|-----------|-----------|-----------|---------------|
| 1 | -1 | -1 | -1 | 1 | 1 | 1 | -1 |
| 2 | 1 | -1 | -1 | -1 | -1 | 1 | 1 |
| 3 | -1 | 1 | -1 | -1 | 1 | -1 | 1 |
| 4 | 1 | 1 | -1 | 1 | -1 | -1 | -1 |
| 5 | -1 | -1 | 1 | 1 | -1 | -1 | 1 |
| 6 | 1 | -1 | 1 | -1 | 1 | -1 | -1 |
| 7 | -1 | 1 | 1 | -1 | -1 | 1 | -1 |
| 8 | 1 | 1 | 1 | 1 | 1 | 1 | 1 |

4

4.3. Results and discussion

4.3.1. Material characterization

The elemental composition of the employed limestone is provided in Table 4.6.

Table 4.6 – Elemental composition of limestone (wt%)

| | Ca | Mg | Fe | Al | Si | Na | K | Ni | Ti | Mn | Cr |
|--------------------------------|-------|------|------|------|------|------|------|------|------|------|------|
| Limestone (CaCO ₃) | 20.33 | 0.19 | 0.41 | 0.65 | 2.81 | 0.00 | 0.00 | 0.01 | 0.05 | 0.03 | 0.02 |

The SSA of the CaCO₃ particles and the calcined sample were measured to be 6.6 m² g⁻¹ and 18.0 m² g⁻¹. The increased SSA upon calcination is in accordance with literature and explained by an increase in porosity due to the escaping CO₂^{40,41}.

4.3.2. Testing criteria

The evaluation of the catalyst performance can be impaired by the presence of external and internal mass transport limitations and to a lesser degree non-ideal reactor behaviour. Moulijn et al.⁴² and Perez-Ramirez et al.⁴³ have therefore compiled a list of criteria to ensure the correct measurement of the intrinsic catalyst activity.

Extra-particle mass transfer

The extent of external mass transfer limitation over the gas film surrounding the particles can be assessed by the Carberry (Ca) number⁴⁴. It relates the catalyst surface concentration of thiophene $c_{C_4H_4S,s}$ to observable quantities.

$$Ca = \frac{r_{v,C_4H_4S}^{obs}}{k_f a_v c_{C_4H_4S,b}} = \frac{c_{C_4H_4S,b} - c_{C_4H_4S,s}}{c_{C_4H_4S,b}} < 0.05 \quad (4.9)$$

In this equation, $r_{v,C_4H_4S}^{obs}$ is the observed volumetric reaction rate per unit of particle volume and $c_{C_4H_4S,b}$ the bulk concentration of thiophene. The specific surface area can be approximated by

$$a_v = \frac{6}{d_p} \quad (4.10)$$

under the assumption of spherical particles of diameter d_p (143 μm). The film transfer coefficient k_f is obtained from a Sherwood (Sh) correlation by Wakao and Funazkri⁴⁵

$$Sh = \frac{k_f d_p}{D_m} = 2 + 1.1 Re_p^{0.6} Sc^{1/3} \quad (4.11)$$

The dimensionless Reynolds number Re_p and Schmidt number Sc in this equation are defined as

$$Re_p = \frac{u_s d_p}{\nu_{mix}} \quad Sc = \frac{\nu_{mix}}{D_m} \quad (4.12)$$

where u_s is the superficial velocity and ν_{mix} the kinematic viscosity, calculated according to Wilke⁴⁶. The molecular diffusivity D_m of thiophene in the gas mixture is obtained from the individual binary diffusivities⁴⁷ according to the Wilke-equation⁴⁸.

The calculated Carberry numbers for all eight experiments are presented in Fig. 4.2a. All experiments lie below the threshold of 0.05, indicating that external mass transfer is negligible.

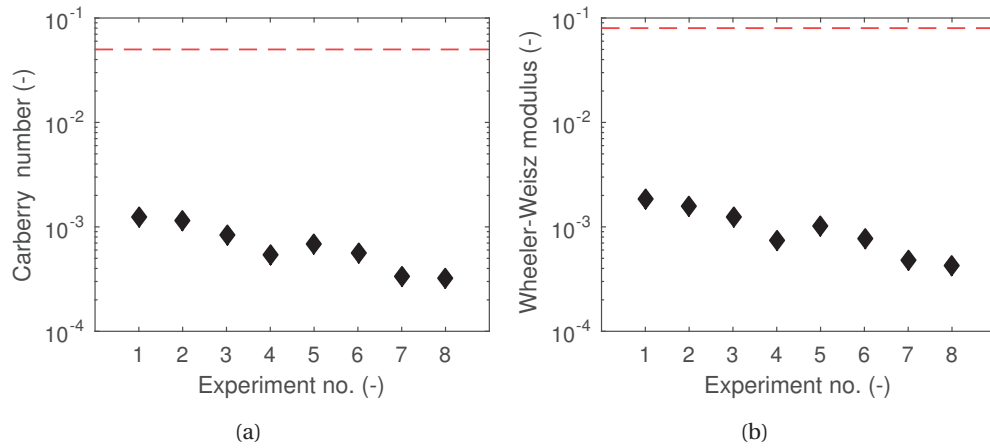


Figure 4.2 – (a) External mass transfer limitation; (b) internal mass transfer limitation.

Intra-particle mass transport

The criterion for intra-particle mass transport limitation is given by the Wheeler-Weisz modulus⁴⁹ as

$$\Omega = \frac{r_{v,C_4H_4S}^{obs}}{D_p c_{C_4H_4S,s}} \left(\frac{d_p}{6} \right)^2 < 0.08 \quad (4.13)$$

The effective diffusivity of thiophene inside the particles D_p is obtained from the Bosanquet equation under the assumption of equimolar counter-diffusion

$$\frac{1}{D_p} = \frac{1}{D_K} + \frac{1}{D_{m,eff}} \quad (4.14)$$

Here, D_K refers to the Knudsen diffusivity and $D_{m,eff}$ to the effective molecular diffusivity. The Knudsen diffusivity is calculated by

$$D_K = 97r_e \left(\frac{T}{\widetilde{M}_{Thio}} \right)^{1/2} \quad (4.15)$$

where \widetilde{M}_{Thio} is the molecular weight of thiophene and r_e the mean pore radius. While typical values of pore radii for calcined limestone (calcination at 850 °C) range from 60 to 200 nm^{50,51}, this work takes a conservative estimate of 100 nm. $D_{m,eff}$ is calculated according to

$$D_{m,eff} = \frac{\epsilon_p D_m}{\tau_{tor}} \quad (4.16)$$

where τ_{tor} is the tortuosity factor and ϵ_p the particle porosity. Reported values for calcined limestone range from 1.7 to 2 for τ_{tor} and from 0.46 to 0.51 for ϵ_p ^{50,51}. This work assumes a tortuosity of 2 and a particle porosity of 0.5.

The calculated Wheeler-Weisz moduli for all eight experiments are presented in Fig. 4.2b. All experiments lie below the threshold of 0.08, indicating that internal mass transfer is negligible.

Axial and radial dispersion

The assumption of plug flow in the reactor can be made by meeting the criterion for axial dispersion (here $Bo \approx 161$)⁵²

$$Bo = \frac{L_{Bed} u_s}{D_{ax}} > 100 \quad (4.17)$$

In this equation, L_{Bed} refers to the bed height. The axial dispersion coefficient D_{ax} is calculated according to a correlation provided by Wakao and Funazkri⁴⁵

$$D_{ax} = \left(\frac{20\epsilon_b}{Re_p Sc} + 0.5 \right) d_p u_{iv} \quad (4.18)$$

Herein, ϵ_b (assumed 0.4) is the bulk porosity and u_{iv} the interstitial velocity. Radial concentration gradients and wall effects were minimized by choosing a sufficiently high ratio between reactor diameter d_t and particle diameters d_p ⁵³

$$\frac{d_t}{d_p} > 8 \quad (4.19)$$

Relative pressure drop

Experiments were performed at total pressures p of 1.5 bara with calculated pressure drops Δp across the catalyst bed of approximately 0.2 bar⁵⁴, resulting in relative pressure drops concurrent with

$$\frac{\Delta p}{p} < 0.2 \quad (4.20)$$

Temperature rise

Isothermal conditions were assumed for the experiments as the reactant thiophene is present at trace concentrations only. The assumption is readily verified by calculating the adiabatic temperature change for the reaction with the highest absolute enthalpy of reaction $|\Delta H_{900^\circ\text{C}}^\circ|$ given in Table 4.1

$$\Delta T = \left| \frac{\Delta H_{900^\circ\text{C}}^\circ y_0}{c_{p,g}} \right| = \left| \frac{583000 \text{ J mol}^{-1} 10^{-4}}{20.8 \text{ J mol}^{-1} \text{ K}^{-1}} \right| = 2.8 \text{ K} \quad (4.21)$$

In this equation, y_0 is the molar gas inlet fraction of thiophene and $c_{p,g}$ the heat capacity of the gas mixture.

4.3.3. Effects of factors on thiophene conversion

The results of the eight performed experiments are plotted in Fig. 4.3. Thiophene conversion in the experiments ranged from 22 to 72 %. High conversion between 52 to 72 % was obtained for low H_2O content while low thiophene conversion was predominantly obtained in gas atmosphere with high steam loading and in presence of H_2S .

4

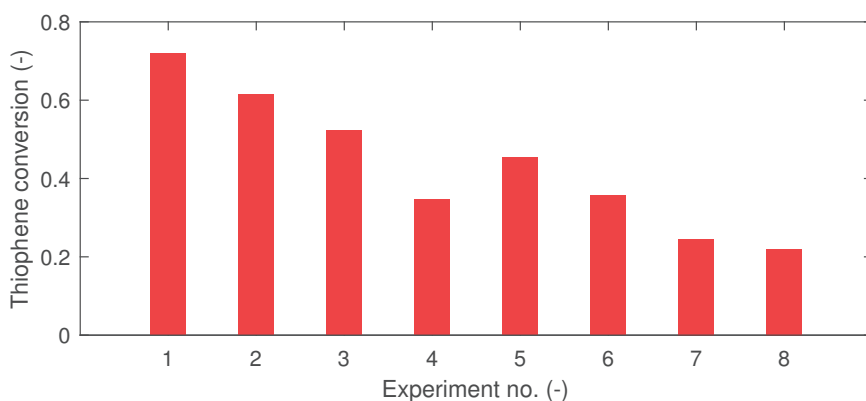


Figure 4.3 – Experimental results of conversion of thiophene

A more rigorous data evaluation was performed by fitting the results to the model described in Eq. (4.8) (least squares approach)⁵⁵. The obtained effects a_i , a_{ij} were normalized by the constant effect a_0 to obtain the so called relative half effects.

In Fig. 4.4, all main effects are negative, implying that an increase in H_2 , H_2S and H_2O concentration cause a decrease in thiophene conversion. Both H_2S and H_2O have similar effects while that of H_2 is smaller. Interaction effects were found to be negligible in comparison to the main effects. Both the negative effect of H_2S and H_2O on toluene and benzene conversion over CaO based materials have been observed before^{36,37} and may, in this case, be attributed to competitive adsorption as well. The negative effect of H_2S on thiophene conversion can be attributed to different causes. H_2S may adsorb competitively on active sites, responsible for thiophene decomposition. Furthermore, the sulphided material CaS can have inferior catalytic performance. Another aspect that could decrease the reaction rate is related to the molar volume of CaO ($16.8 \text{ cm}^3 \text{ mol}^{-1}$) on one hand and CaS ($27.9 \text{ cm}^3 \text{ mol}^{-1}$) on the other. If sulphidation occurs, a product layer with high molar volume compared to the educt is

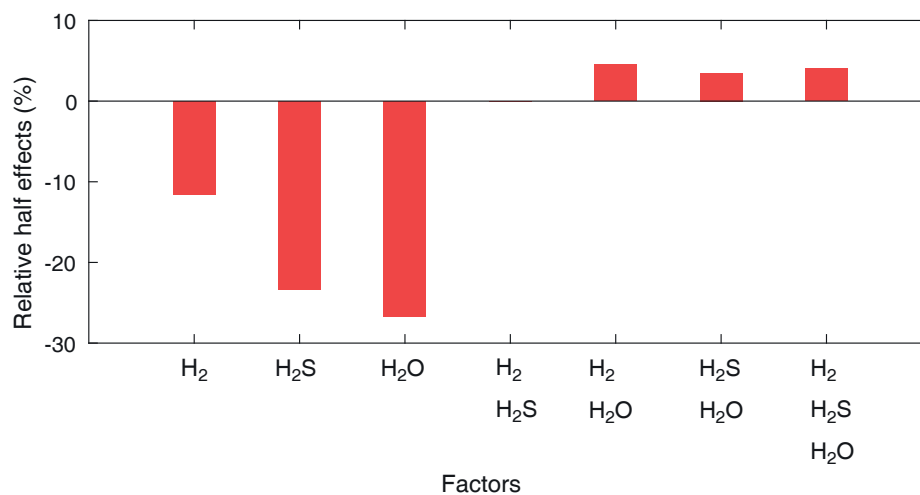


Figure 4.4 – Relative half-effects of the factors

formed thereby causing a pore narrowing or even blocking that increases the internal diffusion resistance and ultimately the reaction rate.

References

- [1] Vineet Singh Sikarwar, Ming Zhao, Peter Clough, Joseph Yao, Xia Zhong, Mohammad Zaki Memon, Nilay Shah, Edward J. Anthony, and Paul S. Fennell. An overview of advances in biomass gasification. *Energy & Environmental Science*, 9(10):2939–2977, 2016.
- [2] Nourredine Abdoulmoumine, Sushil Adhikari, Avanti Kulkarni, and Shyamsundar Chattanathan. A review on biomass gasification syngas cleanup. *Applied Energy*, 155:294–307, 2015.
- [3] E. Magnus Johansson, Magnus Berg, Johan Kjellström, and Sven G. Järås. Catalytic combustion of gasified biomass: poisoning by sulphur in the feed. *Applied Catalysis B: Environmental*, 20(4):319–332, 1999.
- [4] M. D. K. Rechulski, T. J. Schildhauer, S. M. A. Biollaz, and C. Ludwig. Sulfur containing organic compounds in the raw producer gas of wood and grass gasification. *Fuel*, 128: 330–339, 2014.
- [5] Melita Jazbec, Karina Sendt, and Brian S. Haynes. Kinetic and thermodynamic analysis of the fate of sulphur compounds in gasification products. *Fuel*, 83(16):2133–2138, 2004.
- [6] Henrik Wiinikka, Ann-Christine Johansson, Jonas Wennebro, Per Carlsson, and Olov G. W. Öhrman. Evaluation of black liquor gasification intended for synthetic fuel or power production. *Fuel Processing Technology*, 139:216–225, 2015.
- [7] S. Mrowec. The problem of sulfur in high-temperature corrosion. *Oxidation of Metals*, 44 (1-2):177–209, 1995.
- [8] W. D. Fitzharris, J. R. Katzer, and W. H. Manogue. Sulfur deactivation of nickel methanation catalysts. *Journal of Catalysis*, 76(2):369–384, 1982.
- [9] C. G. Visconti, L. Lietti, P. Forzatti, and R. Zennaro. Fischer-tropsch synthesis on sulphur poisoned co/al₂o₃ catalyst. *Applied Catalysis a-General*, 330:49–56, 2007.
- [10] Fatma Nihan Cayan, Mingjia Zhi, Suryanarayana Raju Pakalapati, Ismail Celik, Nianqiang Wu, and Randall Gemmen. Effects of coal syngas impurities on anodes of solid oxide fuel cells. *Journal of Power Sources*, 185(2):595–602, 2008.
- [11] Patrick J. Woolcock and Robert C. Brown. A review of cleaning technologies for biomass-derived syngas. *Biomass & Bioenergy*, 52:54–84, 2013.
- [12] A. O. Omosun, A. Bauen, N. P. Brandon, C. S. Adjiman, and D. Hart. Modelling system efficiencies and costs of two biomass-fuelled sofc systems. *Journal of Power Sources*, 131 (1-2):96–106, 2004.
- [13] Martin Gassner and Francois Marechal. Thermo-economic optimisation of the polygeneration of synthetic natural gas (sng), power and heat from lignocellulosic biomass by gasification and methanation. *Energy & Environmental Science*, 5(2):5768–5789, 2012.
- [14] Tomas Jirsak, Joseph Dvorak, and José A. Rodriguez. Chemistry of thiophene on zno, s/zno, and cs/zno surfaces: effects of cesium on desulfurization processes. *The Journal of Physical Chemistry B*, 103(26):5550–5559, 1999.

- [15] Rudolf P. W. J. Struis, Tilman J. Schildhauer, Izabela Czekaj, Markus Janousch, Serge M. A. Biollaz, and Christian Ludwig. Sulphur poisoning of ni catalysts in the sng production from biomass: A tpo/xps/xas study. *Applied Catalysis A: General*, 362(1–2):121–128, 2009.
- [16] Hong Cui, Scott Q. Turn, Vheissu Keffer, Donald Evans, Thai Tran, and Michael Foley. Contaminant estimates and removal in product gas from biomass steam gasification. *Energy & Fuels*, 24:1222–1233, 2010.
- [17] Luc P. L. M. Rabou and Lex Bos. High efficiency production of substitute natural gas from biomass. *Applied Catalysis B: Environmental*, 111–112:456–460, 2012.
- [18] Christian Felix Julian Konig. *High temperature desulfurization of biomass-derived synthesis gas probed by X-ray absorption spectroscopy*. Thesis, 2013.
- [19] Christian Zuber, Christoph Hochenauer, and Thomas Kienberger. Test of a hydrodesulfurization catalyst in a biomass tar removal process with catalytic steam reforming. *Applied Catalysis B: Environmental*, 156–157:62–71, 2014.
- [20] Lawrence A. Ruth, Arthur M. Squires, and Robert A. Graff. Desulfurization of fuels with half-calcined dolomite. first kinetic data. *Environmental Science & Technology*, 6(12):1009–1014, 1972.
- [21] Laurent A. Fenouil and Scott Lynn. Study of calcium-based sorbents for high-temperature h2S removal. 1. kinetics of h2S sorption by uncalcined limestone. *Industrial & Engineering Chemistry Research*, 34(7):2324–2333, 1995.
- [22] M. Hartman, K. Svoboda, O. Trnka, and J. Cermak. Reaction between hydrogen sulfide and limestone calcines. *Industrial & Engineering Chemistry Research*, 41(10):2392–2398, 2002.
- [23] Y. Q. Hu, M. Watanabe, C. Aida, and M. Horio. Capture of h2S by limestone under calcination conditions in a high-pressure fluidized-bed reactor. *Chemical Engineering Science*, 61(6):1854–1863, 2006.
- [24] Moritz Husmann, Christian Zuber, Viktoria Maitz, Thomas Kienberger, and Christoph Hochenauer. Comparison of dolomite and lime as sorbents for in-situ h2S removal with respect to gasification parameters in biomass gasification. *Fuel*, 181:131–138, 2016.
- [25] A. GhoshDastidar, S. Mahuli, R. Agnihotri, and L. S. Fan. Selenium capture using sorbent powders: Mechanism of sorption by hydrated lime. *Environmental Science & Technology*, 30(2):447–452, 1996.
- [26] S. Mahuli, R. Agnihotri, S. Chauk, A. GhoshDastidar, and L. S. Fan. Mechanism of arsenic sorption by hydrated lime. *Environmental Science & Technology*, 31(11):3226–3231, 1997.
- [27] R. Agnihotri, S. Chauk, S. Mahuli, and L. S. Fan. Selenium removal using ca-based sorbents: Reaction kinetics. *Environmental Science & Technology*, 32(12):1841–1846, 1998.
- [28] M. Diaz-Somoano and M. R. Martinez-Tarazona. Retention of arsenic and selenium compounds using limestone in a coal gasification flue gas. *Environmental Science & Technology*, 38(3):899–903, 2004.

- [29] M. Diaz-Somoano, M. A. Lopez-Anton, F. E. Huggins, and M. R. Martinez-Tarazona. The stability of arsenic and selenium compounds that were retained in limestone in a coal gasification atmosphere. *Journal of Hazardous Materials*, 173(1-3):450–454, 2010.
- [30] Robert H. Borgwardt and Nancy F. Roache. Reaction of hydrogen sulfide and sulfur with limestone particles. *Industrial & Engineering Chemistry Process Design and Development*, 23(4):742–748, 1984.
- [31] Claus E. Weinell, Peter I. Jensen, Kim Dam-Johansen, and Hans Livbjerg. Hydrogen chloride reaction with lime and limestone: kinetics and sorption capacity. *Industrial & Engineering Chemistry Research*, 31(1):164–171, 1992.
- [32] José Corella, José M. Toledo, and Gregorio Molina. Performance of cao and mgo for the hot gas clean up in gasification of a chlorine-containing (rdf) feedstock. *Bioresource Technology*, 99(16):7539–7544, 2008.
- [33] A. H. Johannes and C. E. Hamrin. Characterization and catalytic activity of coal mineral matter: 2. hydrodesulfurization of thiophene. *Fuel Processing Technology*, 13(1):17–39, 1986.
- [34] Z. Abu El-Rub, E. A. Bramer, and G. Brem. Review of catalysts for tar elimination in biomass gasification processes. *Industrial & Engineering Chemistry Research*, 43(22):6911–6919, 2004.
- [35] P. V. Aravind and Wiebren de Jong. Evaluation of high temperature gas cleaning options for biomass gasification product gas for solid oxide fuel cells. *Progress in Energy and Combustion Science*, 38(6):737–764, 2012.
- [36] Pekka A. Simell, Elisa K. Hirvensalo, Visa T. Smolander, and A. Outi I. Krause. Steam reforming of gasification gas tar over dolomite with benzene as a model compound. *Industrial & Engineering Chemistry Research*, 38(4):1250–1257, 1999.
- [37] Georgios Taralas and Michael G. Kontominas. Kinetic modelling of voc catalytic steam pyrolysis for tar abatement phenomena in gasification/pyrolysis technologies. *Fuel*, 83(9):1235–1245, 2004.
- [38] Pekka A. Simell, Jukka K. Leppaelahti, and Esa A. Kurkela. Tar-decomposing activity of carbonate rocks under high CO₂ partial pressure. *Fuel*, 74(6):938–945, 1995.
- [39] Laurent A. Fenouil and Scott Lynn. Study of calcium-based sorbents for high-temperature h₂S removal. 2. kinetics of h₂S sorption by calcined limestone. *Industrial & Engineering Chemistry Research*, 34(7):2334–2342, 1995.
- [40] Ronald Barker. The reversibility of the reaction $\text{CaCO}_3 \rightleftharpoons \text{CaO} + \text{CO}_2$. *Journal of Applied Chemistry and Biotechnology*, 23(10):733–742, 1973.
- [41] R. H. Borgwardt. Calcination kinetics and surface area of dispersed limestone particles. *AIChE Journal*, 31(1):103–111, 1985.
- [42] J. A. Moulijn, A. Tarfaoui, and F. Kapteijn. General aspects of catalyst testing. *Catalysis Today*, 11(1):1–12, 1991.

- [43] Javier Perez-Ramirez, Rob J. Berger, Guido Mul, Freek Kapteijn, and Jacob A. Moulijn. The six-flow reactor technology: A review on fast catalyst screening and kinetic studies. *Catalysis Today*, 60(1–2):93–109, 2000.
- [44] James J Carberry. *Chemical and catalytic reaction engineering*. Courier Dover Publications, 2001.
- [45] N. Wakao and T. Funazkri. Effect of fluid dispersion coefficients on particle-to-fluid mass transfer coefficients in packed beds. *Chemical Engineering Science*, 33(10):1375–1384, 1978.
- [46] C. R. Wilke. A viscosity equation for gas mixtures. *The Journal of Chemical Physics*, 18(4): 517–519, 1950.
- [47] Edward N. Fuller, Keith Ensley, and J. Calvin Giddings. Diffusion of halogenated hydrocarbons in helium. the effect of structure on collision cross sections. *The Journal of Physical Chemistry*, 73(11):3679–3685, 1969.
- [48] Robert H. Perry and Don W. Green. *Perry's chemical engineers' handbook*. McGraw-Hill, New York, 8th edition, 2008.
- [49] Gilbert F. Froment, Juray De Wilde, and Kenneth B. Bischoff. *Chemical reactor analysis and design*. Wiley, Hoboken, N.J., 3rd edition, 2011.
- [50] Tilmur Dogu. The importance of pore structure and diffusion in the kinetics of gas-solid non-catalytic reactions: Reaction of calcined limestone with so₂. *The Chemical Engineering Journal*, 21(3):213–222, 1981.
- [51] B. R. Stanmore and P. Gilot. Review—calcination and carbonation of limestone during thermal cycling for CO₂ sequestration. *Fuel Processing Technology*, 86(16):1707–1743, 2005.
- [52] Manfred Baerns, Hanns Hofmann, and Albert Renken. *Chemische Reaktionstechnik. Lehrbuch der technischen Chemie*. Wiley-VCH, Weinheim, 3rd edition, 2002.
- [53] C. F. Chu and K. M. Ng. Flow in packed tubes with a small tube to particle diameter ratio. *AIChE Journal*, 35(1):148–158, 1989.
- [54] S. Ergun. Fluid flow through packed columns. *Chemical Engineering Progress*, 48(2): 89–94, 1952.
- [55] George E. P. Box, J. Stuart Hunter, and William Gordon Hunter. *Statistics for experimenters design, innovation, and discovery*. Wiley series in probability and statistics. Wiley-Interscience, Hoboken, N.J., 2nd edition, 2005.

5

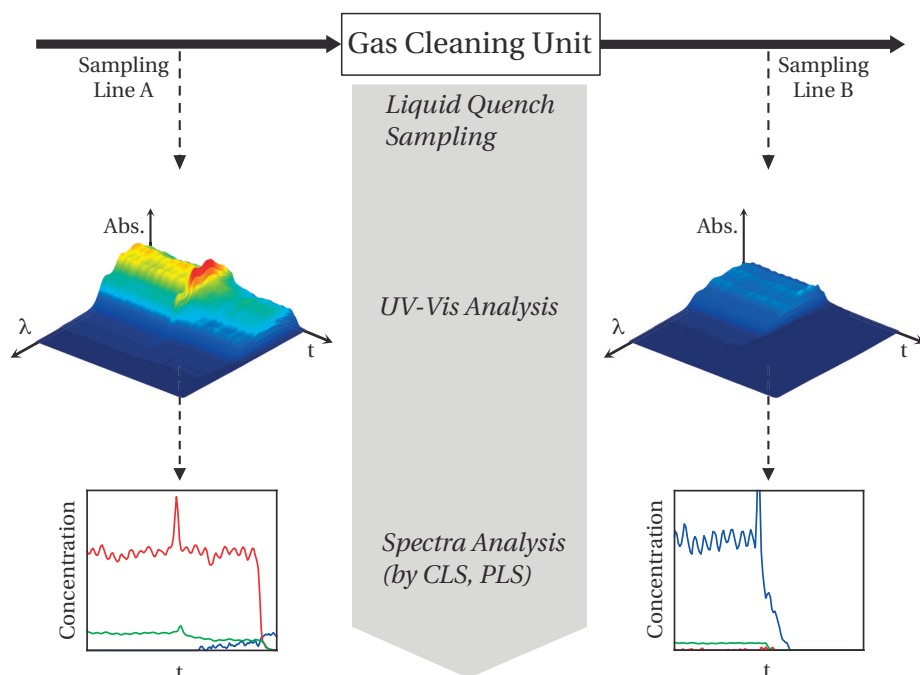
UV-Vis spectroscopy as a tool for online tar measurements in biomass gasification processes

This chapter is adapted from **P. Edinger** et al., *Online liquid quench sampling and UV-Vis spectroscopy for tar measurements in wood gasification process gases*, *Fuel* **184**, 59 (2016).

Abstract

In biomass gasification processes, the formation and handling of tars are of major concern. Robust and versatile analytical tools are needed to online monitor tar compound concentrations in process gases from lab- to industrial scale. This study addresses the development and application of an online UV-Vis method, based on a liquid quench sampling system. The high sensitivity of this method allows to detect UV-Vis active tar compounds in the low ppmv region. Recorded spectra from the liquid phase were analysed for their tar composition by means of a classical least squares (CLS) and partial least squares (PLS) approach. The developed method was applied to two case studies, involving a laboratory-scale tar reformer and a pilot-scale gas scrubber. Quantification results in gases with limited complexity in tar composition showed good agreement with offline reference methods (GC-FID). The case studies show that the developed method is a rapid, sensitive tool that can be applied for qualitative process monitoring with the added benefit of quantification in gases with a limited number of tar compounds.

5



5.1. Introduction

Gasification is one promising technology to convert woody biomass to a range of products, including electricity, heat and chemicals¹. The composition of the gas exiting the gasifier depends on the gasification technology, feedstock quality and operation parameters. The raw producer gas is mainly composed of H_2 , CO , CO_2 , CH_4 and H_2O . Besides, it contains several undesired by-products in form of particulate matter, sulphur compounds, HCl , trace elements and tars which can cause severe problems in down-stream equipment².

Tars can be defined as hydrocarbons with a molecular weight greater than benzene³. They are formed during gasification in a series of complex reactions⁴. Typical concentrations in the raw gas range from 0.01 to 150 g Nm^{-3} ⁵. When cooled down, tars can condense while increased temperatures can result in the formation of more complex compounds with higher boiling points. This can cause clogging and fouling of pipes, heat exchangers, particulate filters or other potential down-stream processes, such as fuel cells or catalysts⁶. As a result, tar formation and its control are still considered as one of the major challenges in the implementation of biomass gasification technology⁷. The impact of tars on down-stream equipment is less caused by the lumped sum of tar compounds but rather the *tar composition*. It is therefore convenient to classify tar compounds based on their condensation behaviour into five classes as presented in Fig. 5.1⁸.

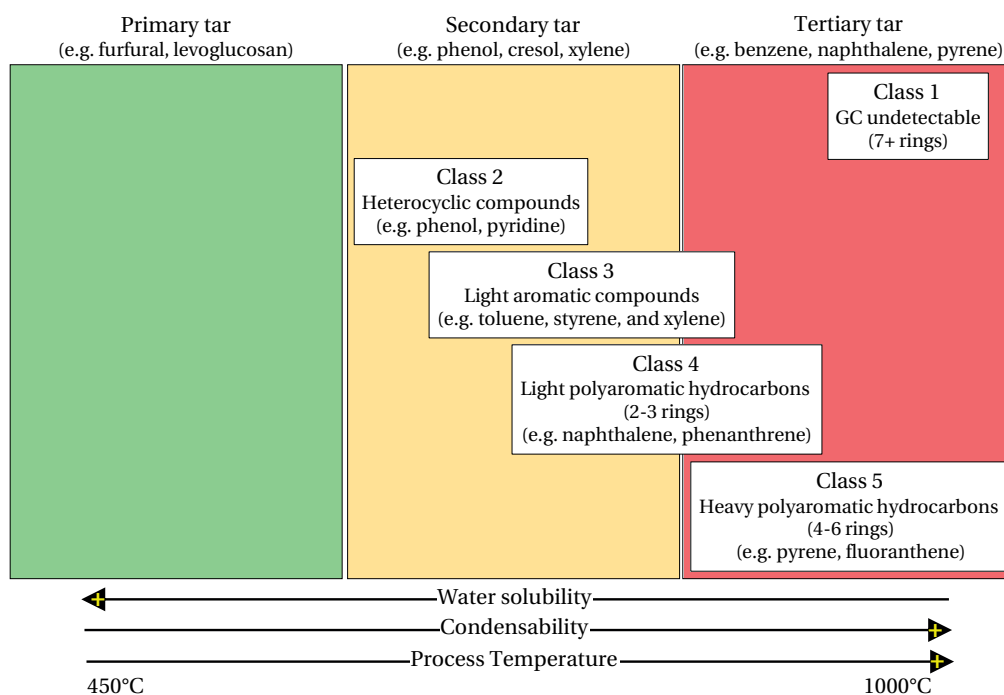


Figure 5.1 – Classification of biomass tar (adapted from ^{8,9})

Research focuses on the reduction of tar content by a combination or individual use of primary and secondary measures. Primary measures encompass the use of bed materials and catalysts in the gasifier and the optimization of biomass fuel properties, gasifier design as well as operating conditions^{8,10}. Secondary measures are methods to remove tars in a

separate step after gasification. The latter can be further divided into physical and chemical tar removal methods. Physical methods include liquid scrubbers, which require the gas to be cooled down (typically 20 to 60 °C), causing efficiency losses. Chemical methods offer a promising alternative to decrease tar concentrations by thermal cracking (typical temperature range of 1000 to 1300 °C) or the use of catalysts to enhance steam reforming and cracking reactions (typical temperature range of 500 to 900 °C)^{5,11,12}.

Regardless of the measure, robust online analytical tools are needed in order to correctly assess gasifier performance and tar treatment. Offline measurement of tar compounds is typically performed by cold solvent trapping (CST) according to the tar protocol¹³ or solid phase adsorption (SPA)^{14,15}. In the CST method, the producer gas is passed through a series of cooled solvent scrubbers, whose content is analysed afterwards. In the SPA method, tar is adsorbed onto a column with a small amount of amino-phase sorbent and later desorbed by a solvent for the analysis of tar compounds. Compared to CST, SPA offers shorter sampling times (ca. 1 min *versus* ca. 20 min), a less complicated sampling procedure and more complete results for most cases¹⁶. This has led to the wide usage of SPA for determining concentrations of tar compounds. Both methods share the disadvantage of being offline where the solvent is later analysed by GC techniques (typically GC-MS, GC-FID). The development of online analytical tools for the determination of tar compounds in biomass gasification atmosphere has therefore gained considerable attention in recent years. Various measurement systems, based on laser spectroscopy (laser-induced fluorescence (LIF), Raman), have been described^{17–19}. Mass spectrometers (MS) in combination with electron impact (EI) ionization as 'hard' ionization method (GC-MS, molecular-beam (MB))^{20–22} as well as 'soft' ionization techniques (ion molecule reaction (IMR), single photon ionization (SPI), resonance-enhanced multiphoton ionization (REMPI))^{23–26}, to reduce spectral overlap, were used for tar compound detection. While all above mentioned methods are, in principle, able to obtain quantitative information about the tar composition, they rely on relatively expensive equipment. More cost-effective tar analysers have been developed in form of a tar dew point analyser (TDA)²⁷ and using methods based on flame ionization detection (FID)²⁸ and photo ionization detection (PID)^{29,30}. They do not, however, provide an indication on the tar composition.

UV-Vis spectroscopy promises to be a quick and robust, yet economical tool to online monitor tar compound concentrations in gases. Most tar compounds have conjugated π -electron systems and absorb light in the UV-Vis range³¹. Non-aromatic tar compounds, on the other hand, typically adsorb light at wavelengths (< 200 nm) which are instrumentally not easily accessible. The fact that most tar compounds are UV-Vis active has been exploited by previous authors. Patuzzi et al.³² used an optical cell, fitted with four LEDs, for online UV-Vis measurements of tars in pyrolysis off-gas, but resulting only in four point spectra. Based on a calibration with naphthalene, the measured spectra were then analysed in terms of a normalized naphthalene content, neglecting the possible presence of tar compounds with widely different extinction coefficients. Di Marcello et al.³³ collected gas samples from different types of gasifiers according to the aforementioned tar protocol. Absorbance spectra of these samples were subsequently measured offline by an UV-Vis spectrometer. A univariate calibration, involving the total tar content of the samples, measured by HPLC analysis, and the absorbance at selected wavelengths was successfully performed. Correctness of the predictions will, however, depend on the premise that the tar composition does not change. Qualitative or quantitative information on the individual tar compounds could not be obtained. Using advanced chemometrics (MCR-ALS), Weide et al.³⁴ were able to obtain qualitative, online information on the composition of a changing tar mixture of five compounds.

The objective of this work is to establish an online UV-Vis method to monitor tar com-

pounds in gases encountered in biomass gasification processes. In the first step, a liquid quench sampling system was adapted for online UV-Vis measurements. The employed liquid quench sampling system transfers condensable gas species, including tars, into an organic solvent flow whose absorbance is detected. Measurement in the liquid phase allows for easy calibration, compared to gas phase calibration, where complex instrumentation is needed. Multivariate calibrations, based on classical least squares (CLS) and partial least squares (PLS) regression were applied to enable the quantification of tar compounds in different applications. In the second step, the established method was used in two case studies. The first involved a lab-scale reactor for investigating the decomposition of a defined number of tar compounds across a catalyst. The second case study concerned the effectiveness of a gas scrubber in a pilot-scale wood gasification plant.

5.2. Experimental section

5.2.1. Chemicals

Pure tar compounds of benzene, toluene (Merck), styrene (Fluka), indene (Sigma-Aldrich) and naphthalene (Riedel-de Haen) for calibration were acquired with a purity > 97 %. The solvent 2-propanol was obtained with analytical grade from VWR chemicals.

5.2.2. Sampling system

Online measurements of tar compounds were conducted with a liquid quench sampling system, whose basic characteristics have previously been described^{35,36}. A schematic representation of the adapted sampling system is given in Fig. 5.2 and photographs are given in Figs. D.1 and D.2.

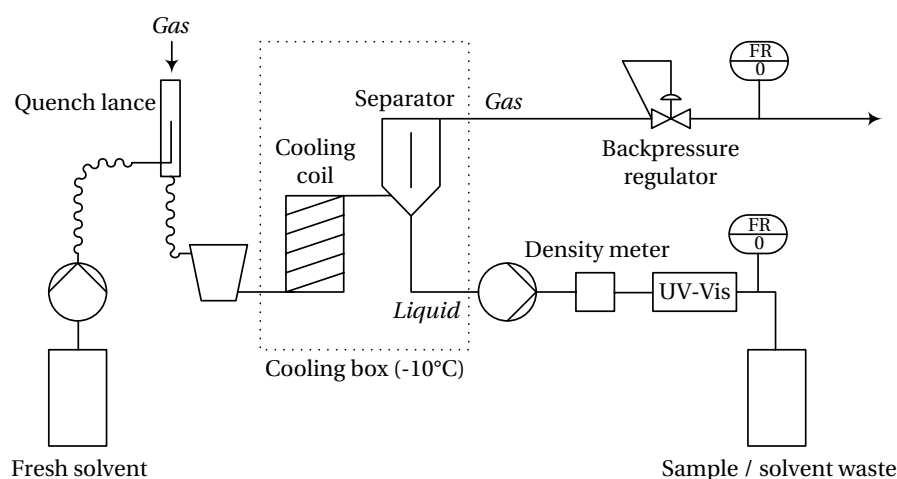


Figure 5.2 – Schema of liquid quench sampling system and online analytical instruments. FR refers to flow rate-recording.

The sample gas flow is drawn into the quench lance by a pump where it is brought into contact with an organic solvent (2-propanol) fed by a rotary piston pump (Reglo-CPF Analog, Ismatec). The resulting two-phase flow is compressed (N86KN, KNF) to 1 barg, cooled down to approximately -10°C and fed to a separator where gas and liquid phases are separated. Previous experiments have shown that compression and solvation of specific tar compounds of classes 3 to 5 have negligible effect on the tar composition^{37,38}. It cannot be excluded, however. After a back-pressure regulator, the gas is sent to a custom-made flow-meter and then optionally sent to a μGC (CP 4900, Varian) for analysis of the permanent gas species composition. The liquid stream from the separator is pumped (Ismatec, Reglo-CPF Analog) through a density meter (DMA 35, Anton Paar), a UV-Vis flow-through cell and a custom-made flow meter. The liquid stream can then either be automatically sampled into vials for later offline analysis or directed to a solvent waste containment. Typical collection times for liquid samples were 20 min.

Measured concentrations $c_{i,liq}$ of condensable species i in the liquid sample phase are

related to their corresponding gas phase concentrations $c_{i,gas}$ by means of

$$c_{i,gas} = \frac{\dot{V}_{i,gas}^{(S)}}{\dot{V}_{permanent,gas}^{(S)} + \dot{V}_{H_2O,gas}^{(S)}} \quad (5.1)$$

$$= \frac{c_{i,liq} \dot{V}_{sample,liq} V_m}{\left(\frac{\dot{V}_{permanent,gas}^{(S)}}{\dot{V}_{sample,liq}} \right) \dot{V}_{sample,liq} + \frac{w_{H_2O} \dot{m}_{sample}}{\bar{M}_{H_2O}} V_m} \quad (5.2)$$

$$= \frac{c_{i,liq}}{\left(\frac{\dot{V}_{permanent,gas}^{(S)}}{\dot{V}_{sample,liq}} \right) \frac{1}{V_m} + \frac{w_{H_2O} \rho_{sample}}{\bar{M}_{H_2O}}} \quad (5.3)$$

It is assumed that the concentration $c_{i,gas}$ can be represented by the ratio of the gaseous volume flow $\dot{V}_{i,gas}^{(S)}$ of species i to a total gas volume flow in the denominator which exclusively consists of the permanent gas species $\dot{V}_{permanent,gas}^{(S)}$ and steam $\dot{V}_{H_2O,gas}^{(S)}$, while other compounds, such as tars, are being neglected. As a result, the gas phase concentration $c_{i,gas}$ will depend on the liquid phase concentration $c_{i,liq}$, the ratio $\dot{V}_{permanent,gas}^{(S)} / \dot{V}_{sample,liq}$ of gas and liquid flows exiting the separator, the mass fraction of water, w_{H_2O} , in the liquid flow and the liquid sample density ρ_{sample} . In this equation, the term (S) refers to standard conditions, V_m the molar volume, \bar{M}_{H_2O} the molecular weight of water and \dot{m}_{sample} to the mass flow of the liquid sample.

Solvent density as a measure of steam content

The density ρ_{sample} of the liquid sample stream in the liquid quench sampling system depends both on its composition and temperature. Measurement of density and temperature can therefore provide information on the sample composition. In the following, a model, to describe this relation, is developed and its underlying assumptions are subsequently checked.

Modelling the water content as a function of sample temperature and density Assuming that only 2-propanol and water contribute to the sample density, a model, describing the mass fraction w_{H_2O} of water as a function of sample temperature T_{sample} and density ρ_{sample} can be defined as

$$w_{H_2O} = f_1 + f_2 T_{sample} + f_3 \rho_{sample} + f_4 \rho_{sample}^2 \quad (5.4)$$

The parameters f_1 to f_4 were obtained from fitting the model to experimental data provided by Egorov et al.³⁹, who investigated the density of the 2-propanol-water system at atmospheric pressure. For the current work, data at temperatures of 15, 25 and 35 °C in the compositional range $0 < w_{H_2O} < 0.54$ were used. The determined fitting parameters are summarized in Table 5.1.

Table 5.1 – Fitting parameters for the model to predict the water content w_{H_2O} as a function of density and temperature

| f_1 | $f_2 \times 10^{-3}$ | f_3 | f_4 | R^2 |
|--------|----------------------|-------|-------|--------|
| -2.267 | 3.517 | 1.629 | 1.483 | 0.9999 |

The obtained response surface and residuals are presented in Fig. 5.3. The coefficient of determination of 0.9999 indicates that the experimental data are well represented by the model.

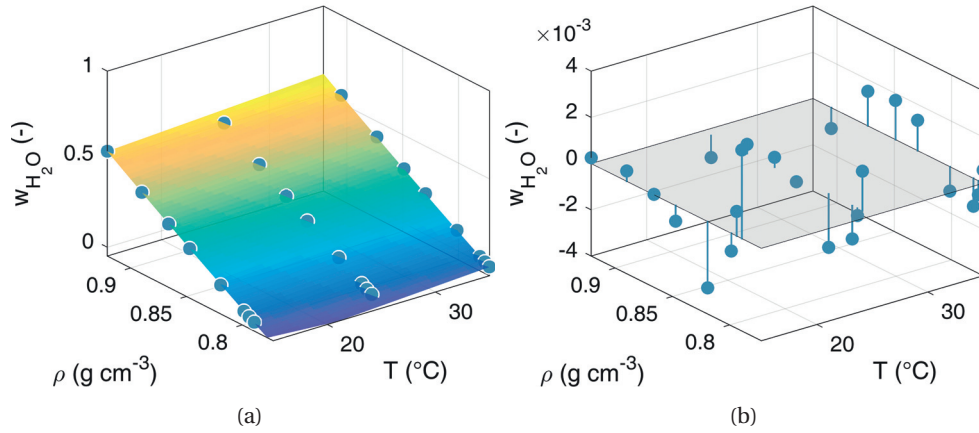


Figure 5.3 – (a) Experimental data and response surface of the water content of the binary mixture 2-propanol-water as a function of density and temperature; (b) residuals of the fit.

5

Effect of tar compounds The presence of tar compounds in the sample solution can have an effect on the measured density, depending on their concentration and properties. In order to evaluate the proposed model and investigate the effect of the presence of tar compounds in the solution, a full factorial design (2^2) with two factors, w_{H_2O} and the tar content was developed. The mass fraction of water was varied between 0 and 10 wt% and the tar content was varied between a low and high case. Gas and corresponding liquid concentrations of tar compounds, typically encountered in gasification processes³⁸, are listed for both cases in Table 5.2.

Table 5.2 – Concentration in gas and liquid phase (of liquid quench sampling system) of tar compounds typically encountered in gasification processes³⁸

| Species | low case | | high case | |
|--------------|--------------------------|---|--------------------------|---|
| | Gas concentration (ppmv) | Liquid concentration (mol l^{-1}) $\times 10^{-4}$ | Gas concentration (ppmv) | Liquid concentration (mol l^{-1}) $\times 10^{-3}$ |
| Benzene | 800 | 286 | 8000 | 286 |
| Naphthalene | 80 | 28.6 | 800 | 28.6 |
| Phenanthrene | 8 | 2.86 | 80 | 2.86 |
| Pyrene | 4 | 1.43 | 40 | 1.43 |

After preparing the four solutions, densities were measured (DMA 35, Anton Paar) and, based on Eq. (5.4), the water content predicted. The results of this experimental design are plotted in Fig. 5.4, where measured densities and predicted water contents are inscribed to the four circles.

Both, the water and tar content have an effect on the prediction error of the water content. An increase in water content causes an average error of 0.34 wt% points, which is close to values of residuals, observed in the parameter fitting process (see Fig. 5.3b). The increase in tar content is more significant with an error increase of 1.21 wt% points. The overestimation of density and thereby water content is caused by the presence of high molecular weight tar compounds in the solution. This screening experiment therefore indicates that the presence

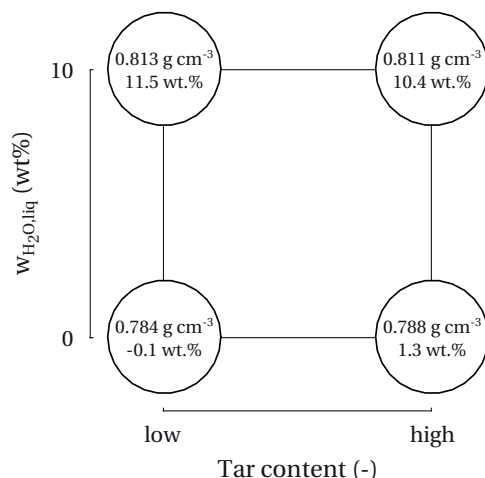


Figure 5.4 – Graphical representation, illustrating the dependence of the measured density (inside circles) on the two factors w_{H_2O} and tar content. Based on the measured density, the water content is predicted according to Eq. (5.4) (inside circles).

of tar compounds at high concentrations can affect the water determination by measurement of the liquid sample density. However, even under such conditions, the method can be used to provide an estimate of water content in the liquid sample (and thereby of steam content in the analysed process).

Response behaviour of the liquid quench sampling system

The response time characteristics of an analytical method can be of importance when transient processes are to be observed. In order to investigate the step response behaviour of the sampling system, it was connected to a pipe, constantly flushed by $1\ NL\ h^{-1}$ of Ar. For comparison, a MS (MAX 300-LG, Extrel) was connected to the same pipe. At time $t = 0$, 10 ppmv of the sulphur containing heterocyclic compound thiophene were added to the gas stream by means of a mass flow controller (MFC, EL-FLOW, Bronkhorst). The resulting signal responses of the UV-Vis, for wavelength 241 nm, and the MS ($m/z=84$) are plotted in Fig. 5.5.

The MS showed a signal increase 1 min after thiophene addition, reaching a stable signal after 4.5 min. The liquid quench sampling system connected UV-Vis on the other hand, had an increase in signal intensity after 7 min and reached a stable signal only after 17 min. Based on the step response signal A_{241} (absorbance at $\lambda = 241\ nm$) of the sampling system, the mean residence time $t_{mean,res}$ can be calculated according to Eq. (5.5)⁴⁰.

$$t_{mean,res} = \frac{1}{A_{241,max}} \int_0^{A_{241,max}} t dA_{241} \quad (5.5)$$

In this equation, $A_{241,max}$ refers to the maximum measured absorbance. Assuming a Dirac input to the system, the majority (90.4 %) of thiophene molecules will pass the UV-Vis detector within ± 4 min of the calculated mean residence time of 11.5 min.

5.2.3. UV-Vis apparatus

Online UV-Vis spectra were taken in a custom-made flow-through cell (path length 2 mm) connected to a deuterium, tungsten-halogen light source (DT-MINI-2-GS, Ocean Optics) and

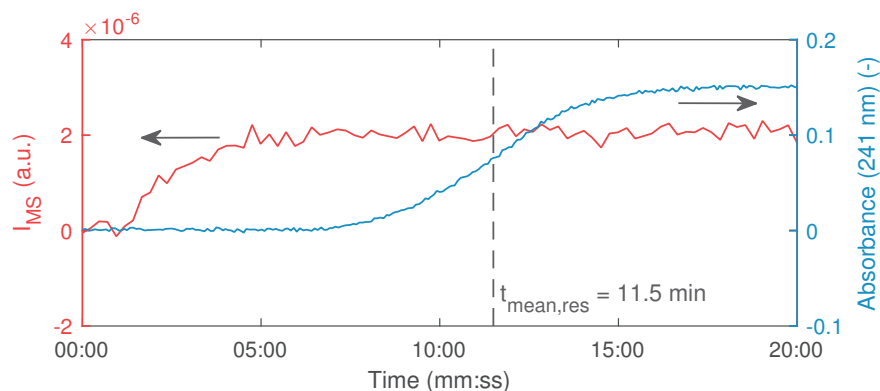


Figure 5.5 – Dynamic response of liquid quench sampling system (blue) and a mass spectrometer (red). The vertical line represents the mean residence time of the sampling system.

5

a single beam spectrometer (USB2000+XR1, Ocean Optics) by optical fibers. Spectra were recorded in the range 188 to 1032 nm at 0.4 nm intervals. Typical spectral detection rates were about 0.02 to 0.03 Hz. Offline measurements of UV-Vis spectra from collected samples were carried out in a standalone split-beam UV-Vis analyser (Carry 4000, Agilent) fitted with a quartz cell of 10 mm path length. With this analyser, spectra were acquired in the range 225 to 400 nm at 0.2 nm resolution. Dilution of samples for offline analysis was performed with 2-propanol to achieve absorbances below two.

5.2.4. Case studies

Two case studies were defined to evaluate the described analytical method. A simplified scheme of the experimental setups including sampling positions is provided in Fig. 5.6. The first case study (see Fig. 5.6a), called model gas case study, is a laboratory application with a defined gas and mixture of tar compounds. The second case study (see Fig. 5.6b), called real producer gas case study, represents an industrial application.

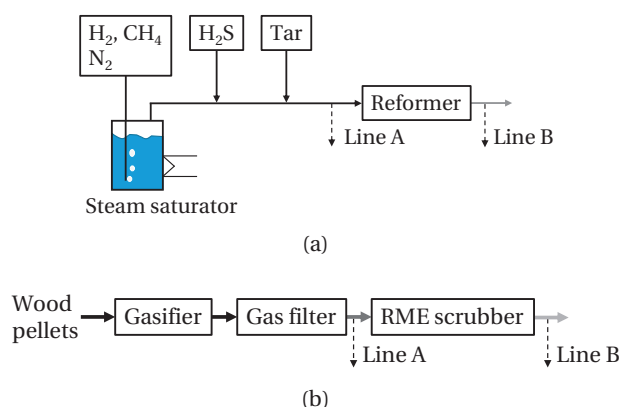


Figure 5.6 – Schematic overview of case studies. (a) Model gas; (b) real producer gas.

Model gas

Experiments in the model gas study were performed in collaboration with KIT (Karlsruhe, Germany) which extended tar reforming experiments previously conducted at PSI^{38,41}. The setup comprised a gas mixing section where a set of mass flow controllers (MFC) was used to create a model gas containing H₂, CH₄ and N₂. The steam content was adjusted by passing the gas through a steam saturator with a controlled outlet temperature. Afterwards, H₂S was added for selected experiments to investigate its effect on catalyst performance regarding tar compound conversion. A defined model tar mixture was fed to the pre-heated inlet gas stream by means of a syringe pump (PHD 2000, Harvard Apparatus). The mixture consisted of naphthalene dissolved in toluene. Naphthalene is typically present at high concentrations (60 to 1200 ppmv) in producer gas³⁸. It was chosen as a representative for class 4 tar compounds. Toluene, replacing benzene for reasons of safer handling, was chosen as a representative of class 3 tar compounds⁴². The resulting gas mixture was sent to a catalyst coated monolith, in the following called reformer, at a temperature of 750 °C. Sampling of the gas was performed by two liquid quench sampling systems before (line A) and after (line B) the reformer, allowing for online observation of tar compound decomposition. Tubing before/after the reactor and the sampling ports were heated to 120 °C to prevent loss of analytes. A summary of the experimental conditions of three experiments presented in this work is provided in Table 5.3.

Table 5.3 – Experimental conditions of model gas case study

| Exp. | Start (hh:mm) | T (°C) | Gas inlet composition | | | | | | |
|------|---------------|--------|-----------------------|-----------------|------------------|----------------|------------------|---------|-------------|
| | | | (vol.%) | | | | (ppmv) | | |
| | | | H ₂ | CH ₄ | H ₂ O | N ₂ | H ₂ S | Toluene | Naphthalene |
| M1 | 14:15 | | | | | | 3800 | | |
| M2 | 14:55 | 750 | 37 | 4 | 15 | 42 | 0 | 100 | 20 |
| M3 | 15:50 | | | | | | 0 | 0 | 0 |

Real producer gas

Measurements were taken at a pilot-plant (Pfaffenhofen, Germany) for gasification of wood pellets⁴³. The plant features a heatpipe-reformer, designed for 500 kW thermal input. The pressurized raw gas, exiting the gasifier is cooled down to 60 to 75 °C, passed through a particulate filter and a rapeseed methyl ester (RME) scrubber for gas cleaning, before it is sent to a gas engine for electricity production. Liquid quench samples were taken using one liquid quench sampling system, connected to either line A or B. The sampling point A was located before the RME scrubber. Samples taken after the scrubber (gas temperature 40 °C) at sampling point B allowed to qualitatively evaluate its effectiveness.

5.2.5. Tar quantification

Analysis of UV-Vis spectra

In this work, UV-Vis spectra of samples taken on lines A and B of the model gas and line B of the real producer gas case study were analysed quantitatively. Absorbance spectra of five identified tar compounds in these streams are plotted at different concentrations in Fig. 5.7.

Since spectra of the tar compounds overlap, it is problematic to perform an univariate calibration. Therefore, two multivariate regression approaches were followed in both case studies. CLS, a well-known calibration method, was chosen for the model gas case study⁴⁴. Two possible limitations of this approach have to be considered. It is assumed that all tar

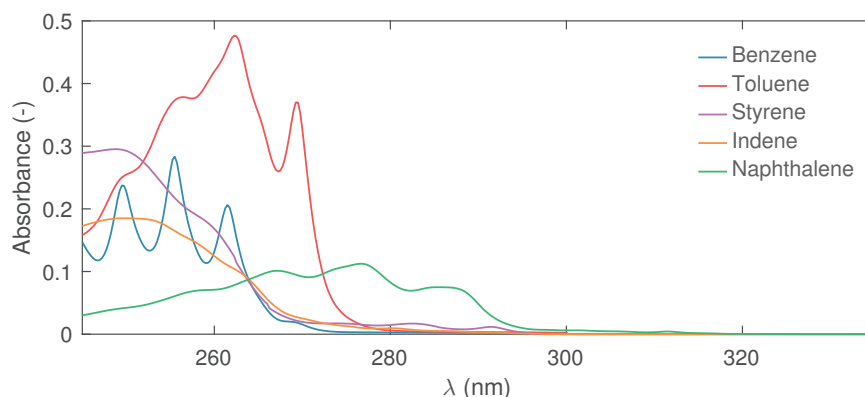


Figure 5.7 – Absorbance spectra (path length 2 mm) of five tar compounds in 2-propanol (concentrations for benzene and toluene: 10 mmol l^{-1} , for styrene, indene and naphthalene: 0.1 mmol l^{-1})

5

compounds in the liquid sample are known. The presence of not considered UV-Vis active compounds can result in biased results as their contribution to the absorbance is assigned to the calibrated tar compounds. An additional limitation can result from collinearity of the analysed tar compound spectra. A high degree of collinearity will result in an unstable system of equations, causing large variations in the solution for only small changes in the measured spectrum⁴⁵. In case of the model gas case study, previous experiments³⁸ have shown that the qualitative composition of tar compounds, represented by benzene, toluene and naphthalene, is not subject to change (i.e. possible reaction products such as xylene and styrene can be neglected). UV-Vis spectra of these three compounds show spectral overlaps, but the degree of collinearity is low. The CLS approach can therefore be used in this case study. When applied to another system, these assumptions have to be verified again.

In the real producer gas case study, liquid samples taken at line B contain at least those five compounds depicted in Fig. 5.7. Especially styrene and indene show a high degree of collinearity (see Fig. 5.8).

The CLS approach is therefore not a viable option for this application and a different calibration method was chosen. Because of its ability to overcome problems like collinearity and interactions, PLS regression has been widely used for such cases of first-order multivariate calibration^{47,48} and was therefore chosen for this application. A good overview of the method is given by Martens and Naes⁴⁹.

Handling of data and implementation of spectra decomposition by CLS and PLS in this work was performed in MATLAB 2015a (The MathWorks).

Partial least squares regression

Five tar compounds (benzene, toluene, styrene, indene and naphthalene) are expected to play a major role when evaluating spectra of gas, exiting the gas scrubber. A calibration set, containing these five compounds as factors at three levels, was calculated according to a full factorial design (3^5)⁵⁰. The levels were varied between zero and upper liquid concentrations expected in later applications (see Table 5.4).

In the resulting set, each calibration spectrum represents the sum of absorbance spectra

¹ Upper level refers to highest liquid concentration expected in the real producer gas case study

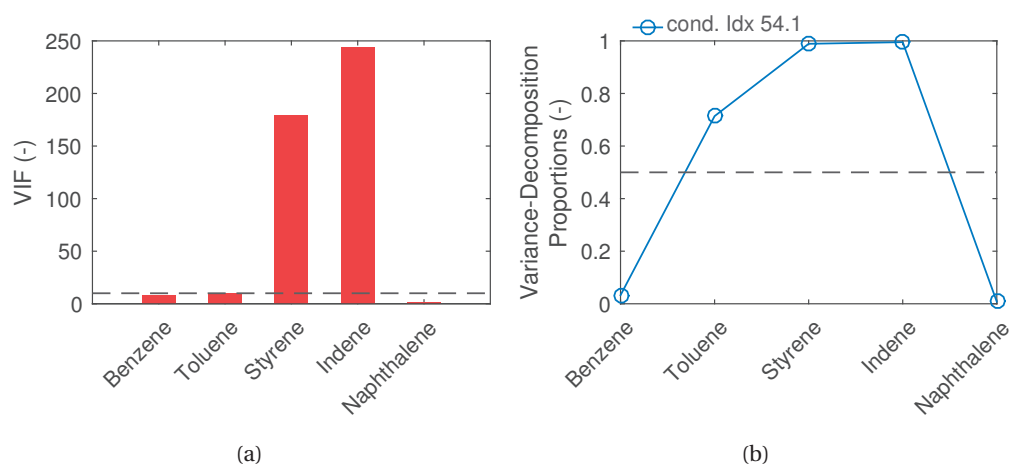


Figure 5.8 – Collinearity diagnostics for tar species analysed in this work. (a) Variance inflation factor (VIF). Values above the horizontal line can indicate a high degree of correlation between the variables⁴⁶; (b) Belsley collinearity diagnostics. Variables exceeding the tolerance indicated by the horizontal line show multicollinearity⁴⁵.

Table 5.4 – Settings and validation results of PLS method¹

| | Benzene | Toluene | Styrene | Indene | Naphthalene |
|--|---------|---------|---------|--------|-------------|
| Concentration, upper level (mmol l ⁻¹) | 25 | 5 | 0.25 | 0.25 | 0.25 |
| # PLS components | 4 | 5 | 5 | 5 | 4 |
| RMSEP (mmol l ⁻¹) | 0.1 | 0.02 | 0.002 | 0.003 | 0.001 |
| REP (%) | 1 | 1 | 1.5 | 2.5 | 0.6 |

of the individual tar compounds according to Beer's law including the addition of Gaussian random noise (0.5 %). The spectral range was limited to 245 to 300 nm to exclude the noisier signal at high wavelengths, as it contains no useful information, and the non-linear range of the instrument at lower wavelengths.

The root mean squared error (RMSE) was used as a measure of the differences between measured and predicted concentrations as defined in

$$\text{RMSE} = \sqrt{\frac{\sum_{j=1}^N (c_{\text{meas},j} - c_{\text{pred},j})^2}{N}} \quad (5.6)$$

Herein, the variables $c_{\text{meas},j}$ and $c_{\text{pred},j}$ refer to the measured and predicted concentration of the j th of a total of N test samples. Based on this definition, both the later introduced RMSE of cross-validation (RMSE-CV) and RMSE of prediction (RMSE-P) can be calculated.

In order to find the optimum PLS model, the number of PLS components for each tar compound was individually selected by means of a 10-fold cross-validation. For each number of PLS components and a given tar compound, the RMSE-CV was calculated. From the resulting plots, the optimum number of PLS components (ranging from 4 to 5, see Table 5.4) was chosen as a trade-off between prediction bias and variance by visual inspection (see also Figs. D.3 and D.4)⁵¹. Validation of the PLS method was performed, using samples of an

independent validation set. This set was created similarly to the calibration set, featuring a 6^5 full factorial design. The prediction ability of the method was measured by means of the RMSE-P and the relative error of prediction (REP) in percent, defined as

$$\text{REP} = 100 \frac{\text{RMSE-P}}{\bar{c}_{cal}} \quad (5.7)$$

where \bar{c}_{cal} refers to the mean concentration of each tar compound included in the validation set. Calculated RMSE-P's and REP's are listed in Table 5.4. For the evaluated method, the calculated REP vary between 0.6 to 2.5 % depending on the tar species. Obtained parity plots of the validation can be found in Fig. D.5.

Reference methods

Qualitative analysis of liquid samples obtained from the liquid quench sampling system, was performed by a GC (6890, Hewlett-Packard) coupled with a MS (5973, Hewlett-Packard). A Supelco SLB-IL59 column (30 m x 250 μm x 0.20 μm) was used for separation of tar compounds. Injection of 1 μl samples was performed at a 10:1 split ratio with a He carrier gas flow of 1 ml/min. The oven temperature was varied as follows: 55 $^{\circ}\text{C}$ (hold 3 min) then 15 $^{\circ}\text{C}/\text{min}$ to 300 $^{\circ}\text{C}$ (hold 15 min). The MS was operated in scan mode (m/z 20 to 250) with an ionization energy of 70 eV.

Quantitative analysis of selected tar species was performed by a GC (7890A, Agilent) equipped with an FID. Separation of tar compounds was done with an Agilent HP-5 column (30 m x 320 μm x 0.25 μm). 1 μl of sample was injected with a 25:1 split ratio and a He carrier gas flow of 1 ml/min. The oven was operated as follows: 40 $^{\circ}\text{C}$ (hold 6 min) then 10 $^{\circ}\text{C}/\text{min}$ to 200 $^{\circ}\text{C}$ (5 min). The FID was operated at 275 $^{\circ}\text{C}$ with H_2 (30 ml/min), air (300 ml/min) and a make-up gas flow of 25 ml/min He. Calibration was performed at five concentration levels with solutions of known tar compound concentrations and 8 replicates each. An exemplary chromatogram is given in Fig. 5.9. Relative standard deviations for quantification were below 10 %.

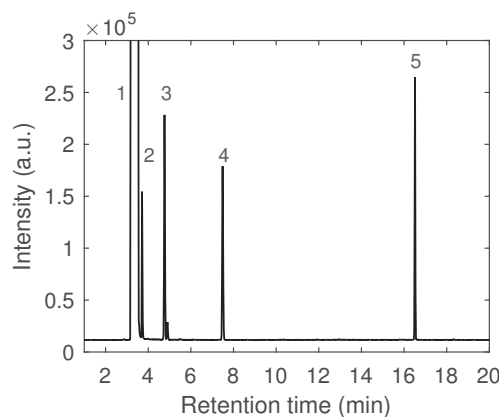


Figure 5.9 – GC-FID chromatogram of calibration for tar compound quantification for model gas case study. Legend of peak numbers: 1. 2-propanol (solvent), 2. 1-propanol, 3. benzene, 4. toluene, 5. naphthalene

5.3. Results and discussion

In the following the developed UV-Vis method is applied to two case studies as defined in section Section 5.2.4.

5.3.1. Model gas

Figure 5.10a and Fig. 5.10b plot the absorbance as a function of wavelength and time before and after the reformer, respectively. The areas, separated by the dotted lines, represent time periods where liquid samples for GC-FID reference analysis were taken.

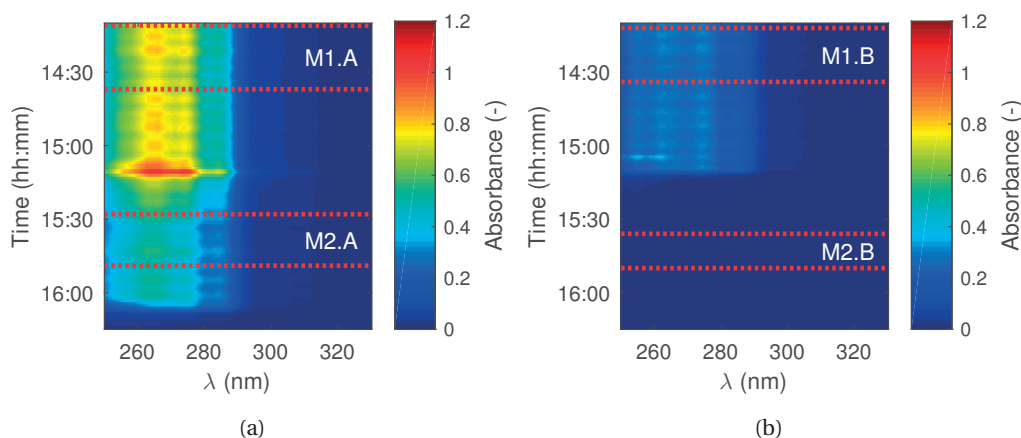


Figure 5.10 – Plots of absorbance as a function of wavelength and time for the model gas case study. Time interval between dotted lines represents periods where different liquid samples for later GC-FID analysis were collected. (a) Before reformer (line A); (b) after reformer (line B).

Already at this point, the plots can provide some qualitative information. Both show absorbance features in the range 250 to 290 nm, indicating the presence of light aromatic compounds (class 3). They also show a synchronous timely variation in absorbance, which can be related to the change in experimental conditions given in Table 5.3. The absorbance in Fig. 5.10a is generally higher than in Fig. 5.10b. Assuming similar liquid quench sampling system operating conditions, this indicates a change in tar composition and/or a decrease in tar compound concentration caused by the reformer. The actual reason can only be elucidated after determining the individual tar compound contributions to the spectra. To achieve this, the individual tar compound concentrations in the liquid phase were determined by CLS. Using Eq. (5.3), these can be related to their actual gas phase concentrations. The resulting tar compound gas concentrations *versus* time are presented by lines in Fig. 5.11a and Fig. 5.11b.

Vertical lines in these plots represent the boundaries between different experimental settings (see Table 5.3) whereas grey shaded areas represent time windows used to take liquid samples. Diamond shaped markers indicate tar compound gas concentrations obtained from GC-FID analysis.

In the following, some general remarks on the concentration plots are made first and the results obtained by the UV-Vis and GC-FID method will be compared thereafter. Finally, the performance of the catalyst is briefly discussed.

The concentration profiles show a response delay to changes in experimental conditions caused by the liquid quench sampling system's residence time characteristics, as discussed

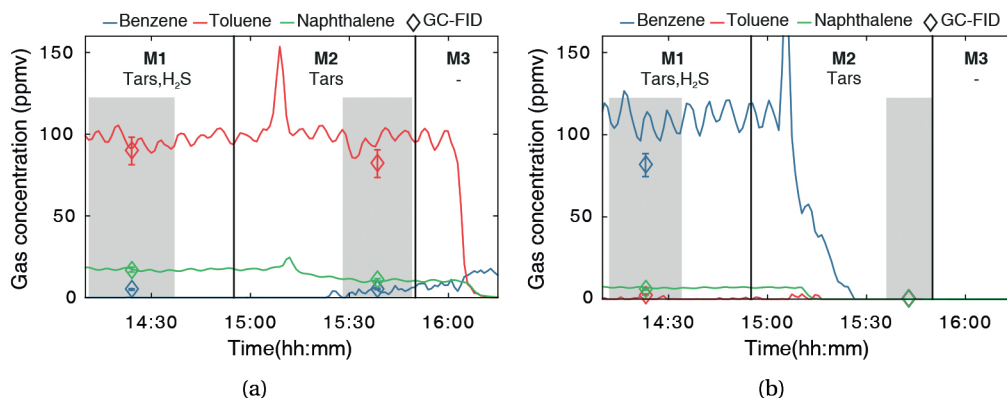


Figure 5.11 – Vertical lines indicate boundaries between different experimental settings. The grey shaded areas represent time periods used to take liquid samples for later analysis. Diamond shaped markers represent GC-FID measurements. (a) Gas concentration at reformer inlet (line A); (b) gas concentration at reformer outlet (line B).

5

in Section 5.2.2. Pulsations in predicted gas concentrations are caused by fluctuations in the gas flow entering the reformer, also indicated by MFC flow readings varying with a similar frequency. The peak at time 15:07 is caused by a momentary decrease in total gas flow as the H_2S addition was stopped. The observed behaviour illustrates the advantages of online UV-Vis detection compared to offline analytical tools. It allows to examine transient processes whereas offline methods will only provide an average of such temporal fluctuation over several minutes.

In order to evaluate the UV-Vis method, predicted concentrations were averaged for time periods for which liquid samples had been taken. This allowed for a direct comparison of UV-Vis and GC-FID derived concentrations (see Fig. 5.11 and Table 5.5).

Table 5.5 – Results of model gas case study². Concentrations refer to the liquid sample phase.

| Exp. | GC-FID (mmol l ⁻¹) | | | UV-Vis (mmol l ⁻¹) | | |
|------|--------------------------------|-------------|-------------|--------------------------------|-------------|-------------|
| | Benzene | Toluene | Naphthalene | Benzene | Toluene | Naphthalene |
| M1.A | 0.22 ± 0.02 | 3.2 ± 0.3 | 0.59 ± 0.05 | $(0.3 \pm 1.3) \times 10^{-3}$ | 3.4 ± 0.2 | 0.61 ± 0.02 |
| M1.B | 3.5 ± 0.3 | 0.10 ± 0.01 | 0.25 ± 0.02 | 4.7 ± 0.4 | 0.01 ± 0.03 | 0.30 ± 0.01 |
| M2.A | 0.24 ± 0.02 | 2.9 ± 0.3 | 0.37 ± 0.03 | 0.14 ± 0.06 | 3.4 ± 0.2 | 0.38 ± 0.02 |
| M2.B | b.d.l. | b.d.l. | b.d.l. | 0 | 0 | 0 |

In experiment M1, at the reformer inlet (M1.A), both toluene and naphthalene concentrations were well estimated by the UV-Vis method with prediction errors within the measurement uncertainty of the GC-FID method. The low concentration (5 ppmv) of benzene was not detected, however. At the reformer outlet (M1.B), benzene (33 % prediction error) and naphthalene (22 %) were predicted reasonably well, while the low concentration of toluene (2 ppmv) was not detected. In experiment M2, all three tar compounds were detected at the reformer inlet (M2.A). Toluene was overestimated (19 %) while benzene was underestimated (−41 %) at low concentration levels. The predicted concentration of naphthalene is good (4 % error). The non-existence of tar compounds at the reformer outlet (M2.B) was predicted by both methods.

²b.d.l.: below detection limit

From the above results it is apparent that prediction errors for toluene and benzene at low concentrations are higher than in the case of naphthalene. This can be attributed to the extinction coefficients of naphthalene which are two orders of magnitude higher than those of the class 3 tar compounds. Consequently, a smaller concentration of naphthalene will suffice to achieve comparable absorbances and measurement errors.

The presented UV-Vis method can be a valuable tool when immediate information for assessing the performance of catalysts is needed. In experiment M1, inlet gas phase concentrations of toluene and naphthalene are close to the set ones, while that of benzene is almost zero. Thermal cracking of tar compounds before the reformer inlet can therefore be neglected under the given experimental conditions. Based on their concentration profiles, the conversion of the reaction educts, toluene and naphthalene, was calculated and plotted in Fig. 5.12a.

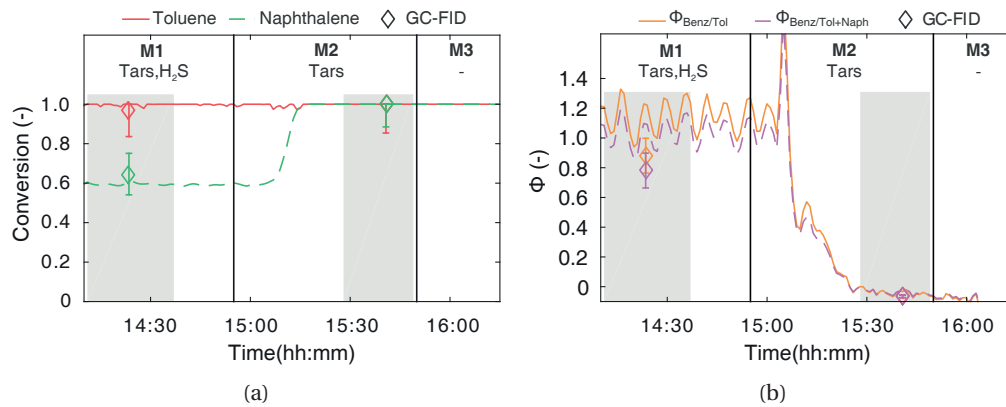


Figure 5.12 – Vertical lines indicate boundaries between different experimental settings. The grey shaded areas represent time periods used to take liquid samples for later analysis. Diamond shaped markers represent GC-FID measurements. (a) Calculated conversion of toluene and naphthalene; (b) calculated overall fractional yields towards benzene as defined in Eqs. (5.8) and (5.9).

Across the reformer, almost all toluene (> 97 %) and 61 % of naphthalene are converted. High exit gas concentrations of benzene indicate that dealkylation of toluene might be a major reaction path. In fact, the overall fractional yield $\Phi_{Benz/Tol}$, defined in Eq. (5.8) and plotted in Fig. 5.12b, indicates that the majority of toluene is converted to benzene⁵².

$$\Phi_{Benz/Tol} = \frac{F_{Benz,out} - F_{Benz,in}}{F_{Tol,in} - F_{Tol,out}} \quad (5.8)$$

In this equation, F_i refer to the inlet or outlet molar flows of the individual tar compounds. Results, obtained by the UV-Vis method, overestimate the fractional yield due to an overestimated outlet concentration of benzene. Assuming that the decomposition of naphthalene can form benzene as well⁵³, an overall fractional yield $\Phi_{Benz/Tol+Naph}$ of benzene from toluene and naphthalene can be defined as

$$\Phi_{Benz/Tol+Naph} = \frac{F_{Benz,out} - F_{Benz,in}}{(F_{Tol,in} - F_{Tol,out}) + (F_{Naph,in} - F_{Naph,out})} \quad (5.9)$$

Based on GC-FID results, it was found that 78 % of the toluene and naphthalene measured at the reactor inlet have been converted to benzene. Further reaction products from toluene and naphthalene decomposition were not accessible to GC-FID and UV-Vis measurements.

Because no experiments, containing the individual tar compounds, were performed, the actual contribution of naphthalene to the exiting benzene cannot be estimated.

As the supply of H_2S is ceased in experiment M2, a slight decrease in toluene and naphthalene inlet concentration is accompanied by an increase in benzene concentration. At the reformer outlet, no tars could be detected, resulting in full conversion. When the tar supply is stopped too, (experiment M3), the tar compound inlet concentrations decline as well, with the exception of benzene. Its concentration increases, only to fall off after approximately 15 min.

Experiments M1 and M2 show that H_2S , which is in part reversibly bound to active sites of the catalyst⁵⁴, has a major effect on tar conversion. When H_2S is present, naphthalene is only partially converted, while the majority of toluene is converted to benzene. As soon as the H_2S supply is stopped, all tar compounds are decomposed⁵⁵.

5.3.2. Real producer gas

Next to catalytic reforming, absorption of tars by a solvent at low temperature ($< 100^\circ C$) presents an alternative secondary method for tar removal. Different scrubber designs and solvents have been investigated. Among them, RME scrubbers have proven to be a viable option⁵⁶. GC-MS chromatograms of liquid samples (see Fig. 5.13), taken before and after an RME scrubber, show complex mixtures of hydrocarbons.

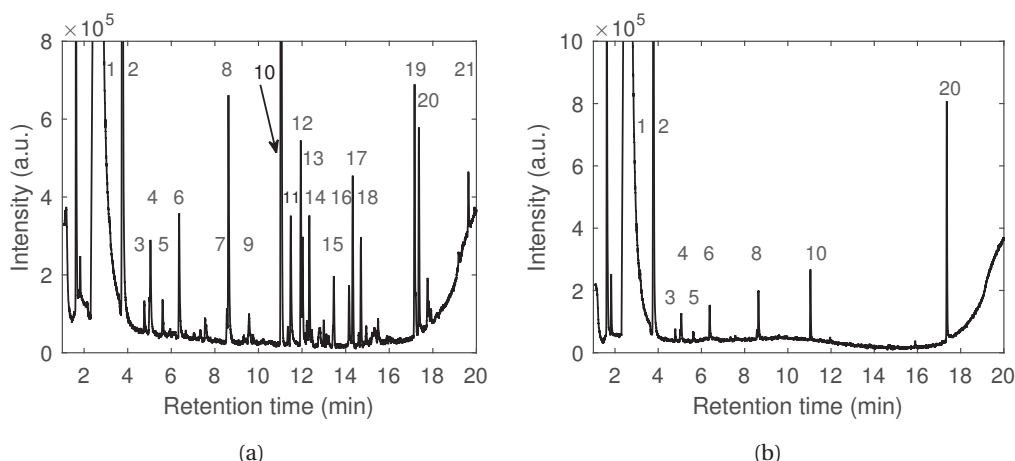


Figure 5.13 – GC-MS chromatograms of samples taken in the real producer gas case. (a) Before RME scrubber (R1.A); (b) after RME scrubber (R1.B). Legend of peak numbers: 1. 2-propanol (solvent), 2. toluene, 3. ethylbenzene, 4. m/p-xylene, 5. o-xylene, 6. styrene, 7. benzofuran, 8. indene, 9. 2-methylindene, 10. naphthalene, 11. phenol, 12. 2-methylnaphthalene, 13. 1-methylnaphthalene, 14. biphenyl, 15. acenaphthene, 16. dibenzofuran, 17. acenaphthylene, 18. fluorene, 19. phenanthrene, 20. artifact, 21. fluoranthene. Benzene is masked by the solvent peak.

At the scrubber inlet, more than 20 tar compounds were detected, ranging from class 3 tar compounds such as benzene to heavy polycyclic aromatic hydrocarbon (class 5) like fluoranthene. The scrubber removes tar compounds with molecular weights typically larger than naphthalene from the gas stream. This is in agreement with previous studies which report increased removal performances for increasing molecular weight of tar compounds^{43,57,58}. An exemplary offline UV-Vis spectrum of a diluted liquid sample (R1.A), taken before the RME scrubber, is presented in Fig. 5.14.

While features at 276 and 287 nm can suggest the presence of naphthalene at high con-

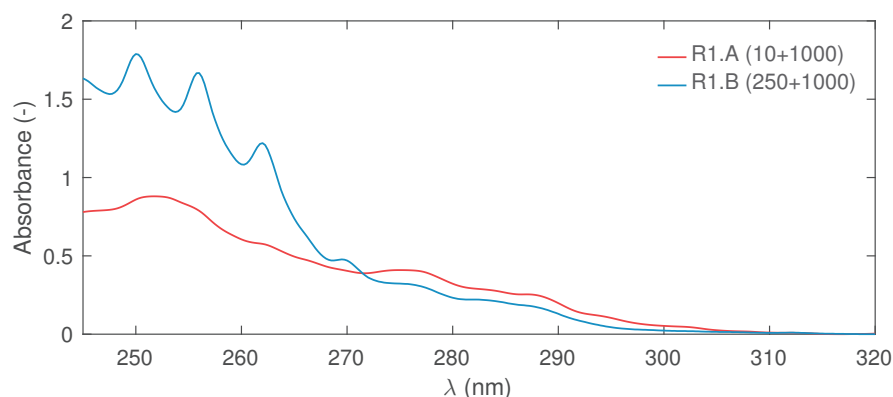


Figure 5.14 – Absorbance spectra of samples taken before (R1.A, diluted 10 μ l sample + 1000 μ l solvent) and after (R1.B, diluted 250 μ l sample + 1000 μ l solvent) the RME scrubber

5

centrations, the high spectral overlap at lower wavelengths complicates quantification of further compounds significantly. Online UV-Vis spectra, taken at the RME scrubber outlet are plotted in Fig. 5.15a. Visual inspection of the plot allows for a qualitative analysis of the tar composition as a function of time. As such, it displays the ability of the developed method to online monitor the stability of pilot-scale processes. The dotted lines represent the time span between which a liquid sample was taken. The figure shows a slight decrease in absorbance with time. Absorption features below 270 nm indicate the presence of aromatic compounds. Between 250 to 255 nm, the observed absorbance is high (> 2.5) and pixels marked black represent areas where the maximum absorbance of the instrument was exceeded.

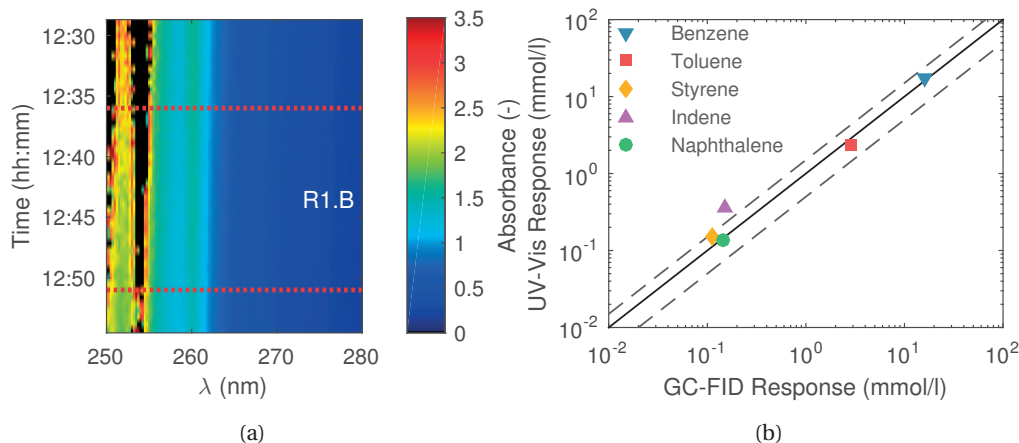


Figure 5.15 – (a) Plot of absorbance *versus* wavelength and time at RME scrubber outlet. The area enclosed by the dotted lines represents the time window where a liquid sample for later GC-FID analysis was taken. Black colours indicate regions where the maximum absorbance of the instrument was exceeded; (b) parity plot of tar concentrations, measured in sample R1.B by GC-FID and UV-Vis (PLS). The dashed lines represent the $\pm 50\%$ deviation lines.

A liquid sample (R1.B) was additionally analysed offline by an UV-Vis spectrometer (after

dilution) and GC-FID (Figs. 5.14 and 5.15b). Quantification of its tar compounds was performed by the PLS method described in Section 5.2.5. The results of obtained liquid phase concentrations are plotted as a parity plot in Fig. 5.15b. Benzene, toluene, styrene and naphthalene were estimated well with prediction errors below 27 %. Indene, with its few distinctive features and rather low concentration, was predicted with large error of 59 %. However, it can still serve as a valuable estimate. Based on Eq. (5.3), gas phase concentrations obtained with the PLS method were calculated to range from 0.9 ppmv for naphthalene to 113 ppmv in case of benzene.

References

- [1] Vincent Claude, Claire Courson, Martina Köhler, and Stéphanie D. Lambert. Overview and essentials of biomass gasification technologies and their catalytic cleaning methods. *Energy & Fuels*, 30(11):8791–8814, 2016.
- [2] Hong Cui, Scott Q. Turn, Vheissu Keffer, Donald Evans, Thai Tran, and Michael Foley. Contaminant estimates and removal in product gas from biomass steam gasification. *Energy & Fuels*, 24:1222–1233, 2010.
- [3] K. Maniatis and Aacm Beenackers. Tar protocols. iea bioenergy gasification task. *Biomass & Bioenergy*, 18(1):1–4, 2000.
- [4] Thomas A Milne, Nicolas Abatzoglou, and Robert J Evans. *Biomass gasifier" tars": their nature, formation, and conversion. Golden (Colorado): National Renewable Energy Laboratory*. 1998.
- [5] Zia Ud Din and Z. A. Zainal. Biomass integrated gasification–sofc systems: Technology overview. *Renewable and Sustainable Energy Reviews*, 53:1356–1376, 2016.
- [6] P. V. Aravind and Wiebren de Jong. Evaluation of high temperature gas cleaning options for biomass gasification product gas for solid oxide fuel cells. *Progress in Energy and Combustion Science*, 38(6):737–764, 2012.
- [7] J. A. Ruiz, M. C. Juarez, M. P. Morales, P. Munoz, and M. A. Mendivil. Biomass gasification for electricity generation: Review of current technology barriers. *Renewable & Sustainable Energy Reviews*, 18:174–183, 2013.
- [8] JHA Kiel, SVB Van Paasen, JPA Neeft, L Devi, KJ Ptasinski, FJJG Janssen, R Meijer, RH Berends, HMG Temmink, and G Brem. Primary measures to reduce tar formation in fluidised-bed biomass gasifiers. *ECN, ECN-C-04-014*, 2004.
- [9] Fenghua Shen, Jing Liu, Zhen Zhang, and Yingju Yang. Temporal measurements and kinetics of selenium release during coal combustion and gasification in a fluidized bed. *Journal of Hazardous Materials*, 310:40–47, 2016.
- [10] Lopamudra Devi, Krzysztof J. Ptasinski, and Frans J. J. G. Janssen. A review of the primary measures for tar elimination in biomass gasification processes. *Biomass and Bioenergy*, 24(2):125–140, 2003.
- [11] Samsudin Anis and Z. A. Zainal. Tar reduction in biomass producer gas via mechanical, catalytic and thermal methods: A review. *Renewable and Sustainable Energy Reviews*, 15(5):2355–2377, 2011.
- [12] Patrick J. Woolcock and Robert C. Brown. A review of cleaning technologies for biomass-derived syngas. *Biomass & Bioenergy*, 52:54–84, 2013.
- [13] S.V.B. Van Paasen, J.H.A. Kiel, J.P.A. Neeft, H.A.M. Knoef, G.J. Buffinga, U. Zielke, K. Sjostrom, C. Brage, P. Hasler, and P.A. Simell. Guideline for sampling and analysis of tar and particles in biomass producer gases. *ECN*, 2002.
- [14] Claes Brage, Qizhuang Yu, Guanxing Chen, and Krister Sjöström. Use of amino phase adsorbent for biomass tar sampling and separation. *Fuel*, 76(2):137–142, 1997.

- [15] Mikael Israelsson, Martin Seemann, and Henrik Thunman. Assessment of the solid-phase adsorption method for sampling biomass-derived tar in industrial environments. *Energy & Fuels*, 27(12):7569–7578, 2013.
- [16] Sergejs Osipovs. Comparison of efficiency of two methods for tar sampling in the syngas. *Fuel*, 103:387–392, 2013.
- [17] S. Karellas and J. Karl. Analysis of the product gas from biomass gasification by means of laser spectroscopy. *Optics and Lasers in Engineering*, 45(9):935–946, 2007.
- [18] Renhui Sun, Nico Zobel, York Neubauer, Christian Cardenas Chavez, and Frank Behrendt. Analysis of gas-phase polycyclic aromatic hydrocarbon mixtures by laser-induced fluorescence. *Optics and Lasers in Engineering*, 48(12):1231–1237, 2010.
- [19] Alba Dieguez-Alonso, Andres Anca-Couce, and Nico Zobel. On-line tar characterization from pyrolysis of wood particles in a technical-scale fixed-bed reactor by applying laser-induced fluorescence (lif). *Journal of Analytical and Applied Pyrolysis*, 102:33–46, 2013.
- [20] Eun-Jae Shin, Mark R. Nimlos, and Robert J. Evans. Kinetic analysis of the gas-phase pyrolysis of carbohydrates. *Fuel*, 80(12):1697–1709, 2001.
- [21] Daniel L. Carpenter, Steve P. Deutch, and Richard J. French. Quantitative measurement of biomass gasifier tars using a molecular-beam mass spectrometer: Comparison with traditional impinger sampling. *Energy & Fuels*, 21(5):3036–3043, 2007.
- [22] Mehmet Kuddusi Akalın and Selhan Karagöz. Analytical pyrolysis of biomass using gas chromatography coupled to mass spectrometry. *TrAC Trends in Analytical Chemistry*, 61: 11–16, 2014.
- [23] Alexander L. Brown, David C. Dayton, Mark R. Nimlos, and John W. Daily. Characterization of biomass pyrolysis vapors with molecular beam, single photon ionization time-of-flight mass spectrometry. *Chemosphere*, 42(5–7):663–669, 2001.
- [24] F. Mühlberger, R. Zimmermann, and A. Kettrup. A mobile mass spectrometer for comprehensive on-line analysis of trace and bulk components of complex gas mixtures: parallel application of the laser-based ionization methods vuv single-photon ionization, resonant multiphoton ionization, and laser-induced electron impact ionization. *Analytical Chemistry*, 73(15):3590–3604, 2001.
- [25] F. Defoort, S. Thiery, and S. Ravel. A promising new on-line method of tar quantification by mass spectrometry during steam gasification of biomass. *Biomass and Bioenergy*, 65: 64–71, 2014.
- [26] Liangyuan Jia, Yann Le Brech, Guillaín Mauviel, Fei Qi, Matthias Bente-von Frowein, Sven Ehlert, Ralf Zimmermann, and Anthony Dufour. Online analysis of biomass pyrolysis tar by photoionization mass spectrometry. *Energy & Fuels*, 30(3):1555–1563, 2016.
- [27] SVB Van Paasen, H Boerrigter, J Kuipers, AMV Stokes, F Struijk, and A Scheffer. Tar dewpoint analyser. for application in biomass gasification product gases. *ECN*, 2005.
- [28] O. Moersch, H. Spliethoff, and K. R. G. Hein. Tar quantification with a new online analyzing method. *Biomass and Bioenergy*, 18(1):79–86, 2000.

- [29] Mozhgan Ahmadi, Claes Brage, Krister Sjoestroem, Klas Engvall, Harrie Knoef, and Bert Van de Beld. Development of an on-line tar measurement method based on photo ionization technique. *Catalysis Today*, 176(1):250–252, 2011.
- [30] Mozhgan Ahmadi, Harrie Knoef, Bert Van de Beld, Truls Liliedahl, and Klas Engvall. Development of a PID based on-line tar measurement method - proof of concept. *Fuel*, 113:113–121, 2013.
- [31] Heinz-Helmut Perkampus. *UV-VIS Atlas of Organic Compounds*. VCH, Weinheim, 2nd edition, 1992.
- [32] Francesco Patuzzi, Davide Roveda, Tanja Mimmo, Jürgen Karl, and Marco Baratieri. A comparison between on-line and off-line tar analysis methods applied to common reed pyrolysis. *Fuel*, 111:689–695, 2013.
- [33] Manuela Di Marcello, Katia Gallucci, Sergio Rapagna, René Gruber, and Muriel Matt. Hptlc and UV spectroscopy as innovative methods for biomass gasification tars analysis. *Fuel*, 116:94–102, 2014.
- [34] T. Weide, V. Guschin, W. Becker, S. Koelle, S. Maier, and S. Seidelt. Analysis of pure tar substances (polycyclic aromatic hydrocarbons) in the gas stream using ultraviolet visible (UV-vis) spectroscopy and multivariate curve resolution (MCR). *Applied Spectroscopy*, 69(1):143–153, 2015.
- [35] M. D. K. Rechulski, J. Schneebeili, S. Geiger, T. J. Schildhauer, S. M. A. Biollaz, and C. Ludwig. Liquid-quench sampling system for the analysis of gas streams from biomass gasification processes. part 1: Sampling noncondensable compounds. *Energy & Fuels*, 26(12):7308–7315, 2012.
- [36] M. D. K. Rechulski, J. Schneebeili, S. Geiger, T. J. Schildhauer, S. M. A. Biollaz, and C. Ludwig. Liquid-quench sampling system for the analysis of gas streams from biomass gasification processes. part 2: Sampling condensable compounds. *Energy & Fuels*, 26(10):6358–6365, 2012.
- [37] P. Edinger. *High Temperature Conversion of Sulfur Containing Hydrocarbons and Tars*. Master's thesis, ETH Zürich, 2012.
- [38] U. Rhyner, P. Edinger, T. J. Schildhauer, and S. M. A. Biollaz. Experimental study on high temperature catalytic conversion of tars and organic sulfur compounds. *International Journal of Hydrogen Energy*, 39(10):4926–4937, 2014.
- [39] G. I. Egorov, V. N. Afanas'ev, and A. M. Kolker. Vtx properties of the system water-2-propanol in the range 275.15–338.15 K. *Russian Journal of General Chemistry*, 74(2):171–173, 2004.
- [40] Octave Levenspiel. *Chemical reaction engineering*. Wiley, New York, 3rd edition, 1999.
- [41] U. Rhyner, P. Edinger, T. J. Schildhauer, and S. M. A. Biollaz. Applied kinetics for modeling of reactive hot gas filters. *Applied Energy*, 113:766–780, 2014.
- [42] Seethamraju Srinivas, Randall P. Field, and Howard J. Herzog. Modeling tar handling options in biomass gasification. *Energy & Fuels*, 27(6):2859–2873, 2013.

- [43] Georg Gallmetzer, Pascal Ackermann, Andreas Schweiger, Thomas Kienberger, Thomas Gröbl, Heimo Walter, Markus Zankl, and Martin Kroener. The agnion heatpipe-reformer—operating experiences and evaluation of fuel conversion and syngas composition. *Biomass Conversion and Biorefinery*, 2(3):207–215, 2012.
- [44] Charles L. Lawson and Richard J. Hanson. *Solving least squares problems*. Classics in applied mathematics. SIAM, Philadelphia, 1995.
- [45] David A. Belsley, Edwin Kuh, and Roy E. Welsch. *Regression diagnostics identifying influential data and sources of collinearity*. Wiley series in probability and mathematical statistics Applied probability and statistics. Wiley, New York etc., 1980.
- [46] Donald W. Marquardt. Generalized inverses, ridge regression, biased linear estimation, and nonlinear estimation. *Technometrics*, 12(3):591–612, 1970.
- [47] Svante Wold, Michael Sjoestroem, and Lennart Eriksson. Pls-regression: a basic tool of chemometrics. *Chemometrics and Intelligent Laboratory Systems*, 58(2):109–130, 2001.
- [48] Alejandro C. Olivieri. Practical guidelines for reporting results in single- and multi-component analytical calibration: A tutorial. *Analytica Chimica Acta*, 868:10–22, 2015.
- [49] Harald Martens and Tormod Næs. *Multivariate calibration*. Wiley, Chichester, 1992.
- [50] George E. P. Box, J. Stuart Hunter, and William Gordon Hunter. *Statistics for experimenters design, innovation, and discovery*. Wiley series in probability and statistics. Wiley-Interscience, Hoboken, N.J., 2nd edition, 2005.
- [51] Nicolaas M. Faber. A closer look at the bias–variance trade-off in multivariate calibration. *Journal of Chemometrics*, 13(2):185–192, 1999.
- [52] P. Simell, P. Ståhlberg, Y. Solantausta, J. Hepola, and E. Kurkela. *Gasification Gas Cleaning with Nickel Monolith Catalyst*, pages 1103–1116. Springer Netherlands, Dordrecht, 1997.
- [53] Yun-liang Zhang, Yong-hao Luo, Wen-guang Wu, Shan-hui Zhao, and Yu-feng Long. Heterogeneous cracking reaction of tar over biomass char, using naphthalene as model biomass tar. *Energy & Fuels*, 28(5):3129–3137, 2014.
- [54] Calvin H. Bartholomew. Mechanisms of catalyst deactivation. *Applied Catalysis A: General*, 212(1–2):17–60, 2001.
- [55] J. Hepola and P. Simell. Sulphur poisoning of nickel-based hot gas cleaning catalysts in synthetic gasification gas - ii. chemisorption of hydrogen sulphide. *Applied Catalysis B-Environmental*, 14(3–4):305–321, 1997.
- [56] RWR Zwart, A Van der Drift, A Bos, HJM Visser, MK Cieplik, and HWJ Könemann. Oil-based gas washing—flexible tar removal for high-efficient production of clean heat and power as well as sustainable fuels and chemicals. *Environmental progress & sustainable energy*, 28(3):324–335, 2009.
- [57] Thana Phuphuakrat, Tomoaki Namioka, and Kunio Yoshikawa. Absorptive removal of biomass tar using water and oily materials. *Bioresource Technology*, 102(2):543–549, 2011.
- [58] Eve Masurel, Olivier Authier, Christophe Castel, and Christine Roizard. Screening method for solvent selection used in tar removal by the absorption process. *Environmental Technology*, 36(20):2556–2567, 2015.

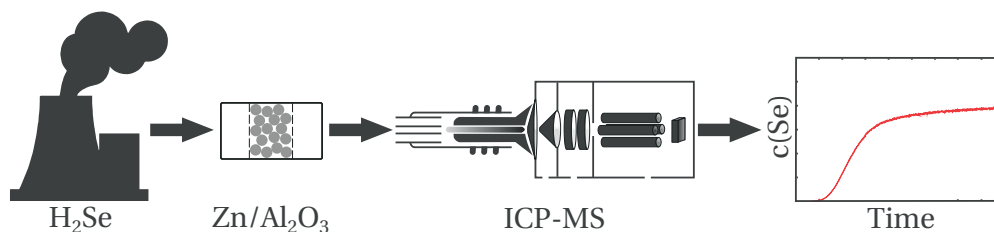
6

Online detection of selenium and its retention in reducing gasification atmosphere

This chapter is adapted from **P. Edinger** et al., *Online Detection of Selenium and Its Retention in Reducing Gasification Atmosphere*, Energy Fuels **30**, 1237 (2016) and **P. Edinger** et al., *Online Detection and Retention of Trace Contaminants in Reducing Gasification Atmosphere*, Proc. 33rd Annu. Int. Pittsburgh Coal Conference, 8-12 August, Cape Town, South Africa (2016).

Abstract

The emission of selenium (Se) from coal gasification processes can cause harm to the environment and downstream equipment. With upcoming legislation, reliable detection as well as control of such gas species become crucial. This study therefore addresses the development and successful employment of an online analytical method, based on the direct introduction of a simplified flue gas (H_2 , H_2O , H_2Se , Ar) into an ICP-MS. In combination with matrix matched calibration, the calculated and verified detection limits of H_2Se lie below 1 ppbv, thus being comparable to current offline methods. These low detection limits and the high temporal resolution (> 1 Hz) enable the use of this method as a quick and robust tool for the lab- and bench-scale performance evaluation of sorbent materials. As a case study, Zn/Al_2O_3 was tested towards H_2Se capturing at warm temperatures (150 to 350 °C). The results show that both, the support and the active phase, interact with the contaminant. While $\gamma-Al_2O_3$ can retain H_2Se at dry reaction conditions, a Zn phase is needed for its capture in steam laden gas.



6.1. Introduction

SELENIUM (Se) is an element of major environmental concern¹. Its anthropogenic discharge can cause harm to human health due to its very narrow margin between dietary deficiency and toxic levels². On the other hand, it can accumulate in the aquatic food chain to cause reduced reproduction and growth in fish^{3,4}. The United States Environmental Protection Agency (US EPA) has therefore recently published a final rule that strives to limit the emission of Se amongst other elements for different types of power plants, including integrated gasification combined cycle (IGCC) plants which are typically coal-fed⁵. These plants offer the advantage of increased process efficiencies compared to conventional electricity generation technologies, thereby producing electricity cleaner and potentially cheaper⁶.

The raw producer gas, exiting the gasifier of such plants, is mainly composed of H_2 , CO, CO_2 and H_2O depending on the gasification technology, the feedstock and operating conditions⁷. Besides other undesired by-products, Se is found predominantly in form of H_2Se ^{8,9} in the vapour phase due to its high volatility and therefore might escape particulate control devices¹⁰. Aside from environmental pollution, the passing Se can also poison downstream equipment in case the gas is used for the production of chemicals or fuels^{11,12}. This makes further emission control a necessity.

In IGCC processes, two options for Se emission control can be identified. One option is the capture of Se (predominant species Se^0 , SeO_2 ^{8,13}) after the gas turbine in oxidizing gas atmosphere. However, the involved gas expansion in the turbine and the addition of an oxidizer for combustion result in increased gas volume flows. The higher gas volume flow and decreased SeO_2 partial pressure necessitate increased equipment sizes, which again raise investment costs. A second option is therefore the removal of H_2Se before the gas turbine in reducing gas conditions. This can proceed either under cold (typically 20 to 100 °C), warm (150 to 300 °C) or hot (> 300 °C) gas clean-up conditions. Compared to the cold gas clean-up, the warm/hot gas clean-up avoids dropping the gas temperature below the dew point of steam, allowing for further efficiency gains of the process¹⁴. An added benefit is that the appearance of Se species in water streams from gas scrubbing can be circumvented¹⁵. There is therefore a strong incentive to perform the gas clean-up at elevated temperatures. Other contaminant control strategies, applied at this point, might serve as a co-benefit for H_2Se retention¹⁶. Because Se and S are similar in most of their chemistry, measures for H_2S removal have shown to be effective for H_2Se capture as well¹⁷. A polishing step to remove residual H_2Se may be required, however.

With expected gas concentrations of H_2Se before gas clean-up being below 1 ppmv (parts per million by volume)¹⁶ and regulated, maximum concentrations (see Appendix E.1 for derivation)⁵ at the gas turbine inlet in the range of 50 ppbv (parts per billion by volume), reliable analytical tools with high sensitivity and temporal resolution are required to evaluate the performance of sorbent material candidates. Traditional offline measurement of trace elements is based on sampling trains, where the flue gas is passed through a series of impinger bottles whose content is analysed afterwards^{18,19}. With sampling times in the range of 1 h, these methods are merely useful to provide average concentration measurements, not information on the breakthrough behaviour of a sorbent. Until recently, most Se sorption studies performed multiple experiments where the sorbent is exposed to H_2Se for different periods of time after which the sorbent is digested and the solution analysed for its Se content. Based on the resulting capacity *versus* time plots, a maximum retention capacity is defined. Besides the effort for performing multiple experiments, the method is destructive and suffers the drawback that the dynamics of the breakthrough curve cannot be observed. The need for an online

method has been acknowledged by Rupp et al.^{20,21}, who developed and applied a tool based on a GC/IT-MS. However, the method has some constraints. The calculated detection limit for H₂Se is restricted to 0.207 to 5.335 ppmv depending on the gas matrix. Steam concentrations are restricted to 0.5 vol%²¹ while in coal gasification steam content ranges from 0.4 to 18 vol%, depending on gasification technology, feedstock and operating parameters¹⁴. A number of methods for the online detection of metal species in industrial processes have been reported in the past decades with a comprehensive overview being given by Monkhouse²². The online detection of metal species in gasification atmosphere has been measured by ICP-OES²³ but not ICP-MS which offers superior detection capabilities.

The removal of Se at elevated temperatures has been investigated by several groups. Various sorbent materials have been used, including fly ash^{24,25}, limestone^{26–30}, kaolinite²⁵ as well as supported metals represented by Pd/Al₂O₃^{21,31,32} and Zn₂TiO₄³³. Supported sorbent materials have the advantage of improved specific surface area (SSA) and mechanical properties. While several supports have been investigated³⁴, recent work showed encouraging results using Zn/Al₂O₃ for the capture of H₂S³⁵. γ -Al₂O₃ as a support can interact with both H₂Se and steam present in the gas. Watanabe et al.³⁶ investigated the adsorption of H₂Se onto γ -Al₂O₃ in dry N₂ atmosphere at room temperature. In their experiments, H₂Se is adsorbed by both physisorption and chemisorption to significant extents. In case of chemisorption, the H₂Se was found to react with oxygen atoms on the Al₂O₃ to form elemental Se. Competitive adsorption with gas phase H₂O was not investigated. However, heating the Al₂O₃ at various temperatures up to a maximum of 200 °C before sorption experiments to remove surface bound H₂O did not have a significant effect on sorption capacity. The adsorption of H₂O on γ -Al₂O₃ has been investigated by several authors^{37–39}. Chemisorbed water on the surface can be present as water molecules bound to surface oxygen by strong hydrogen bonds (investigated at 120 °C³⁸) and by OH groups, whereas the latter type dominates as temperatures are further increased³⁷.

This study aims at establishing and applying an experimental setup that allows for the online detection of Se in reducing gas atmosphere. An ICP-MS was chosen as measurement device. In combination with matrix matched calibration, this allows for a highly time resolved study of sorbent materials even at concentrations in the low ppbv range. Zn/Al₂O₃ was chosen as sorbent, based on the favourable thermodynamics of the reaction of ZnO with H₂Se (see Fig. 6.7). The aim of this study is therefore twofold. The first step is to evaluate the ICP-MS with direct gas introduction as a tool for quantification of Se in reducing gas atmosphere. In the second step, this method is applied to investigate the Se capture performance of Zn/Al₂O₃ as a sorbent at warm gas clean-up conditions.

6.1.1. Gas matrix

For calibration and later H₂Se sorption experiments, a gas matrix representative of IGCC processes has to be defined. If such a synthetic mixture is sent to a laboratory reactor, the individual gas concentrations are subject to change due to a coupling of the concentrations (mainly) by water-gas-shift and methanation reactions listed in Eqs. (6.1) and (6.2), respectively.



Their actual concentration of CO, H₂O, CO₂, H₂ and CH₄ will therefore depend on temperature, residence time and the presence of a catalyst.

Establishing a setup allowing for online measurement of H_2Se is challenging, because the direct introduction of such a gas mixture into an ICP-MS for Se determination can lead to substantial material loss on the tubing walls and severe matrix effects thereby hindering quantification⁴⁰. Indeed, both H_2 ^{41–44}, H_2O ^{45,46} as well as carbon species^{47–49} can change the plasma conditions and hence affect the Se sensitivity and polyatomic interferences.

To tackle these problems, several combinations of gas sampling and calibration strategies were considered. The use of a liquid quench in combination with external, offline calibration minimizes effects of the gas matrix on the plasma, but also results in an increased analyte residence time as well as a convolution of the transient process signal with that of the sampling system⁵⁰. The gas dilution up to a point where gas matrix effects are negligible increases the detection limits and was therefore not considered. Gas sampling with online standard addition as calibration strategy can only be used when the time interval of calibration is comparably small to that of the variation in the gas matrix and analyte which might not be the case for the determination of breakthrough curves on a laboratory scale. The use of gas sampling in combination with an internal standard, is a potential option, only complicated by the availability of an appropriate internal, gaseous standard. A further option is the simplification of the gas matrix to avoid its modification due to (catalysed) gas phase reactions.

For this work, it has therefore been decided to perform experiments with direct gas injection to the ICP-MS and quantification of Se by matrix-matched external calibration. In this case, the gas matrix is represented only by H_2 , H_2O and Ar. H_2 simulates the reductive properties of the syngas⁵¹. H_2O can impede the reaction of H_2Se with ZnO as H_2O is competing with H_2Se for the same active sites. Concentrations of H_2 and H_2O at the reactor inlet were set to 40 vol% and 5 vol%, respectively, with the remaining fraction being Ar and H_2Se .

6.1.2. Matrix effects

Already small amounts of H_2 and H_2O are known to change the plasma conditions and thereby the analytical performance of an ICP-MS. An overview of their effects is provided in Tables E.1 and E.2.

The addition of H_2 to ICP-MS plasmas has been studied by several authors. Guillon and Heinrich⁴⁴ added small amounts of H_2 (0 to 14 ml min⁻¹) to the helium carrier gas flow of a LA-ICP-MS dry plasma. Under optimized ICP-MS operating parameters and H_2 flow rates, a general increase in sensitivity (for ⁷⁷Se by a factor 3) was observed. The limit of detection could generally be decreased, however, in case of ⁷⁷Se, a two-fold increase due to polyatomic interferences was observed. In the work of Ebdon et al.⁴³, the addition of 5 vol% H_2 to the nebulizer gas of a wet plasma caused a significant increase in polyatomic interferences based on Ar but decreased interferences from metal oxides. Louie and Soo⁴² found a slight increase in ⁷⁸Se signal when adding small amounts of H_2 (< 10 ml min⁻¹) to a wet plasma, to be followed by a continuous decline in signal when adding higher amounts of H_2 , resulting in a 50 % signal decrease when 50 ml min⁻¹ H_2 were added. Under optimum conditions (H_2 flow of 20 ml min⁻¹), the authors qualitatively reported a minor increase in the signal to background (S/B) ratio for most elements. Hutton et al.⁴¹ observed an increase of the ¹²⁷I signal by 70 % when adding 7.5 ml min⁻¹ H_2 to the central channel of a dry plasma. The increase was ascribed to an increased energy transfer between bulk plasma and the central channel due to the high thermal conductivity of H_2 . A noted side effect of H_2 addition was the increase in reflected power (30 W for 7.5 ml min⁻¹ H_2).

Liu et al.⁴⁵ investigated the effect of small additions of water vapour (5.1 Nml min⁻¹) to the central gas flow in LA-ICP-MS. For a shielded torch (as used in the current work), they

found an increase in sensitivity for most investigated elements (for ^{82}Se by a factor 2.5) and a change in plasma shape upon addition of H_2O . Alary and Salin⁴⁶ added small amounts of water (4.1 Nml min^{-1}) to the carrier gas flow between an ETV and an ICP-MS and observed a general enhancement of the signals of the measured elements (Zn, Pb, Cu, As, Sb).

6.2. Experimental section

6.2.1. Analytical method

Se calibration and sorption experiments were performed using an Agilent 7700x ICP-MS instrument. Gas sample introduction was achieved by means of an in-house constructed quartz adapter (see Fig. 6.1), directly connected to the plasma torch.

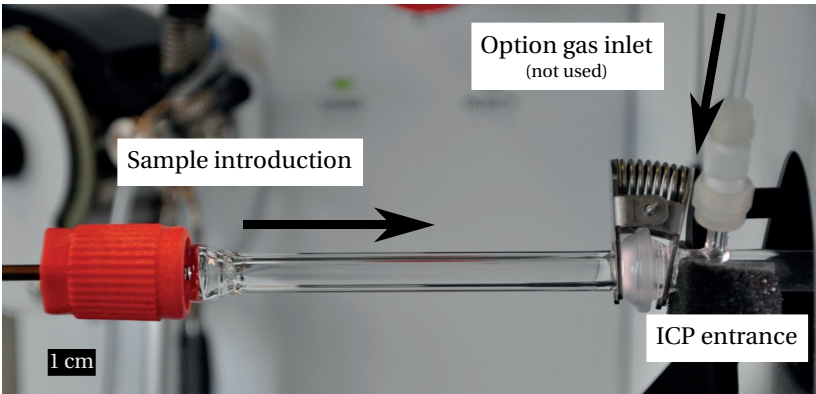


Figure 6.1 – Quartz adapter (similar to the connector tube of the used ICP instrument), directly connected to the plasma torch

All experiments were carried out in time resolved analysis (TRA) mode using peak hopping. Helium was used as collision gas in the octopole reaction system (ORS) to lower polyatomic interferences. At the beginning of the experimental series, different parameters were adjusted in tuning mode for the Se concentration range of interest and then being held constant. The He flow rate was modified in such a way that the signal to background ratio was maximized while the signal for the maximum concentration of Se was kept at about 10^7 counts per second (cps). The ICP-MS main operating conditions including gas flows are listed in Table 6.1.

Table 6.1 – ICP-MS operating conditions

| ICP operating conditions | | |
|--|--------------------------|---|
| RF power | (W) | 1350 |
| Reflected RF power | (W) | < 3 |
| Sample Depth | (mm) | 10 |
| Interface cones (skimmer & sampler) | | Ni |
| Plasma gas flow rate | (Nl min ⁻¹) | 15 |
| Carrier Gas | (Nml min ⁻¹) | 1100 |
| He flow | (Nml min ⁻¹) | 2 |
| Mass spectrometer acquisition settings | | |
| Detector | | pulse mode, analog mode |
| Scan mode | | time resolved, peak hopping |
| Settling + scan time | (ms) | 10 |
| Integration time per m/z | (s) | 0.2 |
| Recorded isotopes | | ¹³ C, ⁶⁶ Zn, ⁶⁸ Zn, ⁷⁶ Se, ⁷⁷ Se, ⁷⁸ Se, ⁸² Se |

6.2.2. Sorbent material

Experimental tests were performed with two materials, prepared in-house, consisting of Zn supported on γ -Al₂O₃ with different Zn loading. It is well-known that ZnO is reduced to elemental Zn in reductive gas at high temperatures (> 600 °C)^{52,53}. However, as experiments in our work are performed at medium temperatures, the term Zn/Al₂O₃ is used to encompass both the forms ZnO/Al₂O₃, ZnAl₂O₄ and possible mixtures thereof⁵⁴.

Preparation

The sorbent materials were prepared by wet impregnation method. γ -Al₂O₃ support (Puralox Nwa-155, Sasol Germany GmbH) was sieved (sieve 125 to 160 μ m) and subsequently degassed in Ar atmosphere at 300 °C for 3 h. The support impregnation was performed using an aqueous solution of Zn(NO₃)₂ (analytical grade, Sigma Aldrich, Switzerland) at room temperature for 3 h. The impregnated support was then dried at 80 °C, 25 mbar for 1 h and calcined in air flow at 500 °C for 7 h.

Characterization

The Zn content of the sorbents was analysed by digestion and subsequent ICP-MS (7700x, Agilent, USA) analysis. The skeletal density of the support was determined by an AccuPyc II 1340 pycnometer (Micromeritics, USA). The SSA (BET method) and pore size distribution (BJH method) of the samples were measured by nitrogen physisorption using an Autosorb-1 (Quantachrome Instruments, USA) after degassing at 200 °C for 2 h. Volume based particle size distributions of agglomerates were measured with a laser diffraction particle size analyser (LA-950V2, Horiba, Japan). The crystalline structure of the sorbents was determined by X-ray diffraction (XRD, D8, Bruker, USA) using Cu K α radiation (λ = 1.5419 Å). The diffraction patterns were recorded between 20 to 80° (2 θ) with an angular step interval of 0.0298° (step time: 9.5 s). The morphology and ZnO dispersion of the prepared sorbents were investigated by scanning electron microscopy (SEM, Ultra 55, Zeiss, Germany) after Cr sputtering.

6.2.3. Experimental procedures

Matrix effects

Even though a change of the gas composition in the current case is not expected during single experiments, as previously discussed, an understanding of their qualitative influence on the plasma is of interest. The investigation of these effects will reveal whether performing a 100 % matrix-matched calibration is necessary and at the same time evaluate the accuracy/reliability of the used setup and the calibration procedure.

In order to evaluate effects and possible interactions of the two factors H₂ and H₂O on the measurement of the ⁷⁸Se isotope, a two-level full factorial design (2²) was performed⁵⁵. The factors were varied within boundaries, representative for gasification processes, with H₂ concentrations ranging from 20 to 40 vol%(rx) and the steam content ranging from 0 to 5 vol%(rx). A geometric representation of the experimental design with the corresponding gas flows and ICP inlet concentrations is presented in Fig. 6.2.

Each factor combination, noted by numbers 1 to 4, in this plot consists of both a blank run and a run containing 250 ppbv(ICP) of H₂Se. For each run, replicates with more than 100 data points were acquired on isotope ⁷⁸Se after signal stabilisation. Based on the performed

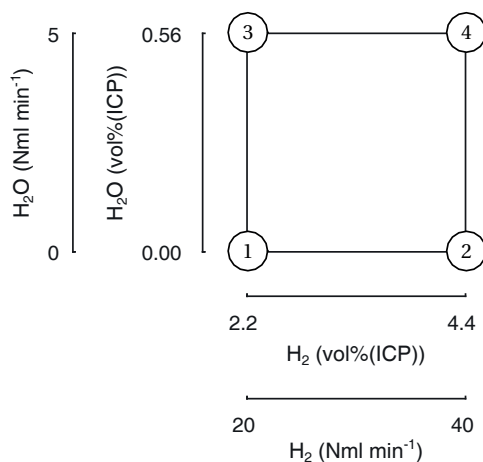


Figure 6.2 – 2^2 factorial design with the gas concentrations of H_2 and H_2O as factors. The run numbers are indicated in the corners.

experiments, the main effects a_{H_2} and a_{H_2O} of H_2 and steam were calculated according to

$$a_{H_2} = \frac{(\kappa_2 + \kappa_4) - (\kappa_1 + \kappa_3)}{2} \quad (6.3)$$

$$a_{H_2O} = \frac{(\kappa_3 + \kappa_4) - (\kappa_1 + \kappa_2)}{2} \quad (6.4)$$

The interaction E_{H_2, H_2O} of these two compounds is calculated according to

$$a_{H_2, H_2O} = \frac{(\kappa_1 + \kappa_4) - (\kappa_2 + \kappa_3)}{2} \quad (6.5)$$

In these equations the response κ can represent the blank signal or the sensitivity obtained from a 2-point calibration. For calculation of the variance, runs were not genuinely repeated but rather a pooled estimate of error averaged from the data points acquired in each run was calculated. The computed error therefore represents the analytical rather than the experimental run-to-run variance and is likely to be smaller than the latter.

Sorption experiments

Before sorption experiments, a three-point calibration (0, 1.2 ppmv(rx), 4.8 ppmv(rx) H_2Se) was performed with a gas matrix representing that of the following experiment (see Table 6.4 on Page 126 for an overview of experimental conditions). Afterwards, the empty reactor tube in the vertical cylindrical oven (MTF 12/25A, Carbolite Limited, UK) was replaced by a quartz reactor ($d_t = 2$ mm) containing the sorbent. The reactor bed consisted of ca. 20.5 mg of Zn/Al_2O_3 sorbent material, held in place by quartz wool. Then the reactor was heated up to reaction temperature and flushed for 30 min with the experimental gas matrix (H_2Se free). Before the sorption experiment, a further reference run was performed. The sorption experiment was started by feeding 4.77 ppmv(rx) H_2Se in the experimental gas matrix to the reactor and acquiring the selenium ICP-MS signal.

To accelerate breakthrough evaluation, increased H_2Se concentrations compared to those expected in flue gases were used¹⁶. After the experiment, the reactor content was emptied into vials at ambient conditions for later BET and XRD analysis.

Capacity calculation

The molar amount $n_{Se,cap}$ retained by the sorbent can be calculated according to

$$n_{Se,cap}(t_{Bt,\chi}) = \frac{\dot{V}_{tot,n}}{V_m} \int_0^{t_{Bt,\chi}} (y_{Se,in}(t) - y_{Se,out}(t)) dt \quad (6.6)$$

In this equation, $\dot{V}_{tot,n}$ represents the volume flow entering the reactor and V_m the molar volume. The gas concentrations of selenium at the reactor inlet and outlet are defined as $y_{Se,in}$ and $y_{Se,out}$, respectively. The concentration $y_{Se,out}(t)$ represents the actual breakthrough curve of the sorbent. The concentration $y_{Se,in}$, on the other hand, was the average of the measured concentration using the empty reactor during 15 min prior to each sorbent experiment. The breakthrough time $t_{Bt,\chi}$ is defined as the point in time when the outlet concentration $y_{Se,out}$ exceeds a given concentration χ (in this work $\chi = 500$ ppbv(rx), representing 90 % Se removal). The capacity of the sorbent on a mass basis $q_{Se}(t_{Bt,\chi})$ can be calculated using

$$q_{Se}(t_{Bt,\chi}) = \frac{n_{Se,cap}(t_{Bt,\chi})M_{Se}}{m_{bed}} \quad (6.7)$$

where M_{Se} refers to the molecular weight of Se and m_{bed} to the mass of the dry sorbent bed before the experiment. Under the assumption that all captured H_2Se reacts to form ZnSe according to Eq. (6.15), we can define the conversion X_{ZnO} of the active compound (ZnO) of the sorbent according to

$$X_{ZnO}(t_{Bt,\chi}) = 1 - \frac{n_{ZnO}(t_{Bt,\chi})}{n_{ZnO}(0)} = \frac{n_{Se,cap}(t_{Bt,\chi})}{n_{ZnO}(t_{Bt,\chi})} \quad (6.8)$$

Herein $n_{ZnO}(0)$ refers to the amount of ZnO in the sorbent bed at the start of the experiment, calculated from m_{bed} , assuming the bed is formed of ZnO/ Al_2O_3 . Assuming ideal sorption behaviour (i.e. a step response in concentration at the reactor outlet), the stoichiometric breakthrough time $t_{Bt,St}$ can be defined as the time required to feed a molar amount of H_2Se that is similar to that of the active compound Zn in the sorbent bed

$$t_{Bt,St} = \frac{n_{ZnO}(0)}{F_{H_2Se,in}} \quad (6.9)$$

6.3. Results and discussion

6.3.1. Analytical performance

Calibration

For calibration, five equally spaced H₂Se concentrations in the range 0 to 4.77 ppmv(rx) were measured in an empty quartz reactor at 250 °C. The gas matrix consisted of 40 vol%(rx) H₂, 5 vol%(rx) H₂O and the remainder being Ar. At each concentration level, 190 data points were recorded. For blank samples, the relative standard deviation (RSD) was below 20 %, while at higher concentrations, RSD values dropped below 1.2 %, indicating a good repeatability.

Table 6.2 – Calibration results

| | ⁷⁶ Se | ⁷⁷ Se | ⁷⁸ Se | ⁸² Se |
|-----------------------------|--|--|--|--|
| R ² | 0.9992 | 0.999 | 0.999 | 0.9992 |
| LOD (ppbv(ICP)) | 0.12 | 0.1 | 0.07 | 0.09 |
| LOD (ppbv(rx)) | 1.36 | 1.15 | 0.74 | 1.03 |
| Abundance (mol/mol %) | 9.37 | 7.63 | 23.77 | 8.73 |
| Interferences ⁵⁶ | ⁴⁰ Ar ³⁶ Ar ⁺ , ³⁸ Ar ³⁸ Ar ⁺ | ³⁶ Ar ⁴⁰ Ar ¹ H ⁺ , ³⁸ Ar ² 1H ⁺ | ⁴⁰ Ar ³⁸ Ar ⁺ | ⁴⁰ Ar ² 1H ₂ ⁺ |

Calibration results are documented in Table 6.2 and an exemplary calibration curve for isotope ⁷⁸Se is given in Fig. 6.3a. The coefficient of determination (R²) for all calibrations is greater than 0.9990, indicating a good linear response. The detection limits (*y*_{LOD}) were calculated on basis of

$$y_{LOD} = \frac{3\sigma_{blk}}{s_{cal}} \quad (6.10)$$

where σ_{blk} is the standard deviation of the blank measurement, assuming a normal distribution, and s_{cal} is the slope of the calibration curve (i.e. the sensitivity).

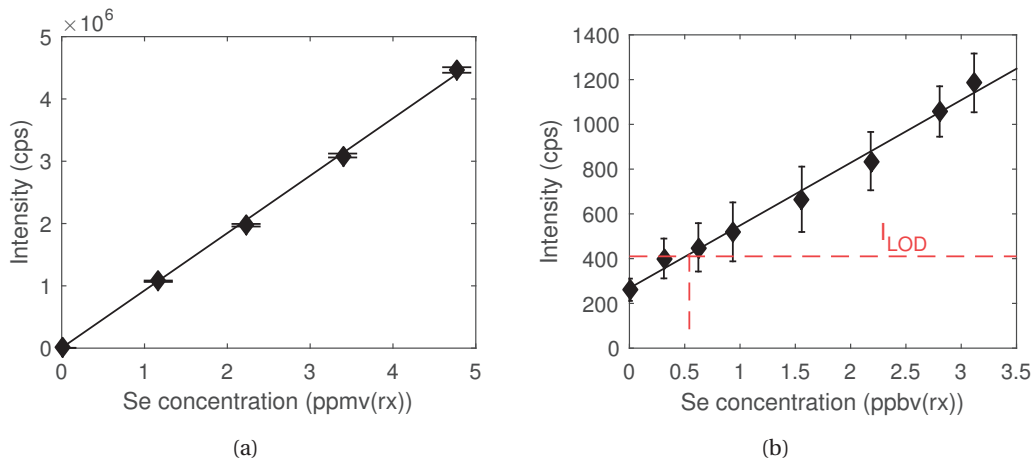


Figure 6.3 – (a) Calibration curve for isotope ⁷⁸Se, performed with experimental setup 1; (b) calibration curve for isotope ⁷⁸Se, performed with experimental setup 2.

The calculated detection limits in the reactor lie between 0.74 to 1.36 ppbv(rx), depending on the Se isotope. These values lie below concentration limits of about 50 ppbv, depending on coal and power plant type, that can be derived from proposed EPA regulations (see Appendix E.1 for calculation)⁵. At the same time they are comparable to detection limits of offline methods (0.34 ppbv for ISO/DIS 17211 with ICP-MS¹⁹).

The variation of the LOD between Se isotopes correlates with their natural abundance, indicated by lower LOD values for isotopes with higher abundance. The observed differences in backgrounds from isotope ratios can be attributed to spectroscopic interferences and different transmission of ions through the ICP-MS^{57,58}. Kr, present in the Ar plasma can cause isobaric interferences on ⁸²Se and ⁷⁸Se. However, the ionization energy is high (14 eV), resulting in an ionization efficiency smaller than 5 %⁵⁹. For this reason and the fact that the absolute gas concentration of Kr in Ar (< 24 ppbv) as well as the abundance of the isotopes (⁷⁸Kr 0.35 %, ⁸²Kr 11.59 %) of interest are small, this might be considered a minor interference. The sorbent material (ZnO) used in this work can also cause isobaric interferences on ⁸²Se if particles reach the plasma. Even though polyatomic interferences were minimized by adjusting the flow of He to the collision cell to maximize the signal/blank ratio, background levels were still not completely suppressed. An overview of formed polyatomic interferences is given in Table 6.2. In the observed system, Ar dimers interfere with all recorded Se isotopes, while the formation of Ar hydrides interferes only with Se isotopes ⁷⁷Se and ⁸²Se⁵⁷.

Based on the lower LOD and comparable R², isotope ⁷⁸Se was chosen for Se quantification. The calculated detection limits lie three orders of magnitude below the range of the calibration curve. In order to verify these results, further investigations with experimental setup 2 were performed. In this experiment, the gas mixture, containing H₂Se and Ar, was fed to a RDD and the exiting diluted gas flow was mixed with a stream composed of H₂, H₂O and Ar and then fed to the ICP-MS. This made it possible to achieve H₂Se concentrations ranging from 0 to 3.2 ppbv(rx) in a gas matrix identical to that found in setup 1. Based on these data points, shown in Fig. 6.3b, a calibration curve can be calculated, which serves as a basis for the definition of another LOD concentration. The obtained concentration of 0.54 ppbv(rx) is close to the one based on data in Fig. 6.3a, indicating that the calculated LOD concentrations provided in Table 6.2 are valid. Fig. 6.4a shows the measured intensities of the ⁷⁸Se isotope for the blank experiment and a feed of 0.6 ppbv(rx) H₂Se as well as the corresponding averages of these experiments marked by dashed lines.

In this plot the dashed line, representing the intensity I_{LOD} of the detection limit is, calculated according to

$$I_{LOD} = 3s_{blk} + I_{blk} \quad (6.11)$$

where I_{blk} refers to the measured background intensity of ⁷⁸Se. The intensity for an H₂Se inlet concentration of 0.6 ppbv(rx) lies clearly above the LOD intensity. It has to be noted, however, that signals recorded at these low (i.e. slow disk rotation speed) Se concentrations show periodicities while the blank signal, when the RDD is stopped, can be described as white noise (see Appendix E.3 for detailed explanation).

Dynamic effects

The response time characteristics of an analytical technique are of importance when transient processes (e.g. sorption of trace elements in an IGCC process) are to be monitored. The response of the experimental setup with an empty reactor to a step increase in H₂Se concentration from 0 to 2750 ppbv(rx), added at time 0 min, is shown in Fig. 6.5.

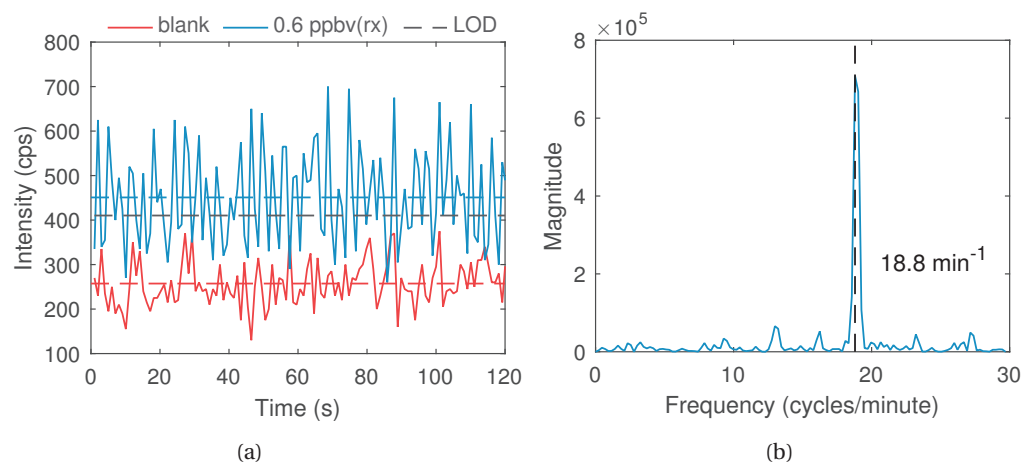


Figure 6.4 – (a) Measured intensities (setup 2) for blank measurement and a H_2Se concentration of 0.6 ppbv(rx); (b) periodogram of recorded intensities for a H_2Se concentration of 0.6 ppbv(rx).

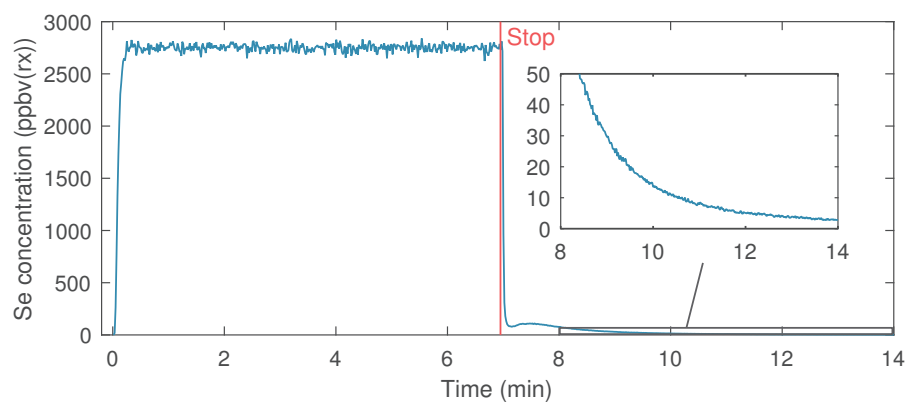


Figure 6.5 – Step response and washout behaviour of system. The inset shows amplified concentration *versus* time data for the time-frame 8 min to 14 min.

A rise of the signal is observed after 2 s, with 98 % of the stable signal being reached after 13 s. The calculated theoretical residence time, assuming plug flow behaviour, is 1.5 s and thereby close to the time resolving capabilities of the ICP-MS. Based on this observation, one can conclude that non-idealities in the flow pattern in form of stagnant regions and fluid recycling as well as the adsorption of H_2Se to the tubing can be neglected.

In order to evaluate the washout behaviour, the H_2Se feed was stopped after 7 min. The resulting curve can be divided into two sections. The first section features a strong signal decrease after 3 s by about 96 %. The following section is marked by significant tailing. The latter results in a limited temporal resolution when measuring online transient processes. While the observed tailing does not impede the measurement of breakthrough curves, it can increase the time interval between sorption experiments when low LODs are of importance. Based on the increased background levels, the detectable LOD increases as well. In case of this experiment, for example, this leads to an increased LOD of 6.5 ppbv(rx) compared to 0.74 ppbv(rx) (on isotope ^{78}Se), 5 min after H_2Se was stopped, based on the recorded background level. The main reason for the observed tailing is the tubing (length 1 cm) between the three way valve and the H_2O addition which is not flushed when the addition of H_2Se is stopped. This causes a constant diffusion flux of H_2Se (and H_2) from this stagnant region into the gas flow towards the reactor. Adsorption effects of H_2Se onto the tubing could be another source for the observed behaviour but were minimized by appropriate choice of materials, gas dilution and uniform heating of the tubing.

6

Matrix effects

Already small amounts of H_2 and H_2O are known to change the plasma conditions and thereby the analytical performance of an ICP-MS as discussed in Section 6.1.2. The calculated absolute values of the effects on the sensitivity and blank signal are plotted as Pareto charts of effects in Figs. 6.6a and 6.6b, respectively, in order to find the most influential factors.

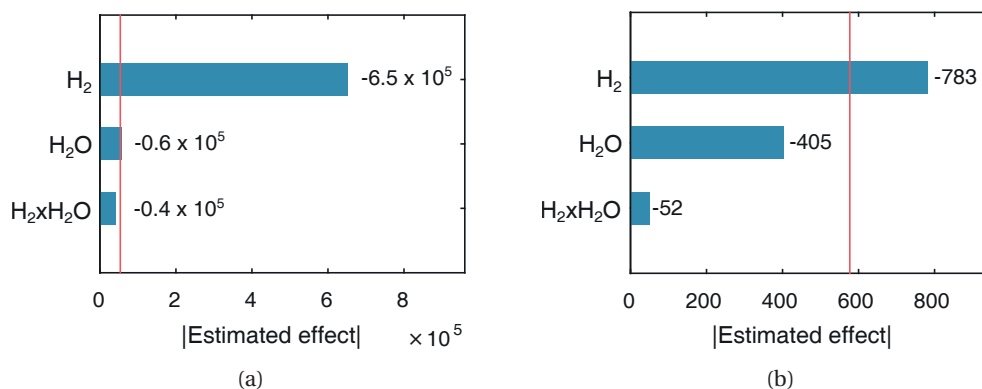


Figure 6.6 – Calculated absolute values of the effects on the: (a) Sensitivity; (b) blank signal. The inscribed numerical values give an indication of the direction of the effect (+/-).

The red lines in these plot represent the 95 % confidence interval, giving an estimate of the significance of the individual effects. In Fig. 6.6a, all bars show a negative effect on the sensitivity. However, only the main effect a_{H_2} caused by a change in H_2 concentration, is significant in the varied range, showing a decrease of 32 % in sensitivity compared to the constant effect. Increase of the H_2 concentration also resulted in a significant increase of reflected power up to 60 W but no plasma instabilities were observed. An optimization of the

matching network was not performed. The effect of the factors on the blank signal is shown in Fig. 6.6b. Again, only the change in H_2 concentration has a significant, negative, effect on the signal, decreasing it by 17 %, compared to the constant effect. The effect of water or the interaction thereof are negligible.

While in literature, the use of mixed-gas plasmas tends to improve figures of merit concerning Se analysis, this work cannot confirm these observations. Two aspects might contribute to these findings. Previous studies investigated mixed-gas plasmas with the intention of improving figures of merit. This typically involved optimization of the plasma parameters that can deviate significantly from all-Ar plasmas. However, measuring a transient process, where the gas composition is subject to change, does not allow for continuous parameter optimization and calibration. Performing no optimization, therefore can, as observed in the current study, lead to adverse effects concerning the analysis of Se. Another difference lies in the introduced sample. Studies typically feature aerosol introduction where the evaporation of droplets and the decomposition of particles plays a central role. In this case however, the introduced sample is a gas.

Keeping in mind that the curvature of the response might not be linear, the obtained results imply that changes in steam content between 0 to 0.56 vol% do not affect the quantification of selenium on ^{78}Se . The effect of H_2 content on the other hand is significant, resulting in increased detection limits. Variation of H_2 concentration in such ranges should therefore be followed by a new calibration. Sorption experiments, performed in this work, were not affected by this issue as the H_2 content was kept constant.

6.3.2. $H_2\text{Se}$ capture by $\text{Zn}/\text{Al}_2\text{O}_3$

When breakthrough curves are investigated, some criteria concerning hydrodynamics and mass transfer in the fixed bed should be verified to ensure validity of the obtained results. External mass transfer effects were minimized by ensuring gas hourly space velocities (GHSV) above 200000 h^{-1} . Experiments were performed at total pressure p with calculated pressure drops Δp across the sorption bed of approximately 0.1 bar, resulting in relative pressure drops concurrent with Eq. (6.12)⁶⁰.

$$\frac{\Delta p}{p} < 0.2 \quad (6.12)$$

The assumption of plug flow in the reactor can be made by meeting the criterion for axial ($Bo \approx 95$) dispersion shown in Eq. (6.13)⁶¹.

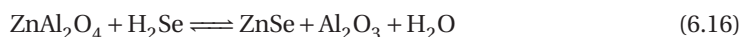
$$Bo = \frac{Lu_s}{D_{ax}} > 100 \quad (6.13)$$

In this equation, L refers to the bed height, u_s the superficial velocity in the empty reactor and D_{ax} to the axial dispersion coefficient (see Appendix E.4 for detailed explanation). The ratio between reactor diameter d_t and particle diameters d_p is chosen sufficiently high ($d_t/d_p = 12$) to neglect wall effects (Eq. (6.14))⁶².

$$\frac{d_t}{d_p} > 8 \quad (6.14)$$

Thermodynamic equilibrium considerations can give an indication on the sorbent bed exit gas concentrations of $H_2\text{Se}$ as a function of Zn phase, steam content as well as temperature. Two

reactions that might describe the decrease in H_2Se gas concentration are given in Eqs. (6.15) and (6.16).



Assuming a batch reactor with an excessive amount of solid material, the equilibrium constants of these reactions can be expressed as a ratio of the activities of the gas phase species H_2Se and H_2O . Calculations were performed with the software package HSC Chemistry 7.193 (Outotec, Finland) using a Gibbs free energy minimization approach. In the calculations, different crystallographic structures of the same species were neglected. Also the previously proposed introduction of surface sites into the equilibrium constant was not included⁶³. Both simplifications and the fact that a steady-state rather than a transient process was assumed, can result in deviations of these calculations from reality^{64,65}.

The calculations show that both reactions are thermodynamically favourable over the examined temperature range between 100 to 500 °C ($\Delta G_r < -55 \text{ kJ mol}^{-1}$). Based on the equilibrium constants (see Fig. E.2), an H_2Se equilibrium concentration in dependence of temperature and steam content can be calculated. The resulting H_2Se equilibrium concentrations for both the reaction of ZnO (upper plot) and ZnAl_2O_4 (lower plot) with H_2Se are plotted in Fig. 6.7.

6

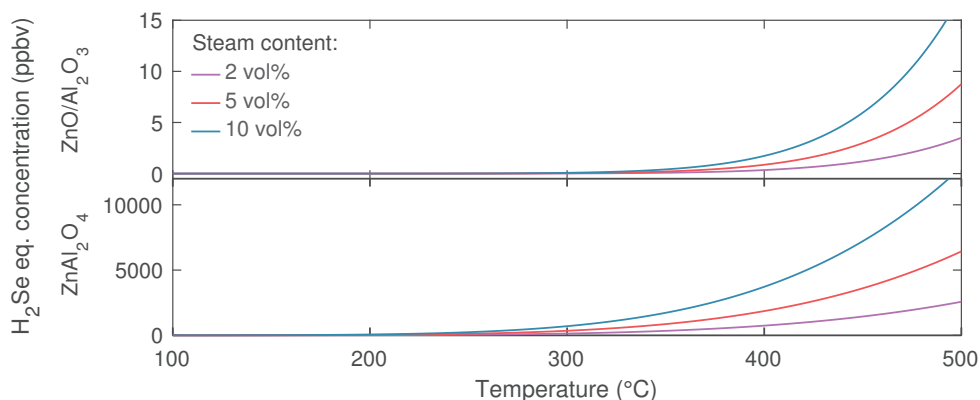


Figure 6.7 – Calculated H_2Se equilibrium concentration versus temperature for three steam contents of 2 vol%, 5 vol% and 10 vol%; for the system $\text{ZnO} + \text{H}_2\text{Se} \rightleftharpoons \text{ZnSe} + \text{H}_2\text{O}$ (upper plot) and for the system $\text{ZnAl}_2\text{O}_4 + \text{H}_2\text{Se} \rightleftharpoons \text{ZnSe} + \text{Al}_2\text{O}_3 + \text{H}_2\text{O}$ (lower plot).

Both solid phases react with H_2Se in the studied range of process parameters, showing increasing equilibrium concentrations as the temperature increases. An increase in steam content also increases the H_2Se concentration for both reactions as the equilibrium is shifted towards the left hand side. The sulfidation reaction is possible for both phases in the observed temperature range. However, it is more favourable for ZnO than for ZnAl_2O_4 . For a gas with a steam content of 10 vol% at 250 °C, this results in an achievable H_2Se concentration of 10 pptv (parts per trillion by volume), for ZnO compared to 242 ppbv for ZnAl_2O_4 . Based on these calculations, it appears that ZnO is better suited than ZnAl_2O_4 for a significant reduction in H_2Se concentration in a wet gas at medium temperatures.

Sorbent characterization

An overview of the prepared sorbents and their properties is given in Table 6.3.

Table 6.3 – Sorbent properties ¹

| Description | Mean Size (mm) | wt% Zn ($\text{g}_{\text{Zn}} \text{g}_{\text{Sorbent}}^{-1}$) | SSA ($\text{m}^2 \text{g}_{\text{Sorbent}}^{-1}$) |
|--|----------------|--|---|
| $\gamma\text{-Al}_2\text{O}_3$ (Sasol) | 163 ± 2 | n.d. | 141 ± 2 |
| 0.89 wt% Zn/ Al_2O_3 | 169 ± 1 | 0.89 ± 0.01 | 134 ± 2 |
| 0.89 wt% Zn/ Al_2O_3 (after experiment) | n.d. | n.d. | 136 ± 2 |
| 8.21 wt% Zn/ Al_2O_3 | 171 ± 2 | 8.21 ± 0.17 | 122 ± 2 |

The support and the Zn/ Al_2O_3 sorbents have mean secondary particle (agglomerate of primary particles) sizes ranging from 163 to 171 μm , which is in agreement with the SEM micrographs (see Fig. E.3). Adsorption isotherms of the investigated sorbents are of Type IV, indicating a mesoporous material with hysteresis loops of Type H1 (see Fig. E.4a)⁶⁶. The measured SSA ranges from 122 to 141 $\text{m}^2 \text{g}_{\text{Sorbent}}^{-1}$, with decreasing SSA as the Zn loading increases. Assuming equi-axed primary particles, their volume-surface mean diameter \bar{d}_{SSA} can be calculated from the SSA measurement A_{SSA} according to

$$\bar{d}_{\text{SSA}} = \frac{6}{\rho_s A_{\text{SSA}}} \quad (6.17)$$

where ρ_s represents the measured skeletal density (3.287 g cm^{-3}) of the support⁶⁶. From this follows a \bar{d}_{SSA} of 13 nm. The average pore size diameter (see Fig. E.4b) is about 8.8 nm, which is compatible with open pores among primary particles of 13 nm.

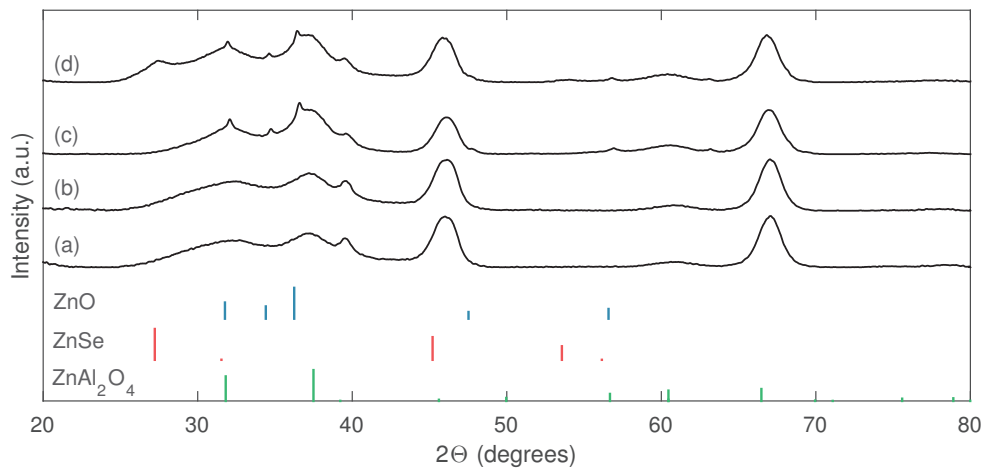


Figure 6.8 – XRD patterns of (a) $\gamma\text{-Al}_2\text{O}_3$ support, (b) 0.89 wt% Zn/ Al_2O_3 , (c) 8.21 wt% Zn/ Al_2O_3 , (d) 8.21 wt% Zn/ Al_2O_3 sorbent after H_2Se contact. The vertical lines represent the position and intensity of ZnO, ZnSe and ZnAl_2O_4 reflections.

After calcining, Zn^{2+} ions can end up in two different forms on the $\gamma\text{-Al}_2\text{O}_3$ support. They might form a bulk-like phase of ZnO or an aluminate phase^{54,67}. The XRD patterns of the

¹n.d.: not determined

fresh $\gamma\text{-Al}_2\text{O}_3$ support and $\text{Zn}/\text{Al}_2\text{O}_3$ with two different Zn loadings are shown in Fig. 6.8. The $\gamma\text{-Al}_2\text{O}_3$ support shows broad, diffuse diffraction lines, indicating poor crystallinity. The sorbent with 0.89 wt% Zn loading shows no significant difference from the support, which can be attributed to the high dispersion of ZnO on the support, to the poor crystallinity of the Zn phase and to instrumental detection limits. For an increased Zn loading of 8.21 wt%, further peaks in the XRD spectrum appear. The increase in intensity at lines specific for ZnO (ICSD 34477) indicates the build up of a ZnO phase. Because diffraction lines of the ZnAl_2O_4 phase (ICSD 94166) overlap with major ones of the support and ZnO, the formation of a ZnAl_2O_4 phase cannot be excluded. The change in diffraction pattern for a 8.21 wt% $\text{Zn}/\text{Al}_2\text{O}_3$ sorbent where breakthrough of H_2Se was observed, is depicted in spectrum (d) of Fig. 6.8. The appearance of a diffraction peak at 27.3° (2θ) indicates the formation of a ZnSe phase (ICSD 77091) which is concurrent with previous experiments performed at room temperature⁶⁸. The decrease in integrated peak area of ZnO is comparably small to the area increase of the peak attributed to a ZnSe phase. This suggests that also an amorphous ZnO or a ZnAl_2O_4 phase exist on the pristine sorbent.

Effect of steam content

The investigation of the effect of steam content on the sorption process is of importance because of its presence in most gasification processes. A list of experimental parameters and results of all performed sorption experiments is provided in Table 6.4.

6

Table 6.4 – Overview of experimental conditions of sorption experiments and resulting measures of sorbent performance

| wt% Zn ($\text{g}_{\text{Zn}} \text{g}_{\text{Sorbent}}^{-1}$) | H_2O (vol%(rx)) | T_{reactor} ($^\circ\text{C}$) | $t_{\text{Bt},500}$ (min) | $t_{\text{Bt},\text{St}}$ (min) | $q_{\text{Se}}(t_{\text{Bt},500})$ ($\text{mg}_{\text{Se}} \text{g}_{\text{Sorbent}}^{-1}$) | $\xi_{\text{ZnO}}(t_{\text{Bt},500})$ (-) |
|---|------------------------------------|--|------------------------------|------------------------------------|--|--|
| 0.89 | 2 | 250 | 8.5 | 130 | 0.673 | 0.063 |
| 0.89 | 5 | 250 | 8.3 | 130 | 0.673 | 0.063 |
| 0.89 | 10 | 250 | 6.3 | 130 | 0.494 | 0.046 |
| 0.89 | 5 | 150 | 14.2 | 130 | 1.132 | 0.105 |
| 0.89 | 5 | 350 | 7.1 | 130 | 0.559 | 0.052 |
| 8.21 | 5 | 250 | 85.6 | 1451 | 5.745 | 0.058 |

Both H_2Se and H_2O are species known to adsorb onto the surface of $\gamma\text{-Al}_2\text{O}_3$ ^{36–38}. In order to evaluate their interaction under the chosen reaction conditions (250°C ; reactor inlet: 40 vol%(rx) H_2 , 4770 ppbv(rx) H_2Se , balance Ar), blank experiments involving only the Al_2O_3 support were performed. These experiments show the formation of a Se phase in dry gas atmosphere as revealed by post-experimental analysis of the sorbent by ICP-MS (7700x, Agilent; about $1.3 \text{ mg}_{\text{Se}} \text{g}_{\text{Sorbent}}^{-1}$, measured from solution of the digested support). This finding is concurrent with earlier studies performed at lower temperatures³⁶. However, as steam (5 vol%(rx)) was added to the gas mixture, no Se (below detection limit of $2 \mu\text{g}_{\text{Se}} \text{g}_{\text{Sorbent}}^{-1}$, measured by ICP-MS from solution of the digested support) on the Al_2O_3 support could be detected. These findings indicate that steam has a major, negative effect on sorbent capacity of Al_2O_3 . An estimation of the chemisorbed H_2O , based on literature data³⁸, show that stoichiometric breakthrough times of H_2O in our work can be expected to be in the range of seconds. It is here proposed that H_2O and H_2Se adsorb onto similar sites of the Al_2O_3 , while H_2O appears to adsorb stronger. That implies that the Al_2O_3 first dries the gas passing through the bed, allowing downstream adsorption of H_2Se . As the H_2O front progresses through the

bed, H_2Se is replaced by H_2O . At these reaction conditions, the sorption of H_2Se onto the support might therefore play a minor role. The result of a sorption experiment that involves 0.89 wt% $\text{Zn}/\text{Al}_2\text{O}_3$ in a gas atmosphere without steam is shown in Fig. 6.9a.

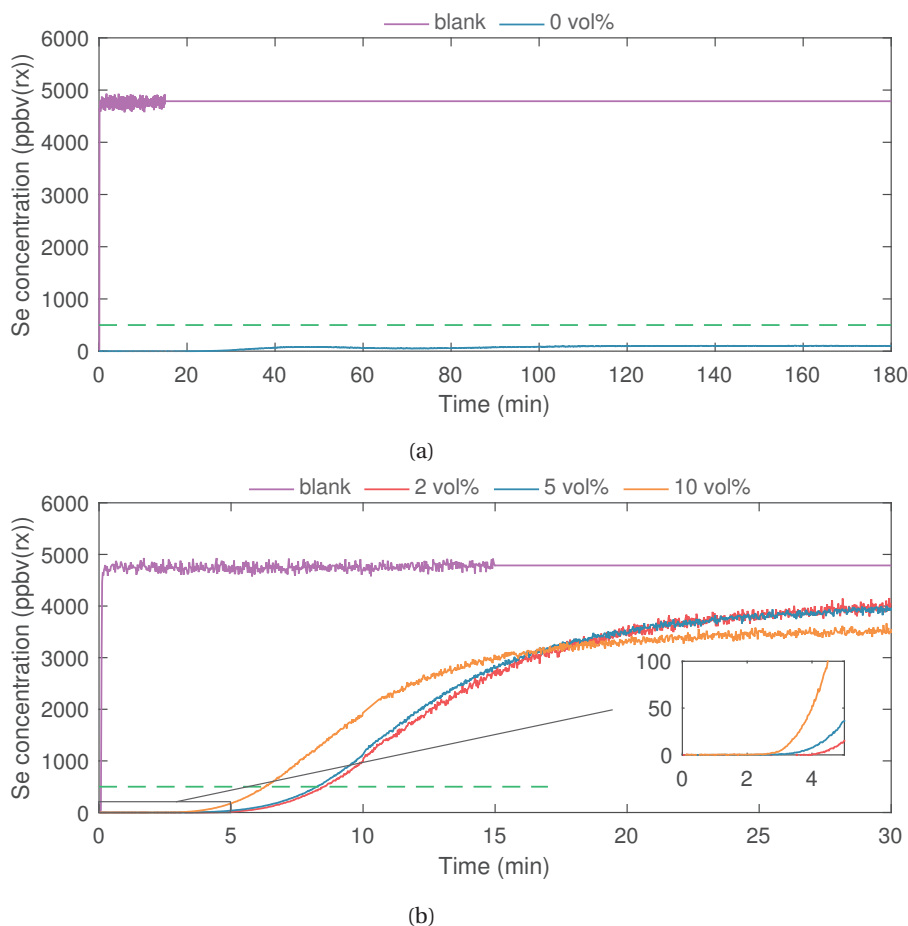


Figure 6.9 – (a) Breakthrough curve for steam content of 0 vol% (0.89 wt% $\text{Zn}/\text{Al}_2\text{O}_3$, 250 °C; reactor inlet: 40 vol%(rx) H_2 , 4770 ppbv(rx) H_2Se , balance Ar); (b) breakthrough curves for three different steam contents of 2, 5 and 10 vol%(rx) (0.89 wt% $\text{Zn}/\text{Al}_2\text{O}_3$, 250 °C; reactor inlet: 40 vol%(rx) H_2 , 4770 ppbv(rx) H_2Se , balance Ar). The inset depicts the outlet concentration for the timeframe 0 to 5 min. The dashed green line marks the breakthrough concentration ($\chi = 500$ ppbv(rx)).

The depicted curve has a characteristic that can be divided into two sections. In the first 20 min, the outlet concentration of the reactor is close to the detection limit of the analytical system. Based on the inlet concentration of 4770 ppbv(rx) this translates into a H_2Se removal efficiency of at least 99.98 %. Then an increase in H_2Se outlet concentration to approximately 100 ppbv(rx) is observed. This concentration remains constant until the end of the experiment, for which, in the given time-frame, no breakthrough was observed. The fact that the stoichiometric breakthrough time of 130 min is surpassed, indicates that next to the sorption of H_2Se by the Zn phases, also a significant contribution by the support has to be considered under dry conditions.

Because the raw gas of IGCC processes contains steam to significant amounts, in the following the focus of this work will lie on experiments containing steam. Breakthrough curves for three different steam contents of 2, 5 and 10 vol%(rx) in a reducing gas atmosphere (40 vol%(rx) H_2) with a 0.89 wt% $\text{Zn}/\text{Al}_2\text{O}_3$ sorbent at a temperature of 250 °C are given in Fig. 6.9b. All observed breakthrough curves, involving steam in the gas phase, have a similar characteristic which can be divided into three sections. In the first few minutes before breakthrough, similar to experiments without steam content, the outlet concentration of the reactor is close to the detection limit of the analytical system. A difference in H_2Se outlet concentration for the varying steam contents cannot be detected at this stage, which is concurrent with thermodynamic calculations that indicate equilibrium concentrations below 10 pptv (assuming a ZnO phase), thus being below the detection capabilities of the employed analytical method. In the following, second section, at breakthrough, the H_2Se outlet concentration increases strongly to about 70 % of the inlet concentration. This is followed by a much slower, asymptotic increase in outlet concentration in the third section. In this figure, breakthrough curves for steam contents of 2 and 5 vol%(rx) are virtually identical, considering the measurement error. The breakthrough curve for 10 vol%(rx) steam content, on the other hand, has a shorter breakthrough time (approximately 6 *versus* 8 min) and shows a slower increase in outlet concentration in the third section. The observed Zn conversion of about 5 to 6 % as well as the actual breakthrough time compared to the stoichiometric one (where the ratio $t_{\text{Bt},500}/t_{\text{Bt},\text{St}}$ can equal $\xi_{\text{ZnO}}(t_{\text{Bt},500})$ only if a step increase in H_2Se outlet concentration is assumed) are low which is concurrent with previous work on the sorption of H_2Se by supported Zn (Zn_2TiO_4)³³. The influence of steam on the sorption capacity of H_2Se is strongest in the dilute region as indicated by experiments with 2 vol%(rx) and no steam content. The difference in shape for experiments with increasing steam content can be explained by the less favourable equilibrium H_2Se to ZnSe and/or competitive adsorption of H_2Se and H_2O on Zn. Due to the fact that both equilibrium constants for ZnO as well as ZnAl_2O_4 are much larger than unity, no inferences from the observed responses to a change in steam content on the actually present Zn phase can be drawn.

The shape of the breakthrough curves with an initial strong increase in H_2Se outlet concentration, followed by a much slower increase, can be interpreted in different ways. While H_2Se interactions with the support might still play a role, this is assumed to be minor at this temperature and steam content. Therefore, two interpretations are possible. Firstly, the reaction of H_2Se with only one kind of exchange site on the active phase. This reaction proceeds fast initially and slows down considerably afterwards. This interpretation could be explained by an initial fast reaction of H_2Se with the surface ZnO. Assuming similarity to the sulfidation of ZnO, this could be followed by a slower solid state diffusion process where Zn^{2+} and O^{2-} ions diffuse through the ZnSe layer to the ZnSe/gas interface where they react to form ZnSe and H_2O ^{69,70}. The second interpretation is the parallel reaction of H_2Se with two different exchange sites that proceed at different rates. This could be explained by the presence of a ZnO as well as ZnAl_2O_4 phase on the support. Previous work shows that the reaction of H_2S with ZnO proceeds much faster than that with ZnAl_2O_4 ⁵⁴. Again, assuming that sulfidation studies can act as an indication, the initial, steep increase in the observed breakthrough curve would mainly be caused by the rapid reaction of H_2Se with ZnO while the subsequent flatter section would be mainly represented by the slow reaction of H_2Se with ZnAl_2O_4 .

Effect of temperature

Breakthrough curves for three different temperatures 150, 250 and 350 °C with a 0.89 wt% Zn/Al₂O₃ sorbent a steam content of 5 and 40 vol%(rx) H₂ are given in Fig. 6.10.

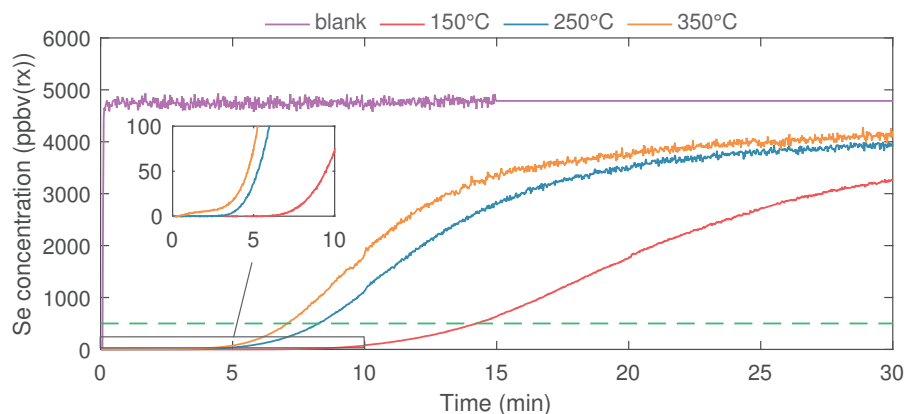


Figure 6.10 – Breakthrough curves for three different reactor temperatures of 150, 250 and 350 °C (0.89 wt% Zn/Al₂O₃; reactor inlet: 40 vol%(rx) H₂, 5 vol%(rx) H₂O, 4770 ppbv(rx) H₂Se, balance Ar). The inset depicts the outlet concentration for the time frame 0 to 10 min. The dashed green line marks the breakthrough concentration ($\chi = 500$ ppbv(rx)).

While at 150 and 250 °C initially very low H₂Se outlet concentrations close to the detection limit are observed, at 350 °C, an almost immediate increase in concentration is observed. Decreasing the reaction temperature from 350 to 150 °C doubles the sorbent capacity from 0.56 to 1.13 mg_{Se} g_{Sorbent}⁻¹ while the effect between 350 and 250 °C is much less pronounced. The breakthrough curve at 150 °C shows a much slower increase in the second section than seen at higher temperatures. Assuming a reaction of H₂Se with Zn, expected effects can be based on thermodynamic equilibrium as well as kinetic considerations. For both ZnO and ZnAl₂O₄, the equilibrium constants decrease when moving from 150 to 350 °C (ZnO: $10^{12} \rightarrow 10^8$; ZnAl₂O₄ $10^7 \rightarrow 10^5$), making the reaction to form ZnSe less favourable. However, the equilibrium remains on the right side of the reactions. On the other hand, with increasing temperature, both reaction rates and the mass transfer of H₂Se to the active sites on the sorbent increase, suggesting an increase in Zn conversion. However, the contrary is observed. This indicates that at decreased temperatures, physisorption of H₂Se and the equilibrium of the underlying reactions have to be considered as well.

Effect of Zn loading

The loading of the active phase is one of the key factors that influence the breakthrough behaviour of the sorbent. The effects of the Zn loading on the breakthrough curves are depicted in Fig. 6.11. In these experiments, two Zn/Al₂O₃ sorbents with 0.89 and 8.21 wt% Zn content were evaluated at 250 °C in a gas atmosphere containing 40 vol%(rx) H₂, 5 vol%(rx) H₂O and the balance Ar. Both sorbents show low H₂Se outlet concentrations in the first section of the breakthrough curve. Based on thermodynamic considerations, outlet concentrations of 121 ppbv and 5 pptv are expected in case of pure ZnAl₂O₄ and ZnO phases, respectively. This suggests that already at a low Zn loading of 0.89 wt%, a ZnO phase exists while no statement on the existence of a ZnAl₂O₄ phase can be made. An increase in Zn loading results in an increased breakthrough time as well as capacity.

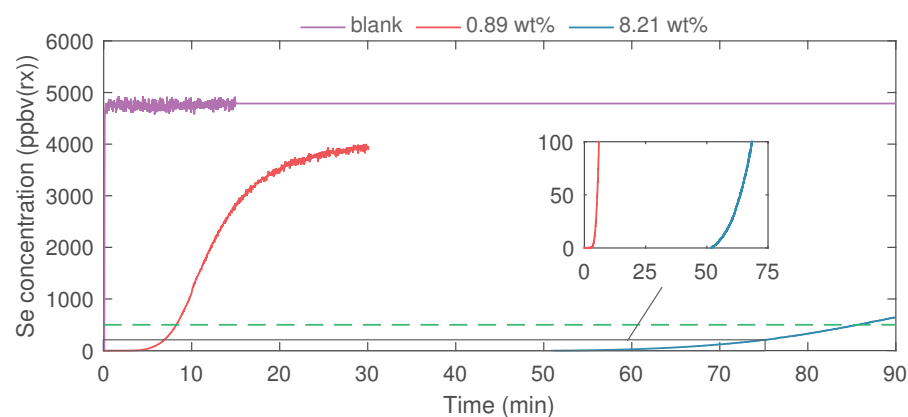


Figure 6.11 – Breakthrough curves for two Zn/Al₂O₃ sorbents with different Zn loadings of 0.89 wt% and 8.21 wt% (250 °C; reactor inlet: 40 vol%(rx) H₂, 5 vol%(rx) H₂O, 4770 ppbv(rx) H₂Se, balance Ar). The inset depicts the outlet concentration for the time-frame 0 to 75 min. The dashed green line marks the breakthrough concentration ($\chi = 500$ ppbv(rx)).

6

The conversion of ZnO $\xi_{\text{ZnO}}(t_{\text{Bt},500})$, at the same time, remains almost constant with a slight decrease in conversion for the higher Zn loading, that, in part, can be related to the decreased BET surface area of the sorbent. This implies that the retention of Se, for the given experimental parameters, is mainly dependent on the Zn loading of the sorbent. Other parameters such as physisorption appear to play a minor role compared to the removal of Se by Zn.

References

- [1] Lenny H. E. Winkel, C. Annette Johnson, Markus Lenz, Tim Grundl, Olivier X. Leupin, Manouchehr Amini, and Laurent Charlet. Environmental selenium research: From microscopic processes to global understanding. *Environmental Science & Technology*, 46(2):571–579, 2012.
- [2] Olle Selinus, Brian J Alloway, José A Centeno, Robert Barry Finkelman, Ron Fuge, Ulf Lindh, and Pauline Smedley. *Essentials of medical geology*. Springer, 2013.
- [3] Peter M. Chapman, William J. Adams, Marjorie Brooks, Charles G. Delos, Samuel N. Luoma, William A. Maher, Harry M. Ohlendorf, Theresa S. Presser, and Patrick Shaw. *Ecological assessment of selenium in the aquatic environment*. CRC Press, 2010.
- [4] Jay Ratafia-Brown, Lynn Manfredo, Jeffrey Hoffmann, and Massood Ramezan. Major environmental aspects of gasification-based power generation technologies. Report, 2002.
- [5] United States environmental protection agency, national emission standards for hazardous air pollutants from coal- and oil-fired electric utility steam generating units and standards of performance for fossil-fuel-fired electric utility, industrial-commercial- institutional, and small industrial-commercial-institutional steam generating units; final rule. 77(32):9304–9513, 2012.
- [6] Costas Christou, Ioannis Hadjipaschalis, and Andreas Poullikkas. Assessment of integrated gasification combined cycle technology competitiveness. *Renewable and Sustainable Energy Reviews*, 12(9):2459–2471, 2008.
- [7] David A. Bell, Brian F. Towler, and Maohong Fan. *Coal gasification and its applications*. Elsevier William Andrew, Amsterdam, 2011.
- [8] R. Yan, D. Gauthier, G. Flamant, and G. Peraudeau. Fate of selenium in coal combustion: Volatilization and speciation in the flue gas. *Environmental Science & Technology*, 35(7): 1406–1410, 2001.
- [9] J. R. Bunt and F. B. Waanders. Trace element behaviour in the sasol-lurgi mk ivfbdb gasifier. part 1 - the volatile elements: Hg, as, se, cd and Pb. *Fuel*, 87(12):2374–2387, 2008.
- [10] F. Vejahati, Z. H. Xu, and R. Gupta. Trace elements in coal: Associations with coal and minerals and their behavior during coal utilization - a review. *Fuel*, 89(4):904–911, 2010.
- [11] Christopher Higman and Samuel Tam. Advances in coal gasification, hydrogenation, and gas treating for the production of chemicals and fuels. *Chemical Reviews*, 114(3): 1673–1708, 2014.
- [12] Calvin H. Bartholomew. Mechanisms of catalyst deactivation. *Applied Catalysis A: General*, 212(1–2):17–60, 2001.
- [13] Mary Theresa Monahan-Pendergast, Michelle Przybylek, Mark Lindblad, and Jennifer Wilcox. Theoretical predictions of arsenic and selenium species under atmospheric conditions. *Atmospheric Environment*, 42(10):2349–2357, 2008.

- [14] Aysel T Atimtay and Douglas P Harrison. *Desulfurization of hot coal gas*. Springer-Verlag Berlin Heidelberg, 1998.
- [15] Panayot K. Petrov, Jeffrey W. Charters, and Dirk Wallschlaeger. Identification and determination of selenosulfate and selenocyanate in flue gas desulfurization waters. *Environmental Science & Technology*, 46(3):1716–1723, 2012.
- [16] C. M. Nyberg, J. S. Thompson, Y. Zhuang, J. H. Pavlish, L. Brickett, and S. Pletcher. Fate of trace element haps when applying mercury control technologies. *Fuel Processing Technology*, 90(11):1348–1353, 2009.
- [17] Hermine Nalbandian. Trace element emissions from coal. Report, 2012.
- [18] United States environmental protection agency, method 29. *Determination of Metals Emissions From Stationary Sources*, 1992.
- [19] ISO. Standard ISO/dis 17211. *Stationary source emissions - Sampling and determination of selenium compounds in flue gas (DRAFT)*, 2014.
- [20] E. C. Rupp, E. J. Granite, and D. C. Stanko. Method for detection of trace metal and metalloid contaminants in coal-generated fuel gas using gas chromatography/ion trap mass spectrometry. *Analytical Chemistry*, 82(14):6315–6317, 2010.
- [21] E. C. Rupp, E. J. Granite, and D. C. Stanko. Laboratory scale studies of pd/gamma-al2o3 sorbents for the removal of trace contaminants from coal-derived fuel gas at elevated temperatures. *Fuel*, 108:131–136, 2013.
- [22] P. Monkhouse. On-line spectroscopic and spectrometric methods for the determination of metal species in industrial processes. *Progress in Energy and Combustion Science*, 37(2):125–171, 2011.
- [23] D. Poole, V. Sharifi, J. Swithenbank, B. Argent, and D. Ardelt. On-line detection of metal pollutant spikes in msw incinerator flue gases prior to clean-up. *Waste Management*, 27(4):519–532, 2007.
- [24] M. Diaz-Somoano and M. R. Martinez-Tarazona. Retention of trace elements using fly ash in a coal gasification flue gas. *Journal of Chemical Technology and Biotechnology*, 77(3):396–402, 2002.
- [25] C. Charpentreau, R. Seneviratne, A. George, M. Millan, D. R. Dugwell, and R. Kandiyoti. Screening of low cost sorbents for arsenic and mercury capture in gasification systems. *Energy & Fuels*, 21(5):2746–2750, 2007.
- [26] M. Diaz-Somoano, M. A. Lopez-Anton, and M. R. Martinez-Tarazona. Determination of selenium by ICp-ms and hg-ICp-ms in coal, fly ashes and sorbents used for flue gas cleaning. *Fuel*, 83(2):231–235, 2004.
- [27] M. Diaz-Somoano, M. A. Lopez-Anton, F. E. Huggins, and M. R. Martinez-Tarazona. The stability of arsenic and selenium compounds that were retained in limestone in a coal gasification atmosphere. *Journal of Hazardous Materials*, 173(1-3):450–454, 2010.
- [28] Wenyue Du, Qin Shuai, and Liwei Yang. *Study on the Control of Selenium Emission During Coal Gasification*, volume 287-290 of *Advanced Materials Research*, pages 289–293. 2011.

- [29] S. H. Zhang, X. Hu, Q. Lu, and J. M. Zhang. Density functional theory study of arsenic and selenium adsorption on the cao (001) surface. *Energy & Fuels*, 25(7):2932–2938, 2011.
- [30] S. R. Xu, Q. Shuai, Y. J. Huang, Z. Y. Bao, and S. H. Hu. Se capture by a cao-zno composite sorbent during the combustion of se-rich stone coal. *Energy & Fuels*, 27(11):6880–6886, 2013.
- [31] J. P. Baltrus, E. J. Granite, E. C. Rupp, D. C. Stanko, B. Howard, and H. W. Pennline. Effect of palladium dispersion on the capture of toxic components from fuel gas by palladium-alumina sorbents. *Fuel*, 90(5):1992–1998, 2011.
- [32] X. Hu, Q. Lu, Y. Q. Sun, and J. M. Zhang. Mechanism of trace element adsorption on a clean and s precoated pd(111) surface: Insight from density functional theory calculations. *Fuel*, 107:290–298, 2013.
- [33] M. Diaz-Somoano and M. R. Martinez-Tarazona. Retention of arsenic and selenium compounds using limestone in a coal gasification flue gas. *Environmental Science & Technology*, 38(3):899–903, 2004.
- [34] T. H. Ko, H. Chu, and L. K. Chaung. The sorption of hydrogen sulfide from hot syngas by metal oxides over supports. *Chemosphere*, 58(4):467–474, 2005.
- [35] S.K. Gangwal, B.S. Turk, and R.P. Gupta. Zinc-oxide-based sorbents and processes for preparing and using same. 2010.
- [36] Tadaharu Watanabe, Takashi Suzuki, and Nobukazu Kinomura. Adsorption of diborane and hydrogen selenide on porous alumina and silica. *Journal of Materials Science: Materials in Electronics*, 9(2):127–132, 1998.
- [37] J. B. Peri and R. B. Hannan. Surface hydroxyl groups on gamma-alumina. *The Journal of Physical Chemistry*, 64(10):1526–1530, 1960.
- [38] J. H. De Boer, J. M. H. Fortuin, B. C. Lippens, and W. H. Meijs. Study of the nature of surfaces with polar molecules ii. the adsorption of water on aluminas. *Journal of Catalysis*, 2(1):1–7, 1963.
- [39] Karl Sohlberg, Stephen J. Pennycook, and Sokrates T. Pantelides. The bulk and surface structure of gamma-alumina. *Chemical Engineering Communications*, 181(1):107–135, 2000.
- [40] Christian Agatemor and Diane Beauchemin. Matrix effects in inductively coupled plasma mass spectrometry: A review. *Analytica Chimica Acta*, 706(1):66–83, 2011.
- [41] Robert C. Hutton, M. Bridenne, E. Coffre, Y. Marot, and F. Simondet. Investigations into the direct analysis of semiconductor grade gases by inductively coupled plasma mass spectrometry. *Journal of Analytical Atomic Spectrometry*, 5(6):463–466, 1990.
- [42] Honway Louie and Susan Yoke-Peng Soo. Use of nitrogen and hydrogen in inductively coupled plasma mass spectrometry. *Journal of Analytical Atomic Spectrometry*, 7(3): 557–564, 1992.

- [43] L. Ebdon, M. J. Ford, P. Goodall, and S. J. Hill. Hydrogen addition to the nebulizer gas for the removal of polyatomic ion interferences in inductively coupled plasma mass spectrometry. *Microchemical Journal*, 48(3):246–258, 1993.
- [44] Marcel Guillong and Christoph A. Heinrich. Sensitivity enhancement in laser ablation ICp-ms using small amounts of hydrogen in the carrier gas. *Journal of Analytical Atomic Spectrometry*, 22(12):1488–1494, 2007.
- [45] S. H. Liu, Z. C. Hu, D. Gunther, Y. H. Ye, Y. S. Liu, S. Gao, and S. H. Hu. Signal enhancement in laser ablation inductively coupled plasma-mass spectrometry using water and/or ethanol vapor in combination with a shielded torch. *Journal of Analytical Atomic Spectrometry*, 29(3):536–544, 2014.
- [46] J. F. Alary and E. D. Salin. Quantitation of water and plasma diagnosis for electrothermal vaporization-inductively coupled plasma mass spectrometry: The use of argon and argide polyatomics as probing species. *Spectrochimica Acta Part B-Atomic Spectroscopy*, 53(12):1705–1721, 1998.
- [47] V. M. Goldfarb and H. V. Goldfarb. ICp-AES analysis of gases in energy technology and influence of molecular additives on argon ICp. *Spectrochimica Acta Part B: Atomic Spectroscopy*, 40(1–2):177–194, 1985.
- [48] Pierre Allain, Laurent Jaunault, Yves Maura, Jean Michel Mermet, and Thierry Delaporte. Signal enhancement of elements due to the presence of carbon-containing compounds in inductively coupled plasma mass spectrometry. *Analytical Chemistry*, 63(14):1497–1498, 1991.
- [49] Geerke H. Floor, Romain Millot, Monica Iglesias, and Philippe Negrel. Influence of methane addition on selenium isotope sensitivity and their spectral interferences. *Journal of Mass Spectrometry*, 46(2):182–188, 2011.
- [50] Marco Wellinger. *Development and Application of Devices for Online Trace Element Analysis of Thermal Process Gases from Woody Feedstocks*. Thesis, 2012.
- [51] M. Grunze, W. Hirschwald, and D. Hofmann. Zinc oxide: Surface structure, stability, and mechanisms of surface reactions. *Journal of Crystal Growth*, 52:241–249, 1981.
- [52] S. Lew, A. F. Sarofim, and M. Flytzani-Stephanopoulos. The reduction of zinc titanate and zinc-oxide solids. *Chemical Engineering Science*, 47(6):1421–1431, 1992.
- [53] Eiji Sasaoka, Shigeru Hirano, Shigeaki Kasaoka, and Yusaku Sakata. Stability of zinc oxide high-temperature desulfurization sorbents for reduction. *Energy & Fuels*, 8(3):763–769, 1994.
- [54] Brian R. Strohmeier and David M. Hercules. Surface spectroscopic characterization of the interaction between zinc ions and gamma-alumina. *Journal of Catalysis*, 86(2):266–279, 1984.
- [55] George E. P. Box, J. Stuart Hunter, and William Gordon Hunter. *Statistics for experimenters design, innovation, and discovery*. Wiley series in probability and statistics. Wiley-Interscience, Hoboken, N.J., 2nd edition, 2005.

- [56] T. W. May and R. H. Wiedmeyer. A table of polyatomic interferences in ICp-ms. *Atomic Spectroscopy*, 19(5):150–155, 1998.
- [57] E. Hywel Evans and Jeffrey J. Giglio. Interferences in inductively coupled plasma mass spectrometry. a review. *Journal of Analytical Atomic Spectrometry*, 8(1):1–18, 1993.
- [58] K. G. Heumann, S. M. Gallus, G. Radlinger, and J. Vogl. Precision and accuracy in isotope ratio measurements by plasma source mass spectrometry. *Journal of Analytical Atomic Spectrometry*, 13(9):1001–1008, 1998.
- [59] Alexandr A. Pupyshev, Vladimir N. Muzgin, and Anna K. Lutsak. Thermochemical processes and ion transport in inductively coupled plasma mass spectrometry: theoretical description and experimental confirmation. *Journal of Analytical Atomic Spectrometry*, 14(9):1485–1492, 1999.
- [60] S. Ergun. Fluid flow through packed columns. *Chemical Engineering Progress*, 48(2): 89–94, 1952.
- [61] Manfred Baerns, Hanns Hofmann, and Albert Renken. *Chemische Reaktionstechnik*. Lehrbuch der technischen Chemie. Wiley-VCH, Weinheim, 3rd edition, 2002.
- [62] C. F. Chu and K. M. Ng. Flow in packed tubes with a small tube to particle diameter ratio. *AIChE Journal*, 35(1):148–158, 1989.
- [63] Wridzer J. W. Bakker, Freek Kapteijn, and Jacob A. Moulijn. A high capacity manganese-based sorbent for regenerative high temperature desulfurization with direct sulfur production: Conceptual process application to coal gas cleaning. *Chemical Engineering Journal*, 96(1–3):223–235, 2003.
- [64] Ivan I. Novochinskii, Chunshan Song, Xiaoliang Ma, Xinsheng Liu, Lawrence Shore, Jordan Lampert, and Robert J. Farrauto. Low-temperature h₂S removal from steam-containing gas mixtures with zno for fuel cell application. 1. zno particles and extrudates. *Energy & Fuels*, 18(2):576–583, 2004.
- [65] P. Sun, J. R. Grace, C. J. Lim, and E. J. Anthony. Co-capture of h₂S and CO₂ in a pressurized-gasifier-based process. *Energy & Fuels*, 21(2):836–844, 2007.
- [66] S. J. Gregg and Kenneth S. W. Sing. *Adsorption, surface area and porosity*. Academic Press, London, 2nd edition, 1982.
- [67] S. A. El-Hakam. Structure, texture and catalytic activity of zno/al₂o₃ catalysts. *Colloids and Surfaces A: Physicochemical and Engineering Aspects*, 157(1–3):157–166, 1999.
- [68] M. L. Fuller and C. W. Siller. Electron diffraction observations of surface reaction of hydrogen selenide on zinc oxide. *Journal of Applied Physics*, 12(5):416–419, 1941.
- [69] Laure Neveux, David Chiche, Delphine Bazer-Bachi, Loic Favergeon, and Michele Pijolat. New insight on the zno sulfidation reaction: Evidences for an outward growth process of the zns phase. *Chemical Engineering Journal*, 181:508–515, 2012.
- [70] Igor Bezverkhyy, Jonathan Skrzypski, Olga Safonova, and Jean-Pierre Bellat. Sulfidation mechanism of pure and cu-doped zno nanoparticles at moderate temperature: Tem and in situ xrd studies. *The Journal of Physical Chemistry C*, 116(27):14423–14430, 2012.

7

Concluding remarks

7.1. Conclusions

THE PRESENT study addressed two aspects of the gas cleanup chain in gasification processes: The analysis of gas contaminants and subsequently their retention. The following paragraphs provide detailed conclusions of Chapters 3 to 6 which formed the main body of this thesis.

Adsorption of thiophene by activated carbon

This study investigated the adsorption of thiophene from a C_4H_4S/Ar gas mixture onto activated carbon experimentally and by means of a model. Experiments were performed in the temperature range from 100 to 200 °C with different thiophene inlet concentrations (8.5 to 30 ppmv) and gas flow rates (30 to 55 Nml min⁻¹). Variation of temperature had the strongest effect in these experiments with breakthrough capacities ranging from 7 to 138 mmolkg⁻¹ at 200 and 100 °C, respectively.

In order to describe the dynamics of adsorption, a 1D mathematical model (LDF approach, including axial dispersion, isothermal) was developed. The effect of all model parameters, including assumptions concerning the type of isotherm model and axial dispersion correlation on breakthrough behaviour were investigated using a global sensitivity analysis (GSA). Based on the chosen range of input factors, the analysis indicated that the type of isotherm model, axial dispersion correlation and temperature have a major effect on the breakthrough time. The slope of the breakthrough curve, on the other hand, is strongly affected by both the isotherm model and axial dispersion correlation. When employing an optimal set of model input factors, experimental and modelling results showed good agreement with deviations between measured and predicted breakthrough times and capacities being well below 15 %.

The work shows that activated carbons are a valid option for thiophene removal from the gas phase. When modeling such process units, performing a sensitivity analysis has several benefits. It aids to gain further process insight by understanding the linkage between input factors, model outputs and their importance on them. At the same time, it can help to increase the model quality by unveiling possible model errors and giving guidance where an improved parameter uncertainty has most effect on overall quality.

High temperature conversion of thiophene over CaO

The effect of H_2 , H_2O and H_2S on the conversion of thiophene over a fixed bed reactor with CaO as bed material was investigated. The performed experiments were planned on the basis of a full factorial design with a total of eight experiments (without repetition experiments). The obtained experimental results were fitted to a linear model with interactions and then analysed for their statistical significance by means of a normal plot.

The results show that H_2O and H_2S have a major negative effect on thiophene conversion while that of H_2 is less pronounced. The screening helped to show a direction for future experiments which will involve a detailed modelling of the thiophene reaction.

Online tar measurement by UV-Vis spectroscopy

In this study, a new online UV-Vis method was developed and proved to be a readily applicable measurement method for the detection of tar compounds in process gases obtained from wood gasification. Two cases of application for the method were tested.

In situations where the tar composition is diverse (e.g. before tar treatment), quantitative analysis is impeded by several factors. A high number and spectral overlap (collinearity) of tar compounds will cause an increased variance of the predicted concentrations. Because

the product of concentration and extinction coefficient of tar compounds can span over orders of magnitude, tar compounds with high absorbance might mask the presence of tar compounds with smaller ones. In such situations the method cannot replace more expensive online analytical tools, but still provide qualitative information for process monitoring. Strip charts, plotting the absorbance of selected wavelengths *versus* time, can give an indication on the process stability. The absence of high molecular tar compounds, which are known to cause condensation issues, can easily be monitored because they tend to absorb light at higher wavelengths¹.

Quantitative analysis becomes feasible when the number of tar compounds is limited (e.g. after tar treatment). Tar compound concentration profiles across a lab-scale reformer were obtained by means of a classical least squares (CLS) approach for spectra decomposition. Concentration predictions for the three involved tar compounds benzene, toluene and naphthalene were comparable to those obtained by GC-FID as a reference method. More complex spectra, collected after a pilot-scale gas scrubber, were analysed by a partial least squares (PLS) calibration and showed good results for five tar compounds.

Detection and retention of selenium

In this study, a new analytical method for the online detection of H₂Se in reducing gas atmosphere has been developed and been employed as a tool for the performance evaluation of a Zn/Al₂O₃ sorbent.

Using a direct gas inlet on an ICP-MS in combination with matrix matched calibration, H₂Se can reliably be detected with high temporal resolution (> 1 Hz). The calculated and verified detection limit lies below 1 ppbv(rx), thus being comparable to current offline methods.

The case study which evaluated a Zn/Al₂O₃ sorbent, shows that the material can act as a sorbent for H₂Se capture in a simplified, reducing gas atmosphere, containing H₂, H₂O and Ar. Observed Zn conversions were generally low (4.6 to 10.5 %). The Al₂O₃ support itself captures H₂Se under dry reaction conditions. However, already the addition of small amounts of steam drastically reduce the observed sorption capacity, indicating competitive adsorption of H₂O and H₂Se on the support. In case of Zn/Al₂O₃, a further increase in steam content from 2 to 5 vol%(rx) shows little influence on the breakthrough behaviour while an increase to 10 vol%(rx), again, results in a decrease in Se sorption capacity. A decrease in reaction temperature from 350 to 250 °C results in a minor increase in sorption capacity. Decreasing the temperature further to 150 °C, however, significantly increases the sorption capacity, indicating that under low temperature operating conditions, further adsorption mechanisms (physisorption) might have to be considered as well. Increasing the loading of the active phase (Zn) results in an according increase in sorption capacity.

7.2. Outlook

The work performed in the course of this thesis can serve as a nucleus for further research beyond the set scopes. The following paragraphs provide suggestions, organized by the respective topics.

Adsorption of thiophene by activated carbon

- The sensitivity analysis was able to provide information regarding the effect of the individual input factors on the outputs. However, the exact propagation of the variance inside the model remains opaque to the modeller. Performing a network analysis might help to elucidate which model paths have a strong effect on the sensitivity if multiple paths can act on the output at the same time.
- The presented model describes and investigates the removal of thiophene from an inert carrier gas stream (Ar) by activated carbon. However, the gas atmosphere in gasification processes is expected to contain more gas species which could interact with the sorbent as well as sorbate, thereby causing a change in the breakthrough behaviour. Further work should therefore include:
 - (i) Use an experimental design of experiments to evaluate the effect of gas components on the breakthrough behaviour. These species should not only include the major gas components (H_2 , CO, CO_2 , CH_4 , H_2O)^{2–5} but also gas contaminants, including H_2S ⁶ and tar compounds^{7,8}.
 - (ii) Having determined gas components with significant effect on the breakthrough curve, more extensive measurements have to be performed to describe the multicomponent adsorption isotherms. A common model to describe the isotherms is the extended Langmuir isotherm model⁹.
 - (iii) Describe the resulting multiple transition system by means of a mathematical model¹⁰.
- The obtained, extended model may then be implemented into different gas cleanup chains to find optimal operating conditions of the unit and evaluate the economic potential of using activated carbons as a sorbent in gasification processes.

High temperature conversion of thiophene over CaO

The present preliminary study demonstrated that CaO can be used to convert thiophene at high temperatures. On this basis, additional work should include:

- Development of mechanistic models of the Langmuir-Hinshelwood type to describe the decomposition of thiophene.
 - An extended screening design should evaluate the effect of further gas species such as CO¹¹ and gas contaminants, including tars and HCl¹² that could affect the catalyst performance. The outcome is a set of gas species, having a major effect on thiophene conversion.
 - Based on the determined set, further experiments should be performed to allow parameter estimation of several proposed models and subsequent model discrimination.
- Thiophene conversions in this study were determined after signal stabilization for more than 1 h. This approach is valid when an application of CaO in the gasifier or in a packed bed reactor is envisaged. When applied as an entrained flow sorbent with subsequent separation at the hot gas filter, shorter time spans should be investigated (3 to 12 min^{13,14}).

- The obtained kinetic model may then be implemented into an techno-economic model to help evaluate the operating and capital costs associated with plants that feature gas cleaning units based on either disposable or regenerable sorbents or a mixture thereof.

Online tar measurement by UV-Vis spectroscopy

- The liquid quench sampling system was substantially improved over its predecessor, employed in previous studies^{15,16}. These improvements include the incorporation of automated flow meters for liquid and gas streams exiting the separator (see Fig. 5.2), a densimeter to determine the water content, an automated sampling unit as well as a process control system. Further steps should include:
 - The measurement of the liquid phase tar compound concentration is subject to several sources of uncertainty, as partly studied and discussed by Kaufman Rechulski¹⁷. A rigorous variation of these factors can help indicate major sources of uncertainty and reveal opportunities for optimization.
 - The possible slip of tar compounds through the gas stream, thereby escaping the liquid phase measurement has to be accounted for. Preliminary experiments by Rechulski et al.¹⁶ focused on the tar model compound toluene. However, additional experiments, including sulphur and nitrogen containing hydrocarbons as well as tar compounds with high vapour pressure (e.g. thiophene, phenol, benzene, styrene, xylene) should be conducted.
 - Gas sampling is currently restricted to particulate free gas in order to avoid clogging of the sampling lance, downstream tubing as well as equipment. The analysis of particulate-laden gas (e.g. directly after the gasifier) therefore involves a filtration step, typically performed by an inertial filter. Both the filter cake¹⁸ and the filter material itself can catalyse the decomposition of tar compounds, in that altering the initial gas composition. Future work should therefore focus on the development of novel sampling techniques to help solve this dilemma.
- Applying a liquid quench sampling system to the gas phase analysis of tar compounds offers several advantages as discussed in Chapter 5. The system's residence time of ≈ 10 min doesn't allow for real-time monitoring, however. Shortening the tubing or increasing the flow rates cause a decrease in capture efficiency¹⁶ and are therefore not an option. An alternative is to perform the UV-Vis analysis *in-situ* in the gas phase. Patuzzi et al.¹⁹ made a step towards this direction by using a LED based UV-Vis measurement cell. The obtained four point spectra obstruct quantification, however. Thus, the current work performed a proof-of-concept experiment for UV-Vis gas phase measurement (Appendix D.4). Based on these promising results, upcoming work should include the integration of a heated, inert (SilcoNert 2000, SilcoTek) measurement cell and the extension of the component spectra database.
- The employed liquid quench sampling system exhibits a residence time distribution (RTD) that deviates from plug flow (see Section 5.2). Analysing a transient process could therefore lead to erroneous conclusions as the measured response comprises in fact a convolution of the process's signal and the RTD of the sampling system. Further work should therefore develop a RTD model of the sampling system in the first step and then use it to deconvolute the measured signal^{20,21}.
- The described RTD characteristics of the sampling system might as well be used to the experimenter's benefit. Preliminary experiments should investigate whether tar classes differ

in their RTD characteristics. This 'chromatographic effect' could help to analyse complex tar mixtures by means of UV-Vis spectroscopy.

Detection and retention of selenium

- The gas matrix is currently limited to H_2 , H_2O and Ar. Future H_2Se sorption experiments should also include other gaseous species which could affect the Se sorption capacity such as H_2S , CO and CO_2 . Associated matrix effects in the ICP-MS may be circumvented by applying more advanced calibration strategies (e.g. internal standard) as discussed in Section 6.2.3.
- In the current work, ZnO was chosen as an H_2Se sorbent. This choice was based on the similarity of Se and S (same group in periodic table) in the first step and the fact that ZnO is an established sorbent for H_2S retention in the second²². Further work should employ a more rational approach to the selection of sorbent materials which may include:
 - (i) A thermodynamic screening of single metal oxides^{23,24} to identify potential materials that are suited for H_2Se capture in gasification atmosphere at warm to hot temperatures.
 - (ii) Perform validation experiments of these selected materials.
 - (iii) Investigate composite materials that may combine the properties of individual metal oxides.
- This work focused on the detection of H_2Se . The developed method can, however, also be applied to the measurement of further trace contaminants, including Hg^0 , AsH_3 and PH_3 . Preliminary work and the successful calibration of these three contaminants in gasification atmosphere is presented in Appendix E.8. Applying matrix-matched calibration, the individually calculated detection limits were <0.01 ppbv for Hg^0 , <0.1 ppbv for AsH_3 and <2 ppbv for PH_3 , thus being comparable to current offline methods. The method therefore provides a quick and robust tool for the lab-scale investigation of further trace contaminants and sorbent materials.

References

- [1] Heinz-Helmut Perkampus. *UV-VIS Atlas of Organic Compounds*. VCH, Weinheim, 2nd edition, 1992.
- [2] Harry Marsh. *Activated Carbon*. Elsevier, Amsterdam, 2006.
- [3] A. M. Mastral, T. Garcia, R. Murillo, M. S. Callen, J. M. Lopez, and M. V. Navarro. Moisture effects on the phenanthrene adsorption capacity by carbonaceous materials. *Energy & Fuels*, 16(1):205–210, 2002.
- [4] Nan Qi and M. Douglas LeVan. Coadsorption of organic compounds and water vapor on BPL activated carbon. 5. methyl ethyl ketone, methyl isobutyl ketone, toluene, and modeling. *Industrial & Engineering Chemistry Research*, 44(10):3733–3741, 2005.
- [5] Nathalie Casas, Johanna Schell, Ronny Pini, and Marco Mazzotti. Fixed bed adsorption of CO₂/h₂ mixtures on activated carbon: experiments and modeling. *Adsorption*, 18(2): 143–161, 2012.
- [6] F. J. Gutiérrez Ortiz, P. G. Aguilera, and P. Ollero. Modeling and simulation of the adsorption of biogas hydrogen sulfide on treated sewage-sludge. *Chemical Engineering Journal*, 253: 305–315, 2014.
- [7] Romain Chauveau, Georges Grévillet, Stéphanie Marsteau, and Cécile Vallières. Values of the mass transfer coefficient of the linear driving force model for voc adsorption on activated carbons. *Chemical Engineering Research and Design*, 91(5):955–962, 2013.
- [8] Kaushal Naresh Gupta, Nandagiri Jagannatha Rao, and Govind Kumar Agarwal. Gaseous phase adsorption of volatile organic compounds on granular activated carbon. *Chemical Engineering Communications*, 202(3):384–401, 2015.
- [9] R. T. Yang. *Gas separation by adsorption processes*. Series on chemical engineering. Butterworths, Boston, 1987.
- [10] Douglas M. Ruthven. *Principles of adsorption and adsorption processes*. Wiley, New York, 1984.
- [11] Pekka A. Simell, Nina A. K. Hakala, Heikki E. Haario, and A. Outi I. Krause. Catalytic decomposition of gasification gas tar with benzene as the model compound. *Industrial & Engineering Chemistry Research*, 36(1):42–51, 1997.
- [12] José Corella, José M. Toledo, and Gregorio Molina. Performance of cao and mgo for the hot gas clean up in gasification of a chlorine-containing (rdf) feedstock. *Bioresource Technology*, 99(16):7539–7544, 2008.
- [13] M. Lupion, B. Navarrete, B. Alonso-Fariñas, and M. Rodriguez-Galan. Hot gas filters for coal-based power generation systems: Operating experiences. *Fuel*, 108:24–30, 2013.
- [14] U. Rhyner, R. Mai, H. Leibold, and S. M. A. Biollaz. Dynamic pressure measurements of a hot gas filter as a diagnostic tool to assess the time dependent performance. *Biomass & Bioenergy*, 53:72–80, 2013.

- [15] M. D. K. Rechulski, J. Schneebeil, S. Geiger, T. J. Schildhauer, S. M. A. Biollaz, and C. Ludwig. Liquid-quench sampling system for the analysis of gas streams from biomass gasification processes. part 1: Sampling noncondensable compounds. *Energy & Fuels*, 26(12):7308–7315, 2012.
- [16] M. D. K. Rechulski, J. Schneebeil, S. Geiger, T. J. Schildhauer, S. M. A. Biollaz, and C. Ludwig. Liquid-quench sampling system for the analysis of gas streams from biomass gasification processes. part 2: Sampling condensable compounds. *Energy & Fuels*, 26(10):6358–6365, 2012.
- [17] Marcelo Daniel Kaufman Rechulski. *Catalysts for High Temperature Gas Cleaning in the Production of Synthetic Natural Gas from Biomass*. Thesis, 2012.
- [18] R. S. Blissett and N. A. Rowson. A review of the multi-component utilisation of coal fly ash. *Fuel*, 97:1–23, 2012.
- [19] Francesco Patuzzi, Davide Roveda, Tanja Mimmo, Jürgen Karl, and Marco Baratieri. A comparison between on-line and off-line tar analysis methods applied to common reed pyrolysis. *Fuel*, 111:689–695, 2013.
- [20] Octave Levenspiel. *Chemical reaction engineering*. Wiley, New York, 3rd edition, 1999.
- [21] Christian H. Hornung and Malcolm R. Mackley. The measurement and characterisation of residence time distributions for laminar liquid flow in plastic microcapillary arrays. *Chemical Engineering Science*, 64(17):3889–3902, 2009.
- [22] Amir Moezzi, Andrew M. McDonagh, and Michael B. Cortie. Zinc oxide particles: Synthesis, properties and applications. *Chemical Engineering Journal*, 185:1–22, 2012.
- [23] Phillip R. Westmoreland, James B. Gibson, and Douglas P. Harrison. Comparative kinetics of high-temperature reaction between hydrogen sulfide and selected metal oxides. *Environmental Science & Technology*, 11(5):488–491, 1977.
- [24] Vincent Girard, Arnaud Baudot, David Chiche, Delphine Bazer-Bachi, Christine Bounie, and Christophe Geantet. Rational selection of single oxide sorbents for syngas desulfurization regenerable at reduced temperature: Thermochemical calculations and experimental study. *Fuel*, 128:220–230, 2014.

A

Co-Authorships

Applied kinetics for modeling of reactive hot gas filters

First order kinetics were developed based on experimental results of a noble metal catalyst. Activation energies and pre-exponential factors were determined by parameter estimation for steam reforming of tars, sulphur tars and ethene. The formation of ethane and benzene was assumed to be at constant rate depending on the decomposition of ethene and toluene respectively. Further, for steam reforming of methane and water gas shift reaction, the kinetic parameters of Langmuir-Hinshelwood-Hougen-Watson (LHHW) type rate laws including equilibrium term and adsorption of sulphur could be determined. With the applied kinetics, catalytic tar conversion of producer gas from biomass gasification was simulated. Simulation results at operating temperatures of 850 °C showed significantly higher conversions rates for sulphur free tars, ethene and methane than at 600 °C or 750 °C while the conversion of sulphur tars was less temperature dependent and high at all temperatures. The simulation results were used to evaluate different possibilities regarding the integration of catalytic material into hot gas filter units with vertical and horizontal filter design. The option of catalytic active filter elements, additional catalytic foam type packing at the inside of the filter element and a monolith at the exit of the filter vessel are feasible assuming the same catalyst material as applied in the reforming catalyst used in this study. These three options can be applied independently of the horizontal or vertical filter design. Placing a catalytic monolith or foam structure at the filter candle exit of a horizontal filter design was found to be unrealistic because the monolith or foam structure would be too long to reach sulfur tar concentrations below 1 ppmv.

Author's contributions to this publication:

- (i) Planned/performed > 90 % of experiments
- (ii) Implemented/validated methods for tar quantification (GC-FID/GC-SCD)
- (iii) Programmed code for data treatment/evaluation of experiments
- (iv) Performed analysis of mass transfer limitations
- (v) Implemented/validated kinetic model
- (vi) Substantial contribution to interpretation of the results

The contents of this section have been published in Appl. Energy **113**, 766 (2014), ¹. A comprehensive overview of the original work can be found in ².



Contents lists available at ScienceDirect

Applied Energy

journal homepage: www.elsevier.com/locate/apenergy

Applied kinetics for modeling of reactive hot gas filters



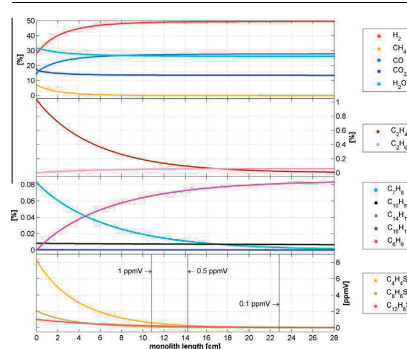
Urs Rhyner, Philip Edinger, Tilman J. Schildhauer*, Serge M.A. Biollaz

Paul Scherrer Institut (PSI), 5232 Villigen PSI, Switzerland

HIGHLIGHTS

- Applied first order kinetics could be developed for a noble metal catalyst.
- Activation energies were determined for steam reforming of tars and sulfur tars.
- Catalytic tar conversion of producer gas from biomass gasification was simulated.
- Possibilities regarding catalyst integration into hot gas filter units were evaluated.

GRAPHICAL ABSTRACT



ARTICLE INFO

Article history:
Received 21 April 2013
Received in revised form 13 July 2013
Accepted 24 July 2013
Available online 3 September 2013

Keywords:
Kinetics
Hot gas cleaning
Hot gas filtration
Desulfurization
Biomass

ABSTRACT

First order kinetics were developed based on experimental results of a noble metal catalyst. Activation energies and pre-exponential factors were determined by parameter estimation for steam reforming of tars, sulfur tars and ethene. The formation of ethane and benzene was assumed to be at constant rate depending on the decomposition of ethene and toluene respectively. Further, for steam reforming of methane and water gas shift reaction, the kinetic parameters of Langmuir–Hinshelwood–Hougen–Watson (LHHW) type rate laws including equilibrium term and adsorption of sulfur could be determined.

With the applied kinetics, catalytic tar conversion of producer gas from biomass gasification was simulated. Simulation results at operating temperatures of 850 °C showed significantly higher conversions rates for sulfur free tars, ethene and methane than at 600 °C or 750 °C while the conversion of sulfur tars was less temperature dependent and high at all temperatures.

The simulation results were used to evaluate different possibilities regarding the integration of catalytic material into hot gas filter units with vertical and horizontal filter design. The option of catalytic active filter elements, additional catalytic foam type packing at the inside of the filter element and a monolith at the exit of the filter vessel are feasible assuming the same catalyst material as applied in the reforming catalyst used in this study. These three options can be applied independently of the horizontal or vertical filter design. Placing a catalytic monolith or foam structure at the filter candle exit of a horizontal filter design was found to be unrealistic because the monolith or foam structure would be too long to reach sulfur tar concentrations below 1 ppm V.

© 2013 Elsevier Ltd. All rights reserved.

* Corresponding author. Tel.: +41 (0)56 310 27 06.
E-mail address: tilman.schildhauer@psi.ch (T.J. Schildhauer).

Experimental study on high temperature catalytic conversion of tars and organic sulfur compounds

A 400 cpsi noble metal catalyst was used to test the conversion of tars and sulphur containing hydrocarbons in the presence of steam, hydrogen sulphide and ethene. In order to reproduce producer gas from biomass gasification, higher molecular hydrocarbons (toluene, naphthalene, phenanthrene, pyrene) and sulphur containing hydrocarbons (thiophene, benzothiophene, dibenzothiophene) were added to a syngas. The syngas consisted of H_2 , CH_4 , H_2O , CO , CO_2 and N_2 . The catalyst was operated at temperatures between 620 and 750 °C and at gas hourly space velocity (GHSV) of $9'000\ h^{-1}$ and $18'000\ h^{-1}$. Conversions of sulphur containing hydrocarbons (41-99.6 %) were on average higher than conversions of sulphur free tars (0-47 %). High temperature, low GHSV, low steam and sulphur content favoured high conversions of tars and sulphur tars. As the catalyst was able to decompose sulphur tars under operating conditions close to a real wood gasification plant, it is possible to use it for hot gas cleaning in any process that includes sulphur sensitive catalysts such as fuel cells, liquid fuel synthesis or methanation processes. In such processes, H_2S produced by the reforming catalyst from sulphur tars can be captured downstream of the reformer in a metal oxide bed such as ZnO .

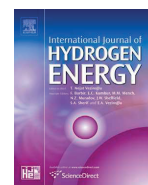
Author's contributions to this publication:

- (i) Planned/performed > 90 % of experiments
- (ii) Implemented/validated methods for tar quantification (GC-FID/GC-SCD)
- (iii) Programmed code for data treatment/evaluation of experiments
- (iv) Performed analysis of mass transfer limitations
- (v) Substantial contribution to interpretation of the results

The contents of this section have been published in the Int. J. Hydrogen Energy **39**, 4926 (2014)³. A comprehensive overview of the original work can be found in².

Available online at www.sciencedirect.com

ScienceDirect

journal homepage: www.elsevier.com/locate/ije

Experimental study on high temperature catalytic conversion of tars and organic sulfur compounds



Urs Rhyner, Philip Edinger, Tilman J. Schildhauer*, Serge M.A. Biollaz

Paul Scherrer Institut (PSI), 5232 Villigen PSI, Switzerland

ARTICLE INFO

Article history:

Received 23 August 2013

Received in revised form

18 December 2013

Accepted 10 January 2014

Available online 22 February 2014

Keywords:

Noble metal catalyst

Desulfurization

Hot gas cleaning

Tar removal

Biomass

ABSTRACT

A 400 cpsi noble metal catalyst was used to test the conversion of tars and sulfur containing hydrocarbons in the presence of steam, hydrogen sulfide and ethene. In order to reproduce producer gas from biomass gasification, higher molecular hydrocarbons (toluene, naphthalene, phenanthrene, pyrene) and sulfur containing hydrocarbons (thiophene, benzothiophene, dibenzothiophene) were added to a syngas. The syngas consisted of H_2 , CH_4 , H_2O , CO , CO_2 and N_2 . The catalyst was operated at temperatures between 620 °C and 750 °C and at gas hourly space velocity (GHSV) of 9000 h^{-1} and 18,000 h^{-1} .

Conversions of sulfur containing hydrocarbons (41–99.6%) were on average higher than conversions of sulfur free tars (0–47%). High temperature, low GHSV, low steam and sulfur content favored high conversions of tars and sulfur tars. As the catalyst was able to decompose sulfur tars under operating conditions close to a real wood gasification plant, it is possible to use it for hot gas cleaning in any process that includes sulfur sensitive catalysts such as fuel cells, liquid fuel synthesis or methanation processes. In such processes, H_2S produced by the reforming catalyst from sulfur tars can be captured downstream of the reformer in a metal oxide bed such as ZnO.

Copyright © 2014, Hydrogen Energy Publications, LLC. Published by Elsevier Ltd. All rights reserved.

1. Introduction

An efficient and effective gas cleaning of producer gas from thermo-chemical conversion of biomass is needed to protect downstream equipment. Particulate matter, tars and contaminants reduce the performance of downstream equipment such as catalysts, internal combustion engines or turbines. Sulfur is known as poison for catalysts containing Ni, Cu, Co or Fe. The removal of sulfur species is therefore crucial for any process applying catalysts such as methanation, liquid fuel synthesis or fuel cells.

State of the art gas cleaning requires cooling of the producer gas below 400 °C in order to fulfill the temperature limits of the filtration system. Tars and steam will condensate in quenching columns operated at temperatures as low as 10 °C. Sulfur species will be captured in cold absorbers such as scrubbers (e.g. Selexol, Rectisol) or fixed beds (active carbon, metal oxide).

Depending on the technology, exit temperatures of biomass gasifiers can be as high as 850 °C supporting the application of hot gas cleaning (HGC). It has been shown by process modeling, that HGC allows significant efficiency improvements by avoiding cooling and reheating of the producer

* Corresponding author. Tel.: +41 56 310 27 06.

E-mail address: tilman.schildhauer@psi.ch (T.J. Schildhauer).

A

References

- [1] U. Rhyner, P. Edinger, T. J. Schildhauer, and S. M. A. Biollaz. Applied kinetics for modeling of reactive hot gas filters. *Applied Energy*, 113:766–780, 2014.
- [2] P. Edinger. *High Temperature Conversion of Sulfur Containing Hydrocarbons and Tars*. Master's thesis, ETH Zürich, 2012.
- [3] U. Rhyner, P. Edinger, T. J. Schildhauer, and S. M. A. Biollaz. Experimental study on high temperature catalytic conversion of tars and organic sulfur compounds. *International Journal of Hydrogen Energy*, 39(10):4926–4937, 2014.

B

Adsorption of thiophene by activated carbon

B.1. Model flow chart

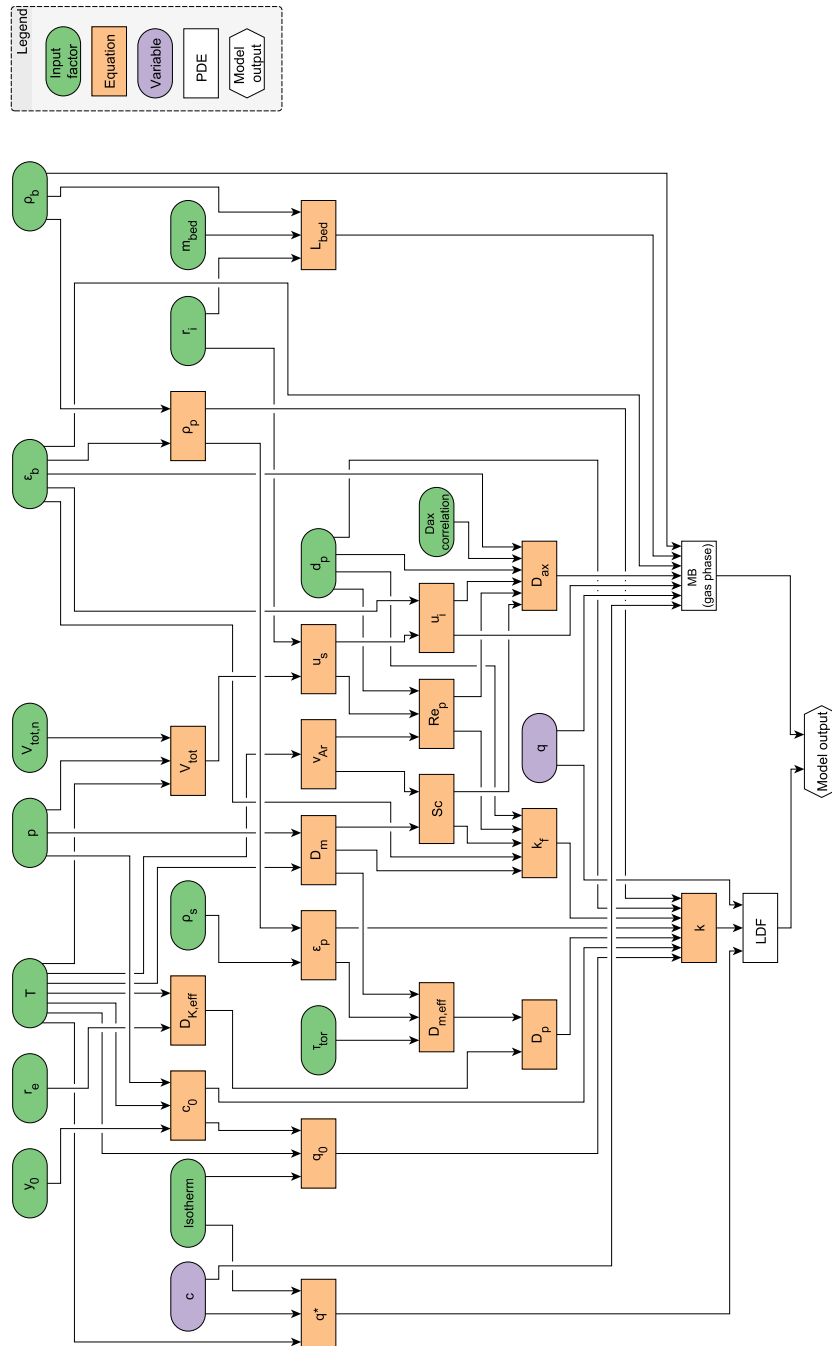


Figure B.1 – Model flow chart of the adsorption model developed in Section 3.2. The chart visualizes how input factors affect the model output through different layers of equations.

B.2. Experimental results

Table B.1 – Experimental conditions and corresponding results for thiophene sorption experiments onto activated carbon. A detailed discussion is provided in Section 3.4.2.

| Run | T (°C) | $\dot{V}_{tot,n}$ (Nml min ⁻¹) | y_0 (ppmv) | t_{90} (min) | q_{90} (mmolkg ⁻¹) |
|-----|--------|--|--------------|----------------|----------------------------------|
| 1 | 150 | 30.0 | 15.0 | 26 | 20 |
| 2 | 100 | 30.0 | 15.0 | 108 | 97 |
| 3 | 150 | 55.0 | 15.0 | 14 | 21 |
| 4 | 150 | 42.5 | 15.0 | 20 | 20 |
| 5 | 150 | 30.0 | 8.5 | 39 | 13 |
| 6 | 150 | 30.0 | 30.0 | 19 | 34 |
| 7 | 100 | 30.0 | 8.5 | 152 | 66 |
| 8 | 100 | 30.0 | 30.0 | 73 | 138 |
| 9 | 200 | 30.0 | 15.0 | 10 | 7 |
| 10 | 200 | 30.0 | 30.0 | 7 | 8 |

B

B

B.3. Convergence plots

The employed elementary effects (EE) method is a sampling based approach to perform the sensitivity analysis (SA)¹. While a too small sample may not yield robust results, an excessively large one may not provide a significant improvement in precision. It is therefore important to investigate how robust the obtained SA results are with respect to changes in sample size.

For this purpose, the normalized sensitivity measure S_j is defined by taking the ratio between EE_j (see Eq. (3.40) on Page 41) and the maximum EE s across all input factors

$$S_j = \frac{EE_j}{\max_i EE_i} \quad (\text{B.1})$$

Convergence was then investigated by taking sub-samples of the original sample and calculating the sensitivity indices and their uncertainty via the bootstrap technique². Based on the width of the 95 % confidence intervals of the individual sensitivity indices, a summary statistic is calculated as

$$\text{Stat} = \max_{j=1 \dots k_{EE}} (S_j^{ub} - S_j^{lb}) \quad (\text{B.2})$$

where S_j^{ub} and S_j^{lb} define the upper and lower bounds of the sensitivity index S_j and k_{EE} the number of input factors³.

Figure B.2 presents the computed statistic for the two model outputs t_{50} and $s_{90,10}$ as a function of the number of model evaluations. Herein, convergence is assumed to have been reached below a threshold of 0.05³. The sensitivity indices for both model outputs converge after 1.5×10^4 to 2.3×10^4 model evaluations.

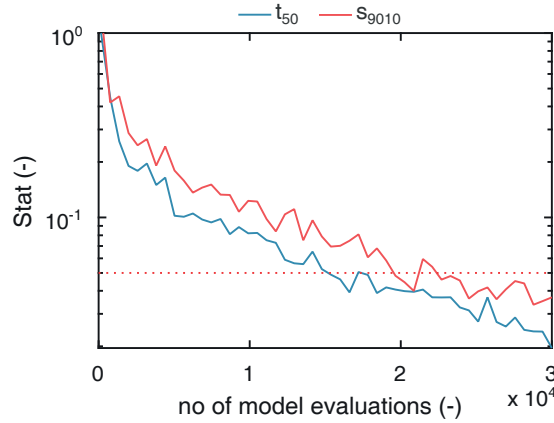


Figure B.2 – Convergence statistics *versus* number of model evaluations for t_{50} and $s_{90,10}$. Convergence is assumed to have been reached below a threshold of 0.05³.

B.4. Numerical results of sensitivity analysis

Table B.2 – Numerical results of sensitivity analysis performed in Section 3.4.3 (EE: Elementary effect; STD: Standard deviation of elementary effect)

| Input factor | Notation | t_{50} | | $s_{90,10}$ | |
|------------------------|------------|----------|------|-------------|--------|
| | | EE | STD | EE | STD |
| volume flow rate | VtotN | 1.20 | 0.21 | 0.0009 | 0.0008 |
| feed mole fraction | yInPpmv | 0.60 | 0.53 | 0.0019 | 0.0019 |
| column temperature | T0 | 3.30 | 0.68 | 0.0039 | 0.0013 |
| column pressure | p0 | 0.63 | 0.42 | 0.0005 | 0.0006 |
| column diameter | di | 0.22 | 0.37 | 0.0008 | 0.0009 |
| particle diameter | dp | 0.13 | 0.08 | 0.0030 | 0.0015 |
| pore radius | re | 0.08 | 0.07 | 0.0025 | 0.0014 |
| bulk voidage | epsBulk | 0.03 | 0.08 | 0.0007 | 0.0018 |
| bulk density | rhoBulk | 0.09 | 0.14 | 0.0020 | 0.0052 |
| skeletal density | rhoS | 0.03 | 0.14 | 0.0007 | 0.0044 |
| tortuosity | tortuosity | 0.09 | 0.09 | 0.0026 | 0.0015 |
| bed mass | mBed | 0.29 | 0.17 | 0.0002 | 0.0007 |
| isotherm model | Isotherm | 6.45 | 4.67 | 0.0113 | 0.0093 |
| axial dispersion model | DaxModel | 4.03 | 5.28 | 0.0215 | 0.0272 |

B

B.5. EE plots without Henry isotherm

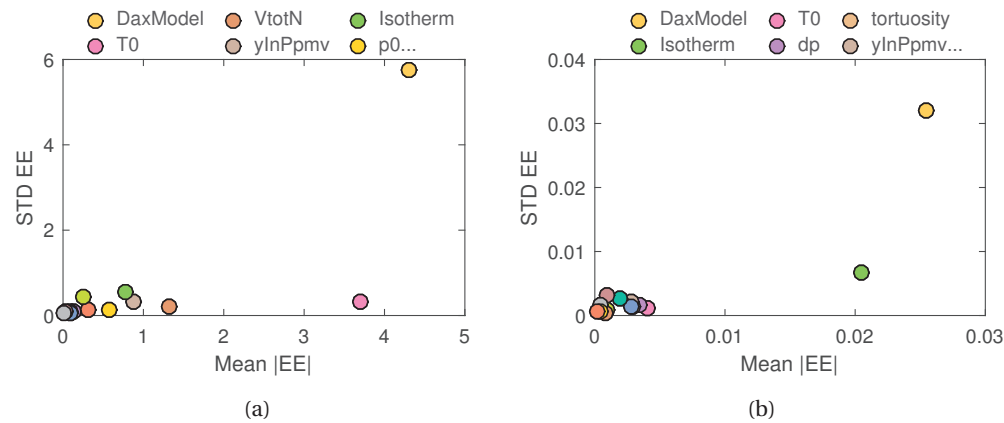


Figure B.3 – Plots of the standard deviation of elementary effects EE *versus* mean |EE| when omitting the Henry isotherm as input factor. The six most important parameters in the legend are listed in decreasing order of importance. (a) Key figure t_{50} ; (b) key figure $s_{90,10}$.

B.6. Parallel coordinate plots

B

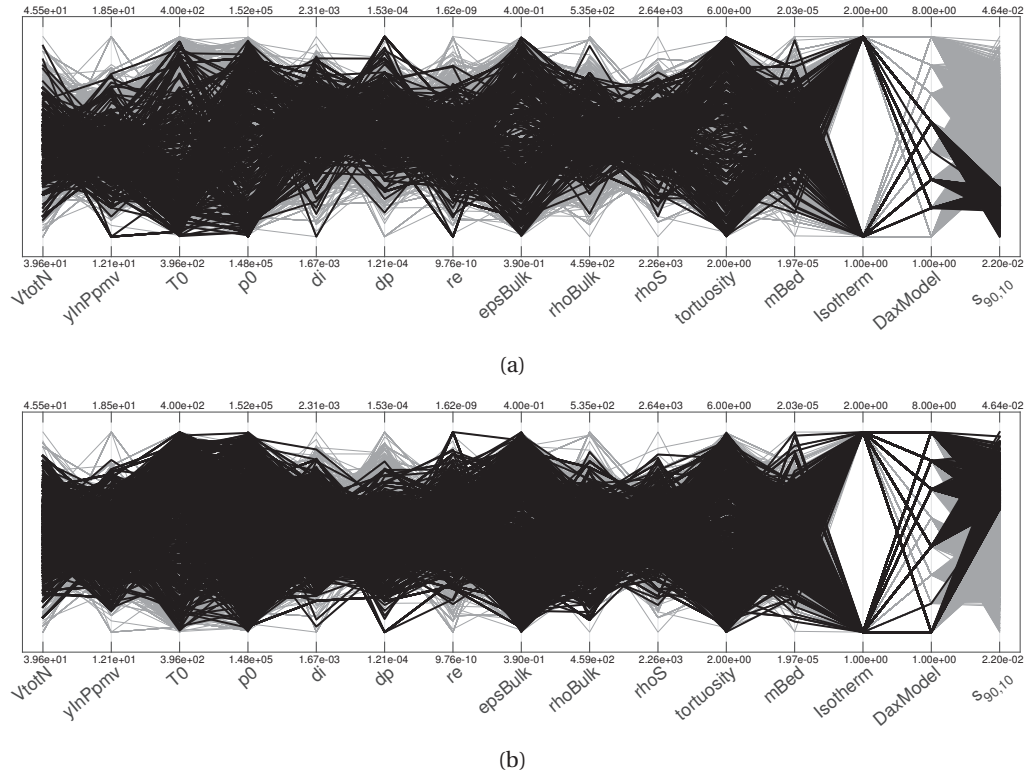


Figure B.4 – Representation of sensitivity analysis results in parallel coordinate plots⁴. The graphs aim to visualize the grouping of axial dispersion correlations with respect to their effect on the breakthrough curve slope $s_{90,10}$ as discussed in Section 3.4.3 by means of Fig. 3.11. In the given plots, grey lines comprise all data points while black lines are brushed. Plots (a) and (b) contain results involving Henry and Langmuir isotherms. (a) Brushed for breakthrough curve slopes $s_{90,10} < 0.028$. These slopes correspond to DaxModels 2,3 and 5 (Hsu(i-ii), Wakao); (b) brushed for breakthrough curve slopes $s_{90,10} > 0.037$. These higher slopes correspond to DaxModels 1,4,6,7 and 8 (Edwards, Wen, Ruthven, Koch, none).

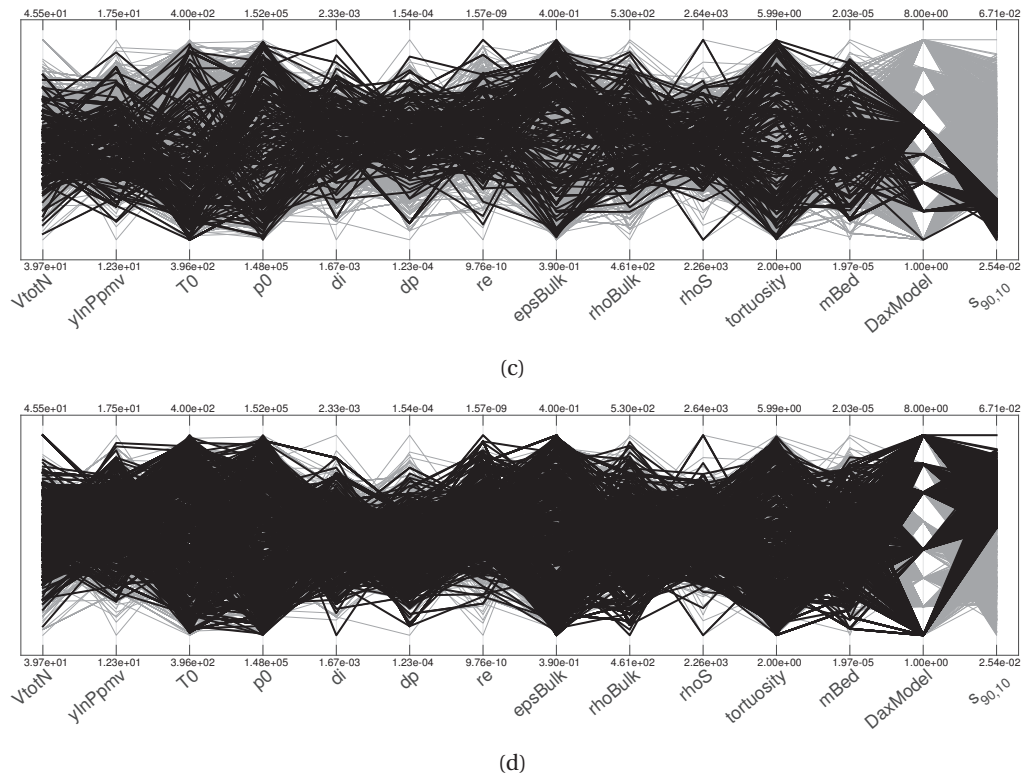


Figure B.4 – Cont. Plots (c) and (d) contain results involving the Tóth isotherm. (c) Brushed for breakthrough curve slopes $s_{90,10} < 0.034$. These slopes correspond to DaxModels 2,3 and 5 (Hsu(i-ii), Wakao); (d) brushed for breakthrough curve slopes $s_{90,10} > 0.047$. These higher slopes correspond to DaxModels 1,4,6,7 and 8 (Edwards, Wen, Ruthven, Koch, none).

B.7. Effect of temperature on breakthrough behaviour

B

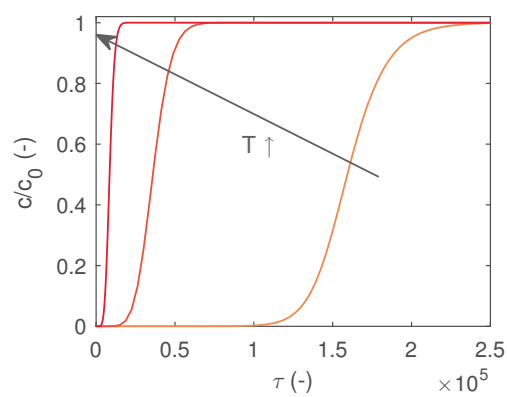


Figure B.5 – Predicted breakthrough curves for three reactor temperatures 100, 150 and 200 °C *versus* normalized time $\tau = tu_s/L_{bed}$ (C_4H_4S inlet concentration: 15 ppmv, total flow rate: 30 Nml min⁻¹)

B.8. EE on model variables

B

B

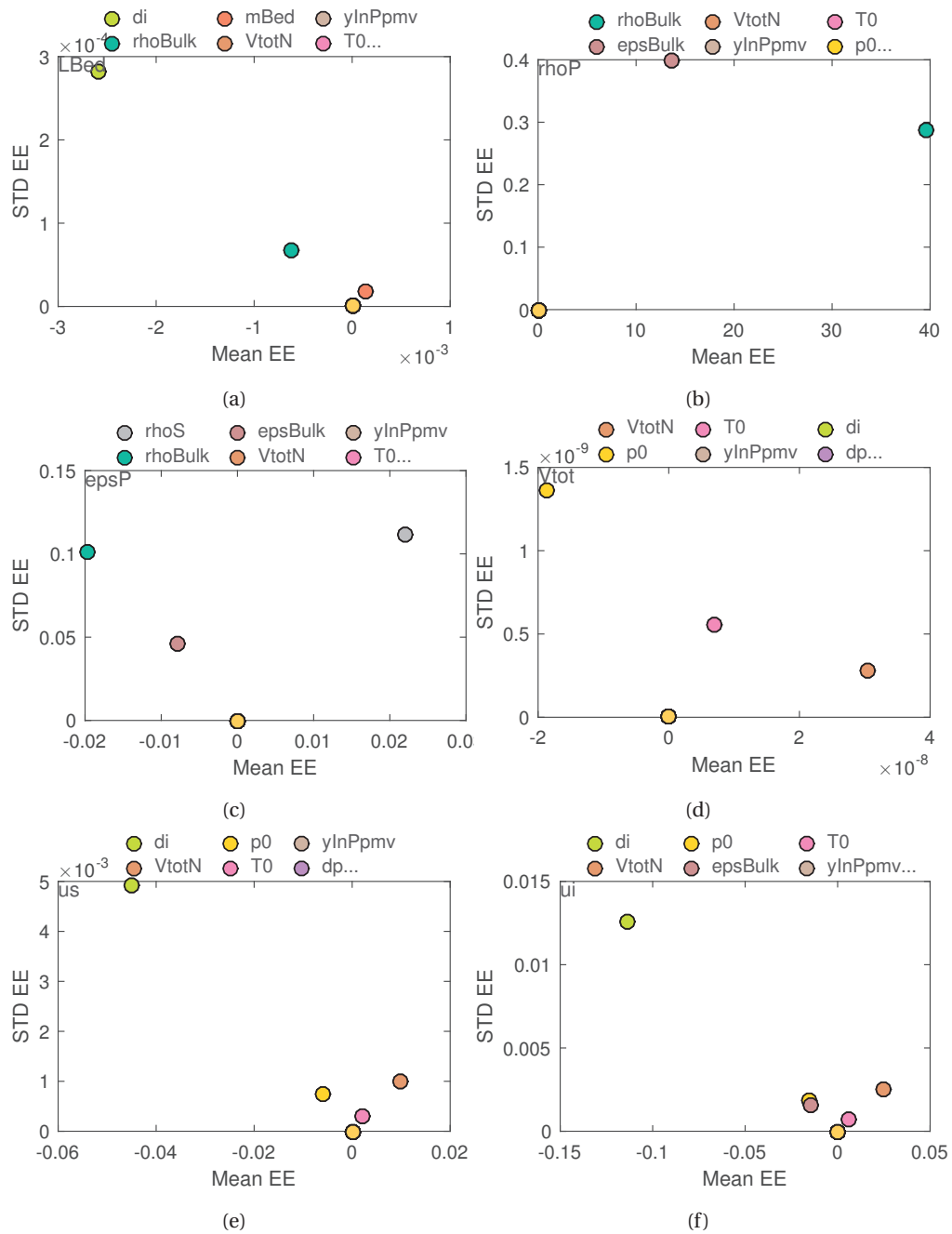


Figure B.6 – Evaluation of the effect of model parameters on internal model variables. For this purpose, a sensitivity analysis, similarly to that described in Section 3.2.2 was performed. In this case, however, the respective model variables are treated as the model output. The results are visualized for each model variable by plotting the standard deviation of elementary effects *versus* the mean EE. The six most important parameters in the legend are listed in decreasing order of importance.



Figure B.6 – Calculated EE for model variables (cont.)

B

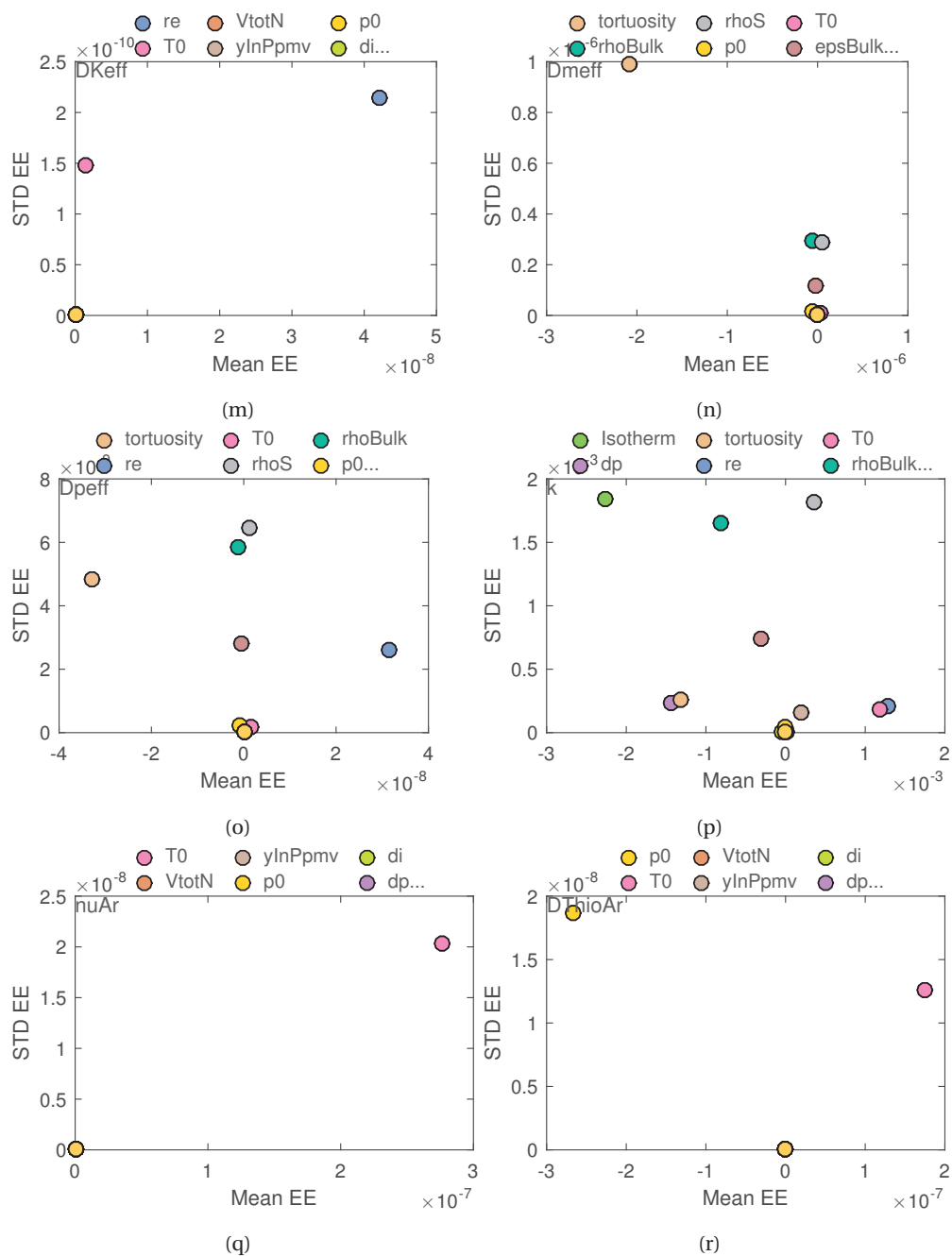


Figure B.6 – Calculated EE for model variables (cont.)

References

- [1] Andrea Saltelli, Marco Ratto, Stefano Tarantola, and Francesca Campolongo. Update 1 of: Sensitivity analysis for chemical models. *Chemical Reviews*, 112(5):1–21, 2012.
- [2] Bradley Efron and Robert Tibshirani. *An introduction to the bootstrap*. Monographs on statistics and applied probability. Chapman & Hall, New York, 1993.
- [3] Fanny Sarrazin, Francesca Pianosi, and Thorsten Wagener. Global sensitivity analysis of environmental models: Convergence and validation. *Environmental Modelling & Software*, 79:135–152, 2016.
- [4] Alfred Inselberg. *Parallel Coordinates*. Springer, 2013.

C

High temperature conversion of thiophene over CaO

C.1. SEM pictures

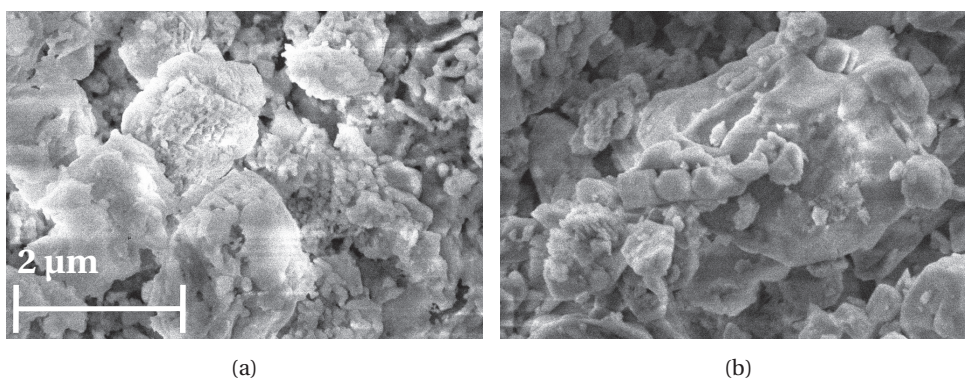


Figure C.1 – Scanning electron microscope pictures taken at 20'000x magnification. (a) Uncalcined limestone (CaCO_3); (b) calcined limestone (CaO) after calcination procedure described in Section 4.2.2.

D

Online tar measurement by UV-Vis spectroscopy

D.1. Experimental equipment

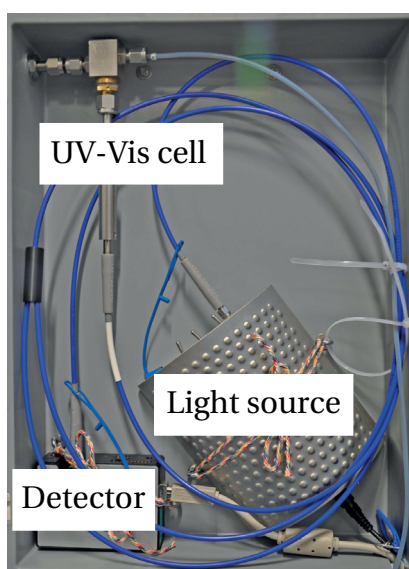


Figure D.1 – Photograph of online UV-Vis measurement unit as described in Section 5.2.3. The depicted unit includes a UV-Vis flow-through cell, light source and detector.

D

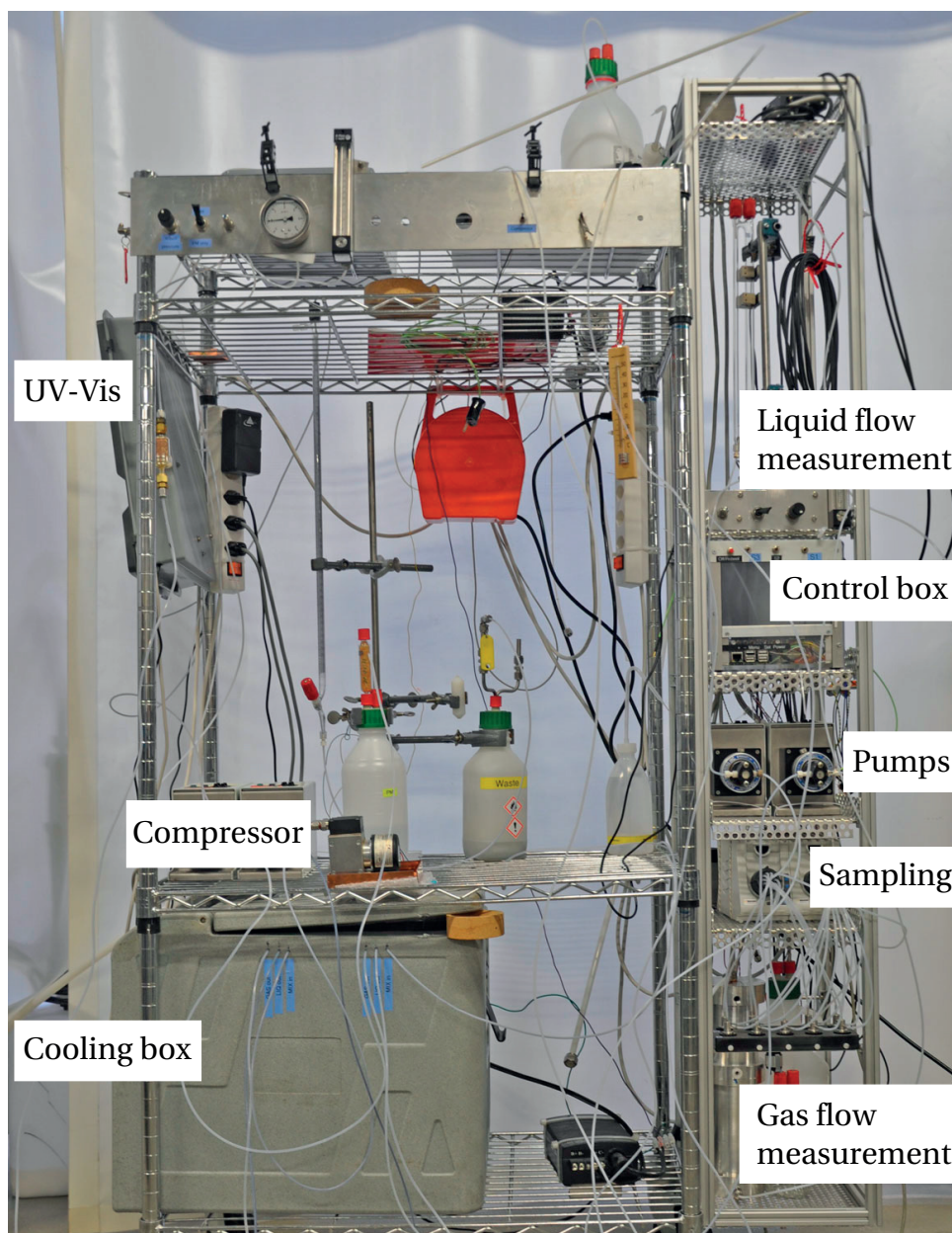


Figure D.2 – Photograph of sampling system described in Section 5.2.2

D.2. Partial least squares calibration

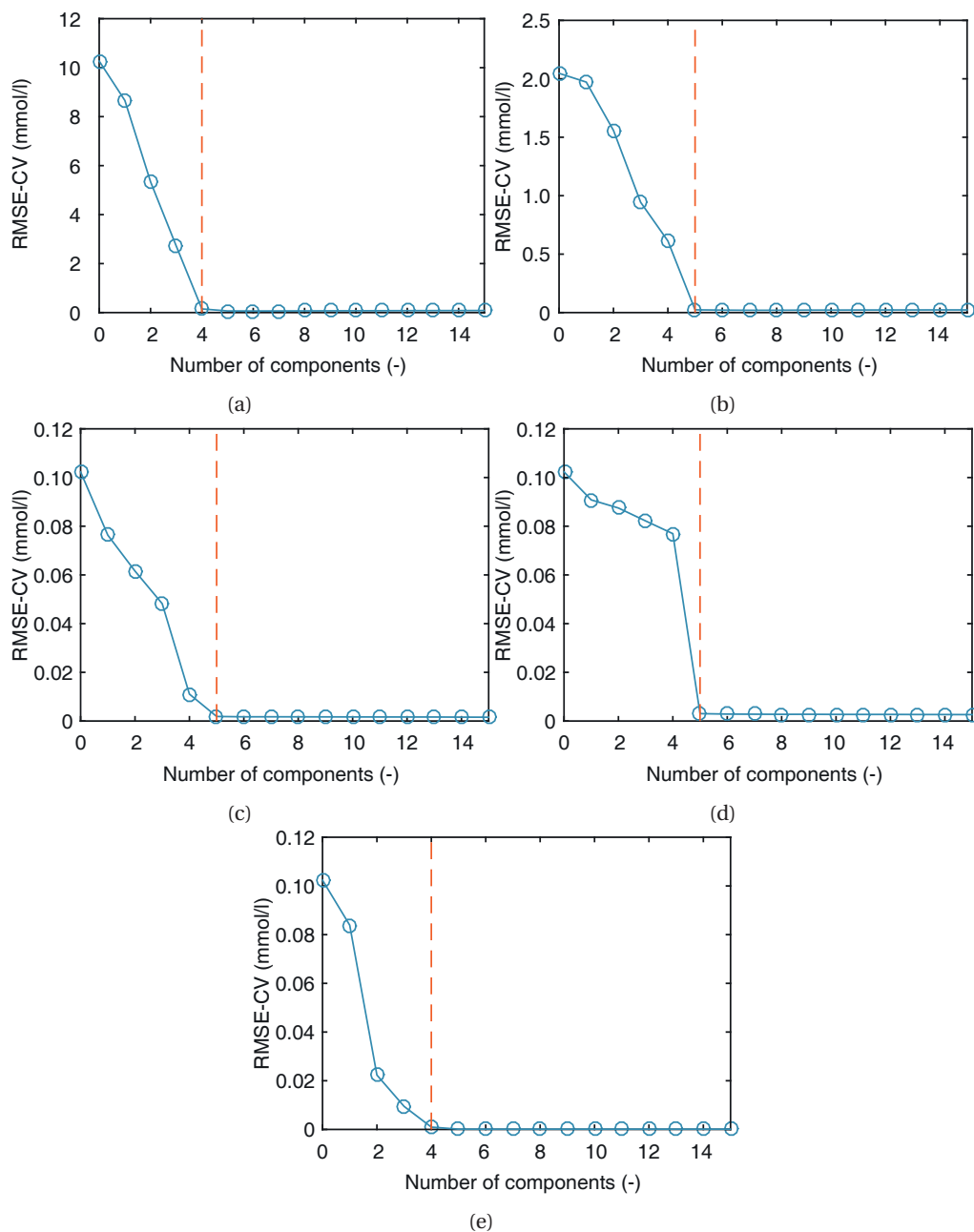


Figure D.3 – Variation of the root mean squared error of cross-validation (RMSE-CV) as a function of number of PLS components for different tar species: (a) Benzene; (b) toluene; (c) styrene; (d) indene; (e) naphthalene. Vertical lines indicate the chosen number of PLS components as discussed in Section 5.2.5.

D

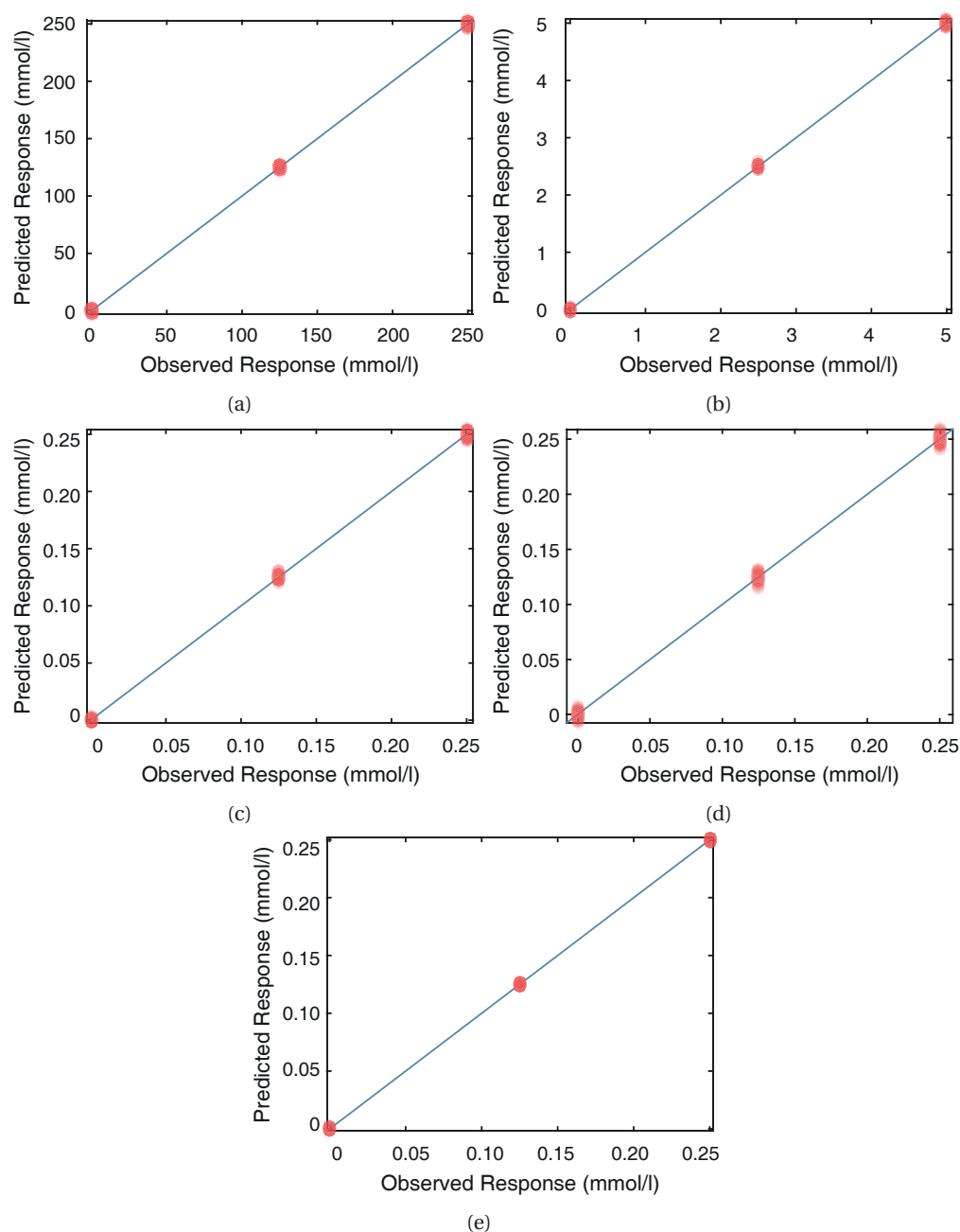


Figure D.4 – Parity plots of the predicted *versus* observed tar species concentration, calculated for the calibration set (see also Section 5.2.5). This set contains five tar compounds as factors at three levels, sampled by means of a full factorial design (3^5). Semi-transparent data points allow visual estimation of the point density. (a) Benzene; (b) toluene; (c) styrene; (d) indene; (e) naphthalene.

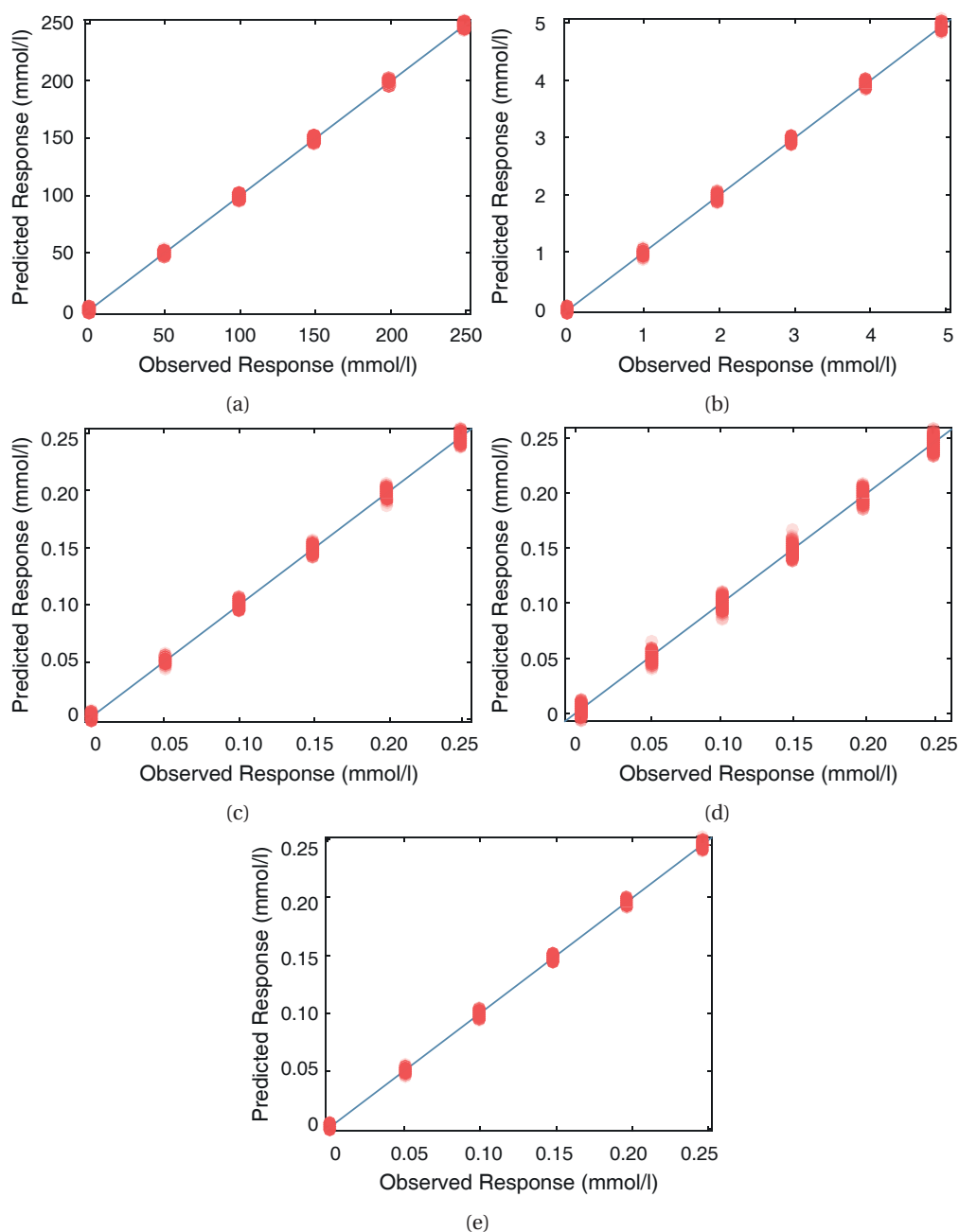


Figure D.5 – Parity plots of the predicted *versus* observed tar species concentration, calculated for the validation set (see also Section 5.2.5). This set contains five tar compounds as factors at six levels, sampled by means of a full factorial design (6^5). Semi-transparent data points allow visual estimation of the point density. (a) Benzene; (b) toluene; (c) styrene; (d) indene; (e) naphthalene.

D.3. Results of model gas case study

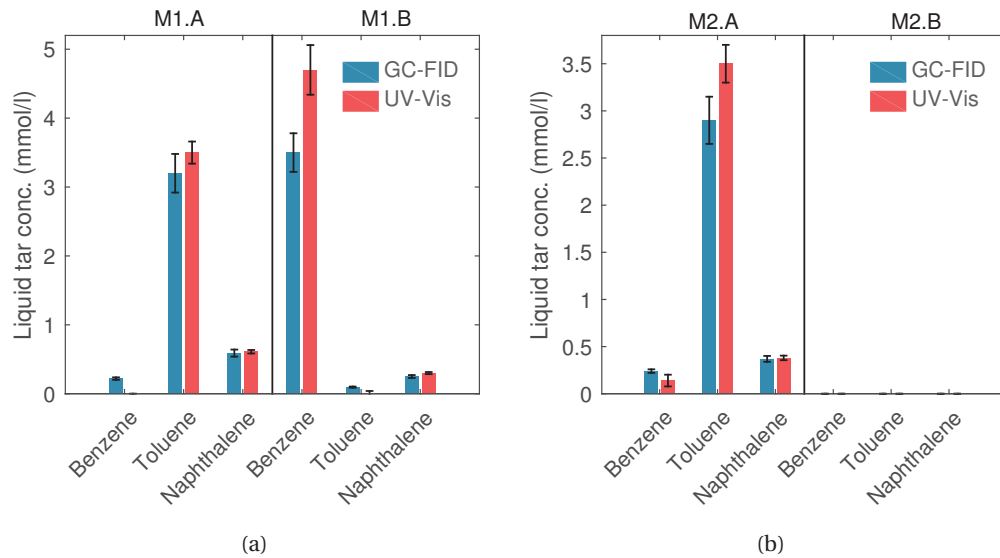


Figure D.6 – Comparison of tar concentrations in the liquid sample, measured by the UV-Vis and the GC-FID reference method (see also Section 5.3.1). A total of four samples from two experiments (M1, M2) with two sampling positions (A/B) each were analysed. (a) Experiment M1; (b) experiment M2.

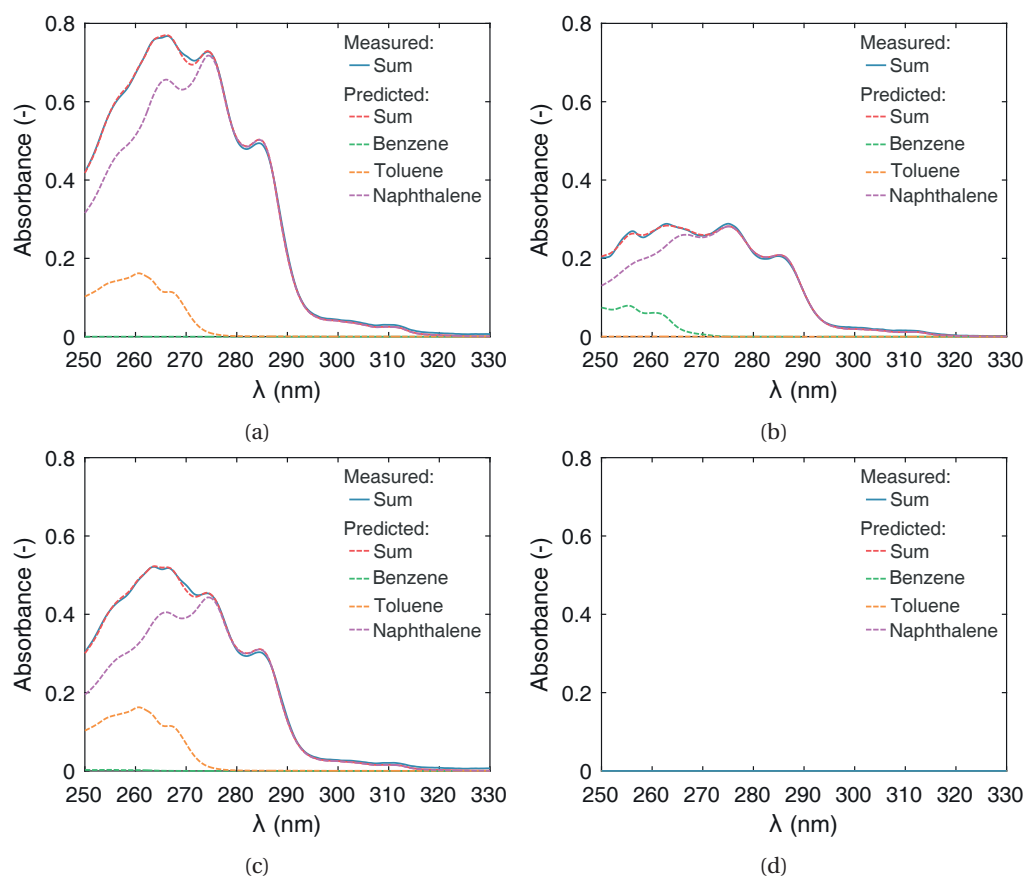


Figure D.7 – Plots containing UV-Vis spectra of the measured sample and predicted spectra of the individual tar compounds. Spectra decomposition was performed by the classical least squares approach (CLS) as discussed in Sections 5.2.5 and 5.3.1. A total of four samples from two experiments (M1, M2) with two sampling positions (A/B) each were analysed. (a) Experiment M1, line A (M1.A); (b) experiment M1, line B (M1.B); (c) Experiment M2, line A (M2.A); (d) experiment M2, line A (M2.B)

D.4. Online gas phase tar measurement by UV-Vis spectroscopy

D.4.1. Experimental

The applicability of UV-Vis spectroscopy for gas phase measurement of UV-Vis active hydrocarbons was demonstrated by means of a simple experimental setup, presented in Figs. D.8 and D.9. Thiophene (C_4H_4S) was chosen as a representative of (sulphur containing) hydrocarbons. Its gas concentration was adjusted by pumping (syringe pump, PHD 2000, Harvard Apparatus) saturated thiophene vapour into an Ar carrier gas flow. The obtained thiophene concentration is hence a function of flow rates, temperature and pressure.

UV-Vis analysis was performed by sending this defined C_4H_4S /Ar mixture to a UV-Vis gas cell (path length 2000 mm). The cell was connected to a deuterium, tungsten-halogen light source (DH-2000-BAL, Ocean Optics) and a single beam spectrometer (USB2000+XR1, Ocean Optics) by optical fibers. Spectra were recorded in the range 188 to 1032 nm at 0.4 nm intervals. Typical spectral detection rates were about 0.27 Hz.

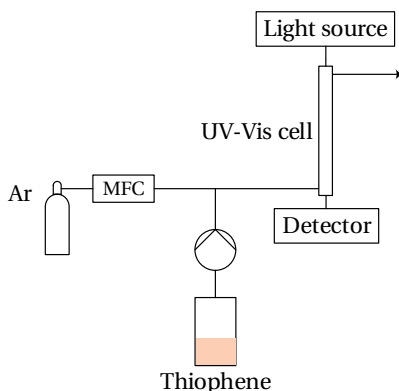


Figure D.8 – Schematic representations of experimental setup for gas phase UV-Vis detection of thiophene

D.4.2. Results

In order to obtain a calibration curve, thiophene concentrations were varied in the range of 36 to 154 ppmv. Figure D.10a presents the recorded absorbance at 241.6 nm as a function of time. The signal changes within seconds upon changing the inlet gas composition, an advantage compared to response times in the order of several minutes when a sampling system coupled with an UV-Vis is used.

The calculated calibration curve is given in Fig. D.10b. The calculated R^2 is good with 0.9919.

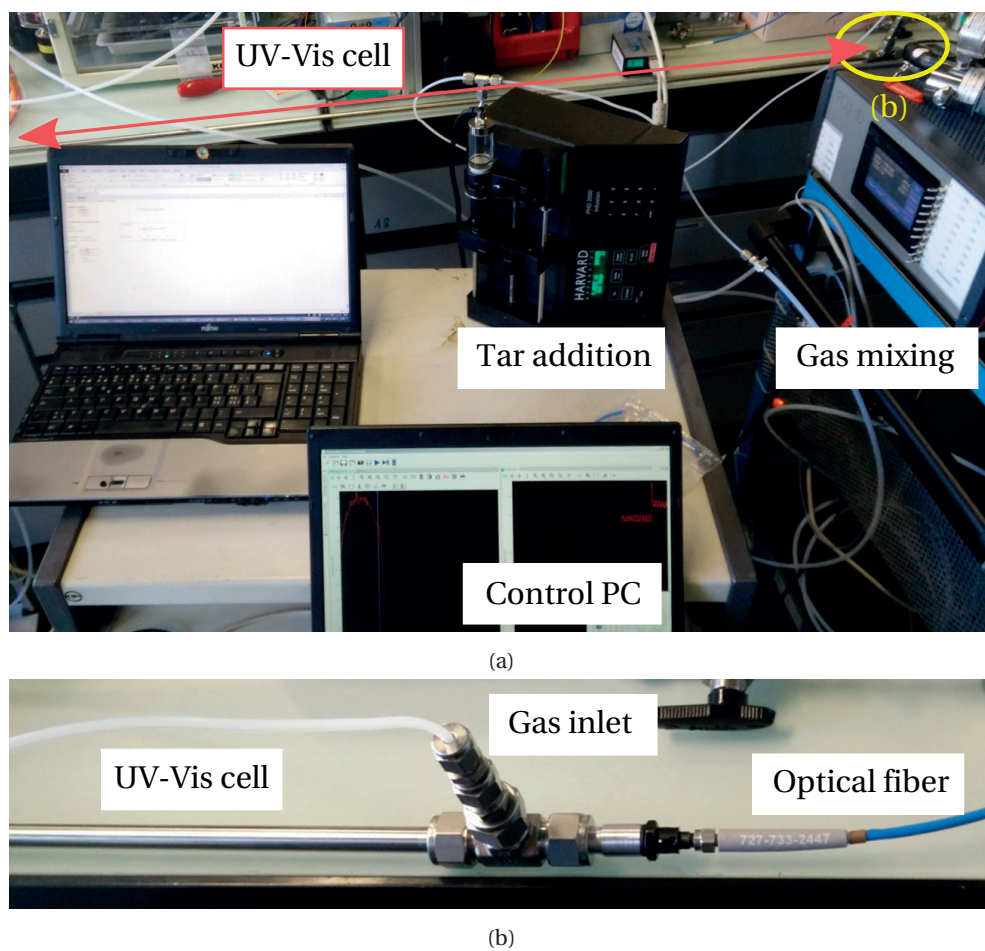
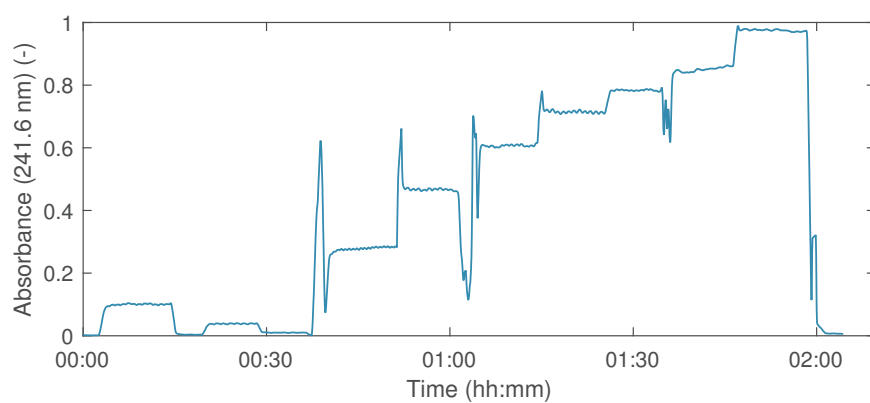
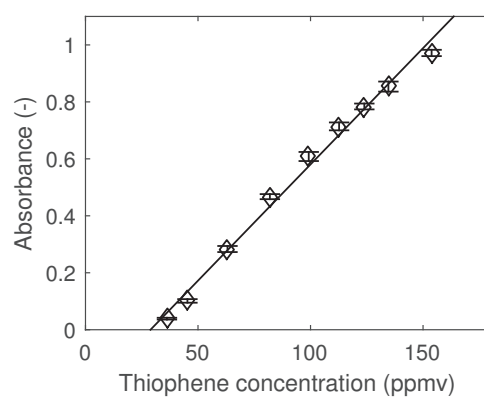


Figure D.9 – (a) Photograph of experimental setup for gas phase UV-Vis detection of thiophene; (b) detailed view of gas inlet of UV-Vis cell.

D



(a)



(b)

Figure D.10 – Results of preliminary gas phase UV-Vis detection experiments. (a) Measured absorbance at 241.6 nm at different thiophene concentrations *versus* time; (b) calibration curve for thiophene.

E

Detection and retention of selenium

E.1. Estimation of expected Se emission limitation

Based on the final US EPA rule¹ concerning the emission of hazardous air pollutants (HAP) an estimation of allowable H₂Se concentrations in the producer gas of integrated gasification combined cycle (IGCC) processes can be made. Because the control of Se concentration is assumed to take place before the gas turbine (see Section 6.1) of the IGCC process, these conditions lay the basis for the following calculations. The given Se emission limitation is expressed by the parameter α_{EPA} , defined as

$$\alpha_{EPA} = 0.3 \frac{\text{lb(Se)}}{\text{GWh}} \frac{0.4536 \text{ kg(Se)}}{\text{lb(Se)}} \frac{\text{h}}{3600 \text{ s}} \quad (\text{E.1})$$

Based on this value, the allowable gas concentration $y_{Se,EPA}$ can be approximated as

$$y_{Se,EPA} = \frac{\alpha_{EPA} V_m \eta_{el} LHV_{coal} \beta}{\tilde{M}_{Se}} \cong 50 \text{ ppbv} \quad (\text{E.2})$$

where V_m represents the molar volume, η_{el} the electric efficiency of the power plant ($\eta_{el} = 0.4$), LHV_{coal} the lower heating value of coal ($LHV_{coal} = 24 \text{ MJ kg}^{-1}$) and \tilde{M}_{Se} the molecular weight of Se. The parameter β describes the relation between the coal feed to the gasifier and the exiting volumetric raw gas flow² as defined in

$$\beta = 0.48 \frac{\text{kg(coal)}}{\text{Nm}^3} \quad (\text{E.3})$$

E.2. Literature overview of matrix effects

The following two tables present a literature overview of effects of H₂ (Table E.1) and H₂O (Table E.2) encountered in ICP spectroscopy.

Table E.1 – Literature overview regarding the effects of H₂ in ICP spectroscopy

| Ref. | Instrument | Feed | H ₂ | Other gases | Plasma temperature | Electron temperature | Note |
|------|------------|---|--|----------------------------|---|---|--|
| 3 | LA-ICP-MS | Aerosol (from laser ablation) | 0-14 ml/min (central channel) | Ar 1.8 l/min He 1 l/min | No evidence for increased plasma T (explained by unchanged slope of lens calibration) | Increased (because of higher doubly charged ratios) | <ul style="list-style-type: none">• Dry plasma• Auto lens after each H₂ gas flow change (lens voltage decreases with increasing H₂)• General sensitivity increase (for ⁷⁷Se factor 3), but dependent on elements. Decreasing sensitivity above certain H₂ flow• LOD generally decreased. For ⁷⁷Se increase two fold due to increased H₂ polyatomic interferences in blank measurement• Maybe change in plasma geometry• Difference in results to previous papers where negligible H₂ effects were observed explained by different laser system (wavelength in specific)• LA leads to complex aerosol with different particle sized and compositions (-> comparable to measurement of gas molecules?) |
| 4 | ICP-AES | Aerosol slurry nebulization) | (from 0-150 ml/min (central channel) | Ar 0.65 l/min | | | <ul style="list-style-type: none">• H₂ could be increased up to 15 vol% (120 ml/min). Higher flows (20 vol%, 160 ml/min) resulted in plasma extinction• With H₂ addition plasma volume decreases• More efficient slurry evaporation in H₂-Ar plasma |
| 5 | ICP | Aerosol (central or intermediate channel) | 0-200 ml/min (central or intermediate channel) | Ar 2.2 l/min | <ul style="list-style-type: none">• H₂ has higher thermal conductivity than Ar, so an increase in T is expected when H₂ is increased• 2000 K increase when H₂ added to central channel for intermediate channel even higher | Increased of ≈1500 K | <ul style="list-style-type: none">• When H₂ is added the plasma changes (plasma pulls away from torch injector tube, plasma volume decreases) |
| 6 | ICP-MS | Aerosol | 5 vol% in nebulizer gas | Ar 1.74 l/min | | | <ul style="list-style-type: none">• H₂ addition caused significant increase of interferences from Ar based polyatomic ions. Interferences from metal oxides were reduced, however• Wet plasma |
| 7 | ICP-MS | Aerosol | 0-50 ml/min | Ar 1.64 l/min | | | <ul style="list-style-type: none">• Wet plasma• Slight signal increase for ⁷⁸Se when H₂ added, then signal decrease of about 50% when reaching 50 ml/min H₂• Background signal on ⁷⁸Se increases slightly (3.6%) when adding 20 ml/min H₂• Cautious, qualitative statement that S/B ratio increases slightly for most elements when adding 20 ml/min of H₂ |
| 8 | ICP-AES | Aerosol | 0-50 ml/min | Ar 0.65 l/min | | | <ul style="list-style-type: none">• Increase in excitation temperature (1000 K) when adding H₂• Addition of 50 ml/min of H₂ to central channel improves energy transfer between ring plasma and the injected species |
| 9 | ICP-MS | Gas | 1-7.5 ml/min | Ar 1-2 l/min | | | <ul style="list-style-type: none">• Dry plasma• Assumed that H₂ addition would be beneficial to energy transfer processes between bulk plasma and the central channel• Signal of ¹²⁷I in dependence of H₂ flow plotted. Results show that the signal increased by over 70% when adding 7.5 ml/min H₂• Increased reflected power observed when H₂ added (30 W at 7.5 ml/min H₂) |

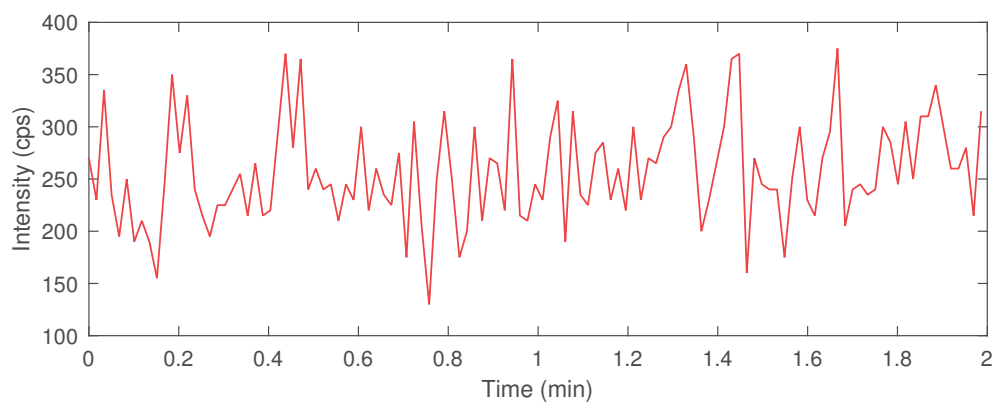
Table E.2 – Literature overview regarding the effects of H₂O in ICP spectroscopy

| Ref. | Instrument | Feed | H ₂ O | Other gases | Plasma temperature | Electron temperature | Note |
|------|------------|------------------|-----------------------|------------------------------|--------------------|----------------------|---|
| 10 | LA-ICP-MS | Aerosol | (from LA) 5.1 NmL/min | Ar 1.4 l/min He 0.5 l/min | | | <ul style="list-style-type: none">• Sensitivity: Without shielded torch decrease (20%) of sensitivity for ⁸²Se• Sensitivity: With shielded torch increase by a factor of 2.5 upon H₂O addition• Addition of H₂O increases and broadens the kinetic energy distribution which reduces the ions transportation efficiency• Change of plasma geometry when adding H₂O |
| 11 | ETV-ICP-MS | Dired (from ETV) | aerosol 4.1 NmL/min | Ar 2 l/min | | | <ul style="list-style-type: none">• Signals enhancement for Zn, Pb, Cu, As and Sb for small water loading |

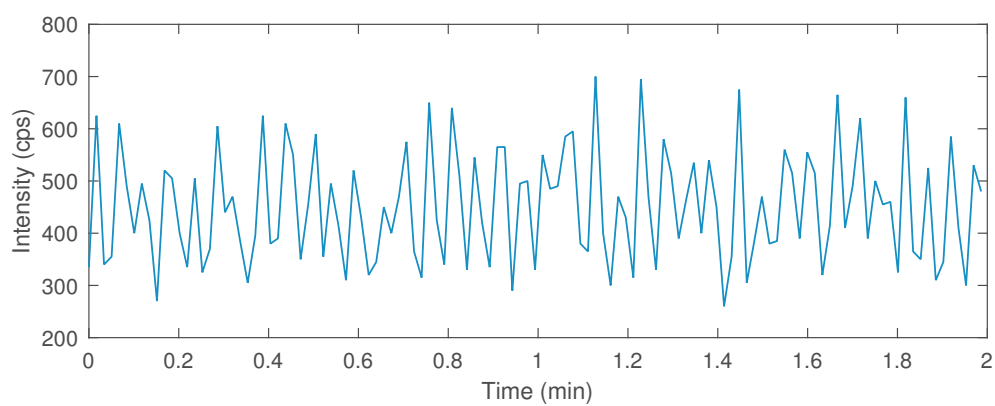
E.3. Spectral analysis of signals measured with setup 2

Experiments with setup 2 were performed as described in Sections 2.2 and 6.3.1. Recorded signals for the blank and 0.6 ppbv(rx) H_2Se concentration experiments are given in Figs. E.1a and E.1b, respectively. In order to find possible dominant frequencies in these time series, periodograms were calculated for each case and are presented in Figs. E.1c and E.1d¹².

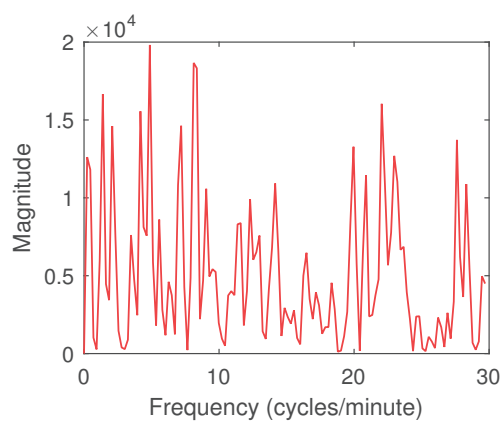
No dominant frequency can be observed for the experiment with 0 ppbv(rx) H_2Se concentration. This is coherent with the fact that the RDD was not rotating. However, at 0.6 ppbv(rx) H_2Se concentration, a feature at 18.8 min^{-1} is observed, a frequency that can be related to the rotating disk speed of the RDD.



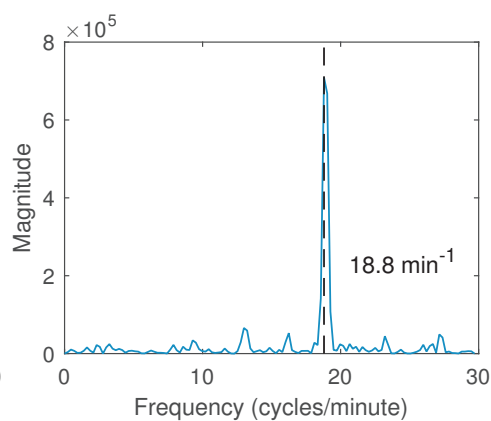
(a)



(b)



(c)



(d)

Figure E.1 – Spectral analysis of signals measured with setup 2. (a) Time series for blank experiment (0 ppbv(rx) H_2Se); (b) time series for 0.6 ppbv(rx) H_2Se experiment; (c) periodogram for blank experiment; (d) periodogram for 0.6 ppbv(rx) experiment.

E.4. Calculation of physical properties of flow through sorbent bed

Calculation of the physical properties of the fluid phase in the packed sorbent bed is based on several assumptions. The viscosity of the fluid is calculated, assuming a binary H_2 -Ar gas mixture¹³. The gas density is calculated assuming ideal gases. Measured values of the diffusivity of H_2Se were not readily available. The diffusivity is therefore calculated from the known, chemically similar, species H_2S , based on the relationship of diffusivities to molecular weight¹⁴

$$D_{H_2Se} = D_{H_2S} \left(\frac{\widetilde{M}_{H_2Se}}{\widetilde{M}_{H_2S}} \right)^{-1/2} \quad (E.4)$$

In this equation, the D_x refer to the diffusivities and \widetilde{M}_x to the molecular weights. Based on the obtained diffusivity D_{H_2Se} , the diffusion coefficient $D_{H_2Se,Ar}$ of H_2Se in Ar is calculated according to the Fuller equation¹⁵.

The axial dispersion coefficient D_{ax} is calculated according to

$$D_{ax} = D_{H_2Se,Ar} \left(1 - \sqrt{1 - \epsilon_B} \right) + \frac{u_s d_p}{2} \quad (E.5)$$

where ϵ_B refers to the bed porosity¹⁶.

E.5. Equilibrium constants

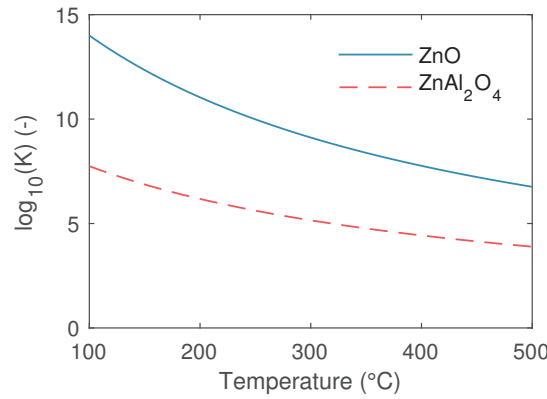
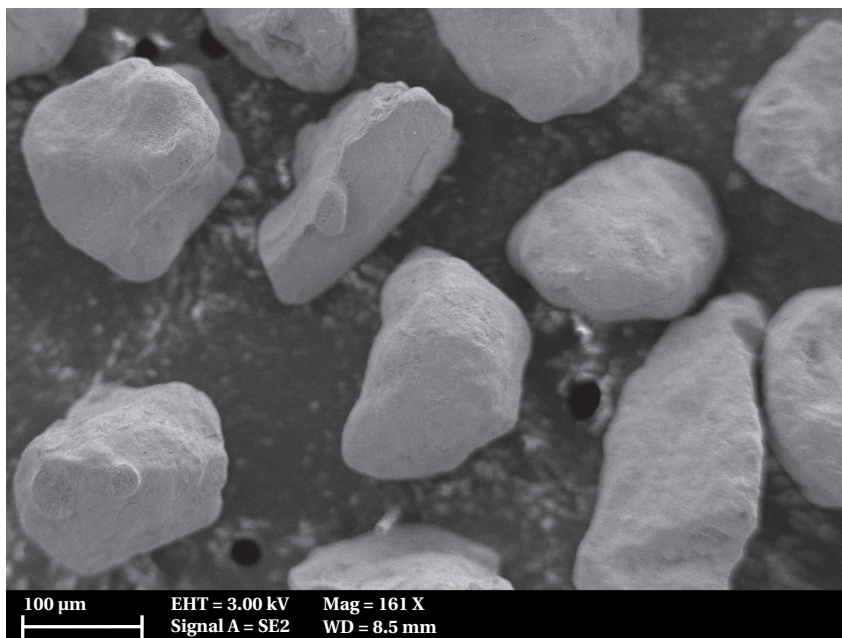
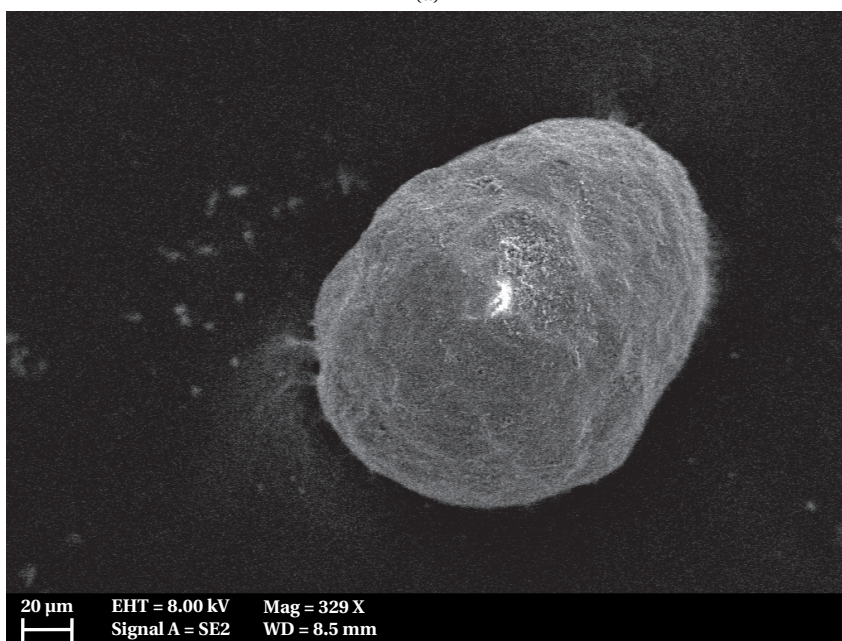


Figure E.2 – Equilibrium constants for the system $ZnO + H_2Se \longleftrightarrow ZnSe + H_2O$ (blue) and for the system $ZnAl_2O_4 + H_2Se \longleftrightarrow ZnSe + Al_2O_3 + H_2O$ (red - dashed)

E.6. Sorbent characterization



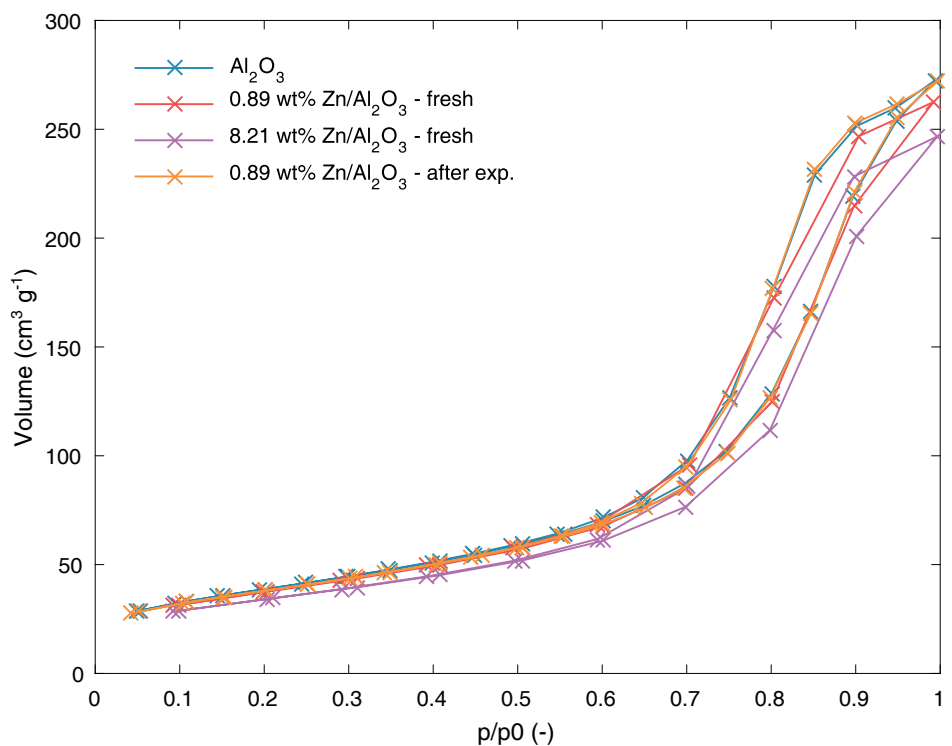
(a)



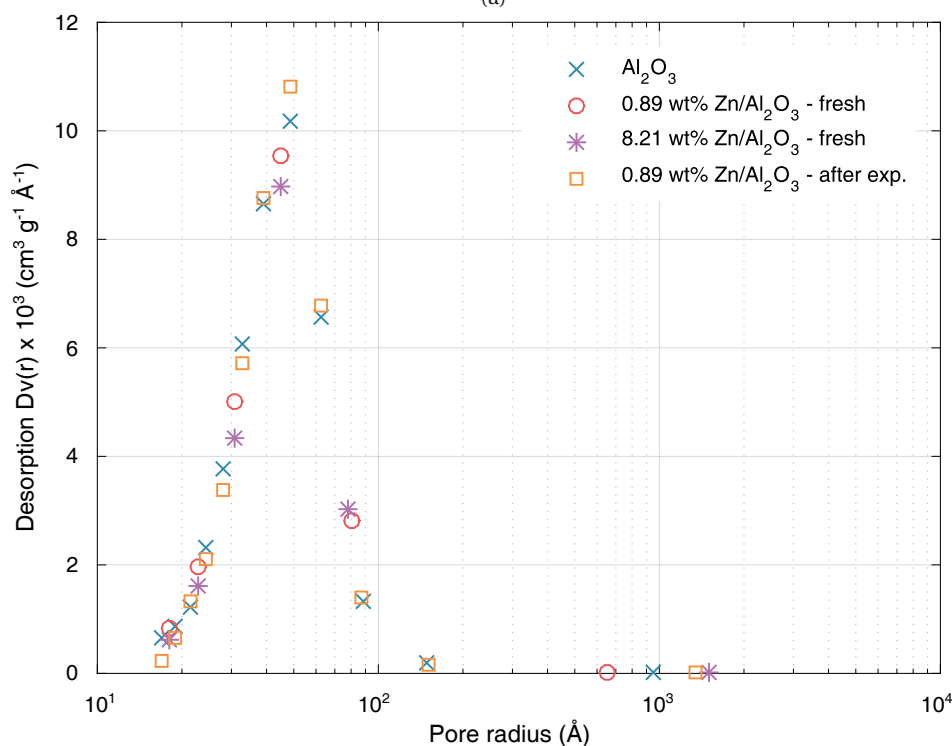
(b)

Figure E.3 – Scanning electron microscope pictures (a) of 0.89 wt% Zn/Al₂O₃ sorbent before H₂Se sorption experiment; (b) of 0.89 wt% Zn/Al₂O₃ sorbent after H₂Se exposure.

E



(a)



(b)

Figure E.4 – (a) N_2 adsorption-desorption isotherms of Al_2O_3 support and Zn/Al_2O_3 sorbent materials at 77 K; (b) pore size distributions (as calculated by BJH method) of Al_2O_3 support and Zn/Al_2O_3 sorbent materials.

E.7. Influence of operating conditions on sorbent capacity

Table E.3 – Expected effects of temperature and steam content on H₂Se capacities of Zn/Al₂O₃ sorbents

| | Reaction | Temperature (↑) | Steam content (↑) | Notes |
|--------------|----------------------------------|---|---|--|
| Support | Physisorption | ↓ | ↓ (competitive adsorption) | • Both chemisorption and physisorption (capacity same OM) for H ₂ Se on alumina at room temperature (in N ₂ , dry) have been reported ¹⁷ |
| | Chemisorption | ↑ | ↓ (competitive adsorption) | |
| Active Phase | ZnO | <ul style="list-style-type: none">• ↑ (reaction rate, e^{-1/T})• ↑ (mass transfer, T^{3/2})• ↘ (equilibrium constant) | <ul style="list-style-type: none">• ↘ (equilibrium constant)• ↘ (competitive adsorption) | <ul style="list-style-type: none">• Reportedly more reactive than ZnAl₂O₄ for sulfidation¹⁸• Low H₂Se equilibrium concentration (≈10 pptv @ 10 vol% H₂O, 250°C)• XRD analysis shows no indication that ZnO or ZnAl₂O₄ phase existent on 0.89 wt% Zn/Al₂O₃ sorbent (too high dispersion)• Sulfidation of ZnO involves two processes: Fast surface reaction. Slow outward growth of remaining Zn to form ZnS^{19,20} |
| | ZnAl ₂ O ₄ | <ul style="list-style-type: none">• • ↑ (reaction rate, e^{-1/T})• • ↑ (mass transfer, T^{3/2})• • ↘ (equilibrium constant) | <ul style="list-style-type: none">• • ↘ (equilibrium constant)• • ↘ (competitive adsorption) | <ul style="list-style-type: none">• High H₂Se equilibrium concentration (≈242 ppbv @ 10 vol% H₂O, 250°C)• Phase maybe existent at low Zn loadings (indications by literature¹⁸), but not measurable |

E.8. Online detection of trace contaminants (Hg^0 , PH_3 , AsH_3) in reducing gasification atmosphere

E.8.1. Experimental

Two experimental setups, based on the Trace element setup described in Section 2.2, have been employed in this work. The first one is based on setup 1, where the $\text{H}_2\text{Se}/\text{H}_2$ gas cylinder was replaced for a gas cylinder containing a mixture of AsH_3 and PH_3 (48 ppmv AsH_3 , 55 ppmv in H_2).

Experiments involving the trace element Hg were performed in setup 3. A schematic of which is given in Fig. E.5.

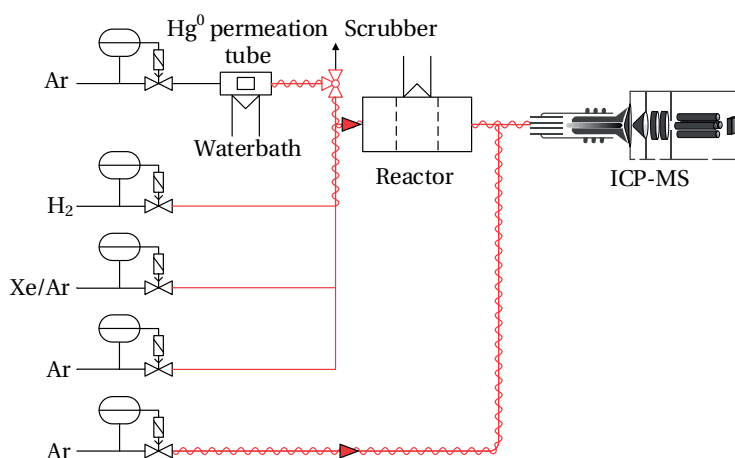


Figure E.5 – Schematic representation of the Trace element setup (setup 3) used for Hg calibration experiments

The setup shares many of the features of setup 1, but has been modified to include a Hg^0 generation device. Steam generation was omitted in this setup. A constant Ar flow of $37.5 \text{ Nml min}^{-1}$ was passed along an Hg permeation tube (Vici). The Hg^0 permeation rate is temperature dependent and controlled by means of a water bath. The Hg^0 containing gas flow was either directed to a gas scrubber or towards an empty quartz reactor. The latter stream was diluted by H_2 , Ar and an Xe/Ar mixture, where the Xe acted as an internal standard.

E.8.2. Results

Calibration

Calibration curves for all three analytes are shown in Fig. E.6.

The calibration results are summarized in Table E.4. The coefficients of determination for all species are > 0.998 , indicating a good linear response. The detection limits for P is below 2 ppbv, while those of As (0.1 ppbv) and Hg (0.002 ppbv) are significantly lower.

Dynamic effects

The response time characteristics of an analytical method become of importance when transient processes such as sorption processes are studied. In order to investigate these characteristics, step response and wash-out experiments involving AsH_3 , Hg and PH_3 were performed. A signal increase of species AsH_3 and PH_3 is detected 2 to 8 s after analyte (2.4 to 2.7 ppmv)

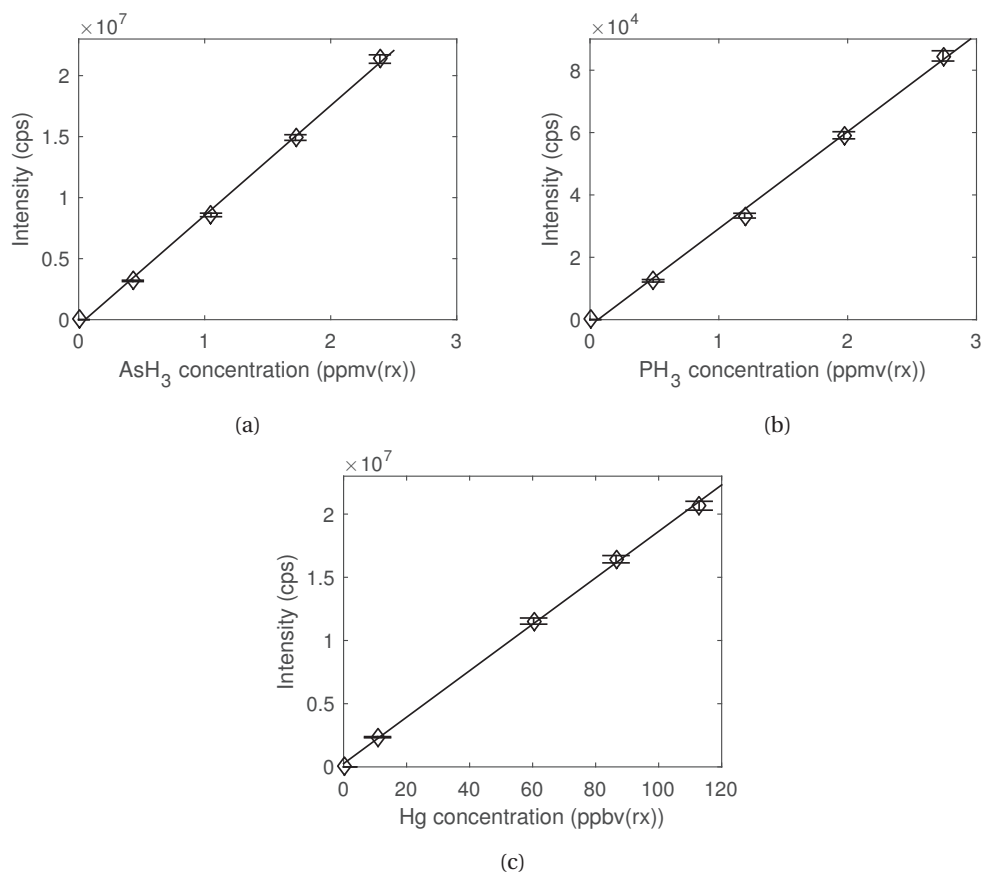


Figure E.6 – Calibration curves for (a) AsH_3 measured on isotope ^{75}As ; (b) PH_3 measured on isotope ^{31}P ; (c) Hg measured on isotope ^{202}Hg .

Table E.4 – Calibration results

| | ^{199}Hg | ^{200}Hg | ^{201}Hg | ^{202}Hg | ^{75}As | ^{31}P |
|-----------------------------|-------------------|-------------------|-------------------|-------------------|--|--|
| R^2 | 0.9992 | 0.9992 | 0.9991 | 0.9990 | 0.9978 | 0.9982 |
| LOD (ppbv(rx)) | 0.003 | 0.003 | 0.004 | 0.002 | 0.1 | 1.6 |
| Abundance (mol/mol %) | 16.9 | 23.1 | 13.2 | 29.9 | 100 | 100 |
| Interferences ²¹ | | | | | $^{36}\text{Ar}^{38}\text{Ar}^1\text{H}^+$ | $^{14}\text{N}^{16}\text{O}^1\text{H}^+$, $^{15}\text{N}^{15}\text{N}^1\text{H}^+$, $^{15}\text{N}^{16}\text{O}^+$, $^{14}\text{N}^{17}\text{O}^+$, $^{13}\text{C}^{18}\text{O}^+$, $^{12}\text{C}^{18}\text{O}^1\text{H}^+$ |

addition to the inlet gas stream. 98 % of the stable signal was reached after 13 to 20 s, depending on analyte. The washout behaviour was analysed by stopping the analyte feed at a certain point in time and observe the signal response. Both species show an initially steep decrease in signal, followed by significant tailing. While this is of no direct consequence when measuring breakthrough curves it can affect the time in-between measurements as detection limits are increased due to the increased background levels. In case of the performed experiments, detection limits of 4 to 7 ppbv were measured, 5 min after the contaminant addition was stopped.

Experiments involving Hg^0 were performed at different concentration (8 ppbv) levels in setup 3. The response time is similar to those of the other analytes, with a stable signal being reached after 40 s. When Hg^0 addition is stopped, a 99 % decrease is observed after 1 min, and the limit of detection after 5 min is 0.07 ppbv.

References

- [1] United States environmental protection agency, national emission standards for hazardous air pollutants from coal- and oil-fired electric utility steam generating units and standards of performance for fossil-fuel-fired electric utility, industrial-commercial- institutional, and small industrial-commercial-institutional steam generating units; final rule. 77(32):9304–9513, 2012.
- [2] Christopher Higman and Maarten van der Burgt. *Gasification*. Elsevier, Amsterdam, 2nd edition, 2008.
- [3] Marcel Guillong and Christoph A. Heinrich. Sensitivity enhancement in laser ablation ICp-ms using small amounts of hydrogen in the carrier gas. *Journal of Analytical Atomic Spectrometry*, 22(12):1488–1494, 2007.
- [4] P. Heitland and J. A. C. Broekaert. Addition of small amounts of helium and hydrogen to the working gases in slurry nebulization inductively coupled plasma atomic emission spectrometry for the analysis of ceramic powders. *Journal of Analytical Atomic Spectrometry*, 12(9):981–986, 1997.
- [5] Norman N. Sesi, Amelia Mackenzie, Kathryn E. Shanks, Pengyuan Yang, and Gary M. Hieftje. Fundamental studies of mixed-gas inductively coupled plasmas. *Spectrochimica Acta Part B: Atomic Spectroscopy*, 49(12–14):1259–1282, 1994.
- [6] L. Ebdon, M. J. Ford, P. Goodall, and S. J. Hill. Hydrogen addition to the nebulizer gas for the removal of polyatomic ion interferences in inductively coupled plasma mass spectrometry. *Microchemical Journal*, 48(3):246–258, 1993.
- [7] Honway Louie and Susan Yoke-Peng Soo. Use of nitrogen and hydrogen in inductively coupled plasma mass spectrometry. *Journal of Analytical Atomic Spectrometry*, 7(3): 557–564, 1992.
- [8] M. Murillo and J. M. Mermet. Improvement of the energy transfer with added-hydrogen in inductively coupled plasma atomic emission spectrometry. *Spectrochimica Acta Part B: Atomic Spectroscopy*, 44(4):359–366, 1989.
- [9] Robert C. Hutton, M. Bridenne, E. Coffre, Y. Marot, and F. Simondet. Investigations into the direct analysis of semiconductor grade gases by inductively coupled plasma mass spectrometry. *Journal of Analytical Atomic Spectrometry*, 5(6):463–466, 1990.
- [10] S. H. Liu, Z. C. Hu, D. Gunther, Y. H. Ye, Y. S. Liu, S. Gao, and S. H. Hu. Signal enhancement in laser ablation inductively coupled plasma-mass spectrometry using water and/or ethanol vapor in combination with a shielded torch. *Journal of Analytical Atomic Spectrometry*, 29(3):536–544, 2014.
- [11] J. F. Alary and E. D. Salin. Quantitation of water and plasma diagnosis for electrothermal vaporization-inductively coupled plasma mass spectrometry: The use of argon and argide polyatomics as probing species. *Spectrochimica Acta Part B-Atomic Spectroscopy*, 53(12): 1705–1721, 1998.
- [12] Petre Stoica and Randolph L Moses. *Spectral analysis of signals*. Prentice Hall, Upper Saddle River, New Jersey, 2005.

- [13] C. R. Wilke. A viscosity equation for gas mixtures. *The Journal of Chemical Physics*, 18(4): 517–519, 1950.
- [14] Louis J. Thibodeaux. *Handbook of chemical mass transport in the environment*. Environmental chemistry & toxicology. CRC Press, Boca Raton, 2011.
- [15] Edward N. Fuller, Paul D. Schettler, and J. Calvin Giddings. New method for prediction of binary gas-phase diffusion coefficients. *Industrial & Engineering Chemistry*, 58(5):18–27, 1966.
- [16] VDI. *VDI Heat Atlas*. Springer reference. Springer, Berlin, 2nd edition, 2010.
- [17] Tadaharu Watanabe, Takashi Suzuki, and Nobukazu Kinomura. Adsorption of diborane and hydrogen selenide on porous alumina and silica. *Journal of Materials Science: Materials in Electronics*, 9(2):127–132, 1998.
- [18] Brian R. Strohmeier and David M. Hercules. Surface spectroscopic characterization of the interaction between zinc ions and gamma-alumina. *Journal of Catalysis*, 86(2):266–279, 1984.
- [19] Laure Neveux, David Chiche, Delphine Bazer-Bachi, Loic Favergeon, and Michele Pijolat. New insight on the zno sulfidation reaction: Evidences for an outward growth process of the zns phase. *Chemical Engineering Journal*, 181:508–515, 2012.
- [20] Igor Bezverkhy, Jonathan Skrzypski, Olga Safonova, and Jean-Pierre Bellat. Sulfidation mechanism of pure and cu-doped zno nanoparticles at moderate temperature: Tem and in situ xrd studies. *The Journal of Physical Chemistry C*, 116(27):14423–14430, 2012.
- [21] T. W. May and R. H. Wiedmeyer. A table of polyatomic interferences in ICp-ms. *Atomic Spectroscopy*, 19(5):150–155, 1998.

List of publications

Journal articles

10. M. Paraskevopoulos, **P. Edinger**, F. Pilger, A. Testino, C. Ludwig, *Synthesis and characterization of ceria-based materials to function as mercury and sulphur compounds sorbents*, In preparation.
9. **P. Edinger**, C. Ludwig, *High temperature conversion of thiophene over CaO*, In preparation.
8. M. Brandenberger, **P. Edinger**, H. Zimmerman, F. Vogel, C. Ludwig, *Microalgae, amino acids and proteins: nitrogen and sulfur removal*, In preparation.
7. D. Gschwend, P. Soltic, **P. Edinger**, A. Wokaun, F. Vogel, *Performance evaluation of gasoline alternatives using a detailed thermodynamic spark-ignition engine model*, In preparation.
6. **P. Edinger**, D. Grimekis, K. Panopoulos, C. Ludwig, *Adsorption of thiophene by activated carbon: A global sensitivity analysis*, Under review.
5. **P. Edinger**, J. Schneebeili, R. Struis, S. Biollaz, C. Ludwig, *Online liquid quench sampling and UV-Vis spectroscopy for tar measurements in wood gasification process gases*, Fuel 184, 59 (2016).
4. A. Hess, M. Tarik, D. Foppiano, **P. Edinger**, C. Ludwig, *Online size and element analysis of aerosol particles released from thermal treatment of wood samples impregnated with different salts*, Energy Fuels 30, 4072 (2016).
3. **P. Edinger**, M. Tarik, A. Hess, A. Testino, C. Ludwig, *Online detection of selenium and its retention in reducing gasification atmosphere*, Energy Fuels 30, 1237 (2016).
2. U. Rhyner, **P. Edinger**, T. J. Schildhauer, S. Biollaz, *Applied kinetics for modelling of reactive hot gas filters*, Appl. Energy 113, 766 (2014).
1. U. Rhyner, **P. Edinger**, T. J. Schildhauer, S. Biollaz, *Experimental study on high temperature catalytic conversion of tars and organic sulfur compounds*, Int. J. Hydrogen Energy 39, 4926 (2014).

Conference proceedings

2. **P. Edinger**, M. Tarik, C. Ludwig, *Online detection and retention of trace contaminants in reducing gasification atmosphere*, Proc. 33rd Annu. Int. Pittsburgh Coal Conf., 8-12 August, Cape Town, South Africa (2016).
1. U. Rhyner, **P. Edinger**, T. Schildhauer, *Warm and hot gas cleaning up to 850°C for high efficient biomass conversion processes*, Proc. 13th Int. Conf. on Polygeneration Strategies, 3-5 September, Vienna, Austria (2013).

Conference presentations and posters

3. **P. Edinger**, C. Ludwig, *UV-Vis spectroscopy as a tool for online tar measurements in wood gasification processes*, To be presented at 4th Eur. Conf. on Process Analytics and Control Technology (EuroPACT), 10-12 May, Potsdam, Germany (2017).
2. **P. Edinger**, M. Tarik, C. Ludwig, *Online detection and retention of trace contaminants in reducing gasification atmosphere*, Proc. 33rd Annu. Int. Pittsburgh Coal Conf., 8-12 August, Cape Town, South Africa (2016).
1. **P. Edinger**, T. Schildhauer, S. Biollaz, C. Ludwig, *Hot gas cleaning of woodgas for electricity and biofuels production*, Presented at NRP 66 Meeting, 9-10 April, Murten, Switzerland (2014).

Acknowledgements

This work owes much to many. For it is the combined support of the following persons that helped shaping this thesis into what it is today.

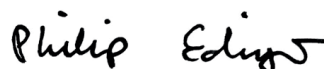
First of all, I am grateful to Christian Ludwig for welcoming me in his research group. Only his continuous backing ensured the successful completion of this thesis. I would also like to thank Andrea Testino for acting as thesis co-director.

Several further persons were involved directly in this work. Mohamed Tarik introduced me into the field of trace analysis using an ICP-MS. His knowledge and commitment were invaluable for the project presented in Chapter 6. Jörg Schneebeli shared his vast knowledge of analytical chemistry in uncounted discussions. These discussions, his enthusiasm and technical ingenuity helped to develop the method for tar analysis by UV-Vis spectroscopy presented in Chapter 5. Discussions with Tilman Schildhauer covering the more fundamental theme of this thesis served as a beacon in the wide sea of opportunities and constraints. The efficient collaboration with Dimitrios Grimekis, culminating in a joint publication presented in Chapter 3 is greatly acknowledged. I would also like to thank Frank Pilger and Miltiadis Paraskevopoulos for our combined investigations concerning the sorption of sulphur and mercury onto ceria.

The final manuscript benefited from countless discussions with Dominic Gschwend during coffee breaks and climbing-work sessions. You showed me that mountains are more than just an obstacle! Frank Schillinger not only provided valuable scientific input but also served as a friend outside PSI. Besides, I would like to thank the keen eyes of Martin Künstle and Rudolf Struis.

Further friends and colleagues that made the stay at PSI a time worthwhile are Simon Maurer and Felix Grygier as well as Adelaide Calbry-Muzyka, Eya Damergi, Erich de Boni, Gisela Herlein, Adrian Hess, Timon Käser, Alexander Knobl, Sergio Rodriguez, Michel Rossi, Albert Schuler, Jessica Settino, Sinan Teske, Vera Tschedanoff, Hansjörg Wagenbach, Tanja Wieseler and Julia Witte.

Owed to the nature of this text, the persons deserving most credit can only be stated last: Thank you Frauke, Dieter, Vanessa and Ana for your support during the past years!



Sven Philip Edinger
Zürich, 12 March 2017

Curriculum Vitæ

Sven Philip Edinger

✉ philip@edinger.email

Education

EPFL (École polytechnique fédérale de Lausanne)

PH.D. IN CHEMICAL ENGINEERING

Villigen-PSI, Switzerland

Nov. 2012 - Apr. 2017

- Dissertation: *Analysis and Removal of Product Gas Contaminants Present in Gasification Processes*
Advisor: Prof. Christian Ludwig

ETH (Eidgenössische Technische Hochschule Zürich)

M.Sc. IN PROCESS ENGINEERING

Zürich, Switzerland

Sep. 2009 - Oct. 2012

- M.Sc. Thesis: *High Temperature Conversion of Sulfur Containing Hydrocarbons and Tars*
Advisor: Prof. Aldo Steinfeld
- Semester Thesis: *Extraction in Micro Reactors*
Advisor: Prof. Philipp Rudolf von Rohr

University of Toronto

M.Sc. IN PROCESS ENGINEERING

Toronto, Canada

Sep. 2009 - Dec. 2009

- Exchange program with ETH Zürich.

ETH (Eidgenössische Technische Hochschule Zürich)

B.Sc. IN MECHANICAL ENGINEERING

Zürich, Switzerland

Oct. 2006 - Aug. 2009

- Thesis: *Studies on the Liquefaction of the Microalga *P. Tricornutum* and the Protein BSA*
Advisor: Prof. Aldo Steinfeld

Gymnasium Altona

CHEMICAL-TECHNICAL ASSISTANT

Hamburg, Germany

Aug. 2002 - Jan. 2006

- Education in parallel to high-school

Gelehrtenschule des Johanneums

GENERAL QUALIFICATION FOR UNIVERSITY ENTRANCE (GERMAN ABITUR)

Hamburg, Germany

Aug. 1996 - Jul. 2005

Awards

- 2013 **Willi Studer Prize**, ETH Zurich, D-MAVT, Process Engineering
- 2005 **GDCh-Abiturientenpreis**, Prize for best abitur in chemistry awarded by the German Chemical Society (GDCh)

Teaching

ETH (Eidgenössische Technische Hochschule Zürich)

TEACHING ASSISTANT, RENEWABLE ENERGY TECHNOLOGIES I

Zürich, Switzerland

Nov. 2012 - Jul. 2015

- Prepared and taught exercises
- Prepared, supervised and graded exams

Paul Scherrer Institute (PSI)

THESIS ADVISOR

Villigen-PSI, Switzerland

Feb. 2014 - Aug. 2014

- Coordinated joint diploma thesis between Karlsruhe Institute of Technology (KIT) and PSI
- Title: *Heißgasreinigung für Schwefelkomponenten aus Synthesegasen der Biomasse-Vergasung*

ETH (Eidgenössische Technische Hochschule Zürich)

TEACHING ASSISTANT, MECHANICS 1: KINEMATICS AND STATICS

- Taught exercises
- Supervised and graded exams

Zürich, Switzerland

Sep. 2008 - Jan. 2009

Internships

ABB Turbo Systems

INTERNSHIP

- Implemented a model to predict future sales of turbo chargers

Baden, Switzerland

Jul. 2012 - Oct. 2012

MTU Friedrichshafen

INTERNSHIP IN MECHANICAL WORKSHOP

- Obtained knowledge of advanced processing techniques

Friedrichshafen, Germany

Feb. 2007 - Mar. 2007

Skills & Interests

Languages

- German (mother tongue)
- English (fluent)
- Latin (Latin proficiency certificate)
- Ancient Greek

Software

- Proficient in: MATLAB, Aspen Plus, Mathematica, \LaTeX , MS Office, Athena Visual Studio, HSC Chemistry
- Experience with: Fluent, CFX, C++, Python, R, NX, AutoCAD, LabVIEW

Personal Interests

Tennis, Sailing, Alpine sports (Bouldering, Hiking, Skiing), Reading, Golf, Traveling

Extracurricular activities

Stiftung KOSTA (2010)